Bacteria as Nanofactories:

Silver Nanoparticle Bioproduction

Thomas M Mabey

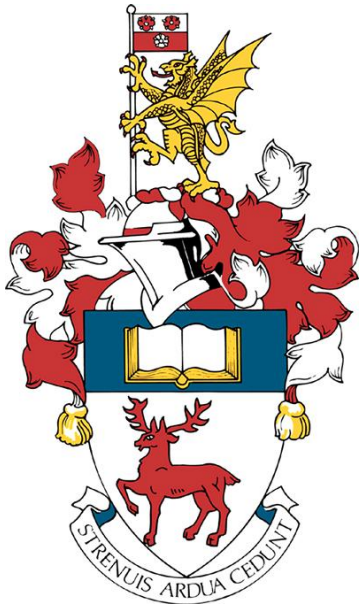

A thesis presented for the degree of

Doctor of Philosophy

Faculty of Engineering and Physical Sciences

University of Southampton

October 2019

Abstract

Silver nanoparticles (AgNPs) have unique chemical and physical properties which make them attractive in a range of applications. However, current productions methods are often hindered by challenges with poor particle stability, the use of hazardous chemicals under harsh conditions, and challenges with scale-up. Bacteria have been proposed as an alternative production route. However, the underlying biological mechanisms remain to be fully understood.

The aim of this project was to develop an environmentally friendly and scalable method for the production of stable AgNPs through the use of bacteria. This project also aimed to improve the understanding of bacterial AgNP production and to gain control over the shapes of AgNPs produced by bacteria.

The reaction conditions under which AgNPs were produced by *Morganella psychrotolerans* were investigated. The conditions examined had little effect on the properties particles being produced, however, the amount of production was affected by Ag^{+}, H^{+}, and Na^{+} concentrations. Moreover, it was observed that light exposure during synthesis was beneficial to production yields. To investigate this further, *M. psychrotolerans* was illuminated with LED light for 48 h during AgNP production. The amount of particles produced was considerably higher when samples were exposed to light compared to those in the dark. Moreover, shorter wavelengths of light were determined to be responsible for this increased. It was also discovered that sterile growth media was capable of photo-reducing Ag^{+} and contributed to the enhanced production.

Following this, laser light was used to increase the rate of production further. Spherical AgNPs were produced on the time-scale of seconds rather than hours when reactions were conducted in the dark. This process was thought to be photo-catalytic rather than a thermal process.

The foundations of larger scale production were laid when the process of photo-enhanced AgNP bio-production was translated from batch to flow production. Through the development of a series of flow reactor prototypes, a larger scale reactor was designed, constructed, and operated. The product was a highly concentrated solution of Ag nanospheres.

The cause of biogenic AgNPs' superior stability was probed with proteomic analysis of the corona. The corona appears to be comprised of proteins which are abundant in the supernatant of cultures and can bind sufficient strongly to remain bound to the particle throughout the sample preparation. There does not appear to be an apparent functional connection between the bound proteins. Further investigation is warranted to identify difference in supernatant proteins which were bound to AgNPs and those which were not bound to the particles.

This project has increased the knowledge surrounding bacterial AgNPs and flow reactor technology developed in this project will likely be useful in increasing the scale of bacterially stabilised AgNPs.

Research Outputs

Presentations

- Poster & Oral Presentations and Elevator Pitch - Dstl Synthetic Biology Showcase (2016), Chicheley, UK
- Poster Presentation and Elevator Pitch - Dstl Synthetic Biology Showcase (2017), Birmingham, UK
- Poster Presentation and Elevator Pitch - Dstl Synthetic Biology Showcase (2018), Edinburgh, UK
- Poster Presentation and Elevator Pitch - Dstl Synthetic Biology Showcase (2019), Wantage, UK
- Oral Presentation - Implementation of Microreactor Technology in Biotechnology (2019), Cavtat, Croatia
- Poster Presentation - American Society for Microbiology Microbe (2019), San Francisco, USA

Publications

- Mabey, T., Cristaldi, D. A., Oyston, P., Lymer, K. P., Stulz, E., Wilks, S., Keevil, C. W., & Zhang, X. Bacteria and nanosilver: the quest for optimal production. Crit Rev Biotechnol. 1549-7801 (2019). - Review -[Published]
- Visible and ultraviolet light enhances AgNP synthesis by *M. psychrotolerans* - Original Research Article [Manuscript prepared to submit]
- A Rapid Green Process for AgNP Production Through Laser-Assisted Photoreduction - Original Research Article [Manuscript prepared to submit]

Awards

- Best Poster Prize - Dstl Showcase (2017)
- Best Poster Prize - Dstl Showcase (2018)

Contents

Abstract I

Research Outputs and Awards III

Contents V

List of Figures XI

List of Tables XVI

List of Equations XVI

Declaration of Authorship XVII

Acknowledgements XVIII

List of Acronyms and Symbols XIX

List of Acronyms and Symbols XIX

1 Introduction 1

1.1 Overview of Project 1

1.2 Aims and Objectives 1

1.3 Organisation of Thesis 2

2 Literature Review 5

2.1 Nanoparticles 5

2.1.1 Localised Surface Plasmon Resonance 6

2.1.2 Production of AgNPs 10

2.2 Biosynthesis of AgNPs 11

2.2.1 Silver Toxicity, Resistance, and Nanoparticle Synthesis 12

2.2.2 Biosynthetic Reaction Conditions . . . 18
2.2.3 Summary of the Biosynthesis of AgNPs . . . 29
2.3 Characterisation Techniques . . . 30
2.3.1 Optical Characterisation . . . 30
2.3.2 Visualisation and Size Analysis . . . 32
2.3.3 Composition Analysis . . . 33
2.3.4 Surface Analysis . . . 35
2.4 Production Considerations . . . 35
2.4.1 Flow Production . . . 35
2.4.2 Harvesting and Isolating . . . 36
2.4.3 Immobilising and Functionalisation . . . 37
2.5 Potential Applications of Nanoparticles . . . 37
2.5.1 Antimicrobials . . . 38
2.5.2 Energy Saving Glazing . . . 38
2.5.3 Signature Management and Low Observable Materials . . . 39
2.6 Conclusions of Literature Review . . . 41

3 The Effects of Reaction Conditions on the Bioproduction of AgNPs by *M. psychrotolerans* 43
3.1 Introduction . . . 43
3.2 Methods . . . 44
3.2.1 Organism and Reagents . . . 44
3.2.2 Biosynthesis of AgNPs . . . 44
3.2.3 Characterisation of AgNPs . . . 45
3.2.4 Data Analysis . . . 45
3.3 Results and Discussion . . . 46
3.3.1 Biogenic Production of AgNPs by *M. psychrotolerans* . . . 46
3.3.2 Effects of Growth Conditions on AgNP production . . . 49
3.4 Conclusions . . . 67

4 Visible and ultraviolet light enhances AgNP synthesis by *M. psychrotolerans* 69
4.1 Introduction . . . 69
4.2 Methods . . . 70
4.2.1 AgNP Biosynthesis . . . 70

4.2.2 Light Source and Setup . . . 70
4.2.3 Characterisation of AgNPs . . . 71
4.2.4 Temperature Monitoring . . . 71
4.2.5 Data Analysis . . . 72
4.3 Results . . . 72
4.3.1 AgNPs Production Under White Light . . . 72
4.3.2 Morphology and Geometry of AgNPs Produced . . . 74
4.3.3 Harvestablity of AgNPs . . . 77
4.3.4 Influence of Wavelengths of Light on AgNPs Production . . . 77
4.3.5 Effects of Thermal Heating . . . 79
4.4 Discussion . . . 79
4.4.1 Photo-Assisted Production . . . 80
4.4.2 Sterile AgNP Production . . . 81
4.4.3 Harvestability of AgNPs . . . 82
4.4.4 Light Wavelength Dependence of Phororeduction . . . 82
4.4.5 Possible Mechanism for AgNPs Formation . . . 83
4.5 Conclusions . . . 84

5 A Rapid Green Process for AgNP Production Through Laser-Assisted Photoreduction 85
5.1 Introduction . . . 85
5.2 Methods . . . 86
5.2.1 Synthesis of AgNPs . . . 86
5.2.2 Laser Source . . . 86
5.2.3 Characterisation of AgNPs . . . 87
5.2.4 Temperature Monitoring . . . 87
5.2.5 Cell Viability . . . 88
5.3 Results . . . 88
5.3.1 Influence of Laser Wavelength on AgNP production . . . 88
5.3.2 Real-time Monitoring of AgNP Production . . . 91
5.3.3 Nanoparticle Morphologies . . . 92
5.3.4 Thermal Heating . . . 92
5.3.5 AgNP Production by Growth Media Components . . . 94
5.3.6 AgNP Stability . . . 94

5.3.7 Cell Viability . . . 95
5.4 Discussion . . . 95
5.4.1 AgNP Characterisation . . . 97
5.4.2 Cell Viability . . . 99
5.4.3 Photocatalytic Activity . . . 99
5.4.4 Mechanism of AgNP Production . . . 100
5.5 Conclusions . . . 101

6 Photo-Assisted Biosynthesis of AgNPs Using Cell Free Extract in Flow Reactors 103
6.1 Introduction . . . 103
6.2 Methods . . . 105
6.2.1 Organism and Reagents . . . 105
6.2.2 Design and Manufacturing of Flow Reactors . . . 105
6.2.3 Setup and Operation of Flow Reactor . . . 106
6.2.4 Characterisation of AgNPs . . . 107
6.3 Results and Discussion . . . 107
6.3.1 Reactor 1 . . . 110
6.3.2 Reactor 2 . . . 115
6.3.3 Reactor 3 . . . 117
6.3.4 Reactors 1 & 2 with UV Lamp . . . 122
6.3.5 Reactor 4 . . . 122
6.3.6 Reactor 5 . . . 127
6.3.7 Comparison of Reactors . . . 135
6.3.8 Comparison with Previous Reactors . . . 141
6.3.9 Future Developments . . . 143
6.4 Conclusions . . . 145

7 Non-Specific Binding of Proteins Form Coronae of Biogenic AgNPs Produced by *M. psychrotolerans* 147
7.1 Introduction . . . 147
7.2 Methods . . . 148
7.2.1 Preparation of AgNPs . . . 148
7.2.2 Visualisation and Spectroscopic Analysis of Corona . . . 149

7.2.3 Gel Electrophoresis . . . 150
7.2.4 Proteomic Analysis of Corona . . . 151
7.2.5 Determining Protease Activity . . . 153
7.3 Results and Discussion . . . 154
7.3.1 Visualising the Corona . . . 154
7.3.2 Spectroscopic Investigation of Corona . . . 156
7.3.3 Detection and Visualisation of Corona by Fluorescent Staining . . . 158
7.3.4 Protease Activity . . . 158
7.3.5 Separation of Coronal Proteins by SDS PAGE . . . 161
7.3.6 Proteomic Investigation of Coronal Proteins . . . 164
7.3.7 Coronae of Other Organisms . . . 176
7.3.8 Considerations and Limitations . . . 178
7.3.9 Future Work . . . 180
7.3.10 Corona of Other Species . . . 181
7.4 Conclusions . . . 181

8 Discussion and Conclusions 183
8.1 Project Summary . . . 183
8.2 Summary of Key Findings . . . 183
8.3 Review of Project Aims and Objectives . . . 185
8.4 Potential Applications of the AgNPs Produced in this Project . . . 185
8.5 Shortcomings and Limitations of this Project . . . 185
8.6 Remaining Research Questions and Proposed Future Work . . . 187
8.7 Concluding Remarks . . . 189

Appendices 191

A Effects of Reaction Conditions on AgNP Bioproduction 193
A.1 *Culturing of M. psychrotolerans* . . . 193
A.1.1 Cell Counts and Viability . . . 193
A.1.2 Growth Kinetics . . . 193
A.2 Assessment of AgNP production by *E. coli* and *P. fluorescens* . . . 193
A.3 Sectioned TEM Imaging of *M. psychrotolerans* . . . 194

B Visible and ultraviolet light enhances AgNP synthesis by *M. psychrotolerans* 197

C A Rapid Green Process for AgNP Production Through Laser-Assisted Photoreduction 201

D Photo-Assisted Biosynthesis of AgNPs Using Cell-free Extract in Flow Reactors 205

E Non-Specific Binding of Proteins Form Coronae of Biogenic AgNPs Produced by *M. psychrotolerans* 209

E.1 Spectroscopic Investigations of the Corona of AgNPs produced by *M. psychrotolerans* . . . 209

E.2 SDS PAGE of AgNP Proteomics Samples 214

E.3 Analysis of Protein Properties 216

E.3.1 Methods 216

References 220

List of Figures

1.1 Outline of thesis narrative 2

2.1 Chemically produced Ag nanoprisms with different optical properties 6
2.2 Schematic of a section of the electromagnetic spectrum 7
2.3 A schematic representation of localised surface plasmon resonance 7
2.4 Predicted scattering, absorption, and extinction spectra of different AgNPs 9
2.5 Examples of monodispersed AgNPs 11
2.6 Proposed mechanism of reduction of Ag^{+} in the formation of nanoparticles utilising the reduction of nitrate 15
2.7 Proposed mechanisms for intracellular and extracellular AgNP production in bacteria 18
2.8 Bacteria known to produce AgNPs 21
2.9 Photographs using visible and NIR light of military vehicles 40

3.1 Samples of supernatant collected from *M. psychrotolerans* cultures exposed to different concentrations of $AgNO_3$ 46
3.2 TEM images of *M. psychrotolerans* not exposed to $AgNO_3$ 47
3.3 TEM images of *M. psychrotolerans* incubated with $AgNO_3$ for 24 h 48
3.4 AgNPs produced by *M. psychrotolerans* 49
3.5 AgNPs collected from the supernatant of *M. psychrotolerans* after 24 h incubation with $AgNO_3$ 50
3.6 UV-Vis spectra of AgNPs produced by *M. psychrotolerans* when exposed to varying concentrations of $AgNO_3$ 51
3.7 UV-Vis spectra of AgNPs produced by *M. psychrotolerans* when exposed to varying concentrations of Ag lactate 52
3.8 UV-Vis spectra of AgNPs produced by *M. psychrotolerans* at 4°C, 22°C, and 37°C 54
3.9 UV-Vis spectra of AgNPs produced by *M. psychrotolerans* in 9 mM $AgNO_3$ under different pH conditions 55

3.10 pH of *M. psychrotolerans* cultures during AgNP production at different temperatures 56
3.11 Centrifuged AgNP samples under different pH conditions 56
3.12 UV-Vis spectra of AgNPs produced by *M. psychrotolerans* in the presence of NaCl and KCl . 58
3.13 UV-Vis spectra of AgNPs produced by *M. psychrotolerans* in the presence of KBr and KI . . 60
3.14 UV-Vis spectra of AgNPs produced by *M. psychrotolerans* in the presence of glucose, fructose, and sucrose 61
3.15 UV-Vis spectra of AgNPs produced by *M. psychrotolerans* in the presence of citrate 63
3.16 UV-Vis spectra of AgNPs produced by *M. psychrotolerans* with varied cell densities and CFE dilutions 64
3.17 UV-Vis spectra of AgNPs produced by *M. psychrotolerans* following heat treatment and autoclaving 66
3.18 UV-Vis spectra of AgNPs produced by *M. psychrotolerans* when exposed to sunlight 67

4.1 Setup used for illuminating samples with LED light 71
4.2 UV-Vis spectra of AgNPs produced in the presence of *M. psychrotolerans* or sterile growth medium under white light or dark conditions 73
4.3 Intensities of LSPR peaks and peak positions over 48 h of AgNPs produced under different lighting conditions 74
4.4 TEM images of AgNPs collected from the supernatant of *M. psychrotolerans* exposed to white light and dark conditions, and sterile growth media exposed to white light 75
4.5 TEM images of AgNPs produced by *M. psychrotolerans* under white light and dark conditions 76
4.6 UV-Vis spectra of AgNPs produced in sterile media exposed to light with and without centrifugal separation 77
4.7 Comparison of AgNP production under different wavelengths of light 78
4.8 Temperature change of reaction solutions over 48 h during AgNP synthesis under white LED light 79
4.9 Mechanism for AgNP bioproduction in the absence of light 84

5.1 Setup for real-time UV-Vis-NIR spectroscopy of samples irradiated with laser light 87
5.2 UV-Vis spectra of AgNPs produced by 405 nm, 532 nm, and 650 nm lasers 89
5.3 UV-Vis spectra of AgNPs produced during irradiation for 10 s with a 405 nm laser with varied output powers 90
5.4 Real-time UV-Vis spectroscopy of AgNPs produced during irradiation with a 405 nm laser . . 91

5.5 TEM images of AgNPs produced with 405 nm laser irradiation 92
5.6 Thermal images of AgNP production in 200 µL sample irradiated with a 60 mW 405 nm laser 93
5.7 UV-Vis spectra of AgNPs produced by tryptone and yeast extract with 405 nm laser illumination 94
5.8 UV-Vis spectra of AgNPs produced under 405 nm laser taken over 150 days 96
5.9 Cell viability of cultures before and after exposure to $AgNO_3$ and 405 nm laser light for 2 min determined by colony forming unit counts 97
5.10 Proposed mechanism for AgNP synthesis from the photo-oxidation of amino acids 100

6.1 General components of a flow reactor 104
6.2 General schematic of a flow reactor setup 106
6.3 Design schematic and photograph of Reactor 1 111
6.4 Reactor 1 channel cross sections 112
6.5 UV-Vis spectra and photograph of AgNPs produced in Reactor 1 under different TFRs . . . 113
6.6 Fouling of Reactor 1 after use 114
6.7 Possible mechanism for AgNP deposition on PDMS reactor walls 115
6.8 Schematic of Reactor 2 design 116
6.9 UV-Vis spectra of AgNPs from Reactor 2 118
6.10 "Heart" design of Reactor 3 119
6.11 UV-Vis spectra of AgNPs produced in Reactor 3 120
6.12 UV-Vis spectra of AgNPs produced in Reactor 1 with fibre optic 121
6.13 UV-Vis spectra of AgNPs produced in Reactor 1 under a UV lamp 123
6.14 UV-Vis spectra of AgNPs produced in Reactor 2 with UV lamp 124
6.15 TEM images of AgNPs produced in Reactor 2 with UV lamp 125
6.16 UV-Vis spectra of AgNPs produced in Reactor 4 (curved serpentine) 126
6.17 Design schematic of Reactor 5 127
6.18 UV-Vis spectra of AgNPs produced in Reactor 5 (coil) under different TFRs 129
6.19 TEM images of AgNPs produced in Reactor 5 130
6.20 Size distributions of AgNPs produced in Reactor 5 131
6.21 UV-Vis spectra of AgNPs produced in Reactor 5 (coil) under different FRRs 132
6.22 PTFE coils from Reactor 5 before, during, and after AgNP production under UV lamps . . . 133
6.23 Output stability of Reactor 5 over time 134
6.24 Comparison of flow reactors illuminated with 405 nm laser 136
6.25 Comparison of flow reactors illuminated with UV lamps 138

6.26 Comparison of all flow reactors . . . 139
6.27 Diagram of annular and droplet flow . . . 144

7.1 Diagram of AgNP and corona . . . 148
7.2 TEM images of AgNPs with low electron density coating . . . 155
7.3 UV-Vis spectra of washed AgNPs . . . 157
7.4 Skimmed milk assay for protease activity . . . 159
7.5 SDS PAGE of AgNPs produced by *M. psychrotolerans* . . . 160
7.6 SDS PAGE of AgNPs processed under different conditions . . . 162
7.7 Comparison of number of proteins identified in replicates of Control and AgNP samples . . . 168
7.8 Comparison of number of proteins identified in at least 4 of the 5 replicates for AgNP and Control samples . . . 169
7.9 Abundance of all proteins bound to AgNPs present in at least 80% of replicates . . . 170
7.10 Abundance of the 37 most abundant proteins present in at least 80% of replicates that did not bind to AgNPs . . . 171
7.11 Abundance of the 37 most abundant proteins present in at least 80% of replicates in the supernatant of *M. psychrotolerans* cultures . . . 172
7.12 Subcellular locations of proteins identified by proteomic analysis . . . 173
7.13 Functions of proteins identified by proteomic analysis . . . 174

A.1 Growth Curve of *M. psychrotolerans* . . . 194
A.2 UV-Vis spectra of supernatant of *E. coli* and *P. fluorescens* cultures after exposure to $AgNO_3$ 195
A.3 TEM images of sectioned *M. psychrotolerans* after incubation with Ag^+ . . . 196

B.1 Emission spectra of LED bulb with coloured filters . . . 198
B.2 Size distributions of AgNPs associated with cells in dark conditions and exposed to white light 199

C.1 Calculations for laser intensity . . . 202
C.2 UV-Vis spectra of supernatant of by *M. psychrotolerans* challenged with $AgNO_3$ in the dark at 24°C and 35°C after 10 min . . . 203
C.3 UV-Vis spectra of AgNPs produced in the presence of CFE and sterile growth medium before and after centrifugation . . . 203
C.4 Relationship between concentration of AgNPs and absorbance at 420 nm . . . 204

D.1 Comparison of t_r of reactors . . . 206

E.1 Raman Spectra of *M. psychrotolerans* cells with and without AgNPs 210
E.2 Raman Spectra of *M. psychrotolerans* cells containing AgNPs 211
E.3 AgNPs stained with SYPRO Ruby 212
E.4 FTIR Spectra of AgNPs 213
E.5 SDS-PAGE of AgNP proteomic samples 215
E.6 Amino acid compositions in sequences of bound and unbound proteins 217
E.7 Amino acids compositions grouped by properties of proteins unbound and bound to AgNPs . 218
E.8 Physiochemical properties of proteins bound and unbound to AgNPs 219

List of Tables

5.1 Absolute absorbance at 450 nm of AgNPs produced by lasers with different wavelengths . . 90

6.1 Reactor parameters 109
6.2 Summary of reactor achievements and limitations 140

7.1 SDS PAGE bands and possible proteins 163
7.2 Proteins identified in the corona of AgNPs produced by *M. psychrotolerans* 175
7.3 Comparison of proteins identified in the corona of AgNPs produced by other organisms in previous studies. 177

D.1 Comparison of residence times of flow reactors used for AgNP production 207

E.1 Amino acid compositions in bound and unbound proteins 221

List of Equations

2.1 Reduction of ionic silver to zero valent silver 10
2.2 Beer-Lambert's law 31
2.3 Bragg's Law 33
5.1 Ratio of Precipitation 94
6.1 Total Flow Rate 107
6.2 Residence Time 107
7.1 Protein Abundance Approximation 153
E.1 Amino Acid Composition 216

Research Thesis: Declaration of Authorship

Print name: Thomas M Mabey

Title of thesis: Bacteria as Nanofactories: Silver Nanoparticle Bioproduction

I declare that this thesis and the work presented in it is my own and has been generated by me as the result of my own original research. I confirm that:

1. This work was done wholly or mainly while in candidature for a research degree at this University;
2. Where any part of this thesis has previously been submitted for a degree or any other qualification at this University or any other institution, this has been clearly stated;
3. Where I have consulted the published work of others, this is always clearly attributed;
4. Where I have quoted from the work of others, the source is always given. With the exception of such quotations, this thesis is entirely my own work;
5. I have acknowledged all main sources of help;
6. Where the thesis is based on work done by myself jointly with others, I have made clear exactly what was done by others and what I have contributed myself;
7. Parts of this work have been published as: *Mabey, T., Cristaldi, D. A., Oyston, P., Lymer, K. P., Stulz, E., Wilks, S., Keevil, C. W., & Zhang, X. Bacteria and nanosilver: the quest for optimal production. Crit Rev Biotechnol. 1549-7801 (2019).*

Signature

Date

Acknowledgements

The completion of this PhD project has been a challenging but rewarding experience. It would not have been possible without the incredible amount of support I have received over the years. First, I am incredibly thankful to my supervisors Prof. Xunli Zhang, Dr. Sandra Wilks, and Prof. Bill Keevil. Without their continued support, guidance, and patience throughout, this project would not have been possible. I would also like to thank my technical partners Petra Oyston, Karl Lymer, and Chris Howle of the Defence Science and Technology Laboratory (Dstl) for their advice, guidance, and feedback throughout this project. Their valuable insights have helped shape this project and focus

Throughout this project I have been lucky enough to have the opportunities to work with many excellent scientist and friends. I would especially like to thank Andrea Cristaldi, Fatih Yanar, and Peijun He with whom I have had the privilege to work with. The many hours of their time given up helping me work with lasers, flow reactors, and TEM imaging have allowed this project, and me, to explore areas which would not have been possible without their expertise and assistance.

I am also grateful for the expertise, assistance, and facilities given by Paul Skipp (FELS), Dave Rowe (ORC), Adam Lister (FELS), Bhavik Barochia (FELS), Ray Allen (FELS), and Patrick James (FEPS), especially when working outside their normal area of research. Their help added great value to this project with a wide range of techniques and approaches not possible without them. Similarly, I would also like to acknowledge the assistance and facilities provided by the Biomedical Imaging Unit (University of Southampton and the University Hospital Southampton NHS Foundation Trust) and the Centre for Proteomic Research (University of Southampton).

The patience and support of the Microbiology lab group have made this project enjoyable. I only hope that one day the smell of my bacteria will one day desperate and we'll no longer need the air fresheners!

I have been lucky to share an office with such a kind and friendly group of people. Erik, Sara, Gareth, Jenny, Sel, Alex, Patricia, Alisha, Elaine, Harry, Giorgia, Federica, and, of course, Crackers the fish have been so supportive, and I wish them all the best in their projects. I would also like to thank the staff and fellow PhD students of the Mechanical Engineering research group who have made the department such a welcoming and fun place to work.

From day 1, I have shared the roller-coaster of a journey with Katy and Josh. The laughs, procrastination, discussions on continuous flow. . . everything, and the occasional stern look for ridiculous ideas have made the 4 years much easier!

I would like to thank my family, especially Mum, Dad, and George for their love and support over the past 26 years. I would not have got to the stage of even beginning a PhD without their help, guidance, and occasional nagging! I would also like to thank my Grandma for proof-reading this thesis and spotting many typos!

Finally, Rosie. I don't think I would have made it to the end without continued your love, support and friendship, not just throughout my PhD, but for the many years before. I promise that I will get a real job soon!

List of Acronyms and Symbols

ϵ	Molar Extinction Coefficient
γ	Gamma Radiation
λ_{max}	Wavelength of Maximum Absorbance
C	Concentration
I_0	Initial Absorbance Intensity After Centrifugation
I_C	Absorbance Intensity After Centrifugation
Q_{AgNO_3}	Flow Rate of Silver Nitrate
Q_{CFE}	Flow Rate of Cell Free Extract
R_P	Precipitation Ratio
t_r	Residence Time
V	Volume
W	Width
3D	Three Dimensional
°C	Degrees Celsius
g	Gravitational Force Equivalent ($1g \approx 9.8$ ms^2)
λ	Wavelength
µg	Microgram
µL	Microliter
µL min^{-1}	Microliter Per Minute
µm	Micromolar
θ	Angle of Incidence
ζ	Zeta Potential
A	Absorbance
Ag	Silver
Ag^+	Silver Ion
Ag^0	Zerovalent Silver Atom

Ag_2O	Silver Oxide
$AgNO_3$	Silver Nitrate
AgNP	Silver Nanoparticle
AgOH	Silver Hydroxide
b	Path Length
C	Carbon
CAD	Computer Aided Design
CCCP	Carbonyl Cyanide M-Chlorophenyl Hydrazone
CFE	Cell Free Extract
CFU	Colony Forming Units
cm	Centimetre
cm^{-1}	Wavenumber
cm^2	Square Centimetre
D	Diffraction Limit
diH_2O	Deionised Water
DLS	Dynamic Light Scattering
DNA	Deoxyribonucleic Acid
DSMZ	Deutsche Sammlung Von Mikroorganismen Und Zellkulturen
DTT	Dithiothreitol
EDTA	Ethylenediaminetetraacetic Acid
FO	Fibre Optic
FRR	Flow Rate Ratio
FTIR	Fourier-Transform Infrared
g	Gram
gL^{-1}	Gram per Litre
H	Height
h	Hour
H^+	Hydrate Ion
H^-	Hydride Ion
H_2O_2	Hydrogen Peroxide
IAA	Iodoacetamide
ID	Internal Diameter

K	Potassium
KBr	Potassium Bromide
KCl	Potassium Chloride
kDa	Kilo Daltons
KDE	Kernel Density Estimation
KI	Potassium Iodide
kV	Kilo Volt
L	Litre
LASER	Light Amplification by the Stimulated Emission of Radiation
LB	Lysogeny Broth
LDS	Lithium Dodecyl Sulphate
LED	Light Emitting Diode
LSPR	Localised Surface Plasmon Resonance
M	Molar
min	Minute
mL	Millilitre
mLh^{-1}	Millilitre Per Hour
mM	Millimolar
mm	Millimetre
mV	Millivolt
mW	Milliwatt
NaCl	Sodium Chloride
NAD(P)H	Nicotinamide Adenine Dinucleotide (Phosphate)
NIR	Near Infrared
nm	Nanometre
$nm.min^{-1}$	Nanometre Per Minute
OD	Outer Diameter
OD_{600}	Optical Density At 600 nm
PBS	Phosphate Buffered Saline
PDMS	Polydimethylsiloxane
PMMA	Poly (Methyl Methacrylate)
PTFE	Polytetrafluoroethylene

PVA	Poly (Vinyl Alcohol)
PVP	Poly(Vinyl Pyrrolidone)
Q	Flow Rate
RADAR	Radio Detection and Ranging
RAM	Radar Absorbing Material
RPM	Revolutions Per Minute
s	Seconds
SD	Standard Deviation
SDS PAGE	Sodium Dodecyl Sulphate Polyacrylamide Gel Electrophoresis
SERS	Surface Enhanced Raman Spectroscopy
SM	Skimmed Milk
SMA	Simple Moving Average
TEM	Transmission
TFA	Trifluoroacetic Acid
TFF	Tangential Flow Filtration
TFR	Total Flow Rate
TSCD	Trisodium Citrate Dihydrate
UV	Ultraviolet
UV-Vis	Ultraviolet-Visible
V	Volt
Vis	Visible
W	Watts
XRD	X-Ray Diffraction

Chapter 1

Introduction

1.1 Overview of Project

This interdisciplinary project brought together a wide range of techniques and methodologies from the fields of microbiology, materials science, chemistry, physics, molecular biology, and engineering to gain an understanding of and begin to exploit bacterial silver nanoparticle production.

Nanoparticles often have very different physical and chemical properties when compared to their macroscopic and bulk counterparts.[1,2] These unique properties make them highly attractive in a range of current and potential applications. In recent years, these materials have gained considerable interest in both research and commercial use; this growth is forecast to continue considerably.[3] However, current nanoparticle production routes suffer from their dependence on hazardous chemicals, often under harsh conditions, poor particle stability, and challenges with scale-up.[4] The biosynthesis of metallic nanoparticles, including nanoprisms, has been described in a range of organisms including plants, fungi, and bacteria.[4,5] Whilst the biological processes for many of these remain poorly understood, they hold great potential for a more environmentally friendly, greener, and up-scalable source of silver nanoparticles.

1.2 Aims and Objectives

The primary aim of this project was to develop an environmentally friendly and scalable method for the production of stable AgNPs through the use of bacteria. The secondary aims were to control the geometries of the AgNPs produced to synthesise non-spherical morphologies, and to gain an understanding of the biological mechanisms underpinning bacterial AgNP synthesis. To achieve this the following objectives were set:

- to optimise the reaction conditions for producing AgNPs in bacteria
- to develop a scalable production method through which the foundations of large-scale production can be laid
- to investigate the composition of the biomolecular coating of biogenic AgNPs

1.3 Organisation of Thesis

This thesis begins with a review of the published literature on the topics of the optical properties of AgNPs, current production methods and their limitations, the biosynthesis of AgNPs and the effects different reaction conditions have on production, methods used for the characterisation of AgNPs, and finally, potential applications of AgNPs (Chapter 2). This is followed by the results of this thesis and consists of 4 main themes, illustrated in Figure 1.1 and outlined below:

- Reaction conditions and AgNP biosynthesis (Chapter 3) – This investigates the extent to which the conditions under which AgNPs are produced in a biological system can impact the product, for instance the amount of AgNPs produced and their geometries.

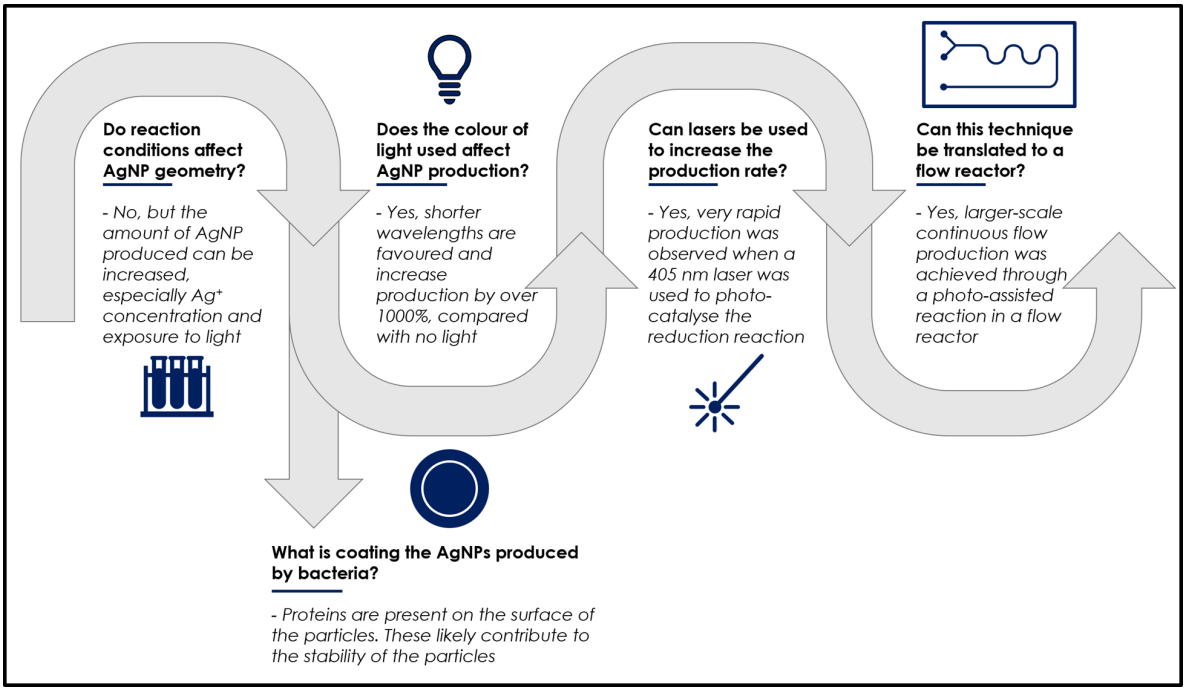

Figure 1.1: Outline of thesis narrative.

- Photo-assisted production of AgNPs (Chapter 4 & 5) – In two manuscripts, light has been used to enhance the production of AgNPs through accelerating the reaction and increasing yields. Different wavelengths of light and light sources were investigated to begin to gain an understanding of the mechanism involved.

- Translation from batch to flow synthesis (Chapter 6) – This work reports the design journey of microreactors developed to take what was learned about the photo-catalysed reactions and implement it in a continuous flow reactor, a key step on the path to large scale production.

- AgNP corona and its composition (Chapter 7) – By gaining an understanding of the material coating the nanoparticles, it was hoped that some degree of control may be had over the crystal growth and ultimately the geometries of the particles. To this end, analysis of the surface corona was performed, and proteomic analysis used to identify key proteins. Finally, a summary of the key outcomes of this project is given along with discussion on remaining gaps in the knowledge and proposed future work.

Chapter 2

Literature Review

This Literature review is split into three main concerns. First, the optical properties of nanoparticles are explored; this section also examines current production methods and their limitations. Second, the biological aspect of this project is explored. Specifically, the ability of bacteria to produce nanoparticles and the proposed biological mechanisms are reviewed. In addition, the impacts of reaction conditions on biogenic nanoparticle formation are discussed. This is followed by a brief summary of the methods used in the characterisation of AgNPs and potential considerations for larger scale production. Finally, the potential applications of nanoparticles are explored. The current limitations of the thermal properties of windows and infrared signature management in military vehicles are reviewed, and the potential of AgNPs to overcome some of these challenges is debated.

Section 2.2 has been published in a review articles titles *Bacteria and nanosilver: the quest for optimal production* by Mabey et al.[6]

2.1 Nanoparticles

Nanomaterials are widely defined as any material with at least one dimension of less than 100 nm. Nanoparticles are a subgroup of nanomaterials and typically have all three dimensions (height, width, and depth) of less than 100 nm.[7] They can be made from any substance, though inorganic and metallic compositions are most common. Metallic nanoparticles can be produced in a wide variety of shapes and sizes and have been studied for many years.[8] To date, production has conventionally been achieved via chemical and physical processes.[7]

The main appeal of nanoparticles is that they have very distinct properties compared to bulk materials of the same composition.[9] This is especially evident in the way they interact with light. For example, AgNPs

in a liquid suspension appear as very vivid colours, as shown in Figure 2.1, while bulk silver is “silver” in colour. These properties make AgNPs attractive in a range of applications and as such have been the subject of increasing interest in recent years.

Figure 2.1: Suspensions of chemically produced citrate-stabilised Ag nanoprisms with different optical properties in water. Adapted and reprinted with Permission from Haber and Sokolov (2017).[10] Copyright 2017 American Chemical Society.

2.1.1 Localised Surface Plasmon Resonance

The electromagnetic spectrum includes all wavelengths of electromagnetic radiation from low energy and long wave radio waves ($\lambda > 10^{-3}$ m) to short wave and high energy γ-rays ($\lambda < 10^{-12}$ m). Between the wavelengths of 400 nm and 10 μm is the thermal radiation region. This includes visible light (400 nm to 700 nm) and the near infrared (NIR) which extends from 700 nm to 2,500 nm), summarised in Figure 2.2.

The phenomenon responsible for the unique optical properties of nanoparticles is localised surface plasmon resonance (LSPR). Localised surface plasmons are the collective oscillation of the free electrons in an electrically conductive nanoparticle.[1] As shown in Figure 2.3, the movement of these electrons is caused by their interaction with the alternating electric field of incident light. As the electron cloud is displaced relative to the positive ion lattice of the metal, coulombic forces act to restore the system to its equilibrium position and cause oscillations.[11,12] When the frequency of incident radiation is equal to the natural frequency of the electron oscillations the system will resonate, known as localised surface plasmon resonance (LSPR). The resonating electrons form a standing wave which causes an accumulation of polarisation charges at the surface of the particle leading to formation of a dipole.[12] The strong electric fields created result in strong absorbance at the resonant frequency.

Nanoparticles are considerably smaller than the wavelengths of visible light (400 nm $\geq \lambda \leq$ 700 nm), and because the electric field of incident light can only penetrate $<$50 nm into a material, LSPR can only make a significant contribution to the electromagnetic properties at the nanoscale.[1] This explains why

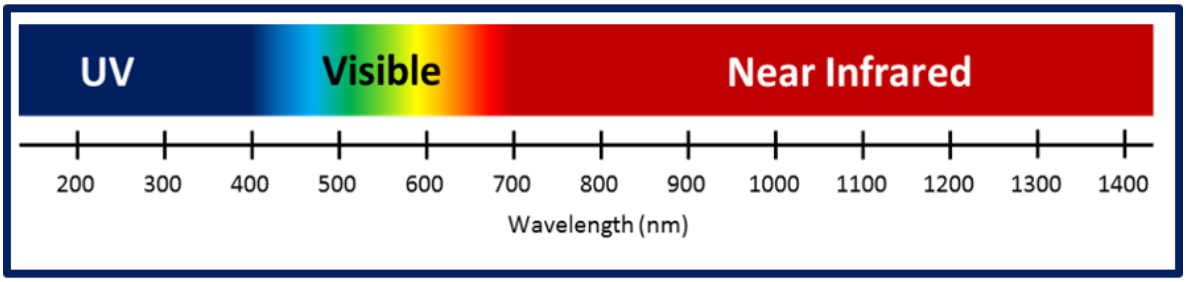

Figure 2.2: Schematic of a section of the electromagnetic spectrum showing the visible region in relation to ultraviolet and infrared. The infrared region is split into three regions: near, mid and far IR. Near infrared is found directly adjacent to the visible region and extends to 2500 nm.

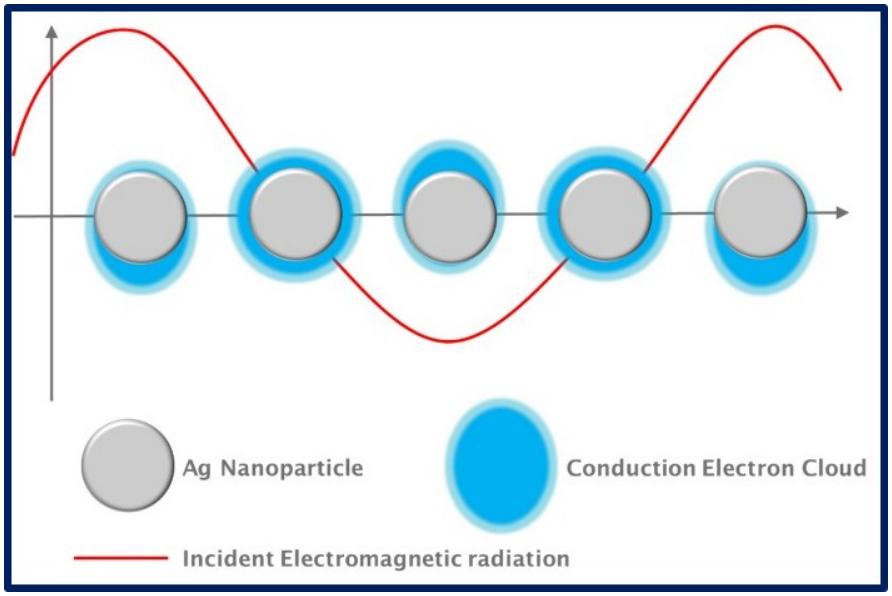

Figure 2.3: A schematic representation of localised surface plasmon resonance. As the incident electric field passes the particle, the electrons are displaced. The electric attraction between the electrons and the positive ion lattice of the metal acts to restore the electron cloud. Image based on figure published by Willets and Duyne[13].

nanoparticles have very different optical properties from their bulk macroscopic counterparts.[1,2] The effect is especially noticeable in noble metals, including Au and Ag, as the LSPR frequencies are situated in the visible and NIR regions of the electromagnetic spectrum. The strong absorbance associated with the LSPR causes the vivid colours in colloidal solution. As shown in Figure 2.4, mathematical modelling can be used to determine the characteristics of plasmon resonances in nanoparticles. Here, the scattering and absorption profiles of AgNPs were reviewed by Lu et al.[1] Image A of this Figure shows a characteristic peak with high relative absorption in the region of 400-420 nm, which is associated with the primary dipole surface plasmon resonance.[1,14,15] This peak is suggestive of small spherical nanoparticles and is widely used to indicate the presence of AgNPs in a solution and the absorption of blue light results in a colloid of Ag nanospheres appearing yellow.[1]

In contrast to the symmetry of nanospheres, morphologically anisotropic particles typically have more complex absorbance spectra with additional peaks and features. Sharp corners found in particles such as triangular nanoprisms cause intense electric fields to form as a result of the accumulation of surface charges appearing of additional peaks.[1] Triangular nanoprisms, like the example shown in image E of Figure 2.4, tend to give much lower intensity peaks at 400 nm and instead have absorption maxima at approximately 335 nm, 470 nm, and 670 nm corresponding to in- and out-of-plane quadrupoles, and in-plane dipoles, respectively.[1,16] The red-shifted absorbance maximum results in the blue appearance of Ag nanoprisms in suspension.

The exact resonance frequency is determined by a number of factors. In the case of Ag, like all nanoparticles, optical properties are heavily geometry-dependent. As the particle size increases, the resonance frequency is red-shifted, whereas less spherical particles typically have broader bandwidths and present multiple absorption peaks.[1] This is demonstrated in Figure 2.4 where cubic (B), tetrahedral (C), and octahedral (D) particles have distinct extinction profiles. Likewise, the aspect ratio of rod-shaped particles can markedly shift the absorbance maxima (F). The composition of the nanoparticles also impacts the resonance frequency by altering the restoring coulombic forces and electron density in the particle.[11] Furthermore, the dielectric environment changes the conditions on the electrons at the surface of the nanoparticle.[1] As a result of the strong link between the physical dimensions and environment of a nanoparticle and how they interact with light, specific regions of the electromagnetic spectrum can be selectively absorbed by producing specifically shaped nanoparticles.

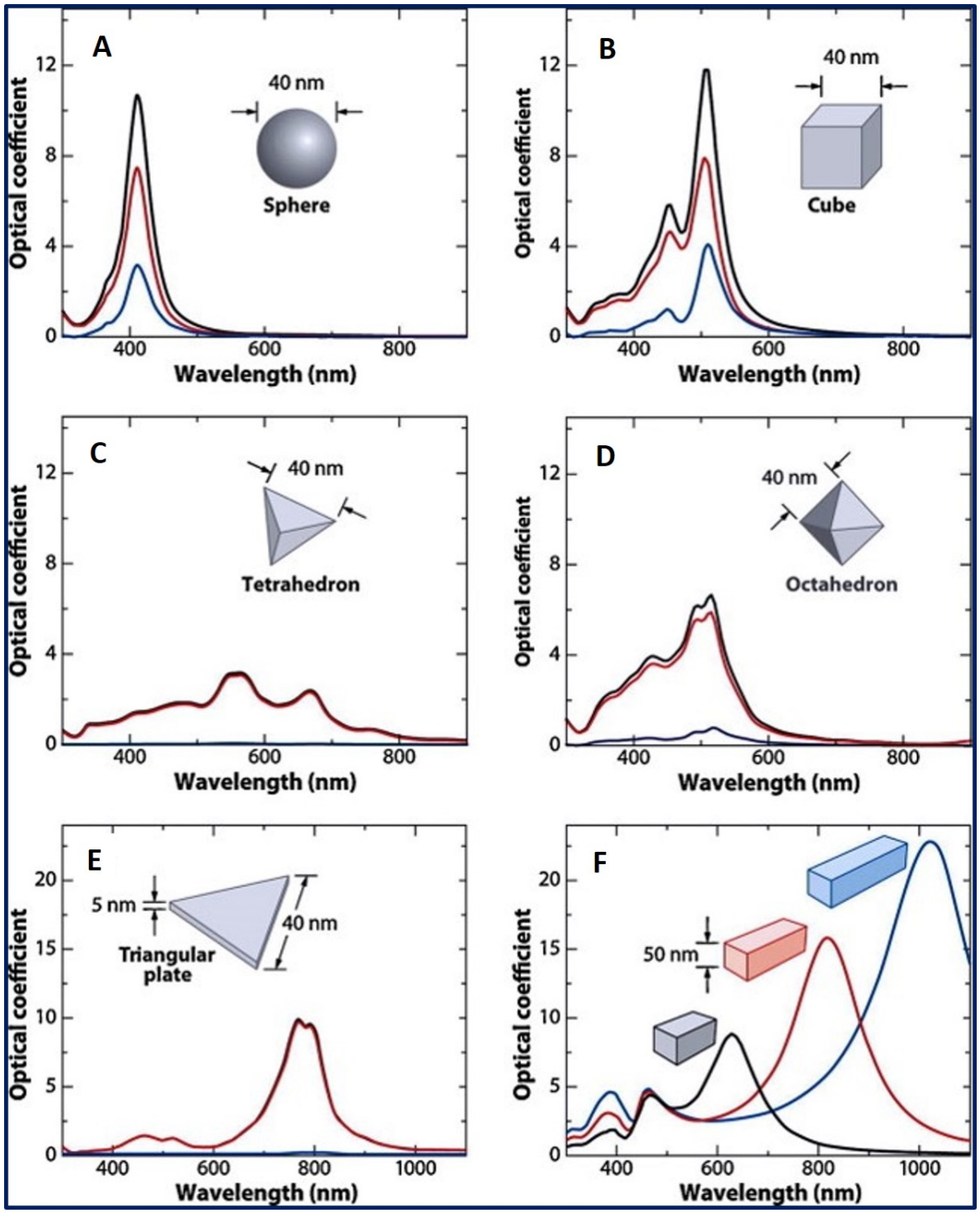

Figure 2.4: Predicted scattering (blue), absorption (red), and extinction (black) spectra of different spherical (A), cubic (B), tetrahedral (C), and octahedral (D) AgNPs, as well as triangular prisms (E). Extinction spectra for rectangular nanorods with different aspect ratios (F). Reproduced from Lu et al.[1]

2.1.2 Production of AgNPs

A range of techniques for the production of nanoparticles have been developed including chemical reduction, physical methods, such as laser ablation[17] and evaporation-condensation techniques,[7] electro and photochemical processes,[18,19] and more recently, biosynthesis routes.[7,20] Chemical reduction routes are the most commonly used methods for producing AgNPs and rely on reducing Ag^+ to zero valent Ag^0 through the addition of an electron, as shown in Equation 2.1.

$$Ag^+ + e^- \rightleftharpoons Ag^0 \qquad +799mV \tag{Eq. 2.1}$$

The reduction reaction requires three main reagents: a Ag^+ source, a reducing agent, and a stabilising or capping agent. The Ag^+ are almost exclusively supplied as silver nitrate ($AgNO_3$) due to its superior solubility in water compared to other Ag salts. The reducing agents can be varied to affect the parameters of the reaction; this is done to change the final geometries of the particles produced. Commonly used reducing agents include sodium borohydride, trisodium citrate, and alcohols.[7,21] The strength of the reducing agent changes the rate of the reaction and the final product. Polymers such as poly(vinyl pyrrolidone) (PVP) and poly(vinyl alcohol) (PVA), along with citrate, are used to stabilise the particles. This stabilisation acts to reduce agglomeration of the particles and can be used to control the growth and shape of the crystal.[7] Following the reduction of Ag^+ nucleation occurs with the formation of small clusters of atoms. The newly formed seed crystals then undergo growth as free Ag^0 atoms preferentially bind to the nucleated cluster leading to the formation of nanoparticles.[7]

Chemical reduction processes can produce highly monodispersed AgNPs, examples are shown in Figure 2.5. However, to reach the full potential of AgNPs a number of caveats with production methods must be overcome.[4,7]

Many physical and chemical production methods to date are hindered by poor particle stability. Ag nanospheres stored at room temperature can undergo dramatic morphological changes with the formation of prisms and rods over 1 year with changes in the optical properties for the particles being observed in the first month post-synthesis.[22] Moreover, laser ablation generated AgNPs suffer from oxidation during long-term storage (up to 405 days). This was associated with changes in the colour of the nanoparticle suspension and a loss of function (antimicrobial activity).[23] While capping agents such as PVP and citrate have been used to mitigate these effects, large biological molecules, such as proteins, offer superior stability against particle agglomeration due to steric repulsion.[24] The ability to maintain colloidally and morphologically stable AgNPs is vital in many applications and increasing the stability opens additional

applications and conditions for use.

Chemical production methods typically employ reducing agents and capping ligands. These are often hazardous and carry environmental safety concerns. Sodium borohydride, ethylene glycol, and amino boranes are among the used reagents and solvents.[10,25–27] The production of organic solvent waste has been a driving factor in the development of green production routes with estimates of up to 98% of waste being solvents in one production method.[28,29] While efforts are being made to find alternative greener and more environmentally-friendly reagents and reduce waste,[29,30] biological routes have been suggested as the reducing and capping agents are supplied from biological sources.

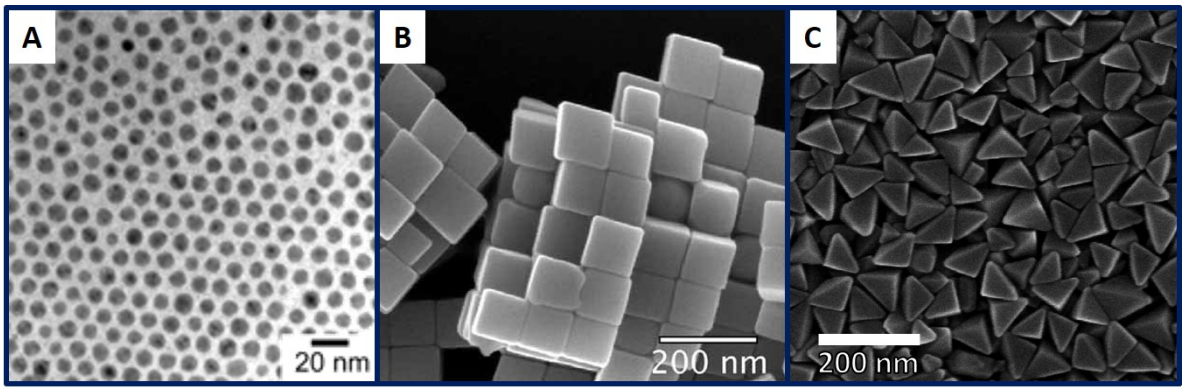

Figure 2.5: Examples of monodispersed spherical (A), cubic (B), and triangular (C) AgNPs. Scale bars: 20 nm (A), 200 nm (B and C). (A) Reproduced from Lin et al. Copyright 2004 American Chemical Society.[35] (B) Reproduced from Xia et al. Copyright 2008 Wiley.[36] (C) Adapted from Zhang et al. Copyright 2010 American Chemical Society.[37]

Many physical production routes require energy-demanding specialist equipment, such as lasers and magnetron sputtering systems.[31–34] These are often accompanied by high capital and maintenance costs which limits their accessibility. While the particles produced can be highly monodispersed and have no ligands on the surface (desirable for surface functionalisation), the costs can be prohibitively high for some applications and research.

While research continues into methods to improve these production processes, biological production has been proposed as an alternative and may offer a scalable and greener process.[7]

2.2 Biosynthesis of AgNPs

The biosynthesis of metallic nanoparticles has been described in a range of organisms spanning plants, fungi, and bacteria, often through metal-toxicity resistance mechanisms.[38–41] Whilst the processes for many of these remain poorly understood, they hold great potential for more environmentally friendly and up-

scalable production of AgNP than chemical synthesis.

A number of review articles have been authored which give useful overviews of bacteriogenic metallic nanoparticle synthesis.[4,7,9,39,42] However, to date, no in-depth summary of findings has been published relating to the reaction conditions under which AgNPs are synthesised and the impact that these conditions have on the products. Therefore, this review of the literature aims to bring together such results and discuss how biosynthetic reaction parameters can be used to optimise AgNP production with a focus on shape and size control. It begins by reviewing the proposed mechanisms for AgNP biosynthesis in bacteria, which is then followed by examining reaction parameters which have been varied in the quest for optimising AgNP production.

2.2.1 Silver Toxicity, Resistance, and Nanoparticle Synthesis

Following the discovery of biogenic metallic nanoparticles by Klaus et al. in 1999,[43] the possibility of controllable biosynthesis has been an ultimate yet elusive goal of the field. However, the mechanistic understanding of the underpinning biology remains limited. Especially for AgNP production, there is a relative paucity of detailed investigations. Despite this, efforts continue to identify the pathways involved in the reduction of soluble Ag^{+} and accumulation of zero valent Ag^{0}.

Silver Toxicity to Cells

To understand how bacteria produce nanoparticles, it is first prudent to understand why bacteria make nanoparticles. It has long been known that silver is either toxic to bacteria or bacteriostatic.[44] This toxicity stems from the high affinity with which Ag^{+} binds to a range of biological macromolecules, particularly those with electron rich sulphur hydryl (including thiol) and amine groups. This results in the side chains of cysteine residues in proteins often being targeted by Ag^{+} which disrupts disulphide bonds leading to the denaturation of the tertiary structure of proteins, and thus their functions.[45] Additionally, Ag^{+} ions complex with the heterocyclic amines in DNA bases, causing disruption to the transcription and replication of genetic material.[46] This activity results in substantial inhibition of major biological processes including DNA, RNA, protein, and peptidoglycan syntheses at levels comparable with commonly used antibiotics.[47] Moreover, complete cell lysis is not induced by Ag^{+}, but membrane disruption has been evidenced.[47,48] These effects, compounded with damage to the cell membrane, have been demonstrated to have detrimental outcomes for the bacterium. Furthermore, high concentrations of Ag^{+} are thought to induce apoptosis in bacterial cells, as demonstrated by the shrinking of cells sizes and fragmentation of DNA, a behaviour more commonly attributed to eukaryotes.[49,50]

This induction of cell "suicide" is hypothesised to result from the increase in the concentration of reactive oxygen species in the cell, attributed to Ag^+ interfering with NADPH dehydrogenase II activity.[50]

The toxicity of Ag^+ exhibits stress on bacteria which has stimulated the evolution and prevalence of resistant mechanisms. A bacterium capable of detoxifying or removing Ag^+ holds a potential survival advantage in environments where Ag^+ is present. The processes that allow Ag^+ resistance are believed to be important for AgNP bioproduction.[51,52]

Resistance of Cells

Reflecting the toxicity of Ag^+ to bacteria, two mechanistically different resistance systems have evolved and are concurrently represented in resistant organisms:

The first mechanism is an efflux system. This functions to sequester Ag^+ ions from the intracellular environment and eject them via a P-type ATPase (SilP) and an efflux transporter (SilCBA).[53,54] Homologous to the Cus copper-efflux system, which acts to sequester and remove Cu^+ from the intracellular environment,[54–56], sil genes have been found in Ag-resistant organisms from both environmental and clinical settings.[53,57] These sil genes were identified from their sequence homology with known Cus genes, and their functions inferred.[54,58] While both systems have a Ag^+ and Cu^+ sequestering protein, SilF and CusF, respectively, which are thought to support the efflux process, the Sil system also has the SilE protein. The SilE protein is a highly specific periplasmic Ag^+ sequestering protein which can bind up to 10 Ag^+ ions per peptide.[53] Homologues of sil genes have been found in organisms capable of producing AgNPs and are thought to be involved, due to their ability to sequester Ag^+, in the production process.[52] However, the mechanism of protein involvement in the process remains to be determined. The ability to sequester ions only provides the bacterium with short-term protection. For a long-term solution to the toxicity of Ag^+, the cell must use alternative methods.

The second mechanism of Ag resistance suppresses the hazard by utilising the reduction of Ag^+ to Ag^0. Ag in its metallic form is less toxic to the cell, so by reducing solubilised Ag^+ to insoluble Ag^0 the bacterium can reduce the chemical stress.[59] Upon creation, Ag^0 atoms undergo nucleation and continue to grow into AgNPs. Like chemical reduction synthesis, this process follows a bottom-up approach building nanoparticles via multistep self-assembly (as opposed to removing material from larger materials in a top-down route), but instead of reducing agents such as sodium borohydride, less hazardous biological components are used. Exactly how this process occurs remains unclear, but two main theories have been postulated as detailed below.

Mechanisms of Silver Nanoparticle Biosynthesis

Of the two hypotheses proposed, the first is that simple biochemicals act as reducing agents for Ag^+ reduction. Aldehyde groups, like those in sugars, have been suggested as key reduction sites and electron donors: for example, in a number of *Lactobacillus* species which demonstrated the ability to rapidly produce AgNPs, both intra- and extracellularly.[60] However, reducing sugars are produced by all bacteria, AgNPs are not. This hypothesis does not account for the distinct species-dependency reported in the literature. Instead, it is likely that an enzymatic component to the mechanism is involved.

The second hypothesis regarding the reducing agent in biological systems has led to NADH or NADPH-dependent nitrate reductase enzymes (Figure 2.6), which have been identified in a number of species as having crucial roles in the detoxification and reduction of Ag^+.[61,62] NAD(P)H-dependent nitrate reductases are part of the molybdenum-containing dimethylsulphoxide reductase (DMSOR) enzyme family.[63] Based on the locations of DSMORs within the cell, three main classes have been identified. Nas and Nar type enzymes are cytoplasmic and respiratory membrane-bound types, respectively. As many studies have indicated that AgNP formation is located at the cell surface or in the periplasmic space,[43] of particular interest here are the dissimilatory periplasmic nitrate reductases, or Nap species.

The enzymes, as their name suggests, utilise the reductive power of NAD(P)H to reduce nitrate to nitrite. To achieve this, NAD(P)H donates two electrons via a hydride ion (H^-) to the NAD(P)H binding site of the reductase. The electrons are passed via iron-sulphur clusters to the Mo active site where the nitrate, which covalently binds to the Mo, then undergoes reduction of nitrate in the presence of H^+ to form nitrite (NO_2^-) and H_2O.[63]

An α-NADPH-dependent nitrate reductase isolated from the fungus *Fusarium oxysporum* was able to produce AgNPs in a reaction which required 4-hydroxyquinoline as an electron shuttle, as shown in Figure 2.6 A.[62,64] The AgNPs were produced *in vitro* under anaerobic conditions at 25 °C with purified α-NADPH-dependent nitrate reductase, $AgNO_3$ (1 mM), α-NADPH, 4-hydroxyquinoline, and phytochelatin as a capping agent. AgNP production was not observed in the absence of α-NADPH, nor in controls lacking 4-hydroxyquinoline, nitrate reductase, or phytochelatin.[64] The requirement of an electron shuttle indicated that the enzyme was not directly reducing the Ag^+ and the NO_3^- in parallel, but instead reduced the nitrate and the generated electron was transferred to the Ag^+ which was subsequently reduced in a series fashion. Additionally, the electrochemistry of the involved species favoured the electron transfer to Ag^+ from NO_3^-, as can be seen in Figure 2.6 B. There is, however, little evidence to support the direct generalisation of this idea to bacteria.

From the relatively limited amount of work presented on the bacterial mechanism, there is some support

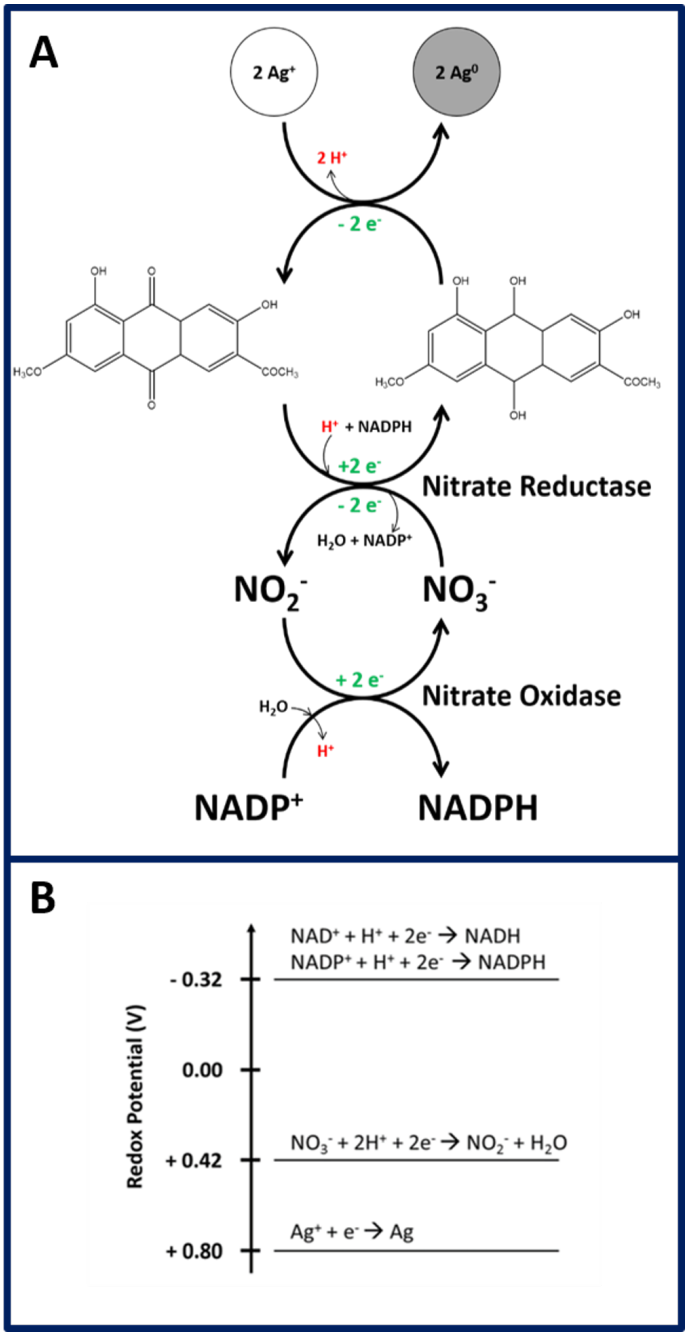

Figure 2.6: A) Proposed mechanism of reduction of Ag^{+} in the formation of nanoparticles utilising the reduction of nitrate to nitrite in the fungus *Fusarium oxysporum*. The electrons are shuttled from the reductase to Ag^{+} by an electron shuttle, in this case 4-hydroxyquinoline. Adapted from Durán et al.[61] originally published by BioMed Central. B) Reduction potentials of reactions thought to be involved in biogenic AgNP production. This figure has been published by Mabey et al.[6]

for the involvement of NAD(P)H-reductases with nitrate reductase activity having been detected in the cell-free extract (CFE) of *Bacillus subtilis* following 120 h extracellular AgNP production and is thought to be the catalyst in the process.[65] In support of this hypothesis, AgNPs were produced by the supernatant of *K. pneumonia* cultured in Muller-Hinton broth. However, the addition of a sub-inhibitory concentration of piperidone (a natural inhibitor of nitro-reduction in Enterobacteriaceae) partially inhibited AgNP synthesis by over 50%.[66] It should be stressed, however, that making the jump from a fungal to a bacterial mechanism needs further investigation to identify the commonalities and differences.

It has been postulated that it is the aforementioned SilE protein that chelates and then presents Ag^+ to a reductase,[42,67] as supported by the discovery that a number of bacteria, which are able to produce nanoparticles, carry the sil genes.[52,57] A summary of this proposed theory is outlined in Figure 2.7. By examining nitrate reductase during AgNP formation in the archaeon *Halococcus salifodinae*, Srivastava et al.[68] suggested that Ag^+ became the favoured electron donor over nitrates, as evidenced by a reduction in the concentration of nitrite in an Ag^+ dose-dependent manner. Indeed, following the conclusion of AgNP production, nitrite concentrations rose to levels above Ag^+-free controls, suggesting the presence of Ag^+ had resulted in increased expression of nitrate reductase. Additionally, by comparing nitrate reductase activity following exposure to KNO_3 and $AgNO_3$ it was possible to attribute the increase to Ag^+ and not the NO_3^-, suggesting that the nitrate reductase was involved in Ag resistance. Furthermore, heat inactivation of *Lactobacillus casei* was shown to inhibit AgNP production, supporting the theory that the process was enzyme mediated.[69] Following boiling for 30 min, the heat-treated biomass did not produce AgNPs over 85 min of observations suggesting the enzyme involved in the biocatalyst were denatured or degraded. Following their formation in cells, the particles were either ejected from the cell or grew in the periplasmic space (Figure 2.7). Larger non-spherical particles have been observed inside cells, with smaller spherical particles frequently observed in the external environment.

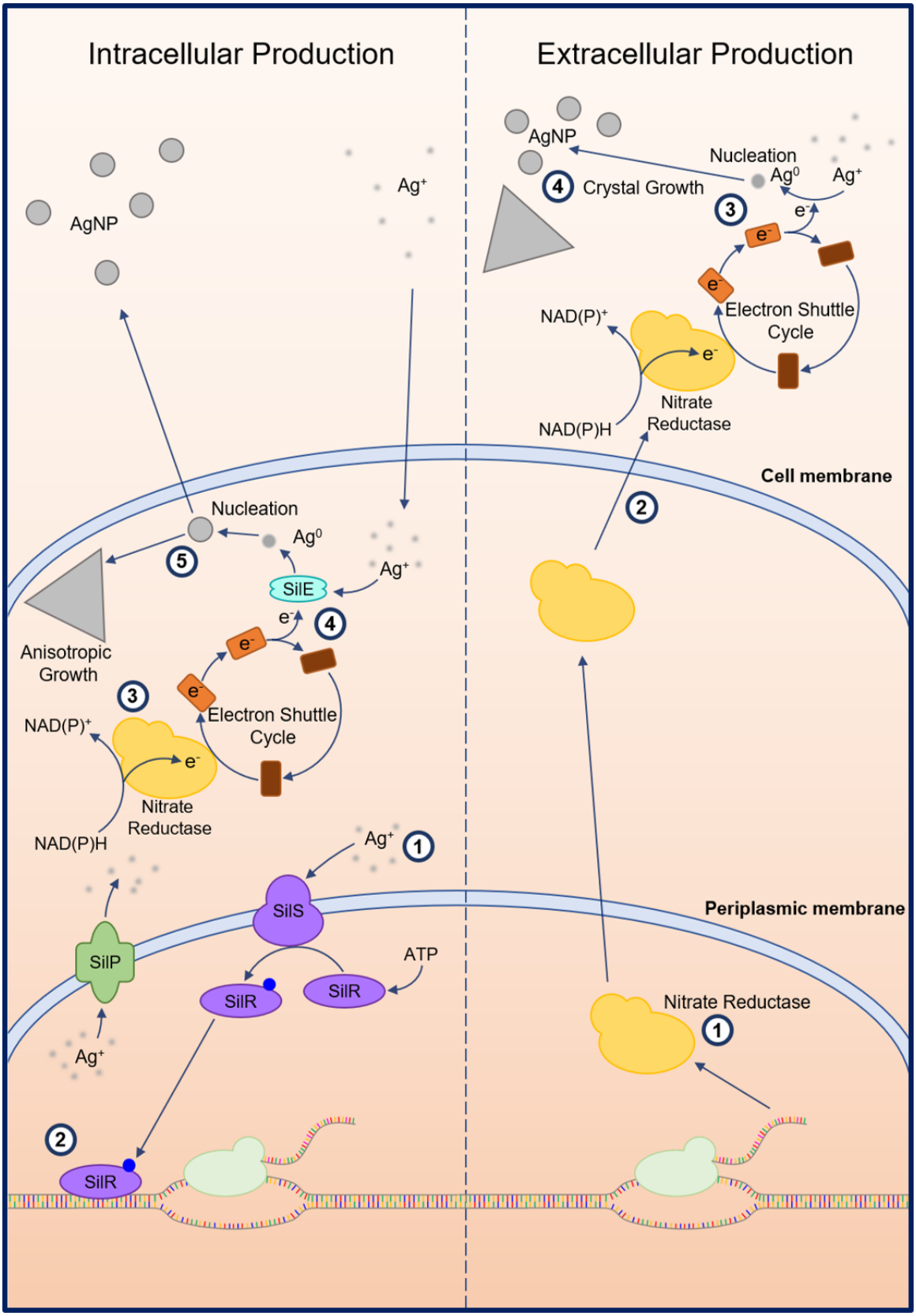
Intracellular Production
Extracellular Production
AgNP
Ag+
Nucleation
Ag0
Crystal Growth
e-
Electron Shuttle Cycle
NAD(P)+
NAD(P)H
Nitrate Reductase
Cell membrane
SilE
Anisotropic Growth
SilP
SilS
SilR
ATP
Periplasmic membrane

Figure 2.7: Proposed mechanisms for intracellular (left) and extracellular (right) AgNP production in bacteria. Intracellular AgNP production using the SIL proteins is thought to be initiated by the sensor kinase SilS protein which phosphorylates the derepresser SilR (1). SilR phosphorylation results in expression of the Sil operon which includes the SilCBA anti-porter complex, a P-type ATPase (SilP), and SilE, which sequesters Ag^{+} ions (2). An NAD(P)H-dependent nitrate reductase is thought to reduce an electron shuttle via the oxidation of NAD(P)H to $NAD(P)^{+}$ (3). The electron shuttle facilitates the electron transfer from the reductase to SilE (4), though the electron exchange does not need SilE to occur. Following reduction, Ag^{0} atoms undergo nucleation to form seed particles (5). Extracellular production of AgNPs, such as when using cell-free extract, through an enzymatic route likely results from the innate expression of an NAD(P)H-dependent nitrate reductase (1), which is secreted or leaked to the extracellular environment (2). Here, the electron shuttle cycling occurs in a similar way to intracellular production (3), and AgNP growth can then occur (4). However, smaller spherical particles are more often observed in extracellular production. Non-enzymatic reducing processes may also occur in both mechanisms. This figure has been published by Mabey et al.[6]

Other enzymes, including amylase, laccases, peroxidase and lysozyme, have been shown to be involved in AgNP formation, but have received relatively little attention.[70] These mechanisms remain to be understood before they can be fully exploited. Moreover, the molecular biology influencing crystal growth has seen little research despite the species dependent nature with which nanoparticles with different geometries are made. Nonetheless, the studies discussed below have investigated the physiochemical impact of various growth conditions on the formation of the nanoparticles.

2.2.2 Biosynthetic Reaction Conditions

Isolated from a silver mine, *Pseudomonas stutzeri* AG259 was the first bacterium found to demonstrate the ability to produce AgNPs.[43] After this discovery at the turn of the millennium, many more species capable of such activity have been identified (Figure 2.8 on page 21). Nonetheless, the biosynthesis of AgNPs can be influenced by chemical and physical factors, such as thermodynamics, reaction and enzyme kinetics, and photo/radio-catalysis, as well as the underlying biology of the host organism. The complex nature of AgNP production means that these factors are connected in ways which are not yet fully understood. However, work has been performed in numerous studies to investigate how the reaction conditions affect AgNP biosynthesis.

Incubation Time

By far, the most investigated variable influencing the biosynthesis of AgNPs is reaction duration, typically in the range of minutes[66,71] to days.[57,72,73] As expected, the longer the duration, the more and potentially larger particles are produced. However, the vast majority of findings report no change in the LSPR peaks

throughout the duration of experiments, indicating no change in the morphologies of the AgNPs being produced over 20 minutes to 120 hours.[51,74,75]

The previous reports notwithstanding, a small number of studies have observed changes in particles morphologies over time. For example, when using *Comamonas acidovorans* CFE, a slight blue shift and broadening of the LSPR peak over 72 hours was observed[76]: this is likely the result of smaller particles forming and an increase in polydispersity.[12] Conversely, the AgNPs produced by *Aeromonas* sp. SH10 over 1 or 6 days showed a slight red shift in the LSPR peak position over 6 days, a phenomenon not observed in the shorter timescale. This slight bathochromic-shift indicates particles with larger sizes being formed.[77,78] These slight changes in LSPR peak position reflect subtle changes in particle morphologies and geometries, and also the surface coating of the particles. The occurrence of these changes is not understood.

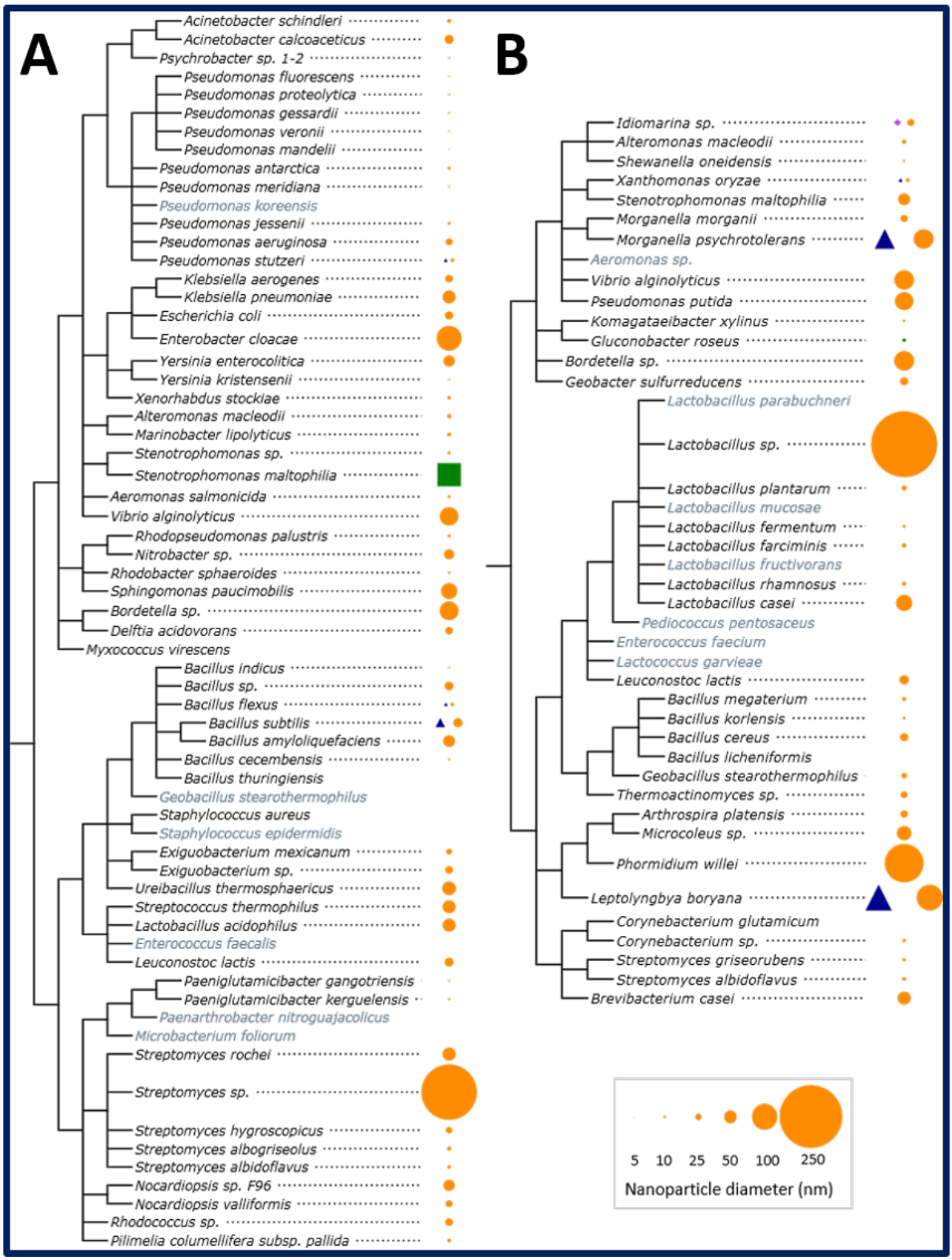
A
Acinetobacter schindleri
Acinetobacter calcoaceticus
Psychrobacter sp. 1-2
Pseudomonas fluorescens
Pseudomonas proteolytica
Pseudomonas gessardii
Pseudomonas veronii
Pseudomonas mandelii
Pseudomonas antarctica
Pseudomonas meridiana
Pseudomonas koreensis
Pseudomonas jessenii
Pseudomonas aeruginosa
Pseudomonas stutzeri
Klebsiella aerogenes
Klebsiella pneumoniae
Escherichia coli
Enterobacter cloacae
Yersinia enterocolitica
Yersinia kristensenii
Xenorhabdus stockiae
Alteromonas macleodii
Marinobacter lipolyticus
Stenotrophomonas sp.
Stenotrophomonas maltophilia
Aeromonas salmonicida
Vibrio alginolyticus
Rhodopseudomonas palustris
Nitrobacter sp.
Rhodobacter sphaeroides
Sphingomonas paucimobilis
Bordetella sp.
Delftia acidovorans
Myxococcus virescens
Bacillus indicus
Bacillus sp.
Bacillus flexus
Bacillus subtilis
Bacillus amyloliquefaciens
Bacillus cecembensis
Bacillus thuringiensis
Geobacillus stearothermophilus
Staphylococcus aureus
Staphylococcus epidermidis
Exiguobacterium mexicanum
Exiguobacterium sp.
Ureibacillus thermosphaericus
Streptococcus thermophilus
Lactobacillus acidophilus
Enterococcus faecalis
Leuconostoc lactis
Paeniglutamicibacter gangotriensis
Paeniglutamicibacter kerguelensis
Paenarthrobacter nitroguajacolicus
Microbacterium foliorum
Streptomyces rochei
Streptomyces sp.
Streptomyces hygroscopicus
Streptomyces albogriseolus
Streptomyces albidoflavus
Nocardiopsis sp. F96
Nocardiopsis valliformis
Rhodococcus sp.
Pilimelia columellifera subsp. pallida
B
Idiomarina sp.
Alteromonas macleodii
Shewanella oneidensis
Xanthomonas oryzae
Stenotrophomonas maltophilia
Morganella morganii
Morganella psychrotolerans
Aeromonas sp.
Vibrio alginolyticus
Pseudomonas putida
Komagataeibacter xylinus
Gluconobacter roseus
Bordetella sp.
Geobacter sulfurreducens
Lactobacillus parabuchneri
Lactobacillus sp.
Lactobacillus plantarum
Lactobacillus mucosae
Lactobacillus fermentum
Lactobacillus farciminis
Lactobacillus fructivorans
Lactobacillus rhamnosus
Lactobacillus casei
Pediococcus pentosaceus
Enterococcus faecium
Lactococcus garvieae
Leuconostoc lactis
Bacillus megaterium
Bacillus korlensis
Bacillus cereus
Bacillus licheniformis
Geobacillus stearothermophilus
Thermoactinomyces sp.
Arthrospira platensis
Microcoleus sp.
Phormidium willei
Leptolyngbya boryana
Corynebacterium glutamicum
Corynebacterium sp.
Streptomyces griseorubens
Streptomyces albidoflavus
Brevibacterium casei
5 10 25 50 100 250
Nanoparticle diameter (nm)

Figure 2.8: Bacteria known to produce AgNPs. Both cell-free extract (A) and whole-cell cultures or biomass (B) have been investigated.[43,51,57,60,66,69,71–73,75–145] The shape and relative size of the nanoparticles produced are shown. If more than one report exists for a given organism, the average has been used. Names in grey did not report particle morphologies. Taxonomy data were collected from the NCBI Taxonomy database and the figure was generated using the ETE3 tool kit.[146]. This figure has been published by Mabey et al.[6]

More substantial changes in particle shape were observed with the formation of a second LSPR peak between 650 nm - 950 nm from AgNPs produced using *Morganella psychrotolerans* over 20 hours.[57] This is likely due to be the result of non-spherical particles forming, but may also reflect aggregation of nanoparticles.

Based on the above findings, the duration of incubation appears to have minimal effect on the geometries of nanoparticles produced, but does seem to be important for yield. It is consistently evident that the longer cultures are exposed to Ag sources, the more AgNPs are being produced. The relatively slow reactions of biological production routes are a potential challenge which remains to be overcome when competing with much faster chemical synthesis routes (in the order of seconds or minutes).

Temperature

Temperature has a critical impact on biological systems by affecting the thermodynamics of biochemical reactions and enzyme activity, as well as physiological alterations to gene and protein expression. This is no different in the case of biogenic AgNP synthesis. As with most biochemical reactions, the rate of reduction of Ag^{+} to Ag^{0} is faster at higher temperatures. Generally, AgNP formation in CFE favours higher temperature conditions than whole cell cultures, but production will decrease if the temperature becomes too high, presumably due to thermal denaturation of the reducing enzymes.[99,104,123,130,137] Reactions using biomass have also been reported at high temperatures; *Aeromonas sp.* and *Corynebacterium sp.* showed optimal production at 60°C.[78,145] In some cases (*Escherichia coli*, *Bacillus cereus*, *Staphylococcus aureus*, and *Yersinia enterocolitica*), higher temperatures are required to observe any AgNP production.[123] This suggests that the reaction is a chemical process with little, if any, enzymatic involvement. Despite the evidence for higher production rates at higher temperatures, it should be noted that this is not universal. For example, the temperature at which *Xanthobacter kerguelensis* CFE was incubated had insignificant effect on AgNP production.[136]

For species with optimal growth temperatures of 37°C, the optimal temperature for AgNP production was often higher when using CFE.[104,123] Similarly, psychrotolerant bacteria have shown greater AgNP production at temperatures above those considered optimal for growth.[57,72] The mechanism has not been

explored.

Temperature appears to be a strong effector of particle morphologies with studies reporting different geometries from different temperatures. Higher temperatures have been associated with smaller spherical AgNPs from *E. coli* and *Acinetobacter calcoaceticus*.[99,116,137] In contrast, at lower temperatures (15°C and 5°C), while production rates are markedly lower, an increased frequency of larger non-spherical particles, including hexagonal plates and triangular prisms has been reported.[57] However, there is conflicting evidence to support this as the nanoparticles produced by psychrophilic bacteria at 4°C were typically smaller and more monodispersed compared with those produced at 30°C, but were produced at a slower rate.[72] Moreover, a slight (+10 nm) red shift was observed at higher temperatures when Ag^{+} was reduced to nanospheres by *P. stutzeri* CFE,[130] indicating the presence of larger particles.

Caution should be taken when using high temperatures in biological systems. Although at 100°C the CFE of *Plectonema boryanum* produced octahedral and triangular prisms more frequently than at lower temperatures,[108] the boiling of the solution ultimately renders any biological or enzymatic involvement moot.

The utility of a colloid relies on its stability, that is, the ability of the particles to remain in suspension. Particles produced at lower temperatures have been reported to be more stable with aggregation occurring at higher temperatures.[57,109,136] The superior colloidal stability of biogenic AgNPs compared with chemogenic particles is thought to stem from protein corona which coat the surface of the particles. At high temperatures, the constituent proteins denature, and the corona become compromised, reducing its stabilising effects. This may explain the increase in aggregation observed.

Although changes in the reaction and enzyme kinetics, as well as reagent, product, and corona stabilities likely play important roles, the mechanism concerning what controls the shape of AgNP produced in biological systems still remains poorly understood.

To summarise, likely through its influence on thermodynamics and enzymatics, the temperature of incubation appears to have strong effects on nanoparticle formation in biological systems. Whilst the thermodynamic factors impact directly on crystal growth, temperature is a well-known effector of enzymatic function and activity. Separating these influences in the complex environment of a bacterial cell or CFE requires further investigation. Non-spherical AgNP production, for instance nanoprisms, appears to be favoured by colder conditions. However, there is a trade-off between achieving the desired particle geometry and the production rate.

Silver Substrate

$AgNO_3$ is the predominant source of Ag^+ used experimentally for bacterial AgNP production. This is principally due to its high solubility in water compared to other Ag salts allowing for sufficiently high bioavailability to be achieved. Many studies have been performed in which the concentration of $AgNO_3$ has been varied and the consequences on nanoparticle synthesis examined.

In most cases, the production of AgNP is higher when more $AgNO_3$ is used, as expected.[101,130,147] While 1 mM $AgNO_3$ is typical,[72,81,93,111,120,124] concentrations of 9 mM or higher have been used.[43,73,113] However, as the reduction of Ag^+ is thought to be a method of detoxifying Ag, it is logical to presume that once the reduction system is saturated any excess Ag^+ will have toxic effects on the cell, that is, there must be an upper limit that the systems can handle. Such toxicity would be detrimental to the enzymatic activity of the mechanism leading to a decrease in reduction activity and will likely be species dependent. Indeed, enzyme saturation has been suggested to explain why higher concentrations do not always result in greater production; numerous reports have shown a decrease in production with more Ag^+ present.[52,99,135,137]

There have been few reports about the effect of $AgNO_3$ concentration on the characteristics of nanoparticles produced beyond the change in production rate. However, the smallest particles produced using *E. coli* CFE were observed at the optimal concentration of $AgNO_3$ for yield, while larger particles were above and below optimal.[99] A similar pattern was seen in LSPR peak intensity suggesting that a greater number of smaller particles were being produced with the optimal concentration compared with fewer larger particles under suboptimal conditions, though this was not thoroughly examined.

The stoichiometric ratio of the reagents is also important. Biomass harvested from *Lactobacillus casei* subsp. Casei cultures demonstrated that a lower $AgNO_3$ to biomass ratio yielded higher AgNP production.[69] In a similar way, the volume ratio of $AgNO_3$ to CFE of *Pseudomonas mandelii* was investigated by Mageswari et al.[109] A volume ratio of 1:99 proved most effective for AgNP production. The ratio reflects the stoichiometry of the reaction with the biomass supplying the reducing agent and the capping agents, suggesting that the limiting reagent in the reaction is the reducing agent (i.e. NAD(P)H) in the CFE.

A paucity of published literature exists on the use of Ag salts other than $AgNO_3$ in the bacteriosynthesis of nanoparticles. Nonetheless, AgCl is an intermediate formed during the bioreduction of $AgNO_3$ by *Klebsiella pneumoniae*. Using AgCl as the primary Ag^+ substrate, very small nanoparticles were formed in a light-assisted process,[74] though questions have been raised about the true usefulness of AgCl because of its very poor solubility in water.[72] AgCl, like most Ag salts such as $AgCO_3$ and Ag_2O, is very insoluble in water making reaching the required concentrations a challenge. However, more soluble Ag_2O_4 has been found to produce larger spherical nanoparticles (diameters of 50 nm - 150 nm) using *Salmonella enterica*

serovar Typhimurium CFE.[148]

Moreover, complexed Ag in the form of diamine Ag ($[Ag(NH_3)_2]^+$) was also utilized for AgNP production. When diamine Ag was added to the biomass of *Aeromonas sp.* and *Corynebacterium sp.*, particles with diameters of 20 nm and 10 nm - 15 nm formed, respectively.[78,145] $[Ag(NH_3)_2]^+$ is resistant to forming AgOH under basic conditions. AgOH is an insoluble compound which forms from hydroxide ions in water and precipitates out of solution when the pH rises above $\approx$8.0 under permitting conditions.

In summary, $AgNO_3$ remains the most frequently used source for introducing Ag^+ ions to reaction media for AgNP production. The concentration of the substrate appears to have little effect on the geometry of particles produced, but production amounts depend on the amount of Ag^+ available. In most cases, there appears to be an optimal concentration, above which the system becomes saturated, and the toxic effects likely have negative impacts on the reduction mechanism.

pH

The typically narrow optimal range of pH conditions processed by enzymes means that they are highly sensitive to conditional changes. As there have been very few extremophiles investigated for AgNP production, it is not surprising that many reports investigating how pH affects AgNP bioproduction show that near-neutral conditions (pH 6-8) are favoured.[79,104,127,143] Nevertheless, slight to extreme acidic environments are optimal for biomass of *Corynebacterium sp.* and *Pseudomonas putida*, respectively.[143,145] Such conditions have also yielded larger particles, though production rates were lower than under basic conditions.[99]

Most studies on optimal pH conditions have suggested basic environments appear desirable for production. In a whole cell culture of *Bacillus megaterium*, pH 8.1 was determined to be best for production across a range from pH 5.6 to pH 8.1.[127] However, the reaction used sunlight exposure to drive the reaction. As sterile growth media can photo-reduce Ag^+, the optimal pH reported likely does not reflect solely the optimal conditions of the organism.[149] Moreover, the optimal reported pH value was the highest tested; further investigation beyond this range would be valuable to see if the trend of favouring basic conditions continues as more basic conditions of pH 9 or pH 10 have frequently been reported as optimal,[99,130,150] with production not observed under acidic conditions.[87]

The investigation into AgNP production using *Streptomyces viridochromogenes* CFE by El-Nagger used a Design of Experiment approach to explore a range of neutral to basic pH conditions.[150] High pH was favoured for production which decreased with decreasing pH conditions. However, sterile controls were not reported, once again leaving the possibility that chemical reduction by the growth medium components

was occurring. Moreover, acidic conditions were not explored. Rajora et al.[130] did, however, explore acidic conditions to pH 3 and through to pH 11 using *P. stutzeri* CFE. An optimal pH of 9 was reported with a decrease in production at pH 11 being suggested to be due to enzyme inactivation, though this was not investigated. When Gurunathan et al.[99] explored a series of reaction conditions on AgNP production by *E. coli* CFE, optimal production was observed at pH 10 (range investigated: pH 5 – pH 12) though production under conditions above pH 9 were all markedly higher than pH 8 or lower. As with the previous studies, the effects of pH of sterile controls were not reported. This is an important consideration as through systematically assessing AgNP formation under pH conditions ranging from 4 to 12 in sterile culture media, it was demonstrated that nanoparticles formed at the highest rate and with higher degrees of uniformity under very basic conditions.[149] As the pH of the reaction environment can change the reduction-oxidation process where its exact effect also depends on the reactants involved, it appears that low H^+ concentrations are favoured to drive the reduction of Ag^+ in an excess of electron donors (Figure 2.6 A). Therefore, without reporting adequate controls, the power of the findings within these studies is limited and ultimately require further investigation for clarification.

While pH (pH = 5, 7, & 10) had little effect on AgNP production in *Pseudomonas antarctica*, and similarly in *A. kerguelensis*, it was noted that particles were least stable in pH 7 conditions.[136] This may be due to the protein corona having a more neutral charge, so, is less effective at repelling other particles. Similarly, particle aggregation was observed at a pH of 5 or below, suggesting the usually high stability of biogenic AgNPs being compromised.[109] Additionally, in *Lactobacillus fermentum* under more basic conditions reduction rates were reduced, however recovery was increased.[60] Denaturation of the proteins may also play a role in this process, but has not been explored in detail.

While it depends on the exact concentrations of reagents used, Ag^+ can complex with hydroxide ions (OH^-) which exist in alkaline conditions to form AgOH, a water insoluble compound observed as a precipitate, typically at pH levels above 8. Although AgOH has been used in chemical AgNP synthesis,[151] its poor solubility reduces the bioavailability of Ag^+ for reduction. Additionally, silver oxide is spontaneously formed in solution which is also very poorly soluble in water. The outcome of the formation of these precipitates is the decrease in Ag^+, concentrations and their availability to reductase enzymes for reduction. As discussed above, this challenge can be overcome by selecting alternative Ag-amine sources.

Halides

Halides, especially chlorides, have high binding affinities with Ag^+; when both Cl^- and Ag^+ are present in solution, water insoluble AgCl forms spontaneously. Combined with the common occurrence of NaCl

in bacterial growth media, the concentrations of halides are consequently important considerations when exploring nanoparticle formation by bacteria.

Of the dearth of reports on the matter, the presence of Cl^- appears deleterious for AgNP production,[72] while indeed many investigations use media without the addition of NaCl.[51,57,99] The production of insoluble AgCl reduces the bioavailability of the Ag^+ for nanoparticle production.

In a cell-free process using extracts of *Bacillus amyloliquefaciens*, 2 mM NaCl was observed to be optimal for photo-assisted AgNP production.[152] However, by adding the NaCl directly to the $AgNO_3$ the researchers produced an AgCl precipitate, whereas by adding the NaCl to the media first the precipitation was avoided. The bioavailability of the Ag^+ was therefore maintained with over 98% of the Ag added reduced to nanoparticles. While these findings were not elaborated in detail, the effect may be due to the formation of an intermediate species. Indeed, AgCl has been suggested to be an intermediate in the production of AgNP in sterile growth media via a photo-catalysed reaction.[149]

The presence of Cl^- ions in the growth medium has been thought to contaminate AgNPs to form AgCl nanoparticles.[129] Durán et al. have discussed the bioproduction of AgCl nanoparticles and stressed the importance of distinguishing, through X-ray diffraction analysis, the different compositions of biogenic nanoparticles.[153] They explained that nanoparticles reported as Ag were frequently not fully characterised or misidentified from AgCl particles or AgCl contaminants. In many applications, knowing the exact composition of the particles is crucial.

Due to the high binding affinity between Ag^+ and Cl^-, considerations into the presence of chlorides in growth media must be made. Conflicting reports have been published on the effects Cl^- ions may have on nanoparticles with limited studies relating to biological systems. There have been no reports of other halides (Br^- and I^-) in bacterial systems.

Media Composition

Related to both pH and halide concentrations is the composition of the growth media in which the nanoparticle producing species are investigated. There has been little direct investigation into how growth media composition affects AgNP production. However, in a comparison between LB growth medium and brewery effluent, the size of AgNPs produced by *B. subtilis* CFE were larger in LB and had a greater tendency to form aggregates.[154] A more minimal media was preferred when investigating the composition of growth media used for culturing *Streptomyces rochei* for AgNP production.[79] Interestingly, it was observed that the lowest concentration of KNO_3 was favoured. This conflicts with the observation that AgNP biosynthesis by *E. coli* DH5-α CFE was higher in nitrate broth compared to LB.[99] The involvement of nitrate reductases in

the reduction of Ag^+ may explain this as their expression may be upregulated in a nitrate rich environment. Nevertheless, further investigations into the complexity and composition of growth media are necessary to better understand this process.

Aerobicity

An interesting confliction has arisen around bacterially produced AgNPs under different aerobic conditions. On one hand, most cultures are reportedly shaken (usually at 200 RPM) during incubation under aerobic conditions, regardless of whether they are aerobes, or obligate or facultative anaerobes.[51,57,60,116,137] On the other hand, some reports have indicated that nanoparticle formation is most efficient under anaerobic conditions.[138,147]

Whilst agitation is used to improve the dissolution of oxygen (among other reasons discussed below), there appears to be no previous investigation in which dissolved oxygen has been measured. A study by Lin et al. showed that AgNP formation in *E. coli* favoured anaerobic conditions, suggesting the enzymes involved to be anaerobically-induced.[147] This is supported by evidence from other researchers that suggest a nitrate-reductase plays a key role in the reduction of Ag^+.[61,62] Nitrate-reductases are typically, though not exclusively, expressed under anaerobic conditions. However, there has been no comparison between cultures of an organism grown aerobically and anaerobically to further investigate this.

Mixing

The mixing or shaking of bacterial suspensions is routinely used to maintain a homogenous solution of cells and nutrients, as well as to promote gas exchange with the ambient atmosphere, be it aerobic or anaerobic. In the case of AgNP biosynthesis, mixing impacts on the relative local concentrations of reagents and acts to disperse any nanoparticles in the extracellular environment. How the mixing process affects AgNP production has received little attention. Such considerations will be crucial if the scale of production methods is increased.

From the paucity of reports on the topic, mixing during incubation appears to delay nanoparticle formation,[74] and may therefore be a potential method for controlling the rate of production. Following a 5 min mix to homogenise the solutions (CFE of *K. pneumoniae* and 1 mM $AgNO_3$), the mixing was continued in one sample for 20 min while the other sample was then left under static conditions. Both samples were irradiated with visible light and production measured over 20 min. The increased mixing may have enabled a greater exchange of oxygen from the atmosphere into the solution. With increased oxygen present, the oxidation of seed particles may explain the decreased rate and over production, though this was not

explored in the study.

If the commercial application of AgNPs are to be fully realised, larger scale production methods are required. Consequently, it is necessary to investigate the effects of different bioreactor setups, aeration techniques, and flow dynamics.

Visible Light

Silver compounds are notoriously sensitive to light, and this fact can be exploited in AgNP production. Many bacteria have been shown to produce AgNPs when exposed to light, and some require light to occur.[81,85,86,88,113,116,136]

Wei et al.[152] have demonstrated that solar radiation intensity influenced the biosynthesis of nanoparticles in CFE. Sunlight caused the reaction rate to increase in an intensity-dependent manner. Sunlight is a free and renewable resource which is beneficial when considering large-scale production. However, energy efficient artificial light sources are more favourable due to the limited reliability and control of solar radiation. As yet, no in-depth investigation into this mechanism or which wavelengths of light are responsible for this phenomenon has been published.

In some chemical production routes, light at specific wavelengths is used to influence the specific geometries of particles;[2] the effects of different colours of light have on the bacterial synthesis of AgNPs have not been explored in detail to date. It is well documented that irradiation of AgNPs can cause polymorphic shifts from spheres to nanoprisms in chemical production.[16] While this does not appear to have been attempted in bacteria, exposure to light altered the size and thus the optical properties of nanoparticles produced in *K. pneumoniae*.[74]

It should be noted, however, that most publications on bacteriogenic AgNPs do not report the lighting conditions of their reactions.[60,75,76,99,102,137,147,154–157] Relatively few explicitly state that reactions were carried out in the dark or have controls in the dark, especially when light was not a primary factor under investigation.[43,51,57,74,116,149] As such, caution should be taken when interpreting the results of studies which lack this information.

In summary, exposing bacterial cultures to varying intensities and wavelengths of light may influence, and therefore may be ultimately used to control bacterial, AgNP formation. However, which wavelengths of light should be used and at which stage of the production process would be most effective still remain to be identified. Ambiguous reporting as to the lighting conditions of many published reactions makes interpretation of many results challenging.

Ionising or Electromagnetic Radiation

Additional conditions have also been investigated alongside those already discussed, though not to the same degree. For instance, γ-ray radiation has been employed to aid in the production of AgNPs in CFE from *Bacillus stearothermophilus* cultures.[92] The γ-rays were thought to cause radiolytic reduction of Ag^+ ions. Higher doses of radiation were associated with increased formation of AgNPs, however, too high doses proved detrimental. Similarly, microwave radiation has also been used with similar effects. Both CFE from *E. coli*[110] and B. subtilis[65] irradiated with microwaves yielded AgNPs. While the *E. coli* produced spherical particles, *B. subtilis* produced both spherical and triangular morphologies. Interestingly, the LSPR peak produced in the latter was sharper and more symmetrical than that without irradiation, indicating a higher monodispersity via the radiolytic process.[65] This may be attributed to the more homogeneous thermal field within the culture media as a result of microwave volumetric heating.

Despite the improved speeds of production and monodispersity, using ionising radiation has several obvious disadvantages, particularly if used on large scale. The risk to human health, higher energy requirements and additional costs of specialist equipment all can limit its application.

2.2.3 Summary of the Biosynthesis of AgNPs

Bacterial biosynthesis of AgNPs is a prime candidate for overcoming shortcomings associated with physical and chemical production methods, such as the use of hazardous reagents and particle instability. Currently, the underpinning biological mechanism remains to be fully resolved, though the involvement of nitrate reductase and Sil proteins have been suggested. While direct molecular biological investigations into the mechanism are sparse, it is clear that the process is heavily influenced by the reaction conditions under which the AgNPs are formed. Gaining a better understanding of this process is undoubtedly valuable for further optimising production.

It is evident from the body of work investigating the effects of reaction conditions discussed here, that most factors impact on the yield of AgNPs. In particular, a longer incubation time, higher substrate concentration, higher temperature, and anaerobic conditions resulted in more AgNPs being formed. In contrast, lower temperatures were associated with a decrease in producing nanospheres, but also with an increase in non-spherical particles. Temperature appears to be the biggest influencer for particle morphology.

Most work has been performed using CFE instead of whole cell culture. This has allowed for more extreme conditions to be investigated, for example pH and temperature. While contradicting results have been obtained between the two states, there have been few direct comparisons made. Exploring these differences may be useful in future applications.

Challenges remain for controlling the morphologies of the AgNPs produced biologically. While manipulating the temperature of reactions may provide some control, a reliable method of producing shaped non-spherical particles with a high degree of monodispersity remains a distant aspiration. The ability to produce monodispersed nanospheres is likely to be more achievable in the near future with continued efforts.

It is clear from Figure 2.8 that many species of bacteria or extracts thereof can reduce Ag^{+} to Ag^{0}. Focus should now be directed to developing a better understanding of the mechanisms involved, both in Ag resistant whole cell cultures, and CFE. Understanding how altered reaction conditions affect, not only the product, but also the components of the mechanism, is critical. Moreover, knowing how nanocrystals form and grow in biological environments is useful for future applications which require specific morphologies of AgNPs.

2.3 Characterisation Techniques

The applications in which AgNPs have potential are highly dependent on the properties of the particles, such as optical and chemical interactions. These properties are in turn dependent on physical characteristics of the particles, namely shape and size. Therefore, it is crucial to be able to characterise AgNPs to ensure they are well suited for their intended use.

2.3.1 Optical Characterisation

As discussed in Section 2.1.1, metallic nanoparticles interact in unique ways with electromagnetic radiation. Consequently, spectroscopic techniques can be used to analyse them. The composition, geometry, proximity to other particles, and dielectric environment all influence the interactions with light. In the case of AgNPs, this interaction mainly occurs within the visible region of the electromagnetic spectrum.

Colour Change

Ag^{+} is colourless in solutions, however, as previously shown in Figure 2.1, colloidal suspensions of Ag nanospheres have a distinctive yellow colour due to their strong characteristic absorption between 400 nm and 450 nm. Due to the chemical complexity of biological environments and the surface coating of biogenic particles, samples of AgNPs produced in bacteria typically appear dark red/brown in colour.[72,74,75,137,147] This colour change can be used as a crude, yet rapid, method to identify AgNP bioproduction. As non-spherical AgNPs have red-shifted absorption peaks, these colloids present with different colours which can

further aid in the assessment of production.

UV-Vis Spectroscopy

UV-Vis spectroscopy can be used to give quantitative support to any apparent colour change as characteristic absorbance peaks can be used to identify AgNPs; the peaks typically have a strong intensity and broad width. Biogenic Ag nanospheres have a single strong peak at 400 nm - 450 nm; samples containing non-spherical particles will show multiple red-shifted peaks. Samples, for example, containing both spherical and triangular particles would exhibit absorbance peaks for both species simultaneously.

AgNPs follow Beer-Lambert law (Equation 2.2) meaning the absorption (A) is proportional to the concentration (C; M) of the analyte. Usually, the path length (b; cm) is constant and based on the design of the spectrometer. The molar extinction coefficient (ϵ; M^{-1} cm^{-1}) is dependent on how the material interacts with the wavelength of light used for analysis. In the case of nanoparticles, this interaction is dependent on the shape and size of the particle leading to great intra-sample variation unless the sample is highly monodispersed. This makes absolute concentration analysis challenging. However, if the morphologies of two samples can be assumed similar, comparative assessments of the concentration of AgNPs present can be made.

$$A = \epsilon b C = \log \frac{I_0}{I} \qquad \text{(Eq. 2.2)}$$

In addition to concentration, the width of the LSPR absorbance peak can give information regarding the dispersity of the sample. Narrower peaks are associated with more uniform product, whereas broad peaks are attributed to a greater degree of variation in the sample.

Some caveats should be considered when using the UV-Vis spectroscopy and the Beer-Lambert law, namely: introduction of false light, false loss of light, and limitations with the spectrometer and software.

False light can be introduced simply from stray light inside the spectrometer or ambient light getting into an insufficiently shielded sample housing.[158] This light will not be monochromatic and may not be constant during experiments resulting in erroneous data. A more complex source of false light is from fluorescence or phosphorescence of molecules in the sample which can alter the amount of light detected at given wavelengths.[158] The detector is not able to distinguish the light from the spectrometer's source or fluorescence emission of the same wavelength. Post-sample monochromators and sample dilution can help to mitigate these effects.

In contrast to the introduction of false light, light can be lost through processes other than absorbance.

Rayleigh scattering occurs in particles much smaller than the wavelength of incident light (d « λ), in the region of 10 nm or smaller for visible light.[158,159] As the detectors in UV-Vis spectrometers are not able to distinguish the light lost through reflection or scattering from absorbed light, the reported value is considered the extinction, rather than true absorption.[12,158]

Engineering limitations in the design and operation of UV-Vis spectrometers can also lead to deviation from the Beer-Lambert law. First, true monochromatic light is not achievable using typical monochromator techniques (as described below) and so a compromise is struck. A combination of nanometre wide slits and diffraction gratings are used to generate the nearest monochromatic light while maintaining a useably high beam intensity.[158]

Absorbance can also be calculated from the intensity of the incident light before (I_0) and after passing through the sample (I), shown in (Equation 2.2). As I decreases, as seen with higher absorbance values, the log of the ratio between the pre and post-sample light tends towards a division by zero; such a computational task introduces considerable signal noise.[158,160] Before this happens though, a flattening of the top of spectral features near the wavelengths of high absorbance will occur.[158] Coupled with the finite resolution of analogue-to-digital converters used to turn the electrical signal from the detector to a numerical value, accuracy is lost at high (or very low) concentrations of an analyte leading to a plateauing of absorbance values.[158] The concentration threshold at which a spectrometer is no longer capable to interpret a linear relationship with absorbance is dependent on the model of spectrometer used and is important to know when performing quantitative analysis.

2.3.2 Visualisation and Size Analysis

Nanoparticles are smaller than the diffraction limit of visible light. Two points closer than this limit are indistinguishable and cannot be resolved, meaning individual nanoparticles are not visible using conventional optical microscopy techniques and so electron microscopy, either transmission electron microscopy (TEM) or scanning electron microscopy (SEM), are employed. TEM is the preferred method for visualising AgNPs and is widely used.[39,43,57,60,116,156,161] The high electron density of Ag means good contrast can be achieved between the AgNPs and the surrounding material. Consequently, no substantial sample preparation, such as staining, is required. With the high resolution achievable with TEM, size and morphology measurements can be taken of individual particles.

As well as information on particle geometries, TEM can also show where particles are localised in cells.[39,43] Advances in TEM techniques have led to the development of "wet" TEM where samples in a liquid form can be analysed allowing for a more representative investigation of the material in its native state.[162]

The localisation of particles in a cell gives insight into the biological mechanisms of AgNP bioproduction.

Dynamic light scattering (DLS) analysis can be used to size particles. While it does not image individual particles, the distribution of particle sizes in a sample can be easily determined. DLS systems work by detecting the Brownian motion of particles in solution by analysing the scattering of light as it passes through the samples. On key difference between TEM and DLS, however, is the measurements of different diameters. As DLS-derived sizes come from the Brownian-motion, the system measures the hydrodynamic diameter which includes any surface coating on the particle. In contrast, TEM measures the electron-dense core and usually does not include the coating. Moreover, DLS is limited to spherical particles and can struggle to distinguish the presence of aggregate from single particles; these distinctions are more easily made using TEM.[162]

2.3.3 Composition Analysis

Electron microscopy can give valuable information on the shape of nanoparticles and a rough indication of their density. It cannot, however, distinguish between materials with similar electron densities. For this, elemental composition analysis is required.

X-ray diffraction (XRD) allows for the interrogation of the crystal structure and atomic spacing of materials.[163] The unique diffraction patterns generated when X-rays interact with a crystal yield information about its physiochemical properties and can be used to determine the composition of the material.[20,163] These patterns are dependent on the interplanar spacing (d) of the lattice structure and relate to the wavelength of X-rays (λ) used and the incident angle of irradiation (θ) through Bragg's Law (Equation 2.3):

$$n\lambda = 2dsin\theta \qquad \text{(Eq. 2.3)}$$

Because only a small sample size is required and due to its non-destructive operation, XRD has frequently been used to analyse the composition of biogenic AgNPs.[51,57,60,74,75,99,102,137,156,164] Particles of pure Ag are distinguishable from Ag-compound particles such as AgCl or Ag_2O by XRD. Such differentiation is important when considering applications which are sensitive to the composition of the particles, for example antimicrobial activity.[165] The limitations of XRD include the requirement to have access to a reference material or diffractograms to make accurate identifications, and the technique suffers when analysing complex samples, requiring prior purification of the AgNPs.

Energy dispersive X-ray spectroscopy (EDX) gives elemental information when X-rays are generated by bombarding atoms with electrons, typically while performing electron microscopy.[166] The electrons in

the sample atoms are excited when exposed to the electron beam. These electrons then undergo either elastic or inelastic scattering and return to their ground state. In doing so, they release characteristic X-rays unique to the energy gap between the excited and ground state which is specific for a given element. The detected X-rays are therefore useful in identifying the presence of atoms in the sample.

The high spatial resolution of EDX achievable has enabled atomic resolution composition analysis which can give important information about the distribution of elements in a sample when coupled with SEM.[167] While EDX can give elemental information, it does not give chemical data such as chemical bonds or whether a sample contains ionic or non-ionic species.[166] However, the convenience of being integrated into electron microscopes, already being used to visualise AgNPs, has lead to the widespread use of EDX in biosynthetic AgNP studies.[74,75,102,137,147,156,164]

Similarly to EDS, electron energy loss spectroscopy (EELS) is usually coupled with electron microscopy and measures the change in the kinetic energy of electrons which have passed through a thin sample ($<$50 nm – 100 nm).[168,169] In contrast to EDS however, the energy lost as the electrons interact with the sample is directly related to the ionisation energy of the material. This can be used to gain information not only about elemental composition, but also chemical bonding and electronic structure.[169] Due to the thinness of the samples required though, this technique is not applicable to AgNPs within cells as the electrons are scattered or absorbed, although it has been used to analyse free AgNPs it has not received much attention in the analysis of biogenic AgNPs.[170]

Also by measuring the kinetic energy of electrons, X-ray photoelectron spectroscopy (XPS) utilises the photoelectron effect to measure energy of electrons ejected from a sample. Incident X-rays generate photoelectrons, electrons ejected from their orbitals by incoming X-ray photons, which are detected and have kinetic energies which relate directly to the core-electron binding energies of the atom whence they were emitted.[171] This relationship allows the information to be used to identify the elemental composition and electronic state of the sample. As the emission of photoelectrons can only be detected from the top 10 nm of a material due to internal scattering of the sample, only the surface of a sample can be probed; this applies to nanoparticles with diameters greater than 10 nm.[171]

XPS has not received the same attention as XRD or EDS in the analysis of bacterially sourced AgNPs. In part, this may be because while XPS can, theoretically, be used to distinguish pure Ag from Ag-oxides, this can be challenging due to the similarities in the core-electron binding energies of the different materials.[172] Moreover, the limited working depth limits the use of XPS in intracellular AgNPs. XPS has, however, been used to analyse chemogenic AgNPs on the surface of materials, especially glass.[173,174]

As XPS does not rely on electorally conductive samples, biological systems can be interrogated using

the approach.[171] Functional groups on the surface of samples, such as bacterial cells, have been identified. This approach may therefore be useful in analysing the surface coronae of biogenic AgNPs, though evidence of its use in the literature could not be found.

Confirming the elemental composition of AgNPs is critical for certain applications, especially therapeutics, and as the optical properties of AgNPs are influenced by their composition, it is also important when considering optical applications.

2.3.4 Surface Analysis

The superior resistance to aggregation shown by biogenic AgNPs has been attributed to a surface coating of amino acids. The ability to remain in solution and not to form aggregates is vital in some proposed applications such as therapeutics. The importance in characterising the surface of AgNPs is, therefore, of great importance. One method commonly employed for this is Fourier transform infrared (FTIR) spectroscopy. FTIR yields information on the presence of functional groups which in turn can be used to predict which biomolecules are present. This has previously been used to demonstrate that there is a protein coat surrounding biologically produced AgNPs.[75,156,175]

The electrostatic properties of the AgNPs also play important roles in stability. Measured as the zeta potential (ζ), nanoparticles with surface charges of either +30 mV or -30 mV are considered stable, whereas particles with ζ values closer to 0 mV (the isoelectric point) are typically less stable as colloids. AgNPs produced by bacteria have been analysed in this way, but it is not a widely used technique.[176]

2.4 Production Considerations

2.4.1 Flow Production

To fully realise the potential use of AgNPs in a range of commercial and industrial applications, one of the biggest challenges to overcome is production scale. Published reports of biogenic AgNP production typically do not exceed 100 mL batches and will require considerable scale-up before being viable on as an industrial method. Two main production philosophies exist for large scale production of materials: batch and continuous flow. Batch productions have discrete steps of a process where reagents undergo each reaction step before being moved on to the next step. These processes are typically less complex to setup compared to a continuous process and do not need to be directly compatible. This makes them useful in friendly to rapid and small-scale reactions for initial research. In contrast, a continuous production method, as the name suggests, utilises a continuous stream of reagents. Reagents are typically in

liquid or gas phases, though solid phase materials can be used.[177,178] Flow synthesis offers several advantages to batch, namely greater control over reaction conditions, such as heating and cooling, and superior mixing control[177–179] This can greatly reduce time, costs, and energy demands (particularly in heating processes).[180] Additionally, continuous flow systems allow for real time monitoring and response in a way batch method cannot allowing for greater control over the final product.

Nanoparticles have successfully been produced in flow reactors with highly uniform products due to the superior control compared to batch.[35,181–185] However, only a small number of reports have utilised biosynthetic routes for AgNP production in a flow system.[157,186,187] This is possibly due to the slow reaction rates of bioproduction methods which are not easily compatible with flow synthesis. However, the superior control over the product and scalability of continuous flow synthesis of AgNPs is an attractive and ongoing area of research.

2.4.2 Harvesting and Isolating

Isolating AgNP produced using bacterial cultures in batch or bioreactors has received little attention in the literature. Kalimuthu et al. briefly describe using sonication to isolate AgNP from cells; however, little detail was given, nor was any comparison with other methods.[102] A way of bypassing this step is to use cell-free extracts as the bioreducing component as this removes the need to lyse cells in order to extract any particles trapped within. In this situation, the AgNPs are likely the most massive material in the sample, meaning centrifugation could be used to separate them. However, this is a time-consuming process which often required speeds only achievable with ultracentrifuges.

When comparing differential centrifugation, density gradient centrifugation, tangential flow filtration, and gel permeation chromatography for preparing monodispersed fractions of polymersomes, Robertson et al. showed that all of these methods proved successful, but each had advantages and disadvantages.[188] For example, tangential flow filtrate allows the filtrate to be concentrated during purification, whereas centrifuging based methods resulted in a more dilute product. However, the specificity of centrifuged approaches was higher allowing populations with 10 nm differences in size to be separated. Shape-specific separation was only observed using density gradient centrifugation, though how this can be generalised to other nanomaterials remains a topic of research.

Filtration also has potential in separating AgNP because of the notable size difference between biological macromolecules and large AgNP or Ag nanoprisms. Ultrafiltration systems exist with pore diameters below 100 nm and nanofiltration membranes extend down to 1 nm, however, large volume filtration can present challenges with membrane clogging. Previously, chemogenic AgNP have been filtered using ul-

trafiltration technique with a pore diameter of 50 nm and compared with ultracentrifugation.[189] Filtering gave greater control over particle size, concentration, and aggregation state. Additionally, Anders and colleagues showed that filtration can be used to separate AgNP aggregates and large particles yielding a highly concentrated, but aggregate-free solution.[190] Despite the higher costs of tangential flow filtration compared to traditional filtration techniques, the benefits of reduced membrane clogging and in-flow operation make it an appealing technology. Using sequentially smaller pore diameters in a tangential flow system, Au nanoparticles were isolated from mixtures of organic impurities and salts using membranes down to 10 kDa in size. The method was also capable of separating a mixture of 1.5 nm and 3.1 nm Au particles.[191]

2.4.3 Immobilising and Functionalisation

Nanoparticles can be used in a native form or can undergo post-synthesis modifications to improve their properties for an intended function. Coatings of individual particles, such as silica and polyethylene, have previously been applied for optical and drug delivery applications to protect against oxidisation of the Ag and the release of Ag^{+}.[192–194] Silica is often used in these coating due to its versatility as surface on to which molecules can be attached. This has proved effective with the adhesion of organic insecticides, dyes, antibiotics.[195–197]

Many applications for AgNPs will require them to be fixed onto a surface as a coating. Finding the best matrix in which to embed AgNPs requires the consideration of a number of factors such as the optical properties of the matrix, liability of Ag^{+} to leach, and production conditions. Indeed, Ag nanoprisms have been coated in 3-mercaptopropinic acid and then embedded in a chitosan matrix with only a very small change in the λ_{max}.[198] Furthermore, by embedding Ag nanoprisms in silicon oxide and poly(methyl methacrylate) (PMMA), Carboni et al. demonstrated a thin film (0.1 mm thick) could be created.[192] AgNPs have also been produced inside PMMA nanofibres protecting the particles from aggregation.[199]

2.5 Potential Applications of Nanoparticles

AgNPs have a range of potential applications including uses as catalysts, anti-cancer therapeutics, antimicrobials, and water treatment, among others.[200–202] Of these, applications exploiting the antimicrobial and unique optoelectrical properties are discussed below.

2.5.1 Antimicrobials

The antimicrobial properties of Ag (discussed in Section 2.2.1) have long been known and are well documented.[203,204] This attractive property has driven the rapid growth in the number of medical, consumer, and agricultural products using Ag over the past decade.[205] This includes the use of AgNPs in products such as antimicrobial gels, dental materials, socks, water purification systems, and a laundry washing machine.[206–210]. However, debate remains over the mechanism by which AgNPs are toxic, though a growing consensus is that it is the release of Ag^+ from the particles which are toxic, rather than the metallic form of the metal.[211]

The use of AgNPs in antimicrobials has received much attention in fabrics as potential wound dressings where AgNPs are often immobilized on to fibres.[212] A myriad of fibres have been investigated, including polyester, acrylic, bacterial cellulose, and plant cellulose, all of which have been shown to have antimicrobial effects.[212–216] Moreover, cotton and silk impregnated with AgNPs were shown to be effective against *S. aureus* and *E. coli* even after up to 50 laundry wash cycles.[217,218]

In addition to the direct antimicrobial effects of Ag, reports have shown synergistic effects of Ag with conventional antibacterial and antifungal agents.[219–221] This effect has been proposed as a method to target drug resistant strains and reduce the impact of the increasing number of antibiotic pathogens. However, concerns have arisen regarding the development of resistance to AgNPs. The rapid development of AgNP resistance has been shown in *E. coli* through repeated exposure to low concentrations of AgNPs.[222,223] Consequently, consideration should be taken when using AgNPs, especially in a clinical setting.

Interestingly, the shape of AgNPs affects their bactericidal activity against *S. aureus* with platelets being more toxic than spheres and cubes.[224] The effect was attributed to different dissolution rates and Ag^+ release that resulted from the different geometries of the particles. A similar observation was made when the green alga *Chlorococcum infusionum* was challenged with Ag nanospheres, nanoplates, and nanowires, and human mesenchymal stem cells were exposed to Ag nanospheres and nanoprisms.[225,226] Therefore, the ability to synthesise triangular Ag nanoprisms on a commercial scale to allow for their use in antimicrobial materials is of great interest. Current production routes are limited in their output scale and so require further development and improvement to reach a viable magnitude.

2.5.2 Energy Saving Glazing

Heat loss through windows is a major source of thermal inefficiencies in buildings with an estimated 20% - 60% of a buildings heat lost through the windows, depending on the design of the windows and architecture of the building.[227] As such, poorly insulated windows contribute considerably to energy consumption and

greenhouse gas emissions.[228,229]

Technologies have been developed to improve the insulating properties of glazing, such as multi-pane glazing and gas or vacuum gap glazing.[230] Low emissivity, or Low-E, glazing has received attention for an additional means by which heat loss can be reduced. Low-E glazing typically use thin films or coating on the surface of the glass and aims to prevent infrared radiation from passing through a window while allowing visible light to be transmitted. Ag-containing layers have been shown to be effective Low-E coatings, though they often suffer from poor transmission of visible light.[230–233]

Nanoparticles have been tested in Low-E glazing with some success as described by Goa et al; monodispersed hollow silica nanospheres have been shown to reduce the reflection of ultraviolet and NIR light when coated onto glass.[234] Moreover, triangular Ag nanoprisms may be a viable option for improving the efficiency of windows. A proof-of-concept study has demonstrated that Ag nanoprisms in a PMMA matrix could greatly reduce the transmission of NIR radiation.[192] Though efforts have been made to increase the scale of production of Ag nanoprisms, challenges remain before an industrial scale process can be achieved.[181] Moreover, the poor photostability of chemogenic AgNPs limits their use in such applications.

2.5.3 Signature Management and Low Observable Materials

The ability to reduce the visibility of a vehicle or personnel gives a strategic advantage in a military environment. Traditionally, this has been achieved through the use of camouflage which employs colours and textures to mimic the surrounding environment. However, many technologies now exist for imaging and detection outside of the visible region of the electromagnetic spectrum, for instance night-vision imaging, thermal infrared imaging, and radar systems. The principles of camouflage can also be applied to these electromagnetic domains to reduce the visibility to their respective detection systems. Night-vision imaging, or NIR image intensifiers, utilise wavelengths from 700 nm to 1000 nm and examples of images taken using night vision imaging systems are shown in Figure 2.9. Surfaces which reflect or emit NIR appear brighter in the night vision images making these surfaces more visible (Figure 2.9 B & D).

Materials which can reduce the reflection of NIR light through absorption may be useful in reducing the visibility of an object when viewed using night vision. However, it is important to not interfere with existing camouflage systems, such as by absorbing visible light. The strong absorption of Ag triangular nanoprisms in the NIR region with relatively low absorption in the visible region makes them a potential candidate for use in novel NIR absorbing materials. However, little published literature is available on this application.

Beyond NIR, the electrical properties of AgNPs have been investigated with regards to their use in radar absorbing materials (RAMs). Many conventional radar systems, for instance those used in air traffic control,

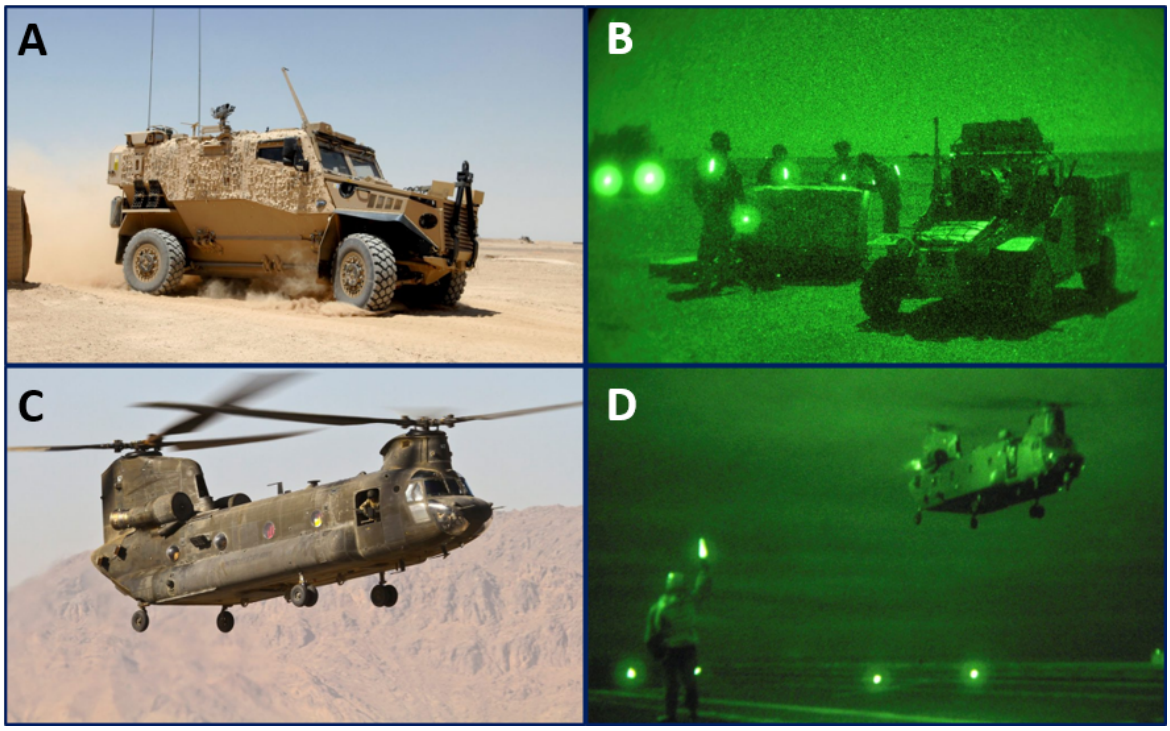

Figure 2.9: Photographs taken of military vehicles using (A & C) visible and (B & D) NIR light (night vision). All images are reproduced from the Ministry of Defence (UK) under the Open Government License.[235]

work by broadcasting microwaves (2 GHz to 12 GHz) and detecting the echoes reflected of objects. In a similar fashion to NIR absorbing materials, a coating which can absorb the microwaves may help to reduce the visibility of an object. For instance, films between 160 nm and 170 nm thick of PVA have been found to absorb microwaves between 8 GHz and 12 GHz when impregnated with $<$10% AgNPs (w/w).[236] Additionally, a AgNPs-carbon nanotubes hybrid nanocomposite embedded in wax was also demonstrated to absorb GHz-range microwaves and could be tuned by changing the thickness of the material.[237] However, the effectiveness of using AgNPs in RAMs beyond the laboratory does not appear to have been reported in the literature.

For use in military applications such as these, the scale of AgNP production must be increased to meet the demands required to cover the large surface areas of vehicles. Moreover, the particles must be durable enough to withstand the harsh conditions in which military vehicles are used, such as salt-water corrosion and sand abrasion. Overcoming these challenges is a crucial step in reaching the full potential of AgNPs.

2.6 Conclusions of Literature Review

From the literature discussed, the following key points can be concluded. First, AgNPs have unique optical properties which make them attractive in a number of applications. The localised surface plasmon resonance which is responsible for these properties can be altered by changing the physical properties of the nanoparticle. Typically, larger and more morphologically anisotropic particles exhibit a red-shifted LSRP absorption peaks relative to smaller more spherical particles. Therefore, the absorption of certain wavelengths of light can theoretically be selected for by producing nanoparticles with the corresponding geometry. This allows AgNPs to be customised for their intended application.

Second, current production methods are constrained by a number of limiting factors. Notably these include the use of hazardous chemicals and limited particle stability. The biosynthesis of metallic nanoparticles exhibited by bacteria may prove to be a solution to these challenges. Bacteria employ mechanisms which sequester and accumulate metals, including Ag. As Ag^{+} is toxic to bacterial cells, resistance mechanisms reduce the ions to an insoluble metallic form, which ultimately leads to nanoparticle formation. The understanding of these mechanisms remains poor, although leading theories suggest a nitrate reductase may be involved. Such an enzyme may work in conjunction with the sil genes which have been shown to enable Ag resistance in a range of bacterial species. By better understanding the biological mechanisms involved in AgNP formation, it may be possible to optimise an organism to selectively produce nanoparticles with desired morphologies and, therefore, desired optical properties. To achieve this, comprehensive investigations into the molecular biology is required. Identifying the key proteins involved will likely prove crucial to being able to control and optimise the process. Additionally, determining the factors which control the shape and size of AgNPs in biological systems will be critical.

Third, a key factor limiting the use of AgNPs in commercial products is production scale. Challenges remain in reliably producing high quality AgNPs with a specific morphology at a scale which is commercially viable. By up-scaling the process though the use of biological systems, it may be possible to overcome this hurdle. Further work is required to reach large scale production when considerations of shape control and appropriate monitoring are necessary.

Chapter 3

The Effects of Reaction Conditions on the Bioproduction of AgNPs by *M. psychrotolerans*

3.1 Introduction

Since the discovery by Klaus et al. that the bacterium *P. stuzeri* AG259 could produce AgNPs in 1999,[43] numerous bacteria have been reported to exhibit similar behaviour when challenged with Ag^+. However, biogenic nanoparticle production is likely dependent on both biological and physiochemical factors and is therefore species specific. This is evident from a number of previous reports which have examined how the growth conditions under which bacteria are cultured affect AgNP production (See Section 2.2.2).

Conditions investigated in previous studies include the concentration of Ag^+, temperature and duration of the reactions, and pH.[57,69,76,104,123] While some trends have appeared, there is no consensus on the optimal conditions for production.[6] This warrants further study to better understand the processes involved as the optimal production conditions can also give information about the mechanisms behind bacterial AgNP production. For example, the observation that AgNP production favoured anaerobic conditions in *E. coli* suggested the involvement of enzymes expressed under such conditions.[147]

More than 120 strains of over 100 species of bacteria have been reported to produce AgNPs when challenged with Ag^+ (Figure 2.8);[6] however, only 6 of these have been shown to produce triangular nanoprisms.[43,57,65,75,108,120] Therefore, the influence of a range of reaction conditions were evaluated for their effects on biogenic AgNP production. Ultimately, it is hoped that the optimal conditions can be de-

termined to selectively produce non-spherical and ideally triangular Ag nanoprisms with a high degree of monodispersity.

3.2 Methods

3.2.1 Organism and Reagents

Morganella psychrotolerans U2/3 (DSM: 17886) was obtained from the Deutsche Sammlung von Mikroorganismen und Zellkulturen (DSMZ; Germany) repository and maintained on lysogeny broth (LB) agar (10% tryptone, 5% yeast extract, 10% NaCl); freezer stocks (13% v/v glycerol) were prepared and stored at -80°C. *E. coli* DH-5α and *Pseudomonas fluorescens* ATCC 13525 were sourced from the culture collection at the University of Southampton and grown in LB with no added NaCl at 37°C overnight with orbital shaking at 150 RPM. Tryptone and yeast extract were purchased from Oxoid, ThermoScientific (USA), glycerol was purchased from Fisher Scientific (USA), and NaCl was purchased from Sigma Aldrich (UK).

Silver nitrate and silver lactate were sourced from Sigma Aldrich (UK). Stock solutions (50 mM) were prepared using deionised water (diH_2O) and filter-sterilised. Stock solutions were protected from light and stored at 4°C until use. Ag-containing solutions were filter-sterilised using syringe filters (pore diameter: 0.22 μm). All other solutions were sterilised by autoclaving at 121°C for 15 min.

All other reagents were purchased from Fisher Scientific (USA) unless stated.

3.2.2 Biosynthesis of AgNPs

M. psychrotolerans was grown aerobically in LB with no NaCl added for 4 days at 22°C with orbital shaking at 180 RPM in 100 mL volumes of LB with no added NaCl in 300 mL Erlenmeyer flasks to stationary phase ($OD_{600} \approx$ 2.2 - 2.4); further details are given in Appendix A.1. NaCl was not added to the growth medium to avoid the formation of poorly soluble AgCl during AgNP synthesis. The general procedure for producing AgNPs was to add 4 mL of stationary phase culture to 15 mL Falcon tubes. To this, sterile $AgNO_3$ was added to a final concentration of 9 mM and made up to a total volume of 5 mL with diH_2O. Samples were then incubated for 24 h at 22°C and 180 RPM on an orbital shaker in the dark. Samples were then centrifuged at 10,000 x *g* for 10 min. The supernatant was collected and used for characterisation. Triplicates of each sample were used throughout. Negative controls were prepared by the omission of *M. psychrotolerans* and use of sterile growth media instead. Care was taken throughout to protect samples from light.

To prepare cell-free extract, stationary phase *M. psychrotolerans* cultures were centrifuged at 10,000 x

g for 5 min. The supernatant was collected and used in experiments. Cell density dilutions were prepared by diluting saturated cultures with LB (with no added NaCl). When investigating the effects of pH on AgNP production, sodium hydroxide (0.1 M) and nitric acid (0.1 M) solutions were used to adjust the pH. NaOH was purchased from Sigma Aldrich (UK) and HNO_3 was purchased from Fischer Scientific (USA).

3.2.3 Characterisation of AgNPs

UV-Vis Spectroscopy

Samples were centrifuged (5,000 x *g* for 10 min) to remove cells and debris and the supernatant diluted with diH_2O where necessary. UV-Vis spectroscopy was performed using a PerkinElmer Lambda 35 spectrometer. Scans were performed between 350 nm and 850 nm at 480 nm min^{-1} and a slit width of 1 nm. Samples were analysed in polystyrene semi-micro cuvettes with a path length of 10 mm.

In high-throughput experiments, non-coated polystyrene 96-well plates were used. To analysed samples on these plates, an Omega FLUOStar UV-Vis plate reader at wavelengths from 350 nm to 850 nm with 1 nm steps was used to collect spectroscopic data. Sample sizes of 200 µL were used.

Samples were zeroed against their corresponding negative control to remove the absorbance from the growth medium, $AgNO_3$, and the plate.

Transmission Electron Microscopy

To confirm nanoparticles had been produced, transmission electron microscopy (TEM) was used by drop casting 5 µL of sample onto a formvar-coated copper grids and incubated at room temperature for 30 s. The excess liquid was then wicked off using filter paper and the grids were air dried. Imaging was performed using an FEI Tecnai T12 transmission electron microscope with an accelerating voltage of 80 kV. No fixing, embedding, or staining was performed.

To image extracellular AgNPs, cells and debris were removed from samples by centrifugation at 10,000 x *g* for 5 min. The supernatant containing the AgNPs was collected and centrifuged at 17,000 x *g* for 30 min. The pellet was resuspended in diH_2O to wash the AgNPs; this was repeated for a total of 3 washes. The AgNPs were then imaged using the same procedure as samples containing cells.

3.2.4 Data Analysis

The UV-Vis spectra for triplicates were averaged and the mean spectra used for analysis. Spectra of sterile negative controls for each condition were used as baselines. Data are presented as mean $\pm$ standard deviation of the mean throughout.

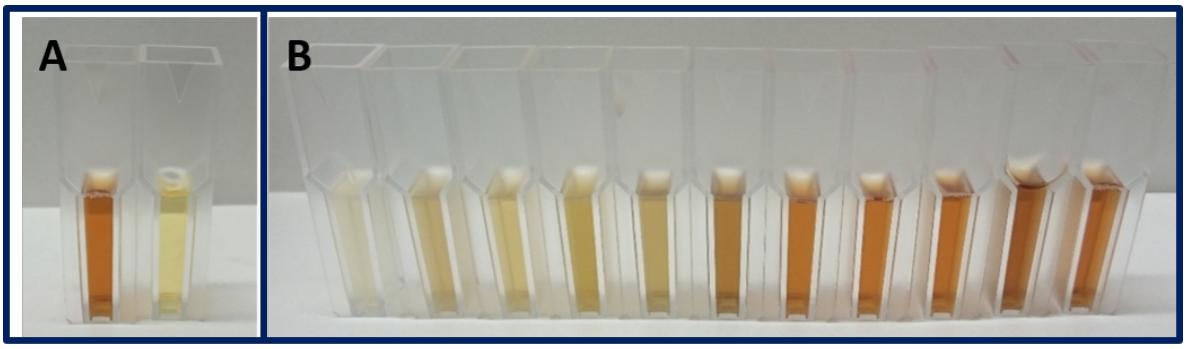

Figure 3.1: A) 9 mM $AgNO_3$ incubated for 24 h in the presence of cells (left) and in the absence of cells (right) B) Samples of supernatant collected from *M. psychrotolerans* cultures exposed to different concentrations of $AgNO_3$. Left to right: 0, 1, 2, 3, 4, 5, 6, 7, 8, 9, and 10 mM. The red/brown colour is a strong indicator of the presence of AgNP.

3.3 Results and Discussion

3.3.1 Biogenic Production of AgNPs by *M. psychrotolerans*

Three species of bacteria were initially evaluated for AgNP production: *M. psychrotolerans*, *E. coli* and *P. fluorescens*. *M. psychrotolerans* was chosen due to the previous reports indicating its ability to produce prismatic and plate-like AgNPs.[52,57] Non-pathogenic strains of *E. coli* and *P. fluorescens* both have higher growth rates than *M. psychrotolerans* which is an attractive characteristic when considering future bioproduction operations and so were screened for AgNP production.

No colour change in the culture of *P. fluorescens*, and combined with a lack of spectroscopic evidence, suggested no AgNP production by was observed using this strain. Conversely, both *M. psychrotolerans* and *E. coli* demonstrated the ability to reduce Ag^+ to Ag^0 (see Appendix A.2 for the UV-Vis spectrum of AgNPs produced by *E. coli*). However, because *M. psychrotolerans* had previously been shown to produce non-spherical particles, it was chosen for further investigation.

M. psychrotolerans cultures are pale yellow and slightly orange in colour. However, following the addition of $AgNO_3$ (as colourless solution) to the culture, the colour changed to dark red/brown after 24 h (Figure 3.1 A). This colour change is widely documented in previous reports of bacterial AgNPs production and was the result of the formation of plasmonically active Ag nanoparticles.[72,74,75,137,147] This was supported by UV-Vis spectroscopy which revealed a strong broad absorbance peak between 400 nm and 450 nm with no other spectra features (Figure 3.6) which is characteristic of spherical AgNPs.[12] There was no evidence of AgNP production in the sterile growth medium incubated with $AgNO_3$ for 24 h.

M. psychrotolerans had a rod-shaped morphology when examined by TEM (Figure 3.2). The cells were 2 – 3 µm in length with rounded end and flagella visible extending from many of the cells. However, when

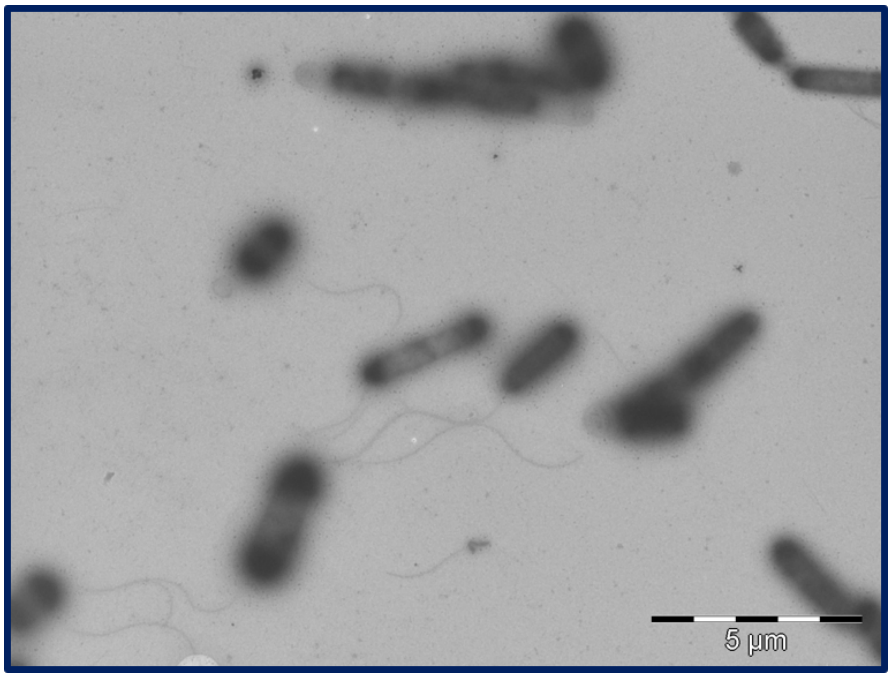

Figure 3.2: Example TEM image of a control sample of *M. psychrotolerans* not exposed to Ag. Scale bar: 5 µm

challenged with $AgNO_3$, dark electron dense material was observed throughout the samples of unwashed cells (Figure 3.3). The density of the particles indicated they were metallic in composition and were concluded to be Ag deposits in the form of AgNPs. The particles were spherical and quasi-spherical in shape and distributed evenly across the samples both in the intra- and extra-cellular environment. Additionally, a small number of larger non-spherical particles were observed and tended to be in closer proximity to the cells. A triangular prism and larger hexagon-like particle can be seen in Figure 3.3 B and D, respectively. Previously, *M. psychrotolerans* has been reported to produce hexagonal and triangular plate AgNPs in the extracellular environment.[57] It is unclear from these images whether the particles are on the surfaces of the cells or inside the cells. While the ability to produce non-spherical particles supports the previous finding, the frequency with which these particles were produced in this study appears to be lower as numerous (+20) prismatic plates were observed in the TEM images presented by Ramanathan et al.[57] However, the concentration of $AgNO_3$ used in this work was higher than the previous finding (9 mM vs 5 mM), which may explain the discrepancy.

Due to the sample preparation method used for TEM, the membranes of the cells were not visible making it challenging to interpret the cellular location of AgNPs. This is highlighted in Figure 3.4. Two cells were aligned end-to-end with a collection of large particles closely associated to the cells. However, at a higher magnification (Figure 3.4 B), the dark region of the cell has no clearly defined border. To visualise

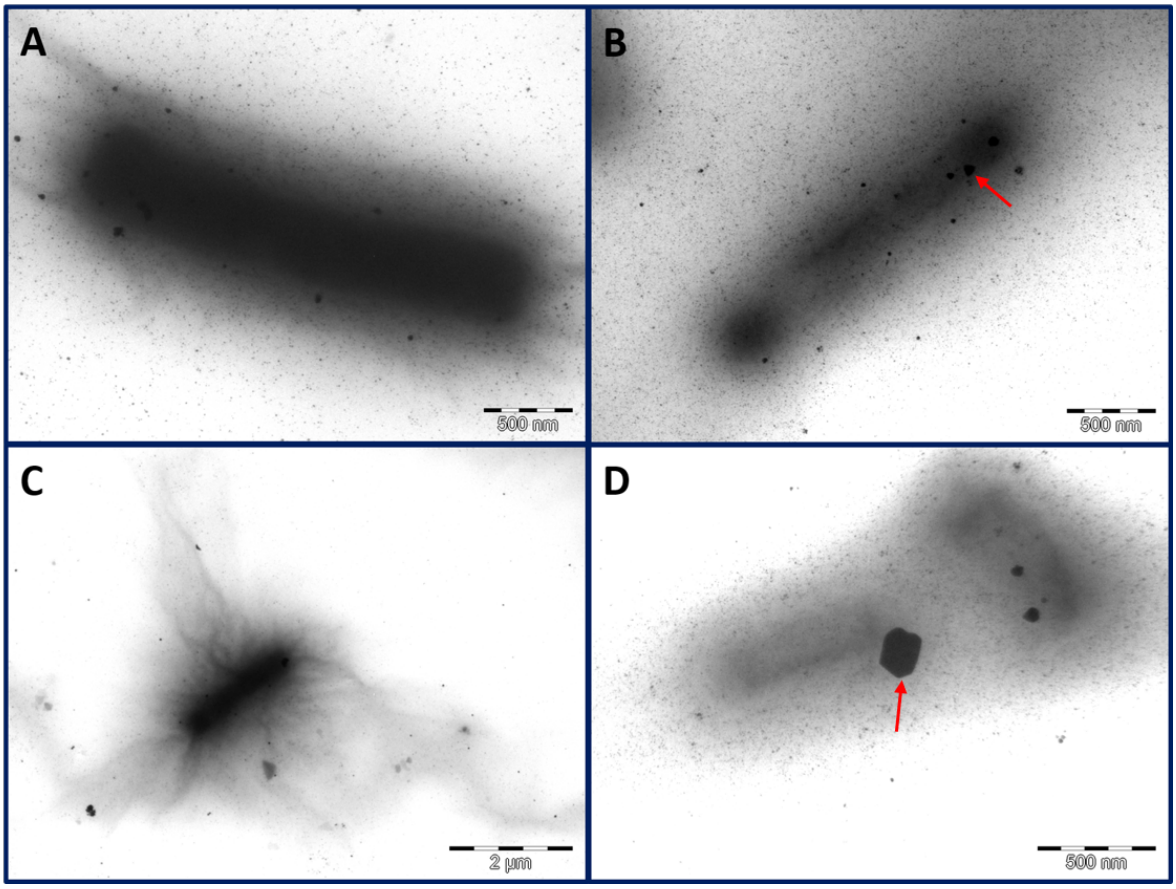

Figure 3.3: Example TEM images of *M. psychrotolerans* incubated with $AgNO_3$ for 24 h. Spherical particles are seen distributed through all images. Non-spherical particles can be seen in image B and D (red arrows). Scale bars: 500 nm (A, B, D) and 2 µm (C)

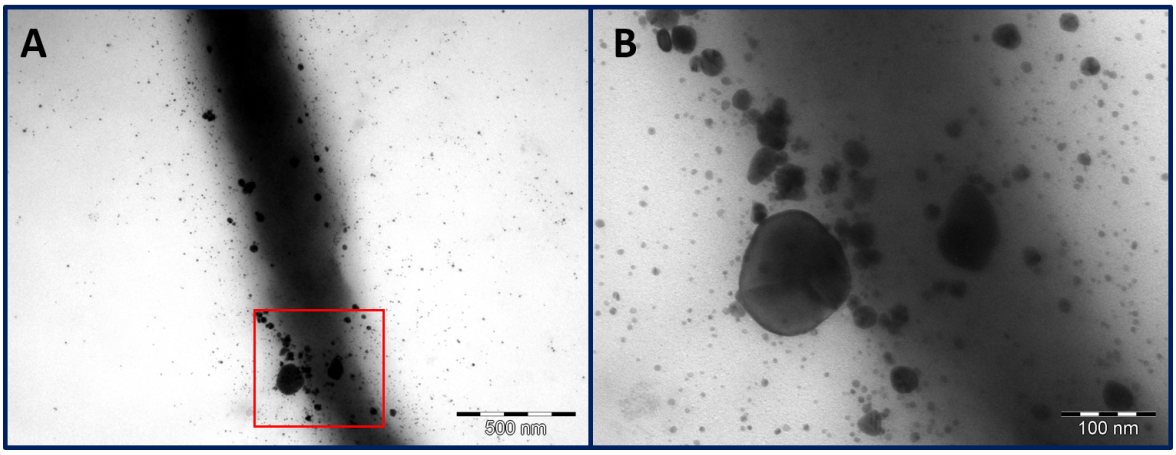

Figure 3.4: AgNPs produced by *M. psychrotolerans* after 24 h incubation with $AgNO_3$. (B) shows the red box of (A) at a higher magnification. Scale bars: 500 nm (A) and 100 nm (B)

membranes, heavy metal stains such as uranyl acetate, lead citrate, and osmium tetroxide are used. However, these stains can leave residue which is indistinguishable from Ag when imaged. This method was used for initial imaging (Appendix A.3), but the technique of not staining was opted for as it was the simpler and could identify AgNPs with less ambiguity. Furthermore, the process of fixing, embedding, and sectioning samples, while useful for obtaining a clearer representation of the localisation of particles in 3D space, raised concerns regarding possible distortion of the samples during preparation and may dislodge or relocate particles during sectioning.

When the extracellular AgNPs were isolated by removing the cells through centrifugation and filtration, all particles observed were spherical or quasi-spherical in morphology. The particles were evenly dispersed throughout the sample with no signs of considerable aggregation (Figure 3.5 A). Higher magnification imaging revealed the particles to be between approximately 4 and 15 nm (Figure 3.5 B); this is smaller than the 46 nm reported by Parikh et al. when *M. psychrotolerans* was challenged with 5 mM. The differences in the product formed in this study and the previous findings was likely due to the differences in the reaction conditions used. To investigate this further, a series of conditions were varied, and the effects measured.

3.3.2 Effects of Growth Conditions on AgNP production

Silver Nitrate

M. psychrotolerans was challenged with varied concentrations of $AgNO_3$. As shown in Figure 3.1 B, the reaction solution change from pale yellow to red/brown. The intensity of this colour change increased with $AgNO_3$ concentration indicating more AgNPs had been produced at higher Ag^+ concentrations. This was

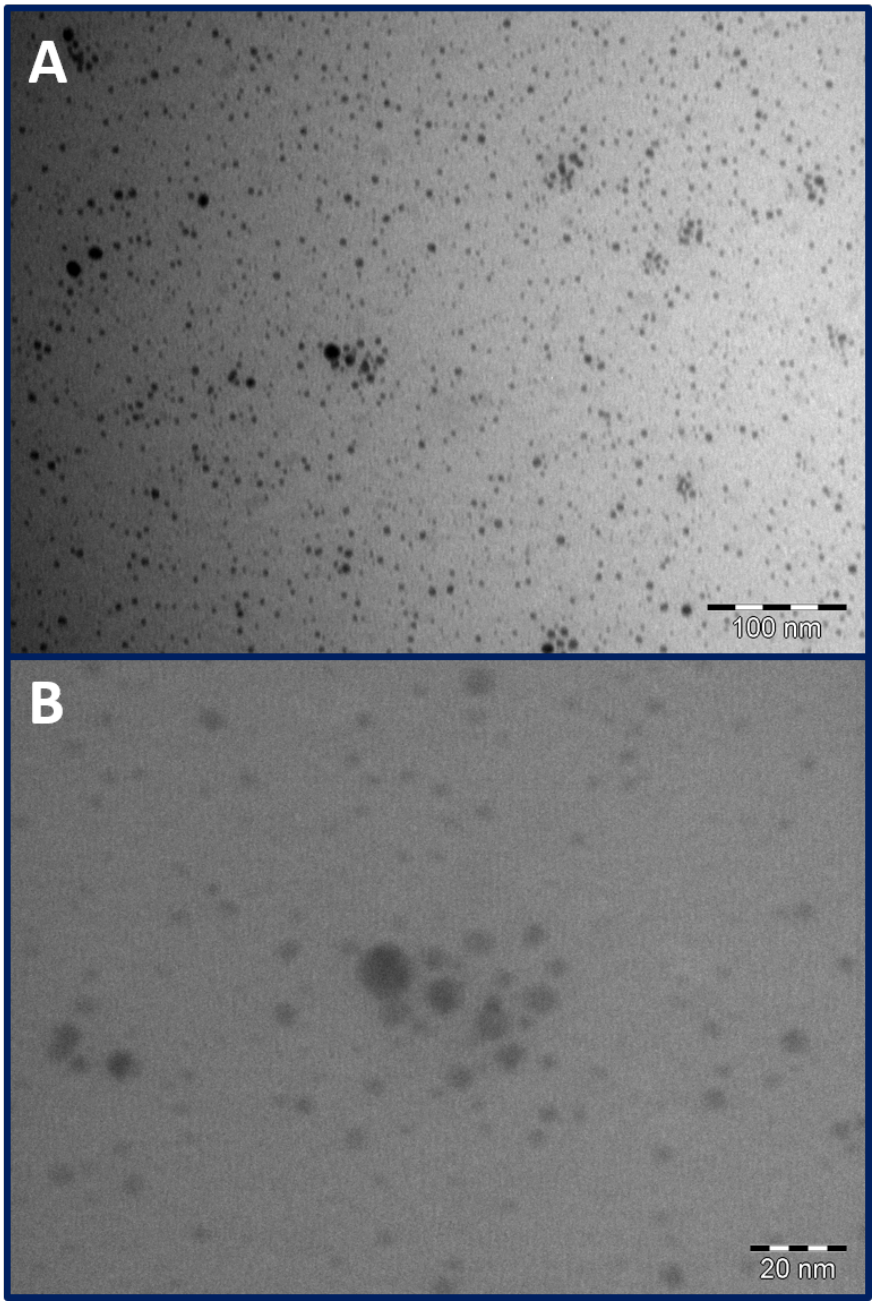

Figure 3.5: AgNPs collected from the supernatant of *M. psychrotolerans* after 24 h incubation with $AgNO_3$. Scale bars: 100 nm (A) and 20 nm (B)

supported in the UV-Vis spectra in Figure 3.6 where the formation of strong absorbance peaks between 400 nm and 450 nm, characteristic of the LSPR of Ag nanospheres,[12] indicated the production of AgNPs. The peak shapes and locations were similar regardless of concentration, though widening of peaks was observed, visible in the spectra of 10 mM and 15 mM shown in Figure 3.6. This suggests the particles being produced did not differ considerably in shape, but aggregation or an increase in particle sizes may have resulted in the high absorbance at longer wavelengths. In general, the intensities of the LSPR peaks, and thus the concentration of AgNPs, increased with increasing $AgNO_3$ concentrations to 6 mM before decreasing with higher concentrations in a near-linear fashion.

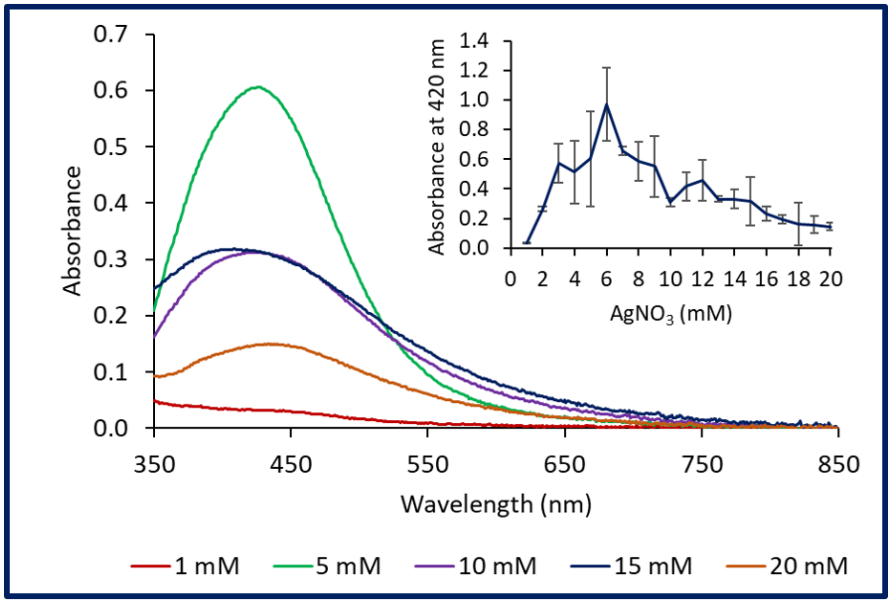

Figure 3.6: UV-Vis spectra of Ag nanoparticles produced by *M. psychrotolerans* when exposed to varying concentrations of $AgNO_3$. Insert: Mean absorbance at 420 nm. Error bars represent SD.

Previously, Parikh et al. have reported the optimal concentration of $AgNO_3$ for AgNP production in a silver resistant *Morganella* sp. to be 5 mM which is comparable with observations made here.[52] When *M. psychrotolerans* has been investigated previously, 5 mM $AgNO_3$ was used without further investigation of other concentrations.[51,57] However, there appears to be considerable differences in AgNP production even between strains of the same *Morganella* species.[51] This emphasizes the organism specificity of reaction conditions and the importance of optimising for each bacterium used.

A similar trend has occurred in most investigations when $AgNO_3$ concentrations have been examined. The concentrations of AgNPs produced increase with Ag^+ concentration to the optima before decreasing in *M. psychrotolerans*, *E. coli*, and *A. calcoaceticus*.[52,99,137] The increase in production is explained by increased substrate availability to the reducing enzymes but once these systems become saturated and the

concentration is beyond that of which the cell can manage, the toxic effects of Ag^+ will become detrimental to the cells. Therefore, it is important to find the balance between maximising AgNP production while minimising the damaging effects.

Silver Lactate

As an alternative Ag^+ source to $AgNO_3$, AgNP production with Ag lactate ($AgCH_3CH(OH)CO_2$) was tested at varying concentration. As shown in Figure 3.7, the UV-Vis spectra are similar to those produced when $AgNO_3$ was used with characteristic strong absorbance peak between 400 nm – 450 nm. The intensities of the peaks also followed a trend that was comparable to $AgNO_3$, increasing rapidly with Ag^+ concentration to 5 mM before decreasing consistently at all concentrations above the apparent optimum.

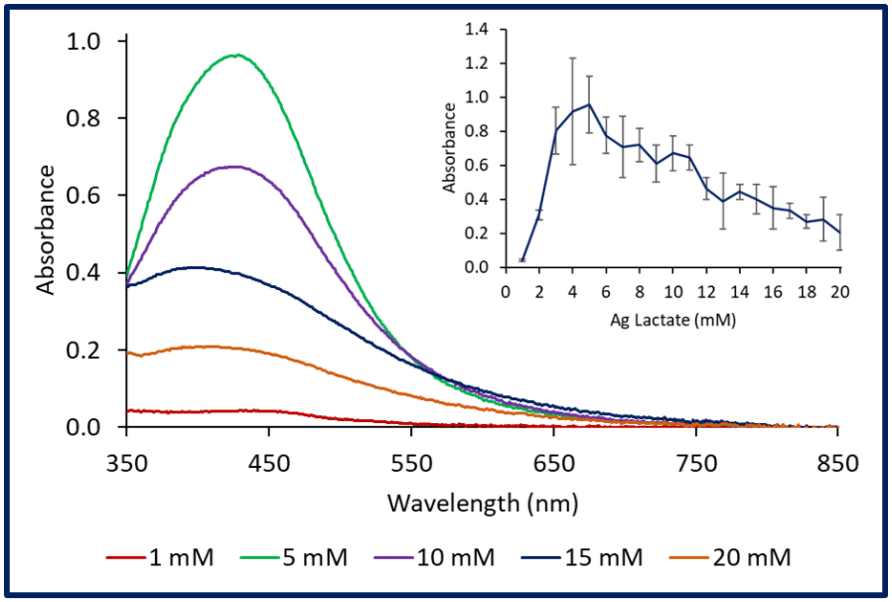

Figure 3.7: UV-Vis spectra of Ag nanoparticles produced by *M. psychrotolerans* when exposed to varying concentrations of Ag lactate. Insert: Mean absorbance at 420 nm. Error bars represent SD.

Very few alternative Ag sources to $AgNO_3$ have been reported in bacterial AgNP production. This is primarily due to the very high solubility of $AgNO_3$, somewhat uncharacteristic of Ag salts. AgCl, Ag_2SO_4, and $Ag(NH_3)_2^+$ have all been investigated, but published findings using Ag lactate have not been found. Moreover, a number of lactic acid bacteria have been shown to produce AgNPs, though the involvement of lactate has been not investigated.[60,69]

Other small carboxyl compounds are known to influence the formation of nanoplates in the presence of H_2O_2 to act as an oxidising agent, though lactate was not investigated.[21] It was shown that molecules containing multiple carboxyl groups with 2 carbon atoms between them were most effective at driving

prismatic growth as they allowed for the selective adhesion of the carboxyl groups on to the (111) facet of the Ag crystal, facilitating asymmetric crystal growth. Lactate contains a single carboxyl group, and without the addition of H_2O_2, was not successful in inducing detectable morphological changes in the particles produced.

Temperature

Production was markedly reduced when the reaction was carried out at 4°C (Figure 3.8 A) compared to 22°C and 37 °C, as indicated by lower intensity LSPR peaks. Ramanathan demonstrated a similar result with low levels of production observed at 4°C, though a considerable number of nanoplates were produced under these conditions.[57] Here, there was no spectroscopic evidence to support the production of hexagonal or triangular prisms, though TEM was not performed to confirm this. When performed at 22°C, analogous to room temperature, production of spherical particles was implied from the shoulder present at 420 nm – 450 nm (Figure 3.8 B). While 22°C is lower than the reported optimal growth temperature for *M. psychrotolerans* of 26°C, Ramanathan et al. showed that *M. psychrotolerans* produced no only spherical but also some prismatic particles at both 20°C and 22°C.[57,238]

At 37°C, production was observed to be the fastest, though with similar spectral results (Figure 3.8 C). Higher temperatures have been associated with the production of smaller spherical AgNPs.[99,116,137] The spectra of particles produced in this study could not add support to this as the peaks were not clearly define in most cases, especially at lower temperatures. Moreover, size analysis of samples by TEM or DLS was not performed.

As production was comparable, albeit slower, at 22°C with 37°C, future experiments were performed at 22°C. The main reason for this decision was the reduction in complexity when considering future production methods. If production can be achieved without additional heating, the need for heat equipment and the energy demands are removed. Producing nanoparticles at room temperature has been reported[239] and offers an environmentally friendly alternative route at the compromise of slower synthesis.

pH

Low pH conditions have been shown to be favourable for AgNP production in *Corynebacterium* sp. and *P. putida*. However, this was not supported in this research where lower pH conditions saw very little AgNP production while neutral and slightly basic conditions appear to be beneficial to production (Figure 3.9).

The pH of *M. psychrotolerans* cultures increased from 6.9 $\pm$ 0.3 of LB to 8.5 $\pm$ 0.1 over normal growth to stationary phase. The generation of an environment with a pH of 8.5 by the bacterium may explain why

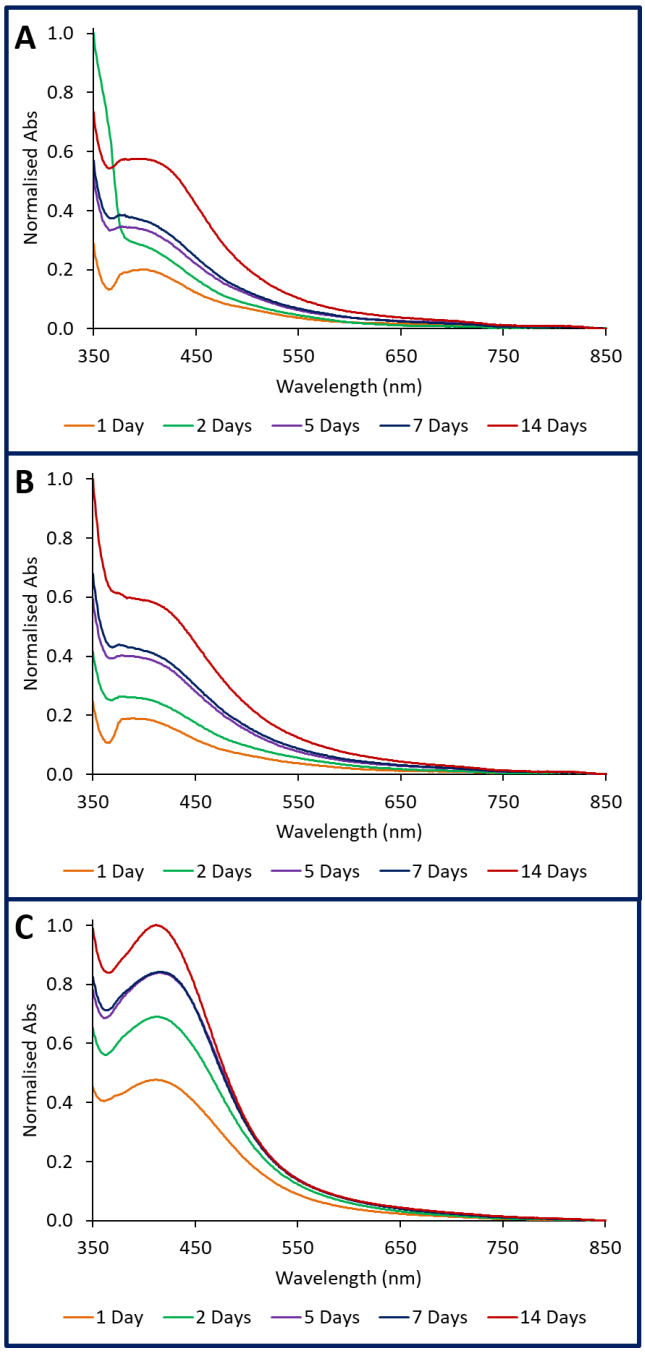

Figure 3.8: UV-Vis spectra of Ag nanoparticles produced by *M. psychrotolerans* at 4°C (A), 22°C (B), and 37°C (C).

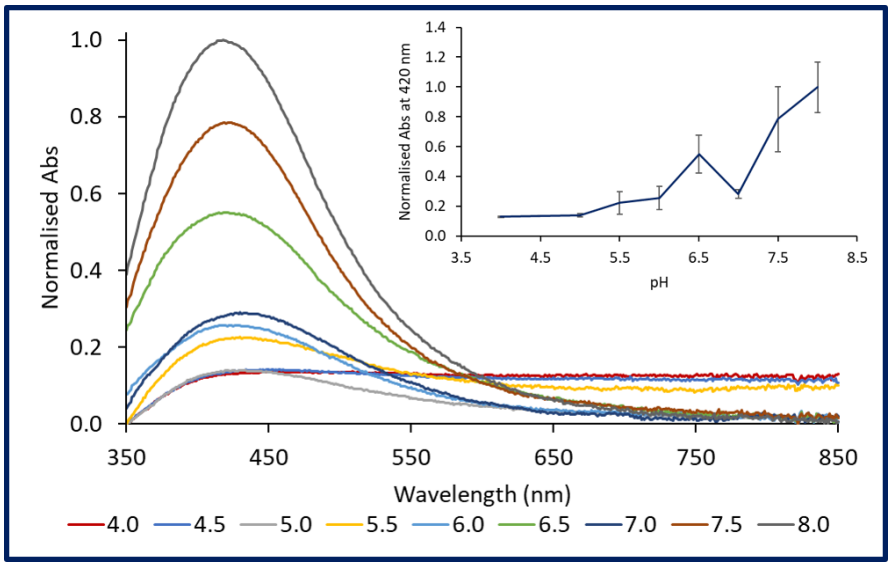

Figure 3.9: UV-Vis spectra of AgNP produced by *M. psychrotolerans* in 9 mM $AgNO_3$ under different pH conditions. Insert: Mean absorbance at 420 nm at varied pH values. Error bars represent SD.

production was highest, under the conditions tested, at pH 8.5. If the cellular machinery is optimised for these conditions, any deviation would likely see reduced activity. Above pH 8.5, the tendency for AgOH to form (as discussed in Section 2.2.2) meant reliable testing could not be performed. AgOH is considerably less soluble in H_2O than $AgNO_3$ and resulted in a reduced bioavailability of Ag^+ for AgNP production.

During the production of AgNPs, when the pH was not initially set, the pH did not change considerably regardless of the temperature at which production occurred (Figure 3.10). This suggests there is no substantial, if any, synthesis of H^+ or basic products during the production process which the system cannot handle. As the mixture of growth media and cells contains components with buffering capabilities, it is possible the solution was able to stabilise itself and not be altered by excess proton formation, as would be expected in nitrate reductase driven process (Figure 2.6 A).

The reduced LSPR peak intensities at lower pH may reflect a reduction in harvestability of the nanoparticles in combination to reduced production, as demonstrated in Figure 3.11. When neutral pH solutions of particles were centrifuged prior to spectroscopy (tube 3), the supernatant remained a dark brown colour and a pellet, also dark brown, formed. The tube (4) with a pH of 4 showed a brown pellet, likely a mixture of cells and nanoparticles but a much lighter supernatant; closer in colour to the colour of the growth media (tube 2). It is unclear whether the nanoparticles were inside the cells, or extracellular with a high propensity to sediment. Visualisation by TEM would be useful in investigating this further. Although, this supports the previous finding that, in *L. fermentum*, recovery of produced particles was increased under basic conditions.[60] In a green chemical production route using glucose as the reducing agent and starch

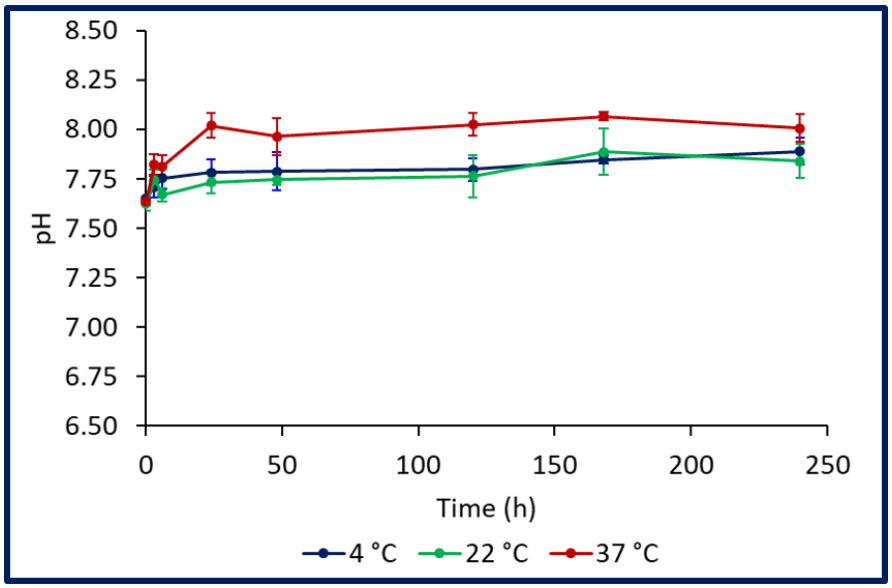

Figure 3.10: pH of *M. psychrotolerans* cultures during AgNP production at 4°C, 22°C, and 37°C.

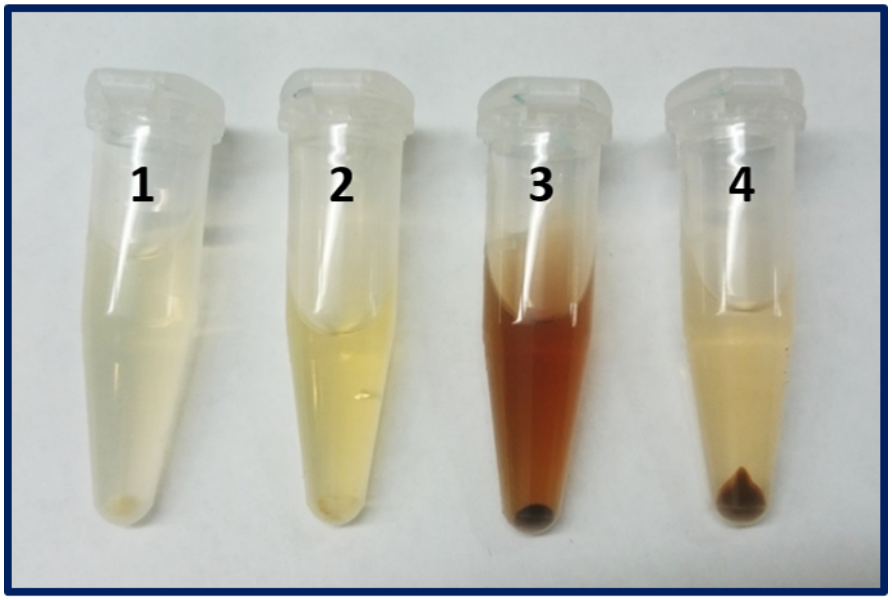

Figure 3.11: Centrifuged samples after incubation for 24 h. 1) *M. psychrotolerans* culture, 2) LB growth medium with no added NaCl, 3) *M. psychrotolerans* at pH 7 exposed to $AgNO_3$, and 4) *M. psychrotolerans* at pH 4 exposed to $AgNO_3$.

as a stabilising agent, pH did not affect the LSPR properties of the AgNP produced in a linear fashion.[240] Instead, different pH conditions were thought to favour different reaction pathways. The highest LSPR peak was observed with a pH of 6.0 and the narrowest peak seen at pH = 2.9. Alqadi et al. demonstrated that chemogenic AgNP exhibited a strong relationship between both absorption maxima and pH conditions as well as pH and particle size.[241] However, lower pH conditions corresponded with higher intensity LSPR peaks and smaller particles.

Halides

Silver halides (AgXs) form easily and are notoriously insoluble in H_2O. For this reason, halides, particularly NaCl, are omitted from growth media when using bacteria to prepare AgNPs. The formation of AgXs reduces the bioavailability of Ag^+ for AgNP production as they are highly insoluble and tend to precipitate out of solution. This is reflected in the findings of Javani et al. who showed NaCl to be deleterious for AgNP production in psychrophilic bacteria.[72] Therefore, the effects of NaCl, KCl, KBr, and KI on AgNP bioproduction were investigated.

The UV-Vis spectra of AgNP produced in the presence of NaCl showed absorbance peaks between 400 nm and 450 nm (Figure 3.12 A). However, when the concentration of NaCl was increased above 100 µM, a reduction in production was observed with the lowest production at 200 µM, in support of previous findings.[72] Moreover, the peak at 150 µM appears less symmetrical that those of lower concentrations. In contrast, KCl showed consistent AgNP production regardless of concentration (Figure 3.12 A). The peak position was comparable with those produced with NaCl and did not change with KCl concentration and the peak intensities were relatively consistent throughout. This indicates the particles produced were of similar morphologies and concentrations regardless of KCl concentration.

Gupta et al. demonstrated halides reduce the resistance of *E. coli* to Ag^+, thought to be the result of cationic halides (AgX_3^{2-} and AgX_2^-) forming which are more soluble than AgXs and increase the bioavailability.[53] However, the concentrations used were orders of magnitude higher than in this study which might explain why no impact was seen in different halides here.

NaCl and KCl both have a 1:1 ratio between Cl^- and their respective metal components (Na^+ or K^+). Combined with their high solubilities in H_2O, at the same molar concentration equal amounts of Cl^- would be present. It therefore suggests that the reduction in production likely came from the Na^+, rather than the Cl^- component of the salt.

While no reports have investigated the effect of Cl^- on AgNP production in biological systems, KCl and KBr have both been used in chemogenic AgNP synthesis.[242,243] Zhang et al. showed that Cl^- induced

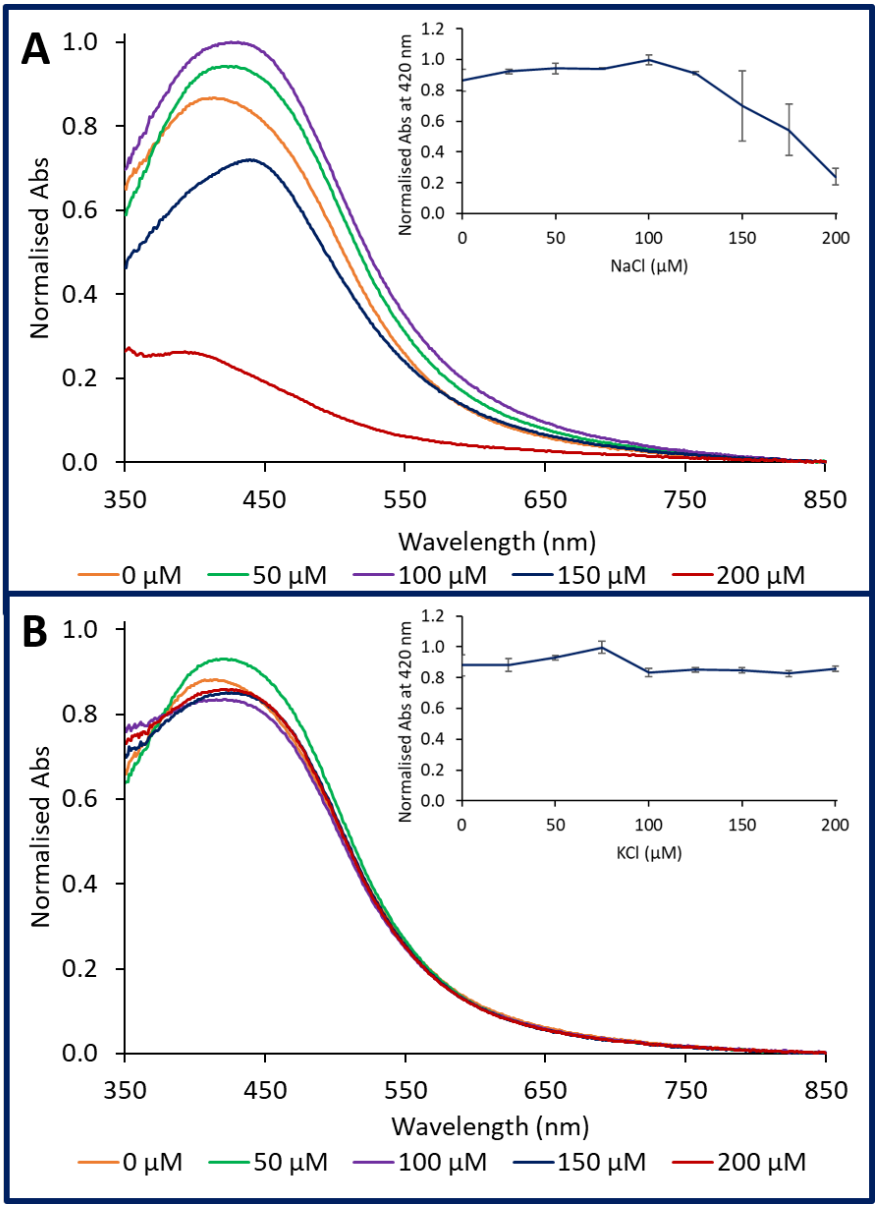

Figure 3.12: UV-Vis spectra of AgNP produced by *M. psychrotolerans* in the presence of NaCl (A) and KCl (B). Inserts: Mean absorbance at 420 nm. Error bars represent SD.

a change from pre-made triangles to nanosphere via a Ag-AgCl heterostructure over the course of 50 days.[242] In contrast to this work, triangular nanoprisms were used as a starting material. However, there was no evidence in the spectra, either as shifts in the peak positions or formation of additional features, to suggest this had been achieved here, despite the comparable concentrations used (Figure 3.13 A & B). This is likely due to the superior stability of biogenic AgNPs over chemogenic particles stemming from the protein corona which encases the particles.

Michele showed that in a microfluidic reactor, Br^- could be used to change the shape of pre-synthesised Ag nanoprisms.[243] Specifically, they noted a blue-shift in the LSPR peak indicating the conversion of triangular to spherical nanoparticles. This effect of Br^- to etch Ag has previously been reported to be greater than I^- , which in turn has a greater effect than Cl^- .[244] Such etching may have occurred here, but as it was predominantly nanospheres which formed, the effects may not have been visible spectroscopically.

Sugars

M. psychrotolerans can ferment glucose and fructose.[245] Additionally, reducing sugars have been suggested as a possible source of AgNP production in biological settings. Therefore, the influence of glucose and fructose, both reducing sugars, and sucrose, a non-reducing sugar, on AgNP bioproduction were investigated.

Over the examined range, production saw little effect from any of the sugars (3.14 A - C). The peak positions remained similar for all concentrations of each of the sugars, suggesting the morphologies of the products were consistently formed. However, the peak of glucose containing samples appeared slightly broader and with greater absorbance over 650 nm compared to fructose and sucrose. Although TEM imaging is required to confirm, it is possible this is due to the formation aggregates, a larger distribution of sizes containing larger particles, or a small amount of non-spherical particles, all of which would lead to increase absorbance at longer wavelengths. Without the appearance of additional peaks, it is not possible to conclude the presence of non-spherical particles.

AgNP biosynthesis is thought to be an energy demanding process through the use of NAD(P)H as an electron donor.[62,66] The addition of an additional energy source in the cases of glucose and fructose may have expected increased production with higher concentrations of sugars added. However, the sugars were added after the cultures had reached stationary phase and so may not have been fully utilised by the cells. Repeating this experiment with the sugars added to the growth medium prior to inoculation would allow the cells to change metabolic pathways and protein expressions which may influence AgNP production more than using the method employed here.

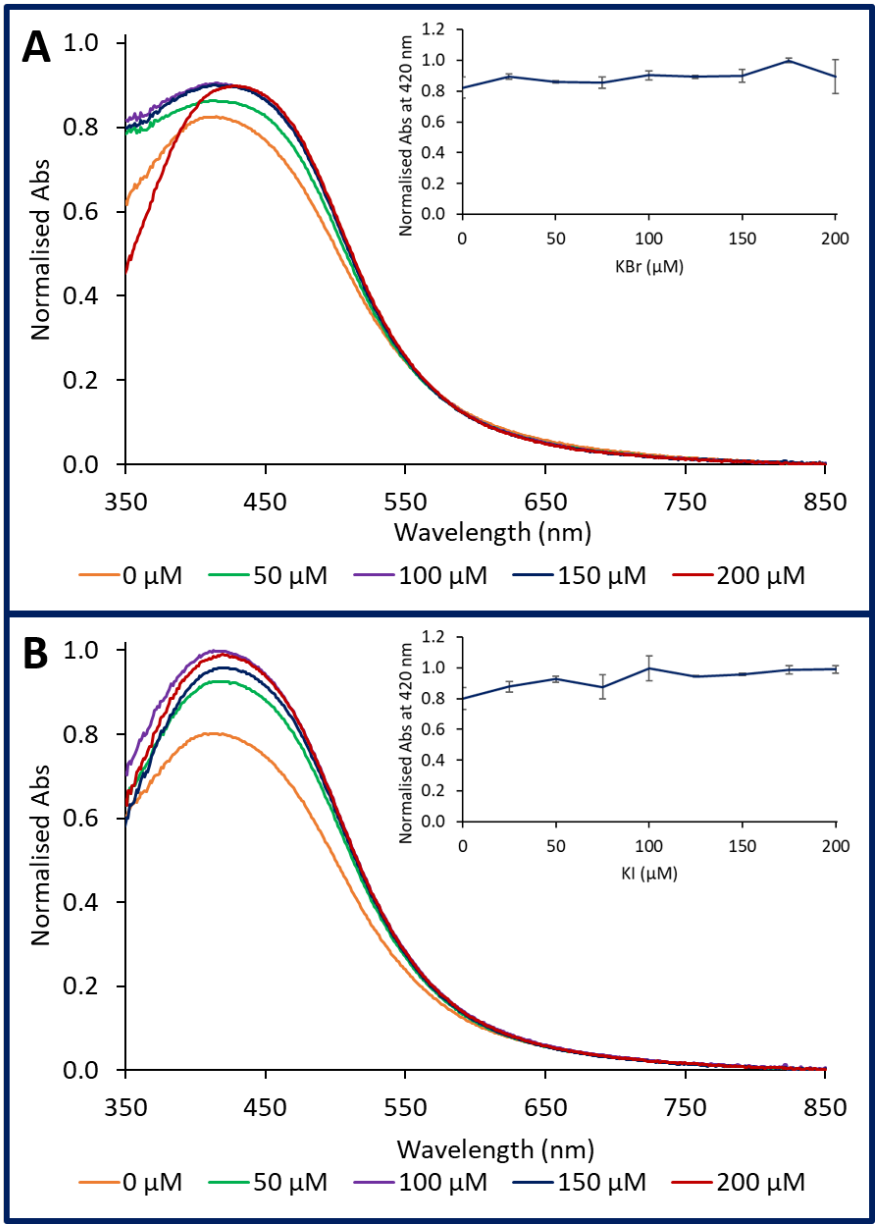

Figure 3.13: UV-Vis spectra of AgNP produced by *M. psychrotolerans* in the presence of KBr (A) and KI (B). Inserts: Mean absorbance at 420 nm. Error bars represent SD.

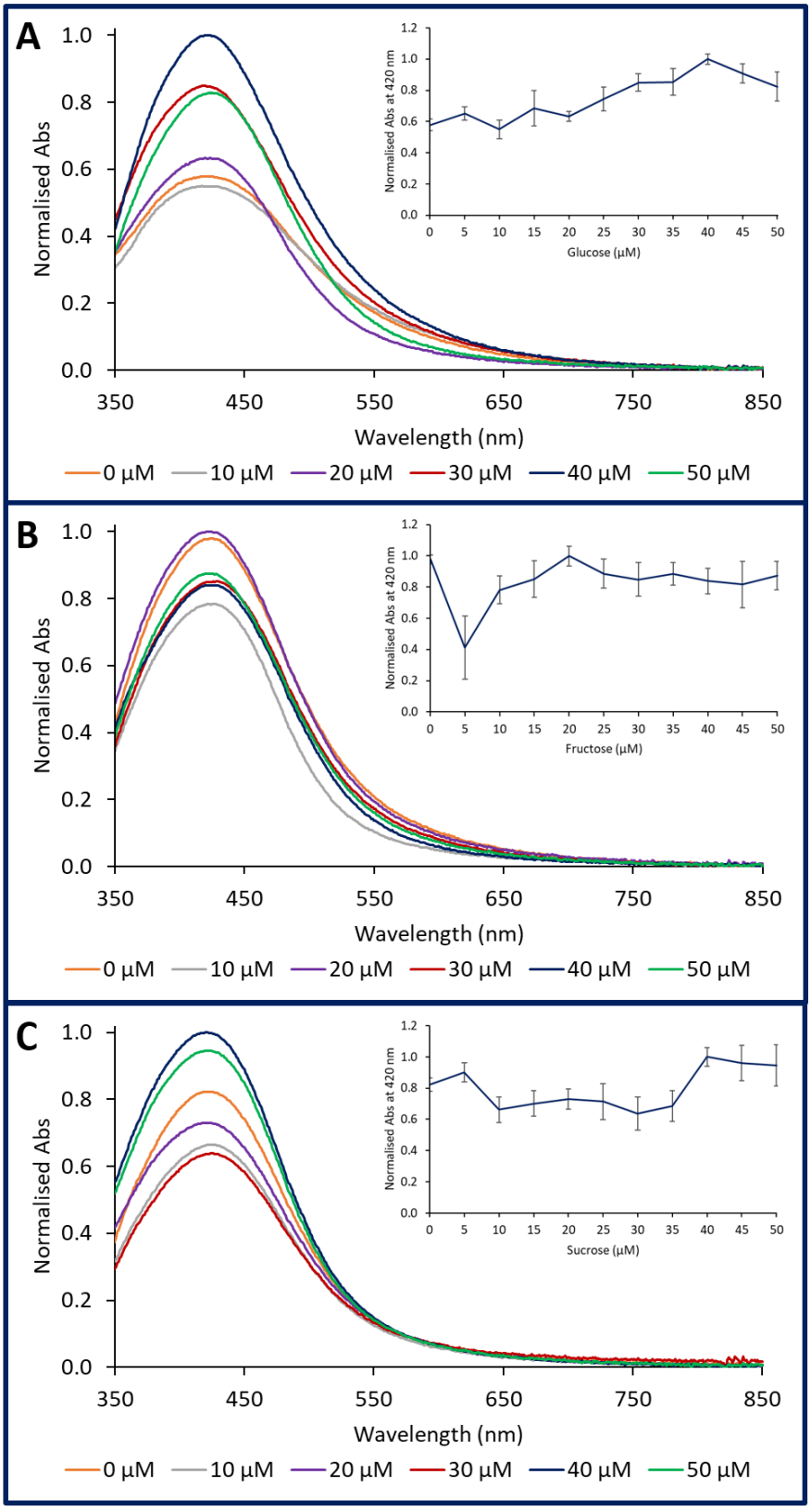

Figure 3.14: UV-Vis spectra of AgNP produced by *M. psychrotolerans* in the presence of glucose (A), fructose (B) and sucrose (C). Inserts: Mean absorbance at 420 nm. Error bars represent SD.

Citrate

Citrate is used in the chemical synthesis of triangular Ag nanoprisms. As mentioned above, it acts by preferentially binding to the (111) crystal facet, and in combination with continued etching of the surface by H_2O_2, leads to asymmetric crystal growth ultimately leading to the formation of triangular particles.[2,21,246] Zhang et al. who demonstrated the use of small organic molecules, especially citrate, could be used for shape control during crystal growth, noted that H_2O_2 was a critical component as it continuously etches the surface of AgNP during production.[21]

This process is sensitive to stoichiometry of the reagents (typically a $NaBH_4$ as the reducing agent, H_2O_2 as the oxidising agent, citrate as the capping agent and $AgNO_3$ as the Ag source). In an attempt to mimic this, citrate was added to cultures with $AgNO_3$. Molar ratios were used due to the critical involvement of stoichiometry and the different Ag^+ concentration used in this work. Previously ratios citrate to Ag^+ between 1:0.5 and 2:1 have demonstrated effective production of triangular particles;[247] similar ratios were used in this investigation.

As shown in Figure 3.15, the UV-Vis spectra did not indicate the formation of non-spherical particles as the LSPR peaks were located between 420 nm and 450 nm with no additional spectral features. Interestingly, higher ratios of citrate to $AgNO_3$ did lead to increased AgNP production (Abs_{420nm} of 0.54 $\pm$ 0.11 vs 0.86 $\pm$ 0.06). Higher molar ratios of 18:1 and 7.5:1 (citrate:Ag^+) have previously been reported in the chemical production of Ag nanoprisms.[10,247] Exploring higher ratios of citrate to Ag^+ may be beneficial as the complex mixture of the culture may hinder the binding of citrate onto the surface of particles, preventing the preferential growth. For example, biomolecules such as proteins are known to bind to AgNPs and sterically hinder citrate binding.[248] Higher relative concentration of citrate may allow more effective coverage of the particles.

In chemical synthesis, the asymmetric growth of AgNPs relies on the H_2O_2 oxidising the surface of the particles. Experiments containing H_2O_2 were carried out to better mimic this process. However, *M. psychrotolerans* appears to exhibit catalase activity and on addition of H_2O_2 to cultures, rapidly degraded it to H_2O and O_2. The use of a catalase inhibitor may help to reduce this and allow the peroxide to be utilised in the reaction, though this was not investigated.

Cell Density and CFE Dilution

To examine the importance of the bacterial cells on production, as changing the cell density is equivalent to changing the concentration of the reducing agent, cultures were diluted with growth media prior to $AgNO_3$ exposure. The production of AgNPs followed a linear relationship with the cell density (Figure 3.16 A).

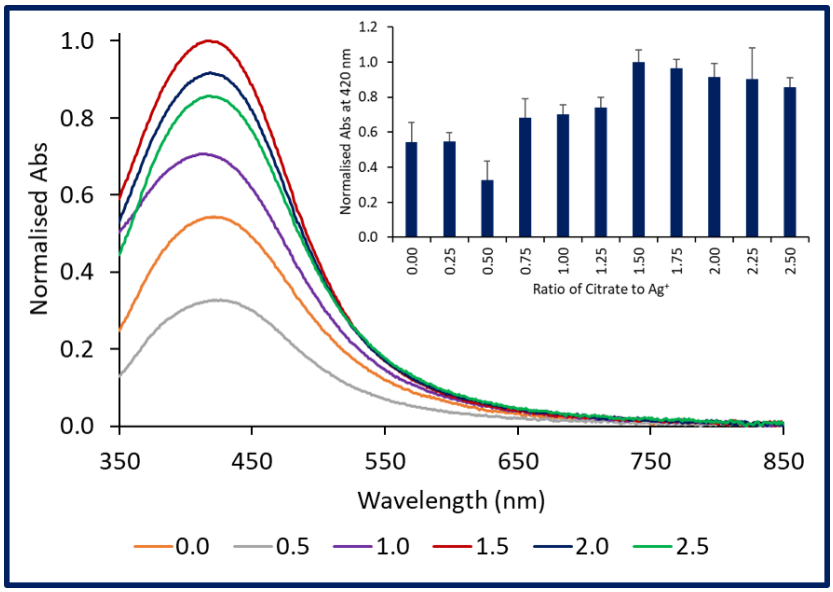

Figure 3.15: UV-Vis spectra of AgNPs produced by *M. psychrotolerans* in the presence of different ratios of citrate to $AgNO_3$. Insert: Mean absorbance at 420 nm. Error bars represent SD.

The amount of cells present did not appear to impact the properties of the particles produced as the peak positions were consistent across the dilution range. Additionally, no AgNP production was observed visually or spectroscopically in sterile growth medium. These observations demonstrate the reducing power is being supplied by the bacterial culture and that the bacteria are vital to this process.

Previous investigations into the effects of biomass proportions in bacterial AgNPs synthesis showed that a 1:99 ($AgNO_3$:CFE) ratio was most effective when using *P. mandelii*. Direct comparison with this study is difficult as the concentration of the reducing agent in the biological component of the reaction is unknown. However, it is clear that while the production continued to increase linearly with cell density in this study, the biomass appeared to be the limited reagent. Production would have been expected to plateau if the stoichiometry had tipped towards Ag being the limiting component.

Many studies into bacteria AgNP production utilise a CFE (or supernatant) of cultures.[57,72,74,75,137] This offers the benefits of reducing effects of the cytotoxicity of Ag^+ as well as simplifying down-stream processing to remove the cells from the product. A downside to this approach is the reliance on secreted proteins and reaction components which likely differ from those found inside the cells.

Demonstrated in Figure 3.16 B, Ag nanospheres appear to have been produced in CFE, based on the characteristic absorbance peaks, which are similar in position and shape to those of whole cell cultures (Figure 3.16 A). The dilutions of CFE also followed a similar linear trend to production in whole cell cultures with more concentrated CFE producing more AgNPs.

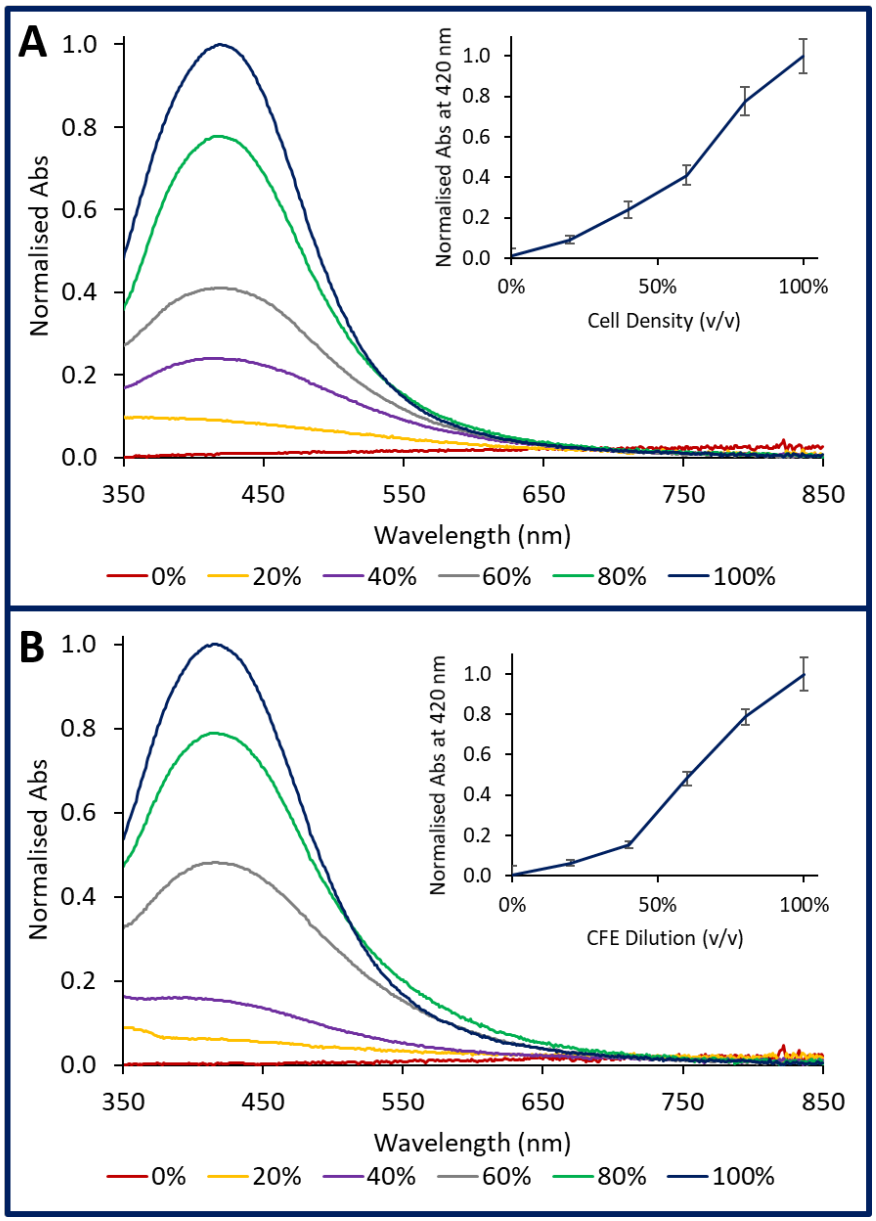

Figure 3.16: UV-Vis spectra of AgNPs produced by *M. psychrotolerans* with varied cell densities (A) and CFE dilutions (B). Inserts: Mean absorbance at 420 nm. Error bars represent SD.

Heat Treatment

The production of AgNPs in bacteria is thought to be an enzymatic process with NAD(P)H nitrate reductase being a leading contender.[61,62] However, previous studies have reported optimal production at temperatures in excess of 60°C but the highest temperature during production tested here was at 37°C.[78,108,145] To investigate whether higher temperatures would have an effect on the enzymatic mechanisms, cultures of *M. psychrotolerans* were heated for 15 min at 30°C, 60°C, and 90°C before being quenched on ice and allowed to reach room temperature prior to the addition of $AgNO_3$. As can be seen in Figure 3.17 A, any heat treatment had detrimental effects on the yield of particles produced with larger decreases in production observed at higher temperatures. Heat treatments of 60°C and 90°C showed similar levels of reduced activity. This is likely due to the denaturing of proteins leading to less efficient reduction pathways.

Interestingly, heat treatment of 30°C, only 8°C above the temperature at which the culture was grown, also showed considerable reduction in production. It is unclear why such a reduction occurred as proteins are unlikely to denature at this temperature. However, *M. psychrotolerans* is known to have an optimal growth temperature of 26°C and experiences a rapid decrease in growth rate when cultured at temperatures above this optimum and is inactivated at 37°C.[238] Therefore, this higher temperature may have resulted in changes in enzyme expressions which led to the reduced AgNP production.

Supporting this, cultures autoclaved at 121°C for 15 min at 106 kPa prior to exposure to $AgNO_3$ also exhibited a markedly reduced ability to produce AgNPs (Figure 3.17 B). The presence of an LSPR peak in the spectrum indicates Ag nanospheres were still produced with similar geometries of those produced without autoclaving. The enzymes were unlikely to be able to tolerate the autoclaving process and so it suggests a second mechanism is responsible for the observed production. Other non-enzymatic production routes have been suggested and may account for this, though further investigation is warranted to identify its components.[60]

Light

Light exposure, specifically sunlight, was serendipitously found to greatly increase the synthesis of AgNPs in *M. psychrotolerans* cultures over cultures kept in the dark during production (Figure 3.18). The spectrum indicated the presence of spherical particles with a similarly shaped peak to those produced in the dark. Previous investigations have also reported this phenomenon in bacterial systems with substantial increases in production having been seen.[74,152] This enhancement warranted further investigation and is explored in greater detail in Chapter 4.

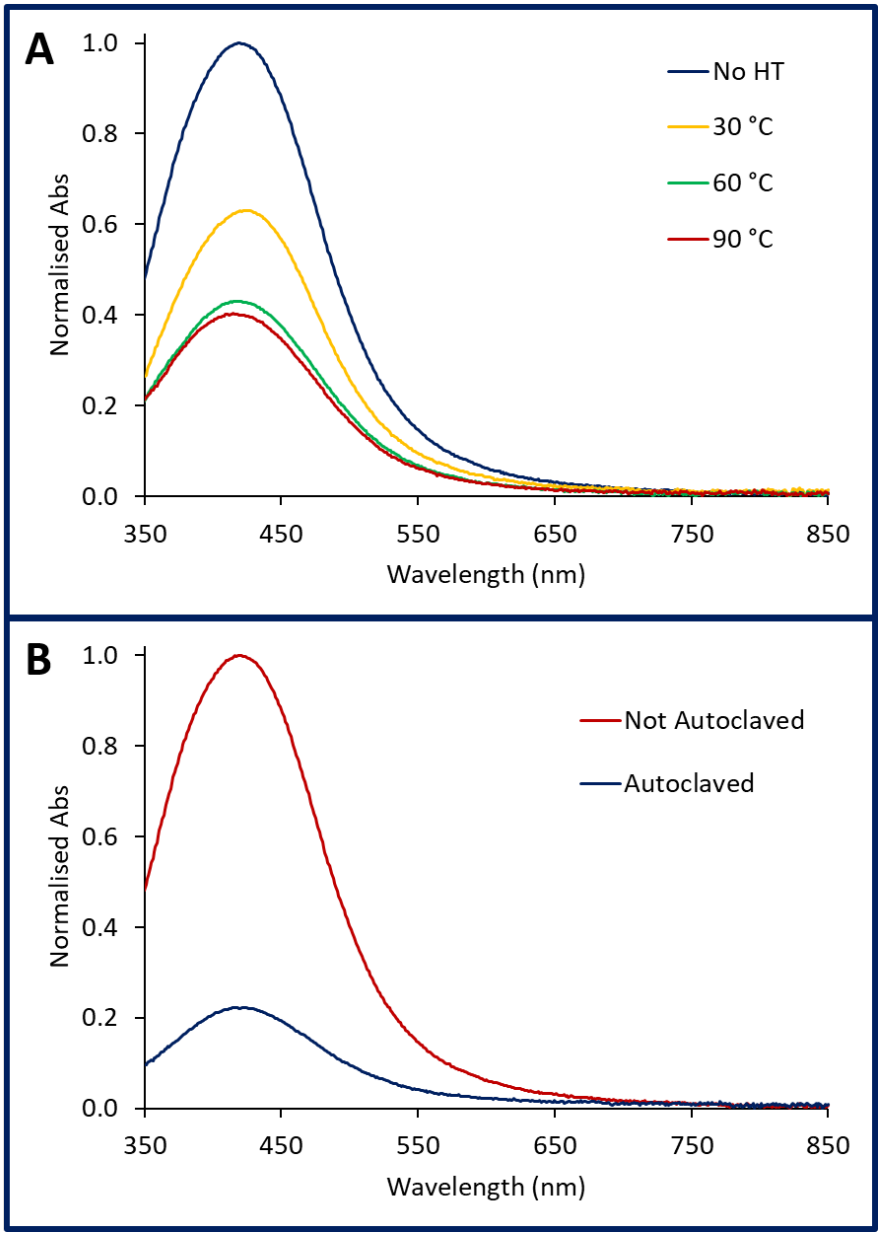

Figure 3.17: UV-Vis spectra of AgNPs produced by *M. psychrotolerans* following heat treatment at 30°C, 60°C, 90°C, and without treatment (No HT) (A). UV-Vis spectra of AgNPs produced by *M. psychrotolerans* with and without autoclaving at 121°C for 15 min at 106 kPa.

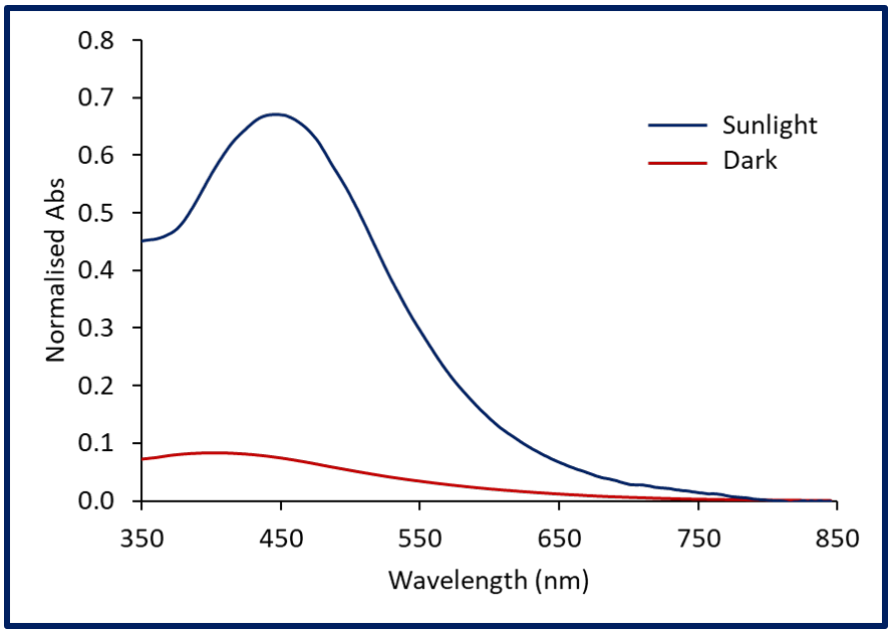

Figure 3.18: UV-Vis spectra of AgNPs produced by *M. psychrotolerans* when exposed to sunlight compared to dark conditions

3.4 Conclusions

It has been demonstrated that the reaction conditions under which the bioproduction of AgNPs was performed affects the yield of the reaction. Of the conditions investigated, the concentrations of Ag^{+}, Na^{+}, and H^{+} appear to have the greatest impact.

Bacterial cells have evolved highly efficient and effective methods for maintaining cellular homoeostasis. These systems, such as cross-membrane ion transfer, may help to "buffer" the conditions inside the cell, and to some extent outside the cell, and so may dampen any effects on nanoparticle production.

Production yields were increased by Ag^{+} to a point above which the system likely becomes saturated and the toxic effects of Ag become apparent leading to a reduced efficiency. Conversely, Na appeared detrimental to production with lower LSPR-associated absorbance peaks recorded at concentrations above 100 µM NaCl.

Despite the ability to influence particle production levels in bacteria, it is also evident that the conditions under which nanoparticles were produced here did little to affect the geometries of the particles produced. This further supports the hypothesis of a biological variable being a key part in shape control. Hitherto, little work has been published on such biological components. In depth analyses of both the biochemical mechanism of AgNP production and potential nanoparticle properties, such as surface coatings, are required to greater understand and exploit this.

The reaction conditions explored in this work were varied only once the cultures of *M. psychrotolerans* had been grown to stationary phase. While this allowed for a consistency in the cultures used, it did not permit the testing of growth conditions, rather than just reaction conditions. The growth of the bacterium with reagents (e.g. halides or sugars) would likely influence the protein expressions more greatly than adding them with the $AgNO_3$. Future investigations might explore this further to better optimise the organism's behaviour.

Attempts to mimic ligand driven prism formation were hampered by the catalase activity of the bacterium. The addition of citrate alone was ineffective at having an effect on the morphologies of the particles. Interestingly, light exposure showed a sizeable enhancement to production. This gave an exciting possible way of improving AgNP production through a controllable and low-energy and low-cost way. Consequently, it was further investigated and the findings are reported in Chapter 4.

Chapter 4

Visible and ultraviolet light enhances AgNP synthesis by *M. psychrotolerans*

4.1 Introduction

AgNPs possess unique physical and chemical properties which make them attractive in a range of potential applications.[20,249] However, limitations with current production methods have hampered the commercial viability of this nanomaterial. While chemical production processes at present remain the most commonly used method for generating AgNPs, biological synthesis approaches are being developed to overcome some of the shortcomings associated with chemogenic particles, such as particle agglomeration, the use of hazardous reagents, and challenges with scale-up, as discussed in Section 2.1.2.

Many organisms including plants, fungi, and bacteria have demonstrated the ability to produce AgNPs when challenged with Ag^{+} ions as a toxicity resistance mechanism.[4,7] Bacteria tend to be favoured for larger-scale production due to their ease of use, quick growth rates, high genetic engineering potential, and the inherent resistance to Ag^{+} possessed by many strains. Indeed, a myriad of bacteria have been shown to produce AgNPs from either biomass or cell-free extracts.[6,39,42]

The optimal conditions for AgNP bioproduction vary greatly depending on the species and component used (biomass or cell-free extract). However, all share a common limitation of relatively slow reaction rates. In chemical synthesis, AgNPs can form almost instantly upon the addition of a reducing agent and the reaction can complete in a matter of seconds. However, biological processes typically take hours, and sometimes days to reach completion depending on the conditions used.[51,57,99] This hurdle needs to be overcome before biosynthetic processes become viable and comparable with chemical routes on an

industrial scale.

Approaches to improving the efficacy of bioproduction have included thermal heating,[99,137] microwave[250] or gamma ray irradiation,[92] and light exposure.[74,136,152] Visible light offers benefits such as no need for expensive specialist equipment, no health risks, and relatively low energy usage and costs. Using light (either UV or visible) to photocatalyse the production of AgNPs is widely reported in chemical synthesis methods.[251] However, very limited investigation has been conducted on the effect of light from light emitting diodes (LEDs) on the production of AgNPs in bacterial systems. In the present study, it was demonstrated the photocatalytic enhancements of white light irradiation on AgNP biosynthesis. Additionally, the dependence of this phenomenon on the wavelengths of light used were explored to gain insight into the mechanism.

4.2 Methods

4.2.1 AgNP Biosynthesis

Cultures of *M. psychrotolerans* were grown as before in Chapter 3. In experiments using an LED light source, reactions were performed in 10 mL volumes in 25 cm^2 optically transparent polystyrene cell culture flasks, to which $AgNO_3$ was added to a final concentration of 9 mM. Orbital shaking at 80 RPM was used to maintain homogenous solutions. Negative controls were prepared using sterile growth media (LB with no added NaCl) instead of *M. psychrotolerans* cultures. Dark samples were securely wrapped in aluminium foil to protect from light. Experiments using LED light were performed in a refrigerated incubator at 22°C.

Upon addition of $AgNO_3$, samples were illuminated with light. At each time interval, 330 µL samples were taken and diluted in deionized water. Every sample was centrifuged at 10,000 x *g* for 5 min to remove cells and debris. The supernatants were then collected for analysis.

When using UV light, 10 mL of reaction mixtures were illuminated under UV lamps in open 9 cm Petri dishes. Cell-free extract (CFE) was prepared by the centrifugation of *M. psychrotolerans* cultures at 3,000 x *g* for 10 min and the filtration of the supernatant through syringe filters (pore diameter 0.22 µm). Aliquots of 100 µL were taken for analysis at each time point and diluted with diH_2O for analysis. Experiments using UV lamps were performed at room temperature of 24°C.

4.2.2 Light Source and Setup

A 10 W 6,500 K white light LED bulb with an 810 lumen output was purchased from Sealey. The bulb was suspended 15 cm above the samples and held within an opaque housing to block external light (Figure

4.1). To investigate the effects different wavelengths of light on AgNP formation, blue, green, and red optical filters were inserted between the light source and the samples. The emission spectrum of the light source and the filters are shown in Appendix B.1.

Low-cost UV lamps with 4 x 9 W 365 nm bulbs were also used. The housing was sealed with aluminium foil to block external light.

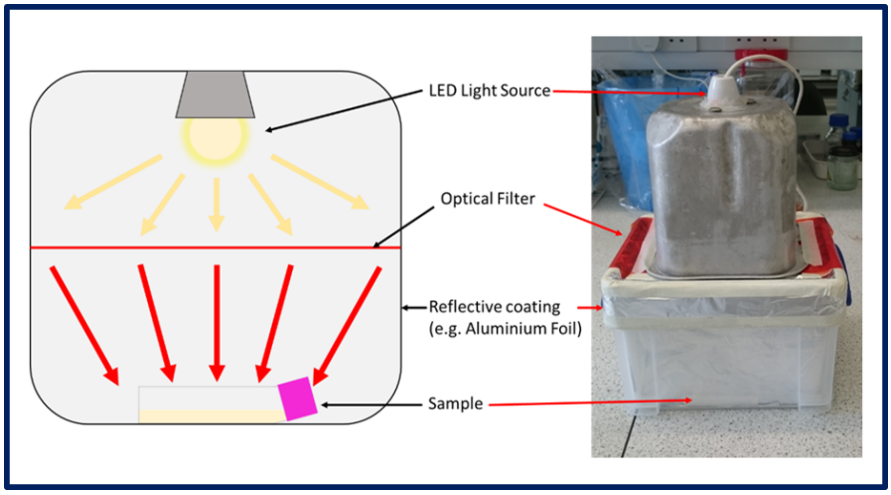

Figure 4.1: Setup used for illuminating samples with LED light. Samples were held in an opaque box and illuminated from above by an LED bulb. Optical filters were inserted between the bulb and the samples when required.

4.2.3 Characterisation of AgNPs

UV-Vis spectroscopy, performed with a using a Lambda 35 spectrometer, and TEM was performed using the methods described in Sections 3.2.3 & 3.2.3.

4.2.4 Temperature Monitoring

The temperatures of solutions were measured using thermocouple probes submerged in the reaction mixtures. Measurements were taken at 10 s intervals through experiments. The lamp was turned on after 15 min to allow for the solutions to reach temperature equilibrium. The measurements collected in the 1 min immediately prior to the lamp being switched on were averaged and used as the baseline and temperature change shown relative to this for each sample.

4.2.5 Data Analysis

Experiments were performed in triplicate and the mean values calculated. Data are presented throughout as mean $\pm$ standard deviation. ImageJ was used to determine the particles sizes from TEM images where ellipses were manually fitted to nanoparticles and the semi-major axis used as an approximation of diameter. Kernel density estimations (KDE) were applied to smooth particle size data using SciPy.[252] A minimum of 3 fields of view and 300 measurements per sample were used for analysis.

4.3 Results

4.3.1 AgNPs Production Under White Light

The production of AgNPs was carried out under white light with *M. psychrotolerans* culture or just sterile growth medium. For comparison, experiments were run under dark conditions. Samples were taken at different time points for UV-Vis spectroscopic analysis and the results are shown in Figure 4.2.

UV-Vis spectra of AgNPs produced in samples of *M. psychrotolerans* exposed to white light revealed a broad absorbance peak formed at 453 $\pm$ 6 nm with 2 h of exposure (Figure 4.2 A), known to be consistent with the LSPR peak of Ag nanospheres.[253] The peak intensity continued to increase over 48 h, indicating continuous formation of AgNPs. However, the peak position drifted slightly to 436 $\pm$ 6 nm without the development of additional spectral features, suggesting insignificant changes in particle shape. The production was also observed visually with a colour change in the solution, from pale yellow to dark brown, corresponding to the spectral peak shift (Figure 4.2 A).

Under dark conditions (Figure 4.2 B), similarly, a peak attributed to the LSPR of Ag nanospheres formed within 2 h, and continued to grow in intensity over 48 h, for AgNPs produced by *M. psychrotolerans*. The position and shape of the peak was also comparable, though the intensities of the peaks were lower than those produced in light.

No features of note were observed in the UV-Vis spectra of samples from growth media incubated in the dark (Figure 4.2 D), combined with a lack of colour change in the reaction solution, it suggests AgNP production did not occur at detectable levels. However, a strong colour change was observed when sterile LB with $AgNO_3$ was exposed to the LED light (Figure 4.2 C) with peak characteristics comparable to the AgNP produced by *M. psychrotolerans* under light.

Solutions of $AgNO_3$ in H_2O were stored in the presence and absence of light no visible change to the clear solutions was observed over several weeks.

When the intensity of LSPR peaks were compared (Figure 4.3), it was clearly indicative that AgNP

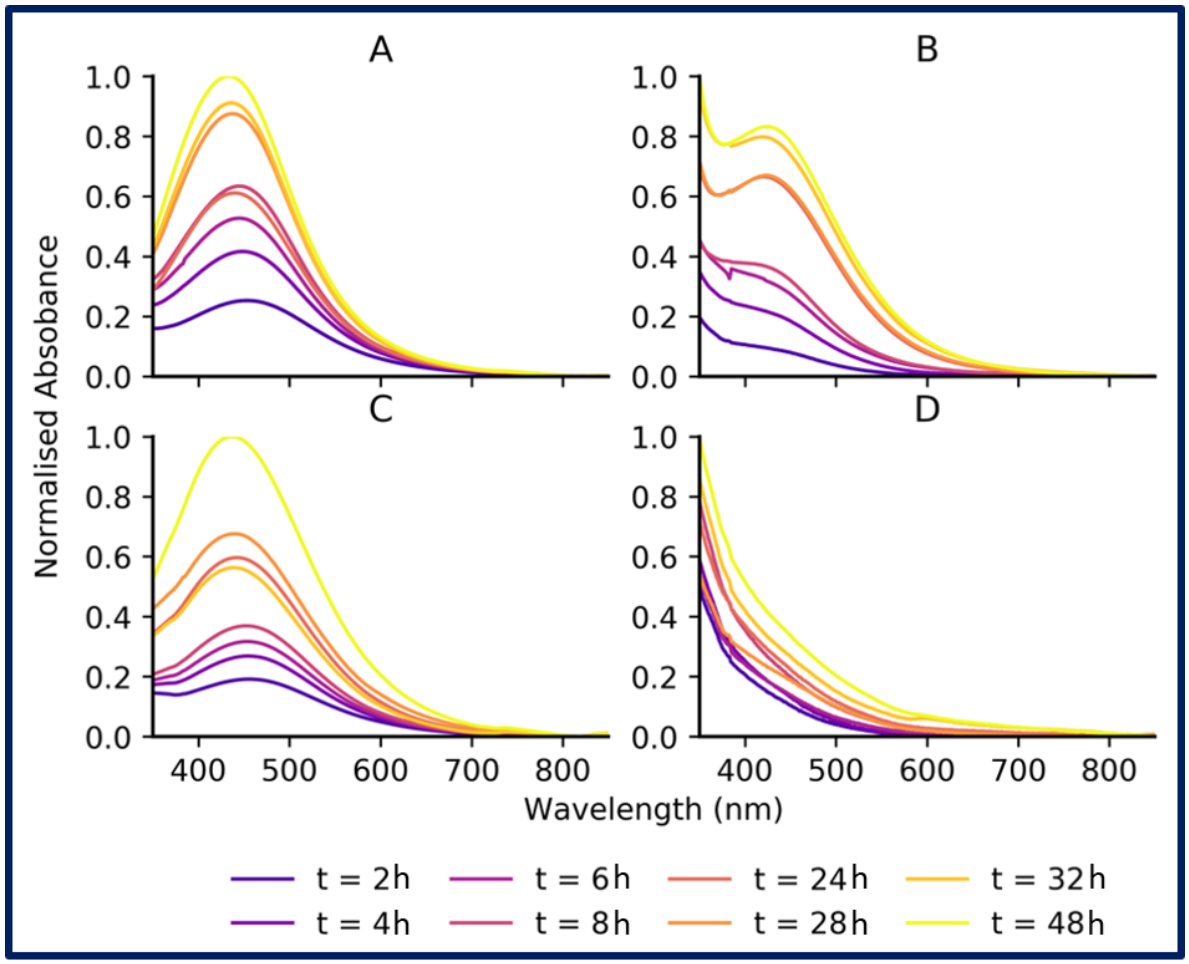

Figure 4.2: UV-Vis spectra of AgNP produced in the presence of *M. psychrotolerans* (A, B) or sterile growth medium (C, D) under white light (A, C) or dark (B, D) conditions.

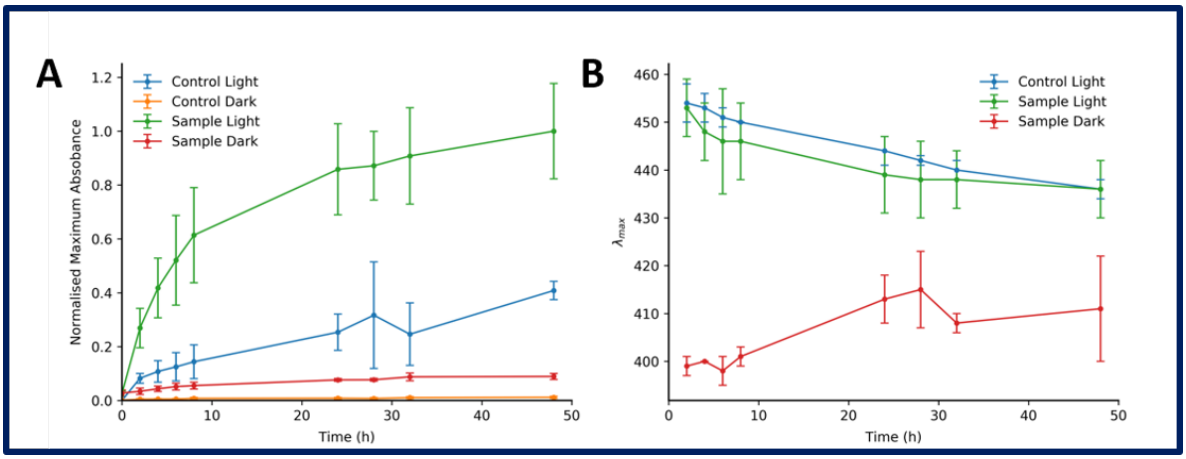

Figure 4.3: Intensities of LSPR peaks over 48 h (A) and peak positions (λ_{max}) over 48 h (B) of AgNPs produced under different lighting conditions.

production by *M. psychrotolerans* under white light conditions was more effective than all other samples (scaled absolute absorbance: 19.85, 8.42, 2.26, and 0.76, for production by *M. psychrotolerans* and sterile media in white light, and *M. psychrotolerans* and sterile media in the dark, respectively). The position of the peaks (λ_{max}) of particles produced in white light, both with and without cells, followed a similar trend of initially forming at 453 $\pm$ 6 nm and 454 $\pm$ 4 nm, respectively, and slowly undergoing a slight hypsochromic shift to 436 $\pm$ 6 nm and 436 $\pm$ 2 nm, respectively (Figure 4.7). Conversely, the peak position of AgNPs produced by *M. psychrotolerans* in the dark did not undergo this change. After 48 h, the positions of peaks from light samples and the dark samples shifted to 436 $\pm$ 6 nm and 411 $\pm$ 11 nm, respectively.

4.3.2 Morphology and Geometry of AgNPs Produced

Characterisation of extracellular AgNPs by TEM confirmed the presence of predominantly spherical and quasi-spherical nanoparticles in all samples where production was observed (Figure 4.4 A-C). Under white light with *M. psychrotolerans* present, particles with a mean diameter of 16.8 $\pm$ 3.7 nm were produced (Figure 4.4 A). These particles were larger than those produced by *M. psychrotolerans* in the dark (5.7 $\pm$ 2.5 nm), as shown in Figure 4.4 B. Particles produced under white light in the absence of bacteria appeared more irregular in shape, though still principally quasi-spherical. The particles were measured to have diameters of 8.6 $\pm$ 4.7 nm (Figure 4.4 C).

Three distinct distributions of particles were observed (Figure 4.4 D). Particles from *M. psychrotolerans* under dark conditions exhibit the narrowest size distribution suggesting the highest monodispersity. Conversely, particles produced under white light without cells were the most polydispersed with the broadest and least symmetrical distribution. A large proportion of the particles have a similar size to the AgNPs pro-

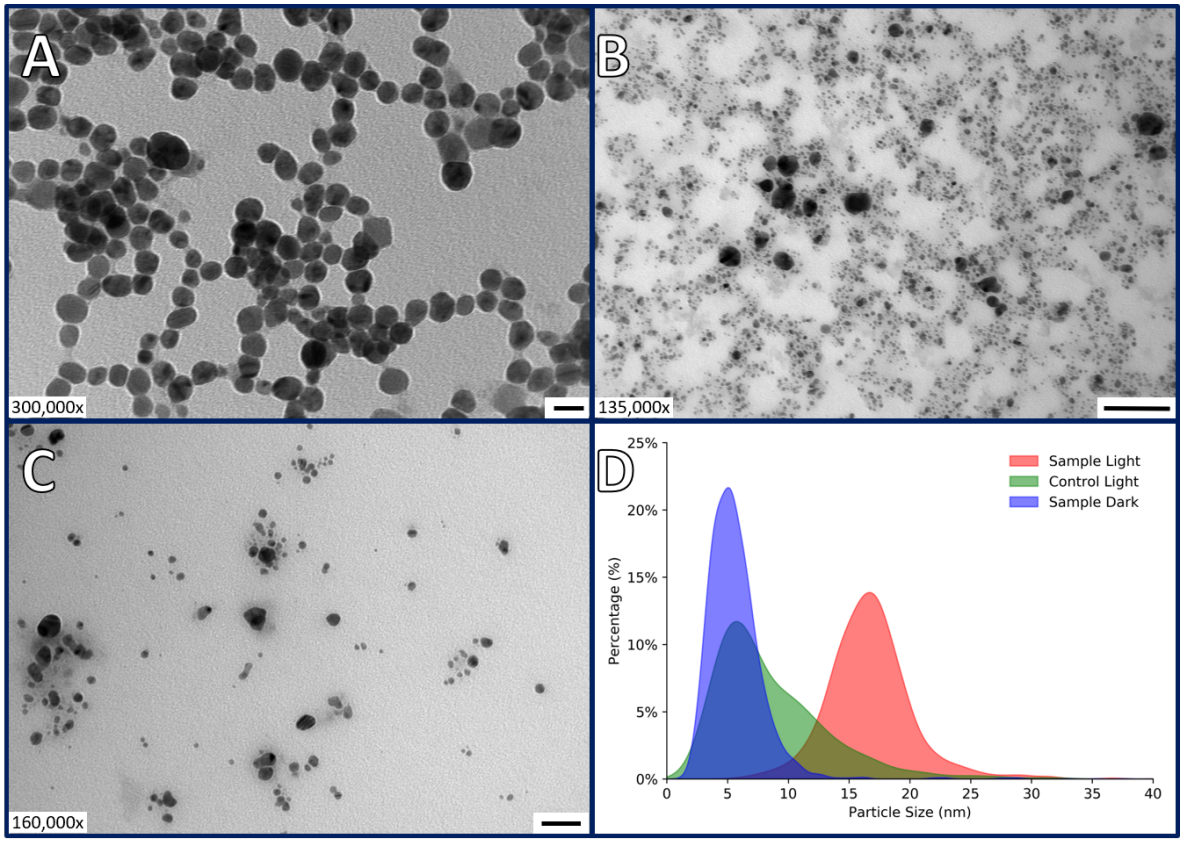

Figure 4.4: TEM images of AgNPs collected from the supernatant of (A) *M. psychrotolerans* exposed to white light, (B) *M. psychrotolerans* in dark conditions, and (C) sterile growth media exposed to white light. (D) Size distributions of AgNPs. Scale bars: 20 nm (A), 100 nm (B), 50 nm (C).

duced by *M. psychrotolerans* in the dark. The presence of a slight shoulder in the distribution may indicate the presence of two or more distinct populations of sized particles. AgNP produced under light conditions with *M. psychrotolerans* present also showed a broad distribution, though to a lesser extent.

The location of AgNPs, inside or closely associated with cells, in light or dark conditions were examined using TEM (Figure 4.5). There was little difference in size distribution of 19.1 $\pm$ 12.4 nm and 17.1 $\pm$ 5.0 nm for light and dark conditions, respectively, and the size distribution of nanoparticles in both samples was similar (Appendix B.2). While spherical particles were present in both, larger non-spherical and triangular particles were observed in the dark sample with an average edge length of 67.7 $\pm$ 9.2 nm (Figure 4.5 C & D marked with red arrows). Though present, very few non-spherical particles were observed in the light-exposed sample (Figure 4.5 A & B). No triangular particles were observed in the extracellular fraction (Figure 4.4 A - C).

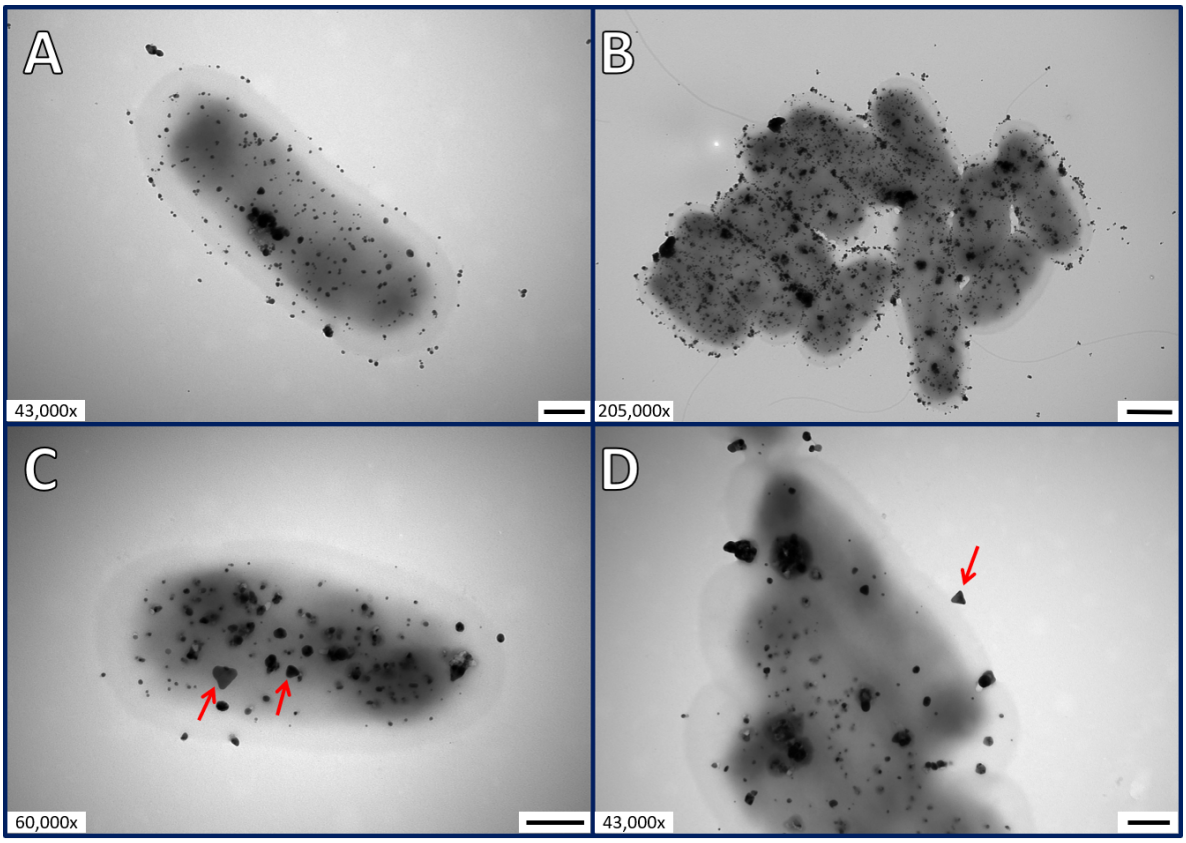

Figure 4.5: TEM of AgNPs produced by *M. psychrotolerans* under white light (A and B), and dark conditions (C and D) after 48 h. Red arrows highlight non-spherical particles. Scale bars: 200 nm (A), 500 nm (B), 200 nm (C), 200 nm (D).

4.3.3 Harvestablity of AgNPs

It was observed that the intensity of the colour of solutions of AgNPs produced in sterile growth media under white light was higher than that of the same samples after centrifugation (a step in the preparation of samples for spectroscopy). Discoloured pellets were formed suggesting AgNPs were being removed from the samples. This was supported by spectroscopy of the samples with a 77 $\pm$ 14% reduction in peak intensity observed following centrifugation (Figure 4.6). The λ_{max} location did not shift substantially (436 $\pm$ 2 nm vs 442 $\pm$ 6 nm; centrifuge vs not centrifuged), however a narrowing of the peak can be seen.

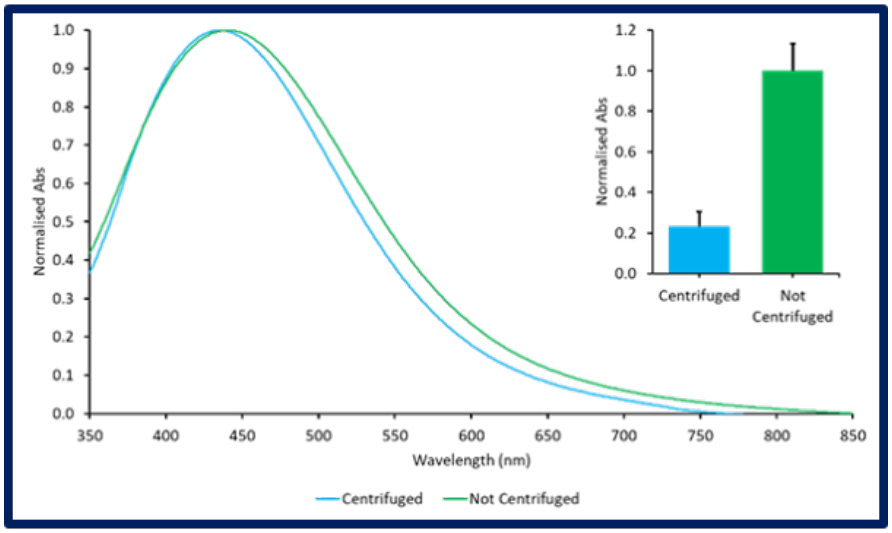

Figure 4.6: UV-Vis spectra and extinction at 450 nm (insert) of AgNPs produced in sterile media exposed to light with and without centrifugal separation.

4.3.4 Influence of Wavelengths of Light on AgNPs Production

To better understand the photo-assisted activity, coloured optical filters were used to determine the roles different wavelengths of light had on this reaction. Both *M. psychrotolerans* and sterile growth media exhibited the same pattern of the highest production with a blue filter used, whilst the green filter gave reduced production (Figure 4.7 A). Interestingly, the red filter only showed production in the sample containing cells, and the final yield was notably lower than that with blue and green filters. No production was observed either in sterile media exposed under a red filter.

When samples were illuminated with UV light (365 nm), AgNPs were produced rapidly in both whole cell cultures, CFE, and sterile broth (Figure 4.7 B). The UV-Vis spectra of samples produced under different wavelengths indicated insignificant differences in the geometries of the particles produced with peak positions between 430 nm and 450 nm without evidence of additional spectral features. The spectra of AgNPs

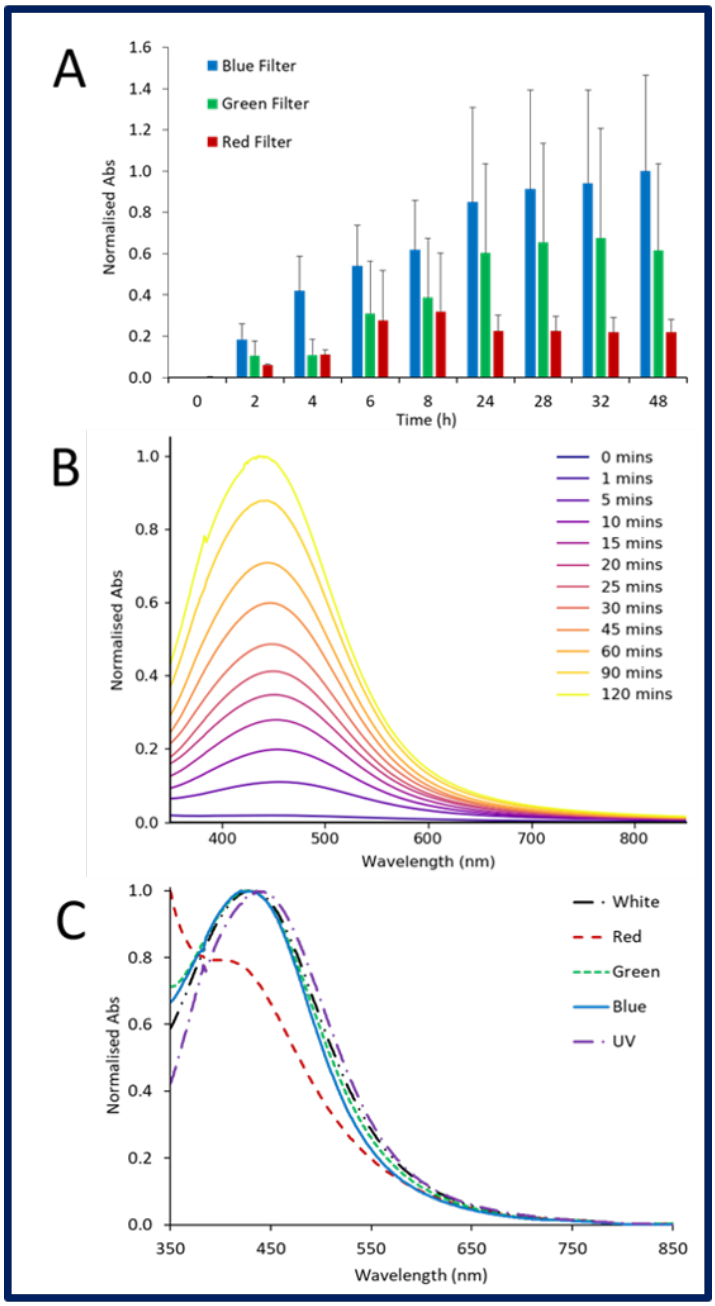

Figure 4.7: Comparison of AgNP production under different wavelengths of light. (A) UV-Vis absorbance peak intensities of AgNPs produced by *M. psychrotolerans* under blue, green and red filters. (B) UV-Vis spectra of AgNP produced by *M. psychrotolerans* under a UV lamp. (C) UV-Vis spectra of AgNPs produced under different wavelengths of light.

produced under white, red, green, or blue LED, or UV light were comparable without noticeable changes with light source (Figure 4.7 C).

4.3.5 Effects of Thermal Heating

Although the temperature of the experiments throughout was controlled at 22°C in a refrigerated incubator where an energy efficient white light LED bulb was used, the potential of thermal heating affecting production was examined by monitoring the temperature variation during experiment runs (Figure 4.8). There was a slight (1.3 $\pm$ 0.3°C) increase in the reaction mixtures in the dark over 48 h; there was no increase when the lamp was kept off. Light-exposed samples saw an increase in temperature of 3.9 $\pm$ 1.5°C. The change in temperature occurred early in the reaction before plateauing and remaining constant. The trends did not appear to be dependent on the sample type (cells present or not), and the use of coloured filters had little difference compared with white light (Figure 4.8). Heating was more substantial under UV lamps with an increase of 14.8 $\pm$ 2.8°C over 2 h.

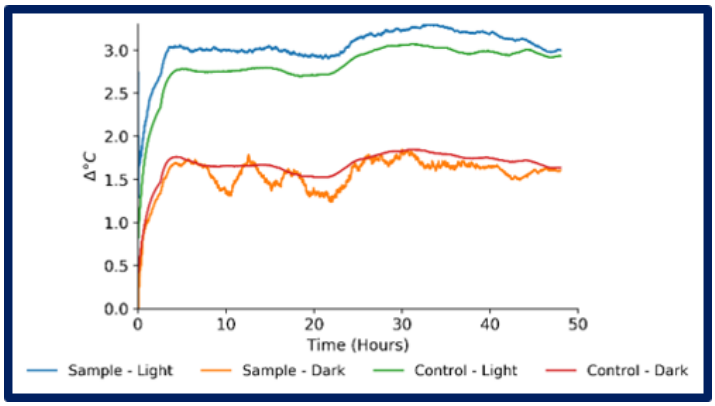

Figure 4.8: Temperature change of reaction solutions over 48 h during AgNP synthesis under white LED light.

4.4 Discussion

The biosynthesis of AgNPs has received attention as a possible solution to the limitations and hindrances associated with physical and chemical production methods. However, this process requires optimisation to reach viability on an industrial scale. Here, it has been shown that illuminating bacterial cultures with light during the synthesis of AgNPs greatly increases production.

M. psychrotolerans is known to produce AgNPs when challenged with $AgNO_3$.[51,57] As shown in Figure 4.2, the characteristic LSPR peaks detected indicate the presence of Ag nanosphere formation in the dark

here with λ_{max} at 411 $\pm$ 11 nm, as supported by TEM imaging (Figure 4.4). While white light substantially increased the production of AgNPs, different colour lights (produced using filters) gave different results where shorter wavelengths appeared to be responsible for the increased activity. This was further supported by the rapid production associated with UV light exposure. While AgNP production was observed in sterile growth media when exposed to white light, this activity was arrested by a red filter.

4.4.1 Photo-Assisted Production

AgNP production was vastly increased over 48 h when exposed to white LED light compared with samples kept in dark conditions (19.85 vs 2.26 bacterial samples in light and dark; 8.42 vs 0.76 sterile control samples in light and dark; values are scaled absolute maximum absorbance), as shown in Figure 4.3. This supports previous attempts to enhance biological AgNP production using halogen, fluorescent, and UV lamps, or solar radiation.[74,136,152]

Solar radiation offers the benefit of being environmentally friendly and free; a significant detriment is the lack of control and reliability. It has been used to produce AgNPs from *Bacillus amyloliquefaciens* over the course of 100 min where the process was accelerated with higher intensity light.[152] The particles produced were spherical and triangular whereas predominantly spherical particles were observed in samples exposed to light in this study. Sunlight has also been used to produce AgNPs in river water. In that study, initially, Ag nanospheres were formed, but on further exposure transformed into triangular, hexagonal, and eventually rod-like structures, accompanied with a loss of colloidal stability. Such morphological changes were observed within the time-frame of the experiment in this study (<48 h), however, in this study no such morphological transformations or a noticeable loss of stability was observed. This is likely due to the formation of a biomolecular coating, likely proteins, which is known to form on the surface of AgNPs produced by bacteria. The concentrations of these biomolecules were likely far greater in the bacterial cultures used here, thus forming a coating more rapidly and completely, stabilising the particles. Moreover, white LED light has a narrower emission spectrum with sharp peaks, whereas solar radiation has a broad spectrum across the visible region and extends into UV and infrared. It is possible that these differences contributed to the morphological varieties previously observed.

Using a 75-W halogen lamp and CFE of *Klebsiella pneumoniae* cultures, AgNPs were rapidly produced over 20 minutes by Mokhtari et al.[74] The particles formed were spherical with an average diameter of 40 nm, larger than the 16 nm obtained in this study. The use of CFE offers the benefit of reducing the turbidity of the solutions which allows for better penetration of light into the reaction mixture. When comparing between CFE and whole-cell cultures under UV light in this study, both performed comparably, likely due

to the very shallow solution depth. When using LED light, the flasks were continuously mixed on an orbital shaker to reduce the impact of cell-derived scattering.

Heating of the reaction solutions was minimised through the use of an LED bulb, rather than halogen or fluorescent sources as used previously,[74,136] and a refrigerated incubator. Over the 48 h experiments, an increase of 3.9 $\pm$ 1.5°C was observed in the solutions exposed to white light, and a 1.3 $\pm$ 0.3°C increase was seen in samples kept in dark conditions. The temperature increase occurred at the beginning of the experiments following the light source being turned on. Once an equilibrium had been reached, the temperatures remained relatively steady. Previous investigations have also explored the effects of temperature on bioproduction (as discussed in Section 2.2.2). While higher temperatures have been associated with increased production, the temperatures used were often far greater than that observed here.[99,130,137] The modest increase in temperature measured in this study is unlikely to be responsible for the enhanced AgNP production. Therefore, the activity was thought to be due to photocatalytic effects rather than thermal heating.

As characterised using TEM, the extracellular AgNPs produced under light conditions were found to be larger than those from dark conditions (16.4 $\pm$ 3.3 nm vs 5.4 $\pm$ 2.3 nm). This difference in size is generally understood to result in the differences in λ_{max} observed, with smaller particles typically having shorter wavelength LSPR peaks.[253] There was no noticeable change in the shape of particles produced. The distribution of particles sizes (Figure 4.4) shows that the nanoparticles produced in the dark were not only smaller, but also had a narrower distribution and thus were more monodispersed, compared with the light samples. The cause of this difference remains unclear; however, it may be due to photo-driven growth of particles in the light samples which may explain the larger sizes observed (further discussed below). It should be noted that the radius of the particles is a variable in Mie's solution for Maxwell's equations, which describe the optical properties, namely the extinction cross-section, of nanospheres.[12] Therefore, the radius of a nanoparticle can theoretically be mapped to a specific λ_{max}, when all other variables remain constant. However, do to the complexity and polydispersity of the samples here, other factors such as changes in the particle coating or subtle morphological changes may also explain the shift in the LSPR peak position.

4.4.2 Sterile AgNP Production

Interestingly, Shivaji et al.[136] reported that AgNP formation only occurred in the presence of fluorescent light in washed bacteria after 2 h; a similar result was observed in this study in sterile broth. Under dark conditions, no evidence of AgNP formation was detected. However, when exposed to white light, particles

were produced that were smaller than those produced in the presence of bacteria, but with a greater size distribution (Figure 4.4 D). This result supports previous findings which show AgNPs form via a photo-driven reaction in sterile growth media, and are not formed in the dark.[149] The growth medium used in this study (LB with no added NaCl) consists of 5% yeast extract and 10% tryptone in deionised water. Tryptone is an amino acid mix comprising of single amino acids and oligopeptides produced from an enzymatic digest of pancreas. Previously, reports have shown amino acids, namely tyrosine, cystine, histidine, methionine, and tryptophan, are able to photo-catalyse the reduction from Ag^+ to form AgNP. The process was thought to be driven by the photo-oxidation of the amino acids which acted as reducing agents. Moreover, tyrosine has been used to produce spherical AgNPs under UV laser and lamp illumination with mean diameters of 9.5 nm and 17 nm, respectively.[254] The photo-catalysed reduction of Ag^+ by amino acids likely explains the large amount of production observed here. However, the recovery of these particles was greatly reduced compared to those prepared in the presence of bacteria.

4.4.3 Harvestability of AgNPs

The colloidal stability of the AgNPs produced in sterile growth media under light conditions was notably lower than that of particles produced in the presence of bacteria. A 63% reduction was observed in the intensity of absorbance at λ_{max} following purification by centrifugation (a process applied to all LED light samples prior to analysis by UV-Vis spectroscopy). While additional work is required to fully understand why this reduction occurred, it is likely due to the capping agents on the surface of the nanoparticles. These molecules offer steric and electrostatic resistance to agglomeration.[255] Bacterially produced AgNPs are known to have a protein corona that provides colloidal stability.[75,95] Without the presence of bacteria, AgNPs in sterile growth medium would likely have been coated in media constituents such as amino acids. While amino acids such as tyrosine and tryptophan have been used as capping agents,[256,257] they may not have been sufficient to maintain the sol through the purification process. Additionally, UV-induced fragmentation of potential capping agents may further explain why the colloidal stability of these particles was reduced.[18]

4.4.4 Light Wavelength Dependence of Phororeduction

Through the use of optical coloured filters, shorter wavelengths of light were found to be favourable for the enhanced in production. Production increased with higher energies of the incident light; red light showed very low levels of production while blue showed the highest (scaled absolute absorbance values: blue: 20.10 ± 9.35; green: 12.71 ± 8.60; red: 5.05 ± 1.38), illustrated in Figure 4.7.

The effects of different wavelengths of incident light in the photoreduction of Ag^+ was previously explored in chemical synthesis using sodium citrate an electron source.[258] In support of the findings presented here, it was observed that longer wavelengths of light did not produce AgNPs. However, blue light was the most effective visible colour investigated, and UV more so.

These results suggest higher energy (shorter wavelength) light is required for photocatalytic production to occur. Supporting this, the results here showed UV light produced AgNPs rapidly. UV-powered photoreduction is well documented in chemical AgNP production where UV light generates free radicals from photoreducing agents which act on the Ag^+.[18]

4.4.5 Possible Mechanism for AgNPs Formation

The formation of AgNPs can take place through two stages as generally understood. First, the reduction of Ag^+ to zerovalent Ag^0 atoms which cluster into small seed particles during the nucleation stage. Then, continued deposition of Ag^0 onto the surface of the particles or the coalescence of particles results in a growth stage.

Photochemical reduction of Ag^+ is known to be performed by free radicals which form by the fragmentation of a photo-reducing agent when exposed to light. For example, 2-hydroxy-2-methylpropiophenone undergoes homolytic C-C bond scission forming radicals which can reduce Ag^+ under UV light.[18] Additionally, citrate ions can be converted to dicarboxy acetone, which reduce Au+ to form Au nanoparticles.[251,259] Here, the formation of superoxides by tryptophan under visible and near-UV through may explain the photo-driven activity.

In bacteria-containing samples, an NAD(P)H-dependent reductase is thought to be responsible for the conversion of Ag^+ to Ag^0 via an electron shuttle cycle (Figure 4.9).[62,64] Possibly assisted by the SilE binding protein,[53] the reductase mechanism likely occurs in the periplasmic space.[43] The depletion of NAD(P)H may explain why the total amount of AgNPs produced in dark bacterial samples was greatly reduced compared to bacteria exposed to white light. This would also suggest that metabolic activity of the cells had decreased or ceased upon exposure to Ag^+.

The growth stage of the reaction may be the result of process driven by localised surface plasmons (coherent oscillations of electrons across the nanoparticles). This is because the localised surface plasmons that form when AgNPs are exposed to visible light can facilitate higher surface chemical activity through localised heating and the enhancement of local electric fields.[260] Electrons and holes are formed as the plasmons decay via a non-radiative route and enable the transfer of charge to adsorbed molecules on the surface of the AgNPs.[251,260] Through oxidation of surface molecules such as citrate ions, the surface

charges can lead to the thermal reduction of Ag^{+} resulting in particle growth. Plasmon-driven growth may explain why larger particles were observed in samples exposed to light, compared to those kept in the dark (Figure 4.4 D). Moreover, small Ag nanospheres have a strong characteristic dipole plasmon absorption band at 400-420 nm,[253] which may explain why the results here indicate blue light is favourable as stronger plasmon excitation can occur.

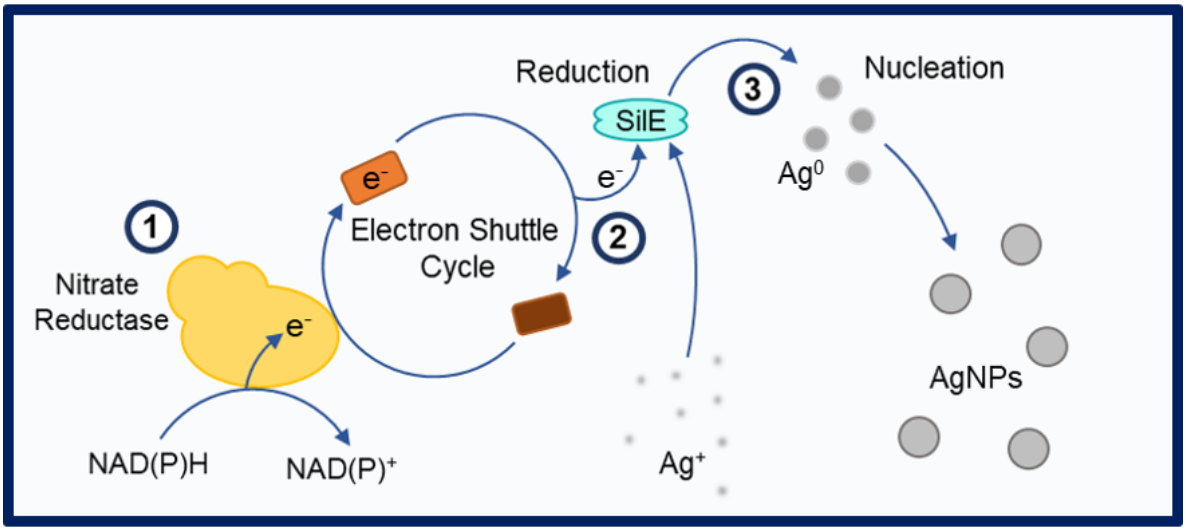

Figure 4.9: Mechanism for AgNP bioproduction in the absence of light. (1) NAD(P)H nitrate reductase transfers an electron from NAD(P)H to an electron shuttle. (2) The electron is then transferred to Ag^{+} which is sequestered by SilE. (3) The Ag^{0} atoms undergo nucleation to form seed particles.

4.5 Conclusions

It has been demonstrated that the powerful effects light can have on biological AgNP production. Shorter wavelengths of light are more effective at enhancing the biosynthesis of AgNP in bacteria, however, much of the production can be attributed to the photoreductive properties of the growth medium. Colloids of AgNP produced in the presence of bacteria are more stable than those produced in sterile media; bacterially produced protein likely causes this.

By using LED light, the process has low energy demands making it low-cost and a suitable candidate for larger scale production. Combined with the use of bacteria to supply the reducing and capping agents, this technique has great potential for the rapid and green synthesis of AgNPs.

Chapter 5

A Rapid Green Process for AgNP Production Through Laser-Assisted Photoreduction

5.1 Introduction

AgNPs have unique physical and chemical properties which give them great potential in a range of applications, for example from antimicrobials to catalysts.[165,202] However, current commonly-used physical and chemical production methods are challenged by a tendency for particles to aggregate, difficulties with scale-up, and the use of hazardous chemicals often under harsh reaction conditions.[7,42]

Biological synthesis routes have been proposed as alternatives to overcome these hurdles.[7] Despite the fact that the current understanding of the mechanisms in these reactions remains poor, and production is considerably slower than chemical or physical methods, the biological approaches are attractive for a more environmentally friendly production route and superior colloidal and particle stability.

Bacteria are often used in the biosynthesis of AgNPs due to their ease of handling, scalability, and cost-effectiveness.[261] However, the major challenge with bacterial AgNP production is the slow production rate, typically on the scale of 24 h.[6] Therefore, more rapid production processes are required to compete with chemical syntheses on a commercially viable scale. Research has been presented to increase the rate and efficiency of AgNP production assisted by heating, gamma or microwave radiation, or the use of visible light.[65,78,92,110] Among these approaches, visible light exposure has demonstrated to be the most promising method due to benefits including the potential for lower costs with reduced energy demands, the

removal of need for expensive specialised equipment, low health risks, and high diversity and control of light sources.

Cell-free extract (CFE) of *Bacillus amyloliquefaciens* has been shown to enhance AgNP production when exposed to solar radiation.[152] Additionally, the ability of *Klebsiella pneumoniae* to produce Ag nanospheres was enhanced by increasing intensities of light from a halogen source.[74] In Chapter 4, it was demonstrated the effects of the wavelengths of light on AgNP production in *M. psychrotolerans*; shorter wavelengths of LED light and UV lamps were able to enhance the bioproduction. Building on this, this work further investigates the application of laser radiation to the AgNP production process by using selected wavelengths of 650 nm, 532 nm, and 405 nm lasers and at different output powers (5 mW to 60 mW).

5.2 Methods

5.2.1 Synthesis of AgNPs

Stationarity phase cultures (OD_{600} = 2.2-2.4) of *M. psychrotolerans* were prepared in LB broth with no added NaCl. Cell-free extract (CFE) was prepared by centrifugation of cultures at 3,000 x *g* for 15 min and filter sterilisation (0.22 µm pore diameter) of the supernatant. $AgNO_3$ was added to samples immediately prior to exposure to the laser with a final concentration of 9 mM used throughout. Reactions were in 2 mL volumes in cuvettes with magnetic bead mixing, unless otherwise stated. Sterile LB with no added NaCl was used as a control.

5.2.2 Laser Source

Low-cost laser diodes ($<$5 mW) with wavelengths of 405 nm, 532 nm, and 650 nm were used to initially determine the most suitable wavelength for AgNP production. A 405 nm Cobolt 06-01 laser source was then used with a maximum output power of 60 mW. The light from this laser delivered to the sample via a fibre optic held above the sample. The height of the outlet was adjusted so that the beam diffused to cover the entire bottom surface of the sample container. Additional experiments were performed with a low-cost 405 nm laser diode with an output power of 50 mW. All testing performed with the 60 mW 405 nm laser was done in collaboration with Peijun He (Optoelectronics Research Centre, University of Southampton).

For experiments conducted in a 4 mL cuvette and a maximum power (60 mW), the area of the laser spot at the air-liquid interface was approximately 0.3 cm^2, giving a calculated irradiance of approximately 195.4 W cm^{-2}. When using a 5 mW laser, the irradiance was calculated to be 16.3 W cm^{-2} under the same experimental setup; details are shown in Appendix C.

5.2.3 Characterisation of AgNPs

UV-Vis spectroscopy was performed using a Lambda 35 spectrometer (PerkinElmer), as described in Section 3.2.3. Real-time UV-Vis-NIR spectroscopy was performed using an Avantes Starline fibre optic spectrometer (AvaSpec-ULS2048L) between 350 nm and 850 nm. A schematic of the setup used for real-time spectroscopy is shown in Figure 5.1. All spectroscopy was performed with a 1 cm path length.

TEM was performed using the method described in Section 3.2.3. Size analysis of particles was performed on TEM images using the method described in Section 4.2.5.

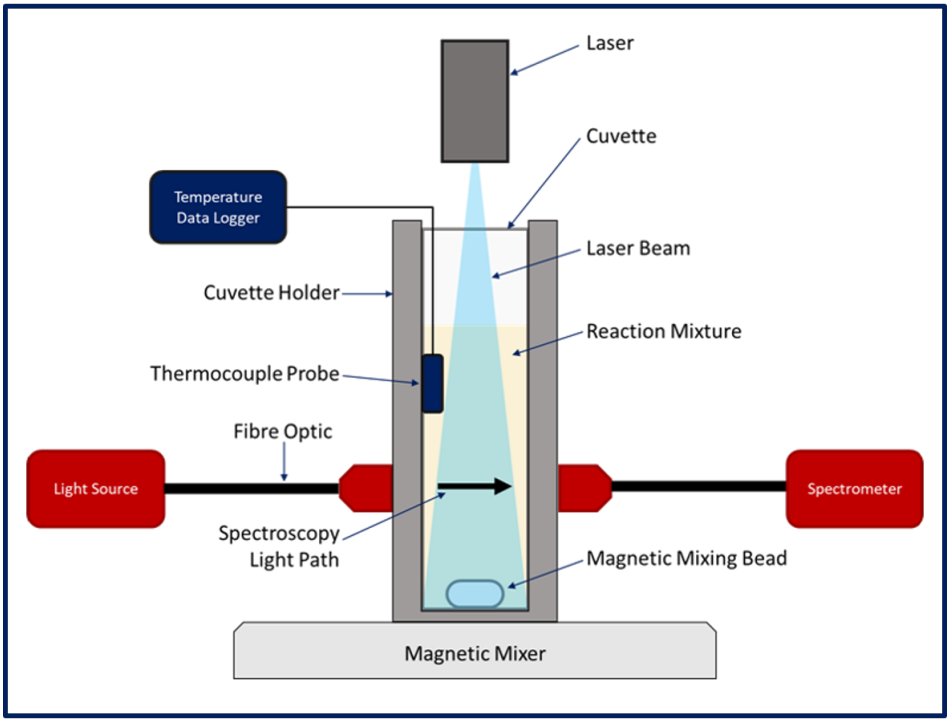

Figure 5.1: Setup for real-time UV-Vis-NIR spectroscopy of samples irradiated with a laser. Reactions were performed in a 4 mL cuvette and irradiated from above by the laser. Spectroscopy was performed via fibre optics mounted to the cuvette holder. A thermocouple probe was submerged in the solution to monitor temperature changes during reactions. The solution was mixed by a magnetic bead mixer. The bead was below the spectroscopy light path.

5.2.4 Temperature Monitoring

A VarioCAM high resolution thermal camera (Jenoptik, Germany) was used to detect temperature changes at the surface of samples when exposed to the laser. A submerged thermocouple was used to measure the solution temperature below the surface. When a thermocouple was used, experiments were performed with mixing from a magnetic mixer in 3 mL volumes. Samples were illuminated from above by a 50 mW

405 nm laser; a diagram of the setup can be seen in Figure 5.1.

5.2.5 Cell Viability

To investigate whether cells were culturable after AgNP production, samples were illuminated with a 405 nm laser in the presence of 9 mM $AgNO_3$ for 2 min. Cell were immediately centrifuged at 5,000 x *g* for 5 min and the supernatant discarded. Cells were resuspended in a thiol-neutralising solution (1.46 g L^{-1} sodium thiosulphate, 1.0 g L^{-1} sodium thioglycolate) and incubated at room temperature for 10 min.[262] Cells were then pelleted again before being resuspended in phosphate-buffered saline (PBS; Oxoid, ThermoScientific, USA). Colony-forming unit (CFU) counts were prepared via serial dilutions in PBS and plated on LB agar (no added NaCl). Colonies were counted after 4 days incubation at 22°C and compared to CFU counts of cultures not exposed to $AgNO_3$ or laser light.

5.3 Results

5.3.1 Influence of Laser Wavelength on AgNP production

To determine the optimal wavelength for AgNP production, three laser sources (5 mW) at wavelengths of 405 nm, 532 nm, and 650 nm, were used to illuminate solutions of whole-cell culture, CFE, and sterile LB growth medium with $AgNO_3$ for 2 min. AgNP production was seen in cell cultures of *M. psychrotolerans* exposed to the 405 nm laser as indicated by a change in the colour of the solution from pale yellow to dark red/brown. This was confirmed spectroscopically by a strong absorption peak at 438 nm, which corresponds to the LSPR peak of Ag nanospheres.[12] LSPR peaks at 437 nm and 452 nm (Figure 5.2) were also visible in the UV-Vis spectra of CFE and growth medium samples, respectively, when exposed to a 405 nm (blue) laser. Slight shoulders at 400 nm - 450 nm were observed in cell cultures and CFE exposure to a 532 nm (green) laser, indicating AgNP production may have occurred, but to a far lesser extent than that of the 405 nm laser (Table 5.1). There was no visible or spectroscopic evidence for AgNP production when a 650 nm (red) laser was used. Therefore, all further experiments were conducted by using the 405 nm laser.

To investigate the effects of the output power of laser on production, *M. psychrotolerans* cultures were exposed to 5 mW, 10 mW, 30 mW, and 60 mW output powers of a 405 nm laser for 10 s. As shown in Figure 5.3, higher output powers were associated with increased production, determined by higher intensity LSPR absorbance bands.

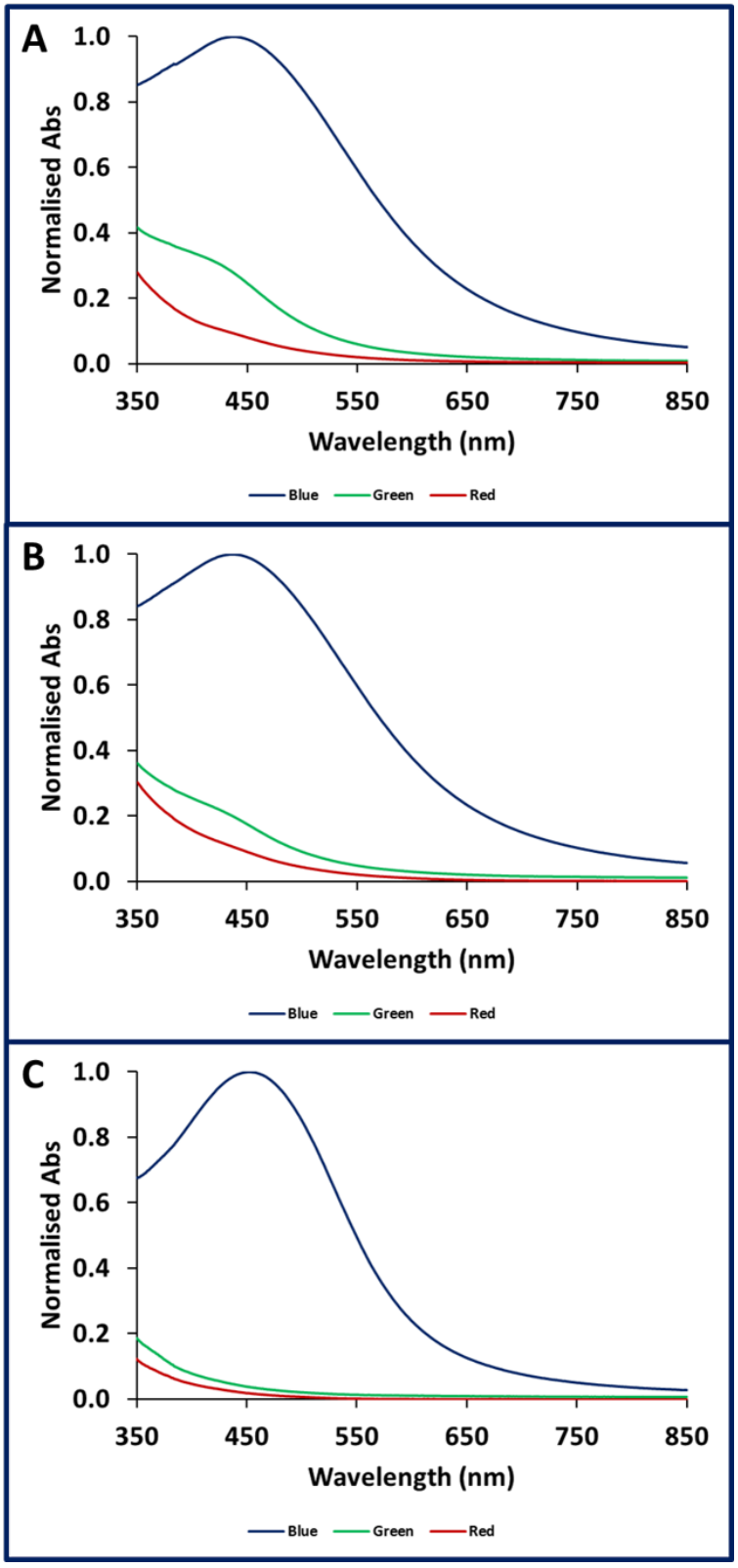

Figure 5.2: UV-Vis spectra of AgNPs produced by 405 nm (blue), 532 nm (green), and 650 nm (red) lasers in (A) whole-cell culture, (B) cell free extract, and (C) sterile growth medium.

Table 5.1: Absolute absorbance at 450 nm of AgNPs produced by lasers with different wavelengths

Laser	Whole Cell Culture	Cell Free Extract	Sterile Growth Medium
405 nm (Blue)	0.72 ± 0.01	0.72 ± 0.05	0.41 ± 0.05
532 nm (Green)	0.26 ± 0.03	0.21 ± 0.01	0.09 ± 0.00
650 nm (Red)	0.15 ± 0.01	0.15 ± 0.00	0.09 ± 0.00

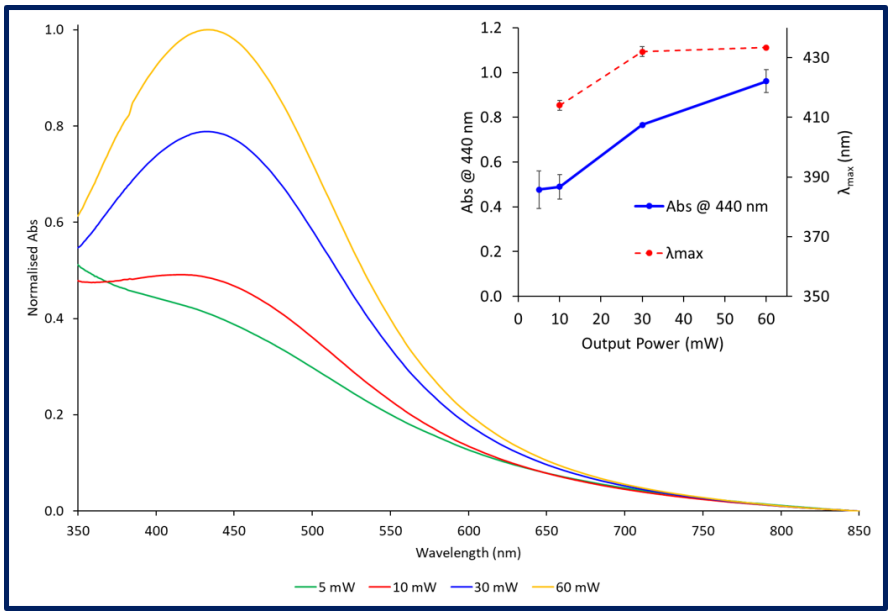

Figure 5.3: UV-Vis spectra of AgNPs produced during irradiation for 10 s with a 405 nm laser with varied output powers. Insert: Absorbance intensity of LSPR peaks at 440 nm, and position of LSPR peaks (λ_{max}).

5.3.2 Real-time Monitoring of AgNP Production

AgNP production was examined using real-time *in situ* UV-Vis-NIR spectroscopy. Figure 5.4 A shows three typical spectra at t = 0 min, 1 min and 5 min. The LSPR peak at 420 $\pm$ 1 nm was observed within the first 10 seconds of exposure to the laser and continued to grow over time before plateauing after approximately 2 min (Figure 5.4 A & B). It was also noticed that the position of the peak (Figure 5.4 C) drifted to 478 $\pm$ 1 nm over the first 2.5 min with a shoulder being present within the LSPR peak at approximately 420 nm – 430 nm. A heatmap of the spectral data is depicted in Figure 5.4 D showing the formation of the LSPR peak with no other spectra features developing with continued laser light illumination.

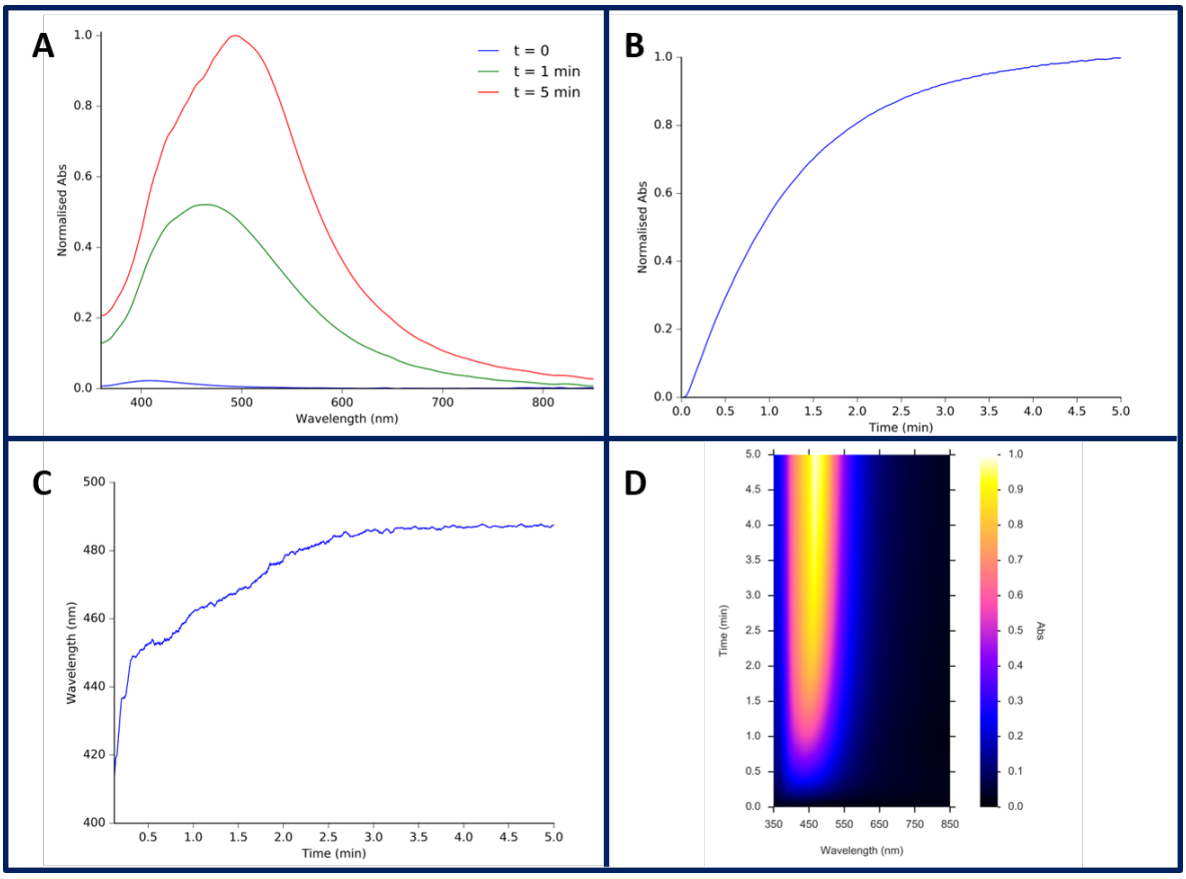

Figure 5.4: Real-time UV-Vis spectroscopy of AgNPs produced during irradiation with a 405 nm laser. (A) UV-Vis-NIR spectra of AgNPs at 0 min, 1 min and 5 min. (B) Maximum Abs intensity over 5 min of illumination. (C) Position of LSPR peak (λ_{max}) over 5 min of illumination. (D) Heatmap of absorption intensity over 5 min.

5.3.3 Nanoparticle Morphologies

TEM examination revealed that AgNPs produced were quasi-spherical in morphology with mean sizes of 6.12 $\pm$ 3.44 nm, 9.49 $\pm$ 4.36 nm, and 16.15 $\pm$ 6.17 nm, in the three sample types of whole cell culture, CFE, and growth medium, respectively (Figure 5.5). The distributions of particle sizes are shown in Figure 5.5 D. When cells were present during the synthesis, the AgNPs were more monodispersed than CFE and growth media, as represented by a narrower distribution. The distribution of sizes in CFE and LB growth media samples were notably more dispersed suggesting a less uniform product.

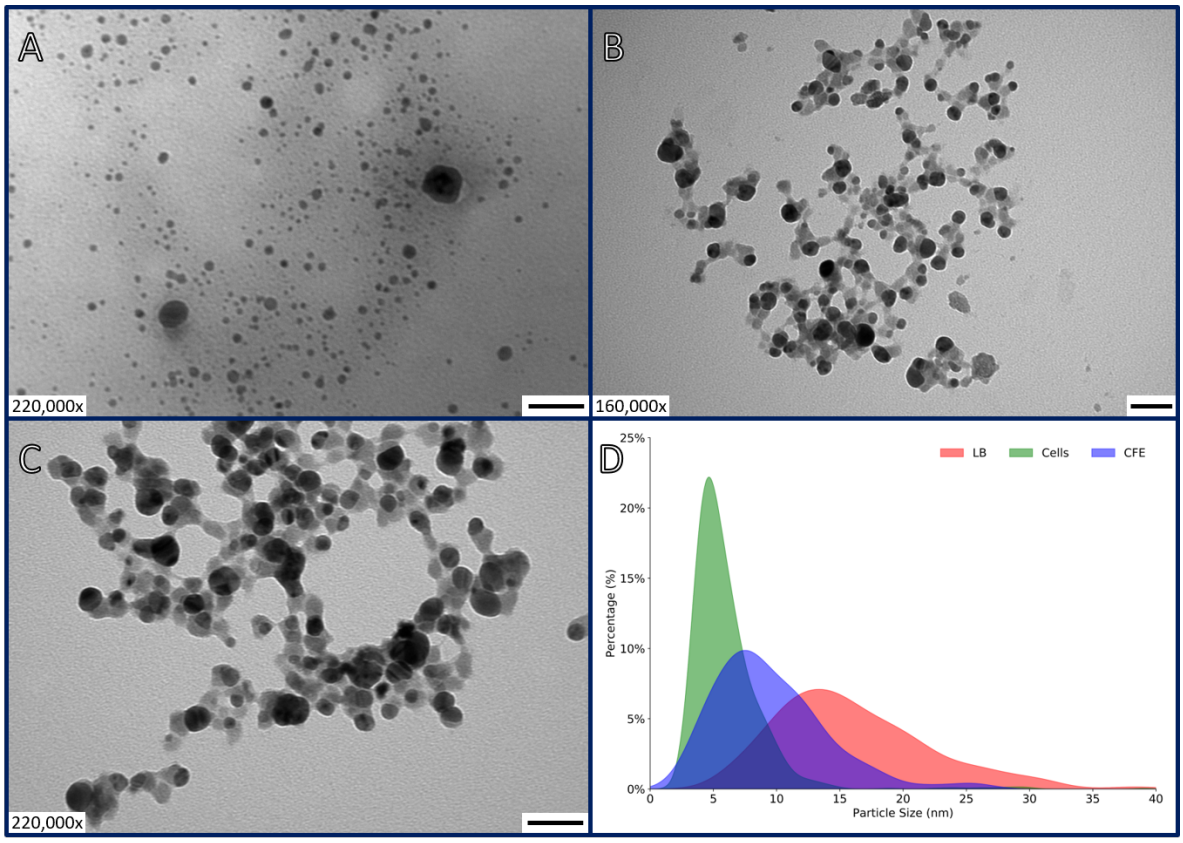

Figure 5.5: TEM images of AgNP produced with 405 nm laser irradiation in whole-cell culture (A), CFE (B), and sterile LB growth medium (C), as well as the distribution of particles sizes (D). Scale bars represent 50 nm in all images.

5.3.4 Thermal Heating

To determine whether the influence of the laser on AgNP production was due to photo or thermal effects, the temperature of the solutions was measured by using thermography and thermocouples.

Thermal imaging revealed an increased temperature on the surface of the solution at the laser spot.

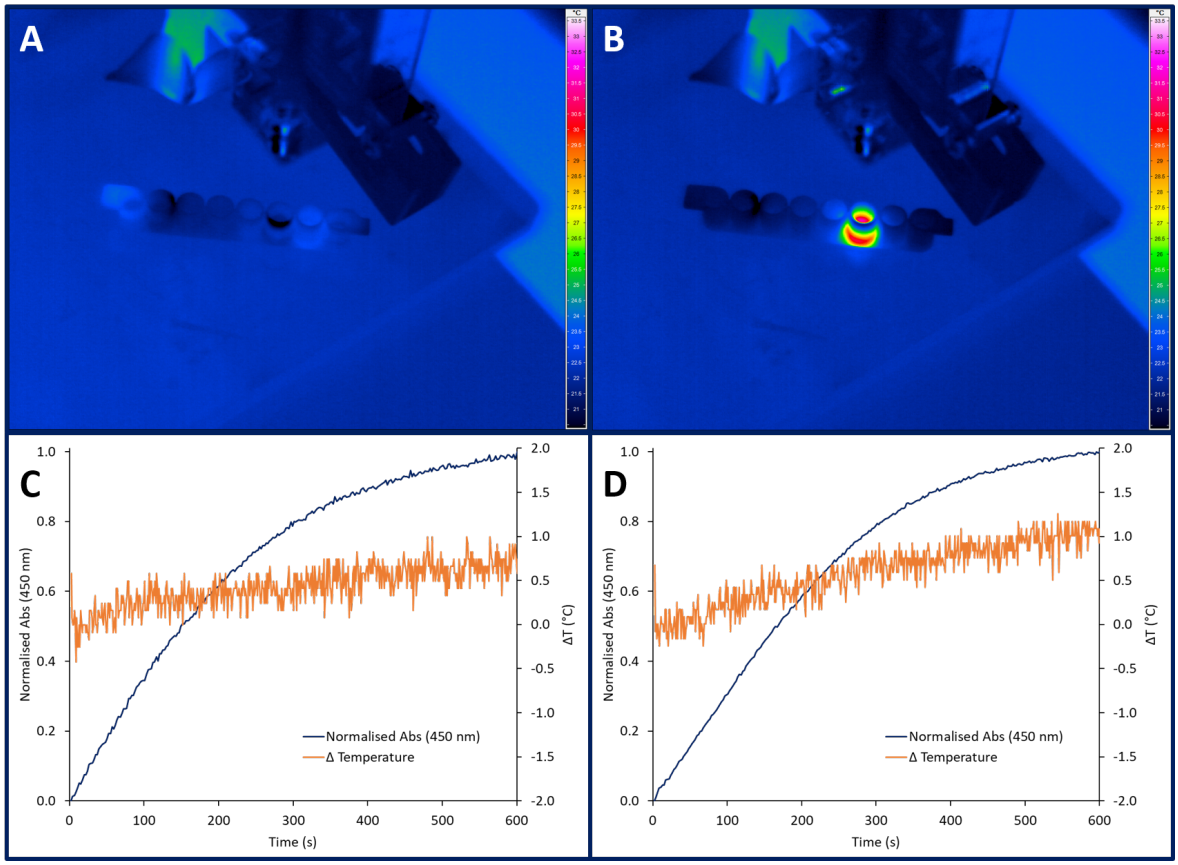

Figure 5.6: Thermal images of AgNP production in a 200 µL sample irradiated with a 60 mW 405 nm laser at t = 0 (A) and t = 5 min (B). Temperature change in 3 mL samples irradiated with a 50 mW 405 nm laser over 10 min with corresponding AgNP production determined by *in situ* real-time absorption measurements at 450 nm in CFE (C) and sterile LB growth media (D).

Before exposure to the laser (Figure 5.6), a 200 µL sample of *M. psychrotolerans* culture and $AgNO_3$ was at ambient temperature (indicated by a consistent blue colour in the image). However, after 5 min of illumination with a 60 mW 405 nm laser, the reaction well appears red and yellow in colour, indicating an increase in temperature of approximately 9°C relative to the surroundings (Figure 5.6 B). However, when the temperature of larger reaction volumes (3 mL vs 200 µL) with mixing were examined, the rise in temperature was greatly reduced regardless of whether CFE or sterile medium was used (Figure 5.6 C & D). The temperature of the solutions increased by 0.7 $\pm$ 0.1°C and 1.1 $\pm$ 0.1°C for CFE and medium, respectively.

AgNP production was simultaneously monitored by *in situ* UV-Vis-NIR spectroscopy and rapid formation was observed without a notable increase in temperature. Additionally, samples were incubated at 24°C (room temperature) and 37°C in the dark to simulate the extremes of this thermal heating. After 10 min, no AgNP production was detectable spectroscopically in these samples (Appendix C.2).

5.3.5 AgNP Production by Growth Media Components

The components of the LB growth medium without the presence of bacterial cells were also investigated to gain an understanding of the AgNP-producing activity observed. As shown in Figure 5.7, while yeast extract was capable of forming AgNPs, it was clear that tryptone was the dominant source of the activity. The UV-Vis spectra of all samples share similar shapes and peak positions indicating that the products formed had similar morphologies, regardless of the component used.

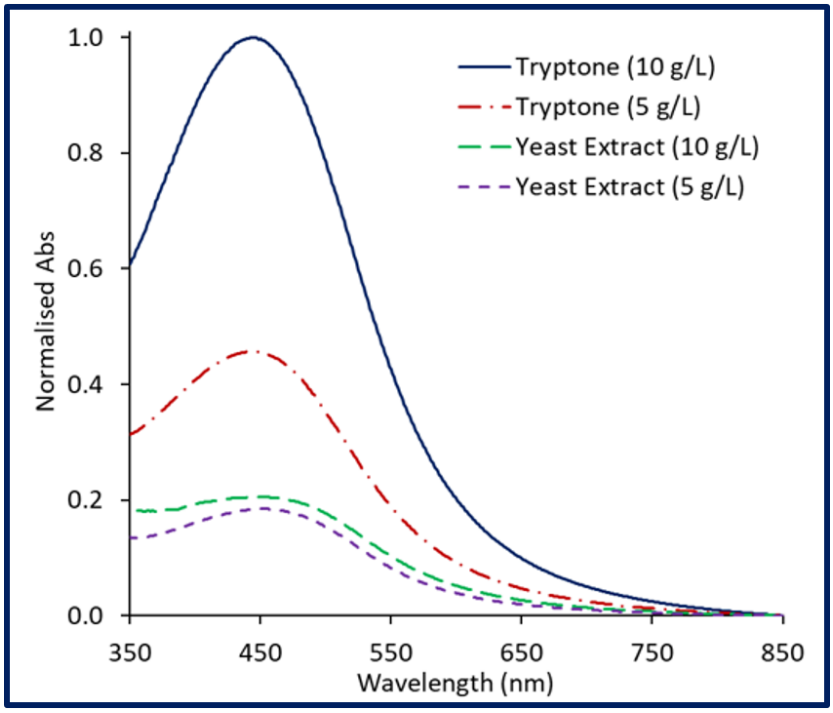

Figure 5.7: UV-Vis spectra of AgNPs produced by tryptone and yeast extract with 405 nm laser illumination.

5.3.6 AgNP Stability

The colloidal stability of samples was quantified by calculating the ratio of precipitation (R_p) with Equation 5.1, where I_0 is the initial concentration of AgNPs and I_c is the concentration following centrifugation (10,000 x *g* for 5 min).[263] UV-Vis spectra were obtained before and after centrifugation and absorbance intensities at 430 nm were used as proxies for the concentrations of AgNPs.

$$R_p = \frac{(I_0 - I_C)}{I_0} \qquad \text{(Eq. 5.1)}$$

The R_p of AgNPs produced in the presence of CFE was 0.07, half that of AgNPs prepared in sterile LB medium where R_p = 0.14. No spectral changes other than peak intensity were observed (Appendix C.3), indicating CFE-derived AgNPs were more colloidally stable and less prone to precipitation.

When observed over 150 days stored at room temperature in the dark, all samples remained stable with little change in UV-Vis spectra (Figure 5.8). The LSPR peaks in all samples undergo a slight bathochromic shift, however the samples prepared in sterile growth media change the most, as shown in Figure 5.8 D. All samples had similar peak positions and shapes by day 150.

5.3.7 Cell Viability

Cell viability was assessed in both liquid and solid phase cultures (Figure 5.9). Ag-neutralised washed cells were cultured in LB (with NaCl) for 4 days. Growth, shown as an increase in turbidity (OD_{600}), was observed. Colony forming unit counts were performed before and after exposure to Ag^{+}. The average viable cell count decreased from 8.0 x $10^{8}\pm$ 9.8 x 10^{7} CFU mL^{-1} to 4.8 x $10^{8}\pm$ 3.5 x 10^{7} CFU mL^{-1}.

5.4 Discussion

The ability to produce stable AgNPs rapidly is a critical step in reaching their full potential in a myriad of applications. Previous findings have shown the production-enhancing effects of visible and UV light in a bacterial environment.[88,136,152] It was previously demonstrated that blue and UV light appeared responsible for the observed increase in production (Section 4.4.4). In the present study, further support of this is given with observations that AgNPs formed when *M. psychrotolerans* cultures were exposed to blue (405 nm) laser light while little and no production was observed under green (532 nm) or red (650 nm) lasers, respectively; the same pattern was observed in CFE and sterile growth medium. The position and shape of the LSPR peaks in the three samples indicated the products had similar morphologies and sizes. Additionally, production was seen to increase with an increase in the light source intensity, being in line with previous findings.[152]

The rate of production, as measured by the intensity of the UV-Vis spectroscopy peak, showed rapid production within 10 seconds of exposure to the laser (Figure 5.4). This production continued before beginning to plateau after approximately 2 min. This rapid synthesis is much faster than those typically described in biological systems which often range from hours to days.[57,72] However, due to the formation of AgNPs in sterile medium, it is likely that much of the increase in production is due to a photo-chemical process, rather than biological.

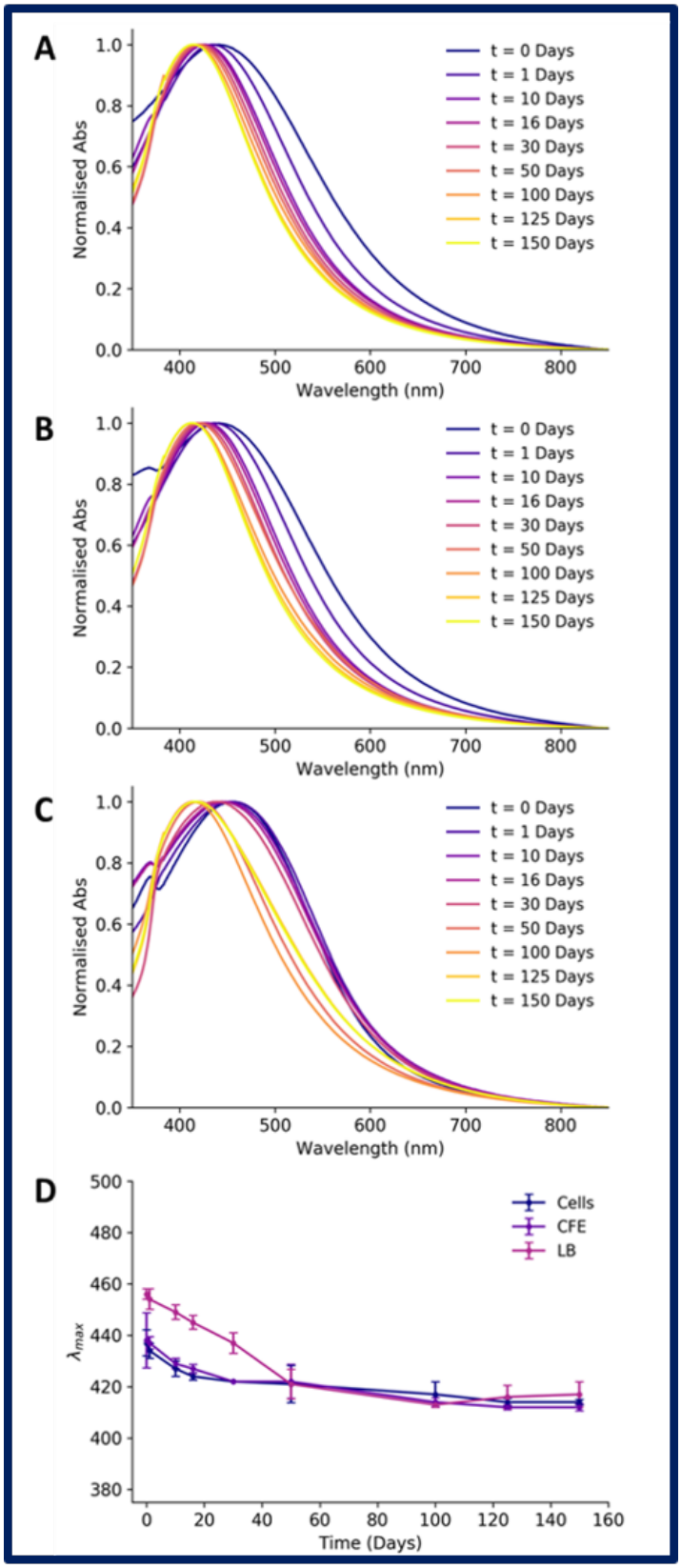

Figure 5.8: UV-Vis spectra of AgNPs produced under 405 nm laser taken over 150 days from cell culture (A), CFE (B), and sterile LB growth medium (C). LSPR peak positions over the 150 days (D).

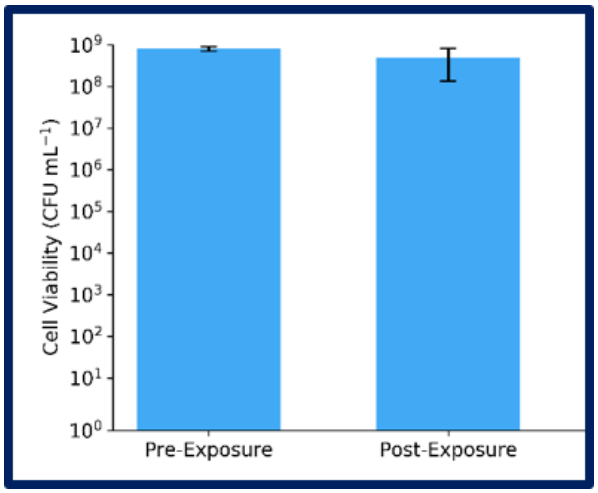

Figure 5.9: Cell viability of cultures before and after exposure to $AgNO_3$ and 405 nm laser light for 2 min determined by colony forming unit counts.

The intensity of the LSPR peak plateaus after 3 min of irradiation. It is presumed this is due to reagent depletion. As the Ag^+ is reduced, the likelihood of reactions decreases and production of AgNPs slows. To test this, additional $AgNO_3$ could be supplemented to the solution after the plateau has formed. If the rate increases, it would suggest Ag^+ is the limiting reagent. Alternatively, saturation of the spectrometer may be observed as a plateauing of peak height.[158] The Beer-lambert law states that absorbance is linearly correlated with the concentration of an analyte. However, this linear relationship is limited and deteriorate at high concentrations due to saturation of the spectrometer. Dilution of the sample at the end of the reaction and comparing the scaled absorbance value comparing to the reported value here would help to understand this.

5.4.1 AgNP Characterisation

The AgNPs produced with a 405 nm laser had an LSPR peak at 438 nm, suggesting the presence of Ag nanospheres.[12] Indeed, TEM imaging confirmed this with spherical and quasi-spherical particles visualised with mean diameters of 6.12 $\pm$ 3.44 nm and 9.49 $\pm$ 4.36 nm for whole cell culture and CFE, respectively. The smaller particles produced in the cell-culture sample may be due to the greater abundance of cellular material, such as proteins and lipid membranes. These are known to form corona stabilising the particles, but which may also prevent particle growth.

In previous reports, *M. psychrotolerans* has been shown to produce Ag nanospheres and nanoprisms under dark conditions with diameters of 70 nm – 100 nm (when grown at 4°C) and 46 nm (when grown at 20°C).[51,57] This is much larger than observed here, and indeed the AgNPs previously obtained under

LED light exposure with *M. psychrotolerans* which had a mean diameter of 16.8 nm and 5.7 nm in the dark (Chapter 4).

Real-time spectroscopy allowed the production process to be investigated. The characteristic spectral peak between 400 nm – 450 nm formed rapidly after the sample was exposed to the light source, indicating Ag nanosphere synthesis.[12] The peak intensity continued to increase with no observable additional spectral features, indicating the sustained production of AgNPs with similar geometries. The position of the LSPR peak did, however, undergo a bathochromic shift from 420 nm to 487 nm over 2.5 min of illumination suggesting the formation of larger spherical AgNPs.[12]

The formation of larger particles can occur through two main process. First, by Ostwald ripening, whereby smaller particles re-dissolve due to their higher surface energies and the ions reduced and deposited on the surface of larger particles, facilitating their growth. Second, the merging of smaller particles through coalescence can occur. Through the use of *in situ* time resolved small-angle X-ray scattering, the photo-reduction of Ag^{+} in a chemical setting was monitored and shown to proceed through both Ostwald ripening and then particle coalescence. In the present study, particles produced in sterile growth medium were measured to be the largest particles, whereas those produced with cells present were the smallest. While amino acids have been used as capping agents to stabilise AgNPs,[256,257] the presence of larger biomolecules such as proteins, known to form a stabilising coating on the particles, may have impeded the growth process in whole-cell culture samples resulting in smaller particles with a narrower size distribution. Such coatings may also affect the photostability of the particles during the process as the exposure to light has been used to convert spherical seed particles into different morphologies.[16] There is no direct evidence to support this in the findings of this work over the time-frame investigated, as shown by the lack of additional spectral features observed (Figure 5.4), though longer exposures are typically required.

The growth medium, with no cells or CFE, produced AgNPs when exposed to the 405 nm laser. This activity has been observed in a previous study and in Chapter 4.[149] and is likely due to the presence of amino acids which can act as photo-reducing agents, possibly via the formation of free radicals through molecular fragmentation. The use of a sterile reducing solution is an attractive idea as it removes the need to maintain and culture organisms and minimises downstream processing. However, as is evident in Figure 5.8 and the calculated ratios of precipitation, AgNPs produced in the absence of bacterial components appeared less stable. The stability of bacterially produced AgNPs is conveyed by a protein corona which reduces aggregation of the particles through electrostatic or steric repulsion. It was this coating that likely increased the stability of bacterially produced AgNPs in the present study.

The hypsochromic shift in the LSPR peaks observed over 150 days could be explained by the particles

getting smaller. This may be due to oxidation of the Ag back into solution. TEM imaging at time points throughout the experiment would be a valuable addition to explore this further. Alternatively, the protein-coat affects the LSPR frequency as it alters dielectric conditions at the surface of the particle leading to a red-shift in LSPR peak position. The deterioration of the coating over time may explain the observed shift. Interrogating the coating with spectroscopic techniques, such as Raman or FTIR spectroscopy, over the same time course may confirm this.

5.4.2 Cell Viability

It is widely accepted that Ag^+ is toxic to bacteria through disruption of the cell membrane and binding with nucleic acids and proteins.[45–48] However, a paucity of literature exists on the viability of bacteria following AgNP production. It is important, for a better understanding of the mechanisms involved and industrial considerations, to know whether bacteria are viable during and after process. A modest reduction was observed in culturable cells following 2 min laser exposure with $AgNO_3$. Further investigation is therefore required into the importance of cell viability on the production process, especially with regards to dependence of time on culturability, but it is clear due consideration must be shown when using bacteria as a production route.

5.4.3 Photocatalytic Activity

To ascertain whether the enhancements in AgNP production observed were photocatalytic or the result of thermal heating from the laser light, thermography was used to imaging the temperature variation in the samples exposed to a 405 nm laser. As can be seen in Figure 5.6, while small samples experienced surface heating, larger volume with mixing saw only very modest temperature increases with laser exposure over 10 min. Further to this, samples were heated in the dark to 37°C and the AgNP production assessed (Appendix C.2). No production was visually or spectroscopically evident following the 10 min incubation. While heating, especially over long exposures, may have an impact on production,[108] over the time frames investigated here, it would appear the increases in production are the result of photocatalytic processes, rather than thermal heating. Nevertheless, heating should be a consideration in future studies and larger scale applications of this technique. Alternative laser sources, such as pulsed or modulated laser, may also be interesting to consider for reducing thermal heating of the solutions.

5.4.4 Mechanism of AgNP Production

Bacteria are thought to produce AgNPs as through a resistance mechanism to the toxicity of Ag^{+}.[9] By reducing the ions to a metallic form, the stress can be detoxified. However, the exact biochemical mechanism of this process still remains poorly understood. These processes typically occur on timescales far longer than the experiments observed here.[57,76] Combined with the ability of sterile growth medium to produce AgNP, it would appear that the activity observed here is a different mechanism than that used by the bacteria in the dark.

The photochemical synthesis remains to be examined in detail in a biological setting, however, it is understood in chemical environments. The photo-induced fragmentation of molecules such as amino acids generates electron donors which in turn reduce the Ag^{+} ions.[18] Previous reports have demonstrated the Ag^{+}-reducing activity of amino acids including tryptophan and tyrosine.[257] Moreover, bacterial extracellular polysaccharide exposed has been shown to produce AgNPs on exposure to light.[113] This mechanism also explains why AgNPs were formed in sterile growth medium with no enzymatic machinery present. When the constituent parts of LB were investigated, it was clear that tryptone contributes the most to this activity (Figure 5.7). Tryptone is an amino acid mix containing monomeric and oligomeric digest products of peptides. A mechanism is proposed here for the formation of AgNPs through this method is shown in Figure 5.10.

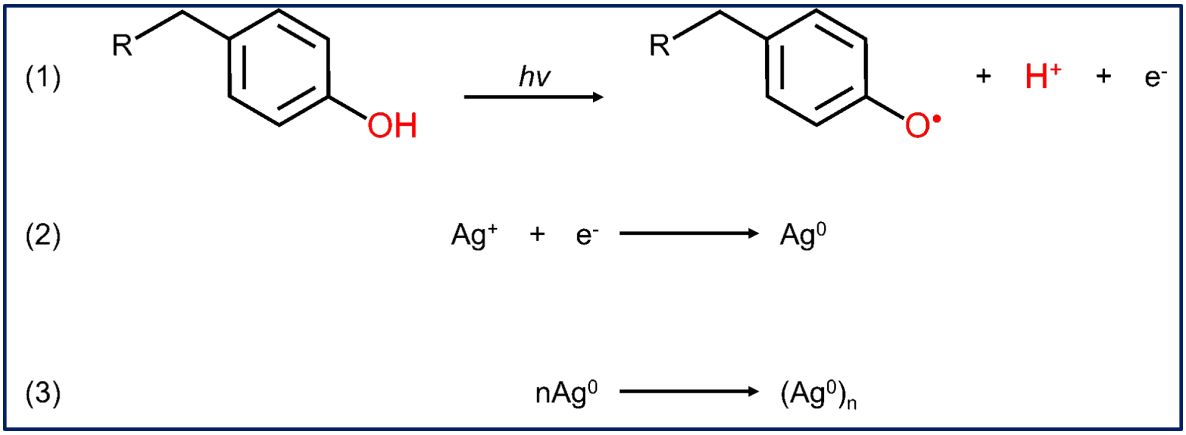

Figure 5.10: Proposed mechanism for AgNP synthesis from the photo-oxidation of amino acids. (1) Amino acid side chains, tyrosine is used in this example, are photo-oxidised by the laser light forming a radical and releasing a proton and electron. (2) Ag^{+} is then reduced by the liberated electron to a zero-valent atom. (3) Seed particles are formed as the Ag^{0} undergo nucleation.

Once small AgNPs have formed, a second step of LSPR-driven reduction can occur. The formation of electron-hole pairs on the surface of the particles as the light-driven plasmons decay drives REDOX reactions which facilitate the continued reduction of Ag^{+} and the growth of the particles.[251,260] For the

LSPR-driven process to occur, AgNP must be present and must have LSPR bands within the bandwidth of the incident light. In this case, a 405 nm laser is well placed to excite the plasmons of Ag nanospheres, known to exhibit strong LSRP absorption peaks at 400 – 450 nm, depending on size.[12]

5.5 Conclusions

Stable AgNPs were produced with a 405 nm laser in a rapid photocatalysed production method. The particles were spherical or quasi-spherical in shape with sizes dependent in production conditions and that are stabilised by a bacterially-derived coating. While the exact mechanism remains to be fully elucidated, the process appears photocatalytic rather than the result of thermal heating. The photo-reducing abilities of amino acids likely contribute to the production process. This green and rapid method has the potential to be scaled up and used for producing AgNPs for a range of applications.

Chapter 6

Photo-Assisted Biosynthesis of AgNPs Using Cell Free Extract in Flow Reactors

6.1 Introduction

The enhancing effects of light on AgNP production have been demonstrated in Chapters 4 & 5. It is clear that light exposure during the synthesis process results in considerably increased yields and faster rates of production. However, it is also expected that improved control over the mixing of reagents and thermal heating will likely lead to a higher quality product and further optimisation of production rates and yields. To achieve this, the technique of light driven production was translated from batch synthesis to flow synthesis.

There are many types of flow reactors, but all follow a similar basic concept and an outline of a basic flow reactor's components is shown in Figure 6.1.[177,178] In general, reagents, typically in a liquid phase (although gas phase can be used) are pumped into a reaction channel via a mixing system, often simple "T" or "Y"-mixers.[177] As flow reactors are usually operated at a steady state, the flow rate of the reagents into the reactor is constant. Once in the main reactor channel, stimuli in the form of heat or light can be applied. The product is then collected at the end of the reactor. Additional steps including quenching of reactions, in-line analysis, and purification, can be added to improve the performance of reactors.[178]

Flow reactors offer a number of advantages over batch reactions, especially when producing nanomaterials.[264–266] However, the more complex designs and parameters often require considerable optimisation to reach a viably operating configuration.

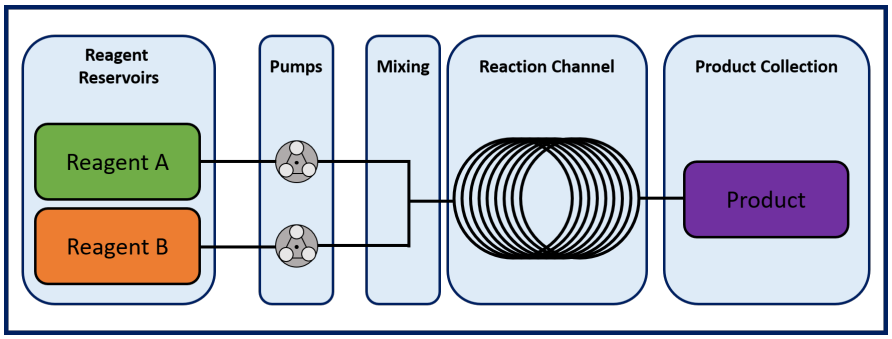

Figure 6.1: General components of a Flow reactor. Based on a figure published by Plutschack et al.[178]

A fully optimised flow reactor will generate the most product possible at the highest possible flow rate. To do this, the reaction parameters can be adjusted to allow a reaction to reach completion before the end of the reactor. In batch systems, the stoichiometry of the reagents is determined by the initial concentrations added to the reaction vessel. However, in a flow system the ratio in which the reagents are introduced can also be varied as the flow rate ratio (FRR). Highly controllable stoichiometry is advantageous in nanoparticle production as it can be used to control particle growth.[181,182,267]

Beyond the simple addition on differing amounts of reagents, flow reactors can be designed to give great flow control and induce rapid mixing or to impede the mixing of reagents.[179,268] Through the use of active micro-mixers and passive channel geometry designs, such as serpentine structures, mixing can be fast and consistent.[268]

Flow reactors also offer the ability to reduce the impact of thermal heating from light sources used in photocatalysed reactions. In Chapter 5, it was shown that laser induced heating occurred in the reaction solutions when preparing AgNPs. While increased temperatures are known to increase production rates in biological systems and so is not necessarily a negative impact,[123] the lack of control presents a possible variable to remove in order to gain more control, and thus a more uniform product. By continuously flowing the reagents past or through a laser beam, the heat generated is prevented from building up at the reaction site, but rather is transported away and dissipated. Moreover, the scale of micro-fluidic and meso-fluidic reactors allows for very high heat transfer giving high degrees of temperature control and consistent heating when required.[269]

Perhaps one of the most attractive reasons to use flow synthesis over batch processes is the potential for increasing the scale of production. Either through increasing the reactor size (scaling up) or by running multiple reactors in parallel (scaling out), many industrial processes prefer flow systems over batch for increasing output.[270] Flow synthesis opens up more opportunities for the use of light in chemical syntheses.[270,271] In batch, the penetration of the light into the reagents can be challenging, whereas in flow, the

penetration depth can be minimised through the use of narrower tubing or vessel, improving photocatalytic performance.

In this chapter, the development of a flow reactor for the photo-enhanced bioproduction of AgNPs is presented. The design process is explored and the testing and improvements of each design iteration is shown.

6.2 Methods

6.2.1 Organism and Reagents

M. psychrotolerans was grown in 100 mL LB (no added NaCl) for 4 days in a 300 mL Erlenmeyer flask at 22°C and 120 RPM orbital shaking. CFE of *M. psychrotolerans* cultures was prepared by 3,000 x *g* centrifugation for 20 min and filtration through a 0.22 µm filter. $AgNO_3$ was purchased from Fisher Scientific (UK), and reservoir solutions prepared at 20 mM in diH_2O.

6.2.2 Design and Manufacturing of Flow Reactors

Design and Manufacturing of Flow Reactors

The designs of the reactors used in this project were conceptualised in collaboration with D. A. Cristaldi, P. He, and X. Zhang. The detailed final design and manufacturing of the chip-based devices (Reactors 1 - 4) used in this work were solely performed by D. A. Cristaldi.[272] The coil-based reactor (Reactor 5) was designed and manufactured by T. M. Mabey.

Briefly, a computer aided design (CAD) model of the negative mould was generated and then printed by high-resolution stereolithography 3D printing. Polydimethylsiloxane (PDMS) was added to the printed mould and cured. Separately, a PDMS sheet was prepared to form the base of the reactor. After being released from the moulds, the two pieces of PDMS were bonded using coronal plasma bonding to form the finished reactor. Inlet and outlet holes were then punched into the finished device.

When fibre optics were integrated into the devices, the fibre was added to supports in the mould and aligned with the reaction channel prior to the PDMS pour. Alternatively, when fibres were added after the PDMS was cured, a small hole was made in the device using a hypodermic needle with an external diameter smaller than that of the fibre being used. The elastic nature of the PDMS was sufficient to seal the hole with the fibre inserted without the need for a sealant.

Light Sources

Depending on the reactor design and mode of operation, either a 60 mW 405 nm laser was used to illuminate samples (the same as used in Chapter 5) or low-cost UV lamps containing 4 x 9 W bulbs with emission maxima of 365 nm were used (the same as in Chapter 4). Laser light was supplied via a fibre optic and was delivered into the reactors differently depending on each design.

6.2.3 Setup and Operation of Flow Reactor

The PDMS-based flow reactors were tested in collaboration with D. A. Cristaldi with assistance from P. He. The coil reactor was tested by T. M. Mabey following technical advice from D. A. Cristaldi.

Syringe pumps (World Precision Instruments; Aladdin 1010) were used to supply *M. psychrotolerans* CFE and $AgNO_3$ via two polytetrafluoroethylene (PTFE) inlet lines (1.6 mm outer diameter (OD), 0.6 mm inner diameter (ID)). The tubing was joined to devices through direct push fit into the PDMS. The elastic properties of PDMS resulted in good seals forming with no need for additional integrated fittings or connectors. The seals were sufficient for the flow rates and pressures used throughout with no evidence of leaking observed. An outlet line of PTFE tubing was affixed to the reactor in the same way and used for sample collection. The reactors were operated in a flat orientation with the inlets and outlet in the same plane, unless otherwise stated. A general schematic of the reactor setup is shown in Figure 6.2.

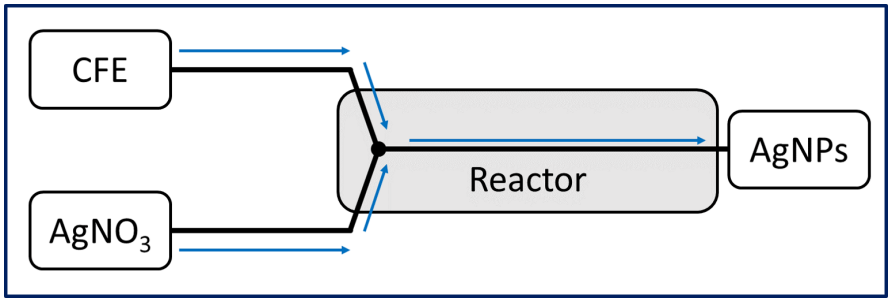

Figure 6.2: General schematic of a flow reactor setup. CFE and $AgNO_3$ is supplied by syringe pumps to the reactor via separate inlet lines. The reagents mix in the reactor and exit via an outlet. Blue arrows indicate direction of flow.

Total Flow Rate and Flow Rate Ratio

Two main flow properties were investigated when operating the reactors: total flow rate (TFR) and flow rate ratio (FRR). The total flow rate (Q; mL min^{-1}) was calculated as the sum of the inlet flow rates of the CFE

and $AgNO_3$. The flow rate of each inlet was set using calibrated syringe pumps.

$$Q = Q_{CFE} + Q_{AgNO_3} \quad \text{(Eq. 6.1)}$$

The ratio of Q_{CFE} to Q_{AgNO_3} was referred to as the FRR and adjusted to investigate the stoichiometry of AgNP production.

Residence Time

The residence time (t_r; s) of reactors was calculated for each reactor where V (mL) is the volume of the reactor where reagents are exposed to the light source (reaction channel).

$$t_r = \frac{V}{Q} \quad \text{(Eq. 6.2)}$$

6.2.4 Characterisation of AgNPs

UV-Vis spectroscopy was performed using an Avantes Starline fibre optic spectrometer (AvaSpec-ULS2048L) and a PerkinElmer Lambda 35 UV-Vis spectrometer, as described in Sections 5.2.3 & 3.2.3. TEM was performed using the method described in Section 3.2.3. Image analysis of TEM samples was performed using ImageJ, as described in Section 4.2.5.

In-line UV-Vis Spectroscopy

To monitor the output of the reactors in real-time, *in situ* monitoring was provided by in-line UV-Vis spectroscopy. A quartz flow-through cuvette with an optical path length of 1 mm was installed at the outlet of the reactor with all of the reactor output passing through the cuvette. The Avantes Starline fibre optic spectrometer was then used to perform continuous real-time spectroscopy when the reactor was operating.

6.3 Results and Discussion

Rapid laser-enhanced AgNP production in *M. psychrotolerans* cultures and CFE was achieved in Chapter 5. However, a major limitation of the method was the tendency for the AgNPs to form near the surface of the solution, at the laser spot, and absorb the 405 nm light with great efficiency. This resulted in very little

light penetrating in the to the rest of the solution. Mixing, with a magnetic mixing bead, ameliorated this by homogenising the solution and allowing unreacted reagents to be exposed to the laser. However, this process took time and meant the particles were not exposure to a uniform amount of light; this would have been exacerbated if the process was scaled up.

Flow systems offer benefits, such as rapid mixing and greater stoichiometric control, which were hoped would aid in the further enhancement of the synthesis process and advancement towards large scale production.

Low-cost and easily manufactured PDMS-PDMS bonded reactors allowed for multiple designs to be tested. Here, a series of flow reactors were developed throughout the design process (Table 6.1). Each reactor employed different design ideas to optimise the production of AgNPs. A summary of the achievements and limitations of each reactor is presented in Table 6.2 on page 140.

Table 6.1: Reactor parameters

Reactor	Design	Material	Illumination	Channel Cross Section Shape	Reaction Channel Dimensions (mm)			Channel Cross Sectional Area (mm^2)	Volume (mL)	t_r at 1 mL min^{-1} (s)
					Higher	Width	Length			
1	Laser In-line	PDMS	In-line 405 nm Laser	Rectangle	3	3	80	9	0.720	43
2	Laser Perpendicular	PDMS	Perpendicular 405 nm Laser	Rectangle	0.5	3	30	1.5	0.045	2.7
3	Heart	PDMS	405 nm Laser by Integrated FO	Rectangle	1	1	80	1	0.080	4.8
4	1 + FO	PDMS	405 nm Laser by Inserted FO	Rectangle	3	3	80	9	0.720	43.2
5	1 + UV	PDMS	UV Lamp	Rectangle	3 1	3 1	80 180	9 1	0.900	54
6	2 + UV	PDMS	UV Lamp	Rectangle	0.5	3	260	1.5	0.390	23
7	Serpentine	PDMS	UV Lamp	Square	1	1	1,000	1	1.0	60
8	Coil	PTFE	UV Lamps (2x)	Circular	1	1	20,000	0.79	15.7	942

FO: Fibre optic; PDMS: Polydimethylsiloxane; PTFE: Polytetrafluoroethylene.

6.3.1 Reactor 1

The first flow reactor designed, a schematic of which is shown in Figure 6.3 A, utilised a serpentine channel to mix CFE and $AgNO_3$ supplied from syringe pumps via two inlets. The mixed solution then entered the main reaction channel and immediately passed into the beam of a 405 nm laser which was aligned along the channel (Figure 6.3 B). The laser, supplied by a fibre optic, was flush mounted against the external wall of the device (5mm thick PDMS) with a flange adapter. Before introducing the reagents, the laser was aligned visually to maximise the amount of the beam in the reaction channel. The channel dimensions, as shown in Figure 6.4 were 1 mm x 1 mm in the serpentine mixing channel and 3 mm x 3 mm in the main reaction channel.

The principle design criterion of Reactor 1 was to flow the reagents past, and the newly formed AgNPs away from, the laser source to allow continual production. This was achieved by introducing the freshly mixed reagents into the reaction channel directly in front of the laser beam; the newly formed product was then displaced along the reaction channel towards the outlet. Having the laser aligned along the reaction channel meant that any light not initially involved in a reaction or absorbed by AgNPs was more likely to be utilised by reagents in the channel.

The reaction channel in front of the laser had a cross-section of 3 mm x 3 mm. This was larger than the 1 mm x 1 mm dimensions of the serpentine mixing channel. The larger cross-section was used to maximise the amount of light in the channel. From the source, the laser was constrained by a 1.06 mm glass fibre optic until it reached the mounted adapter. Here, the light then began to diffuse in a cone shape. The light was then diffracted and scattered as it passed through the PDMS wall of the reactor. Consequently, the beam entering the channel was larger than that immediately exiting the fibre optic. The larger channel size, therefore, allowed for this larger beam and increased the amount of usable light.

Reactor 1 was tested with a 60 mW 405 nm laser aligned with the reaction channel. Upon exposure to the laser light, the reaction mixture in the channel turned brown, indicating AgNPs were being produced, this was supported by UV-Vis spectra of samples collected at the reactor outlet (Figure 6.5). Strong absorption peaks in the region of 450 nm were observed in the spectra which indicated the presence of Ag nanospheres.[12] The change from pale yellow of the growth medium to brown of the nanoparticles only occurred when the laser was on and did not occur in the serpentine mixing channel or reagent inlet lines; this colour change can be seen in Figures 6.3 B and 6.5. This colour-change was maintained as the reactor was operated demonstrating continuous flow production was achieved. The intensities of the LSPR peaks indicated higher production was observed at the lowest TFR (Figure 6.5 A & B), which is to be expected due to the longer t_r experienced at lower flow rates. However, with time, the intensity of the LSPR peaks

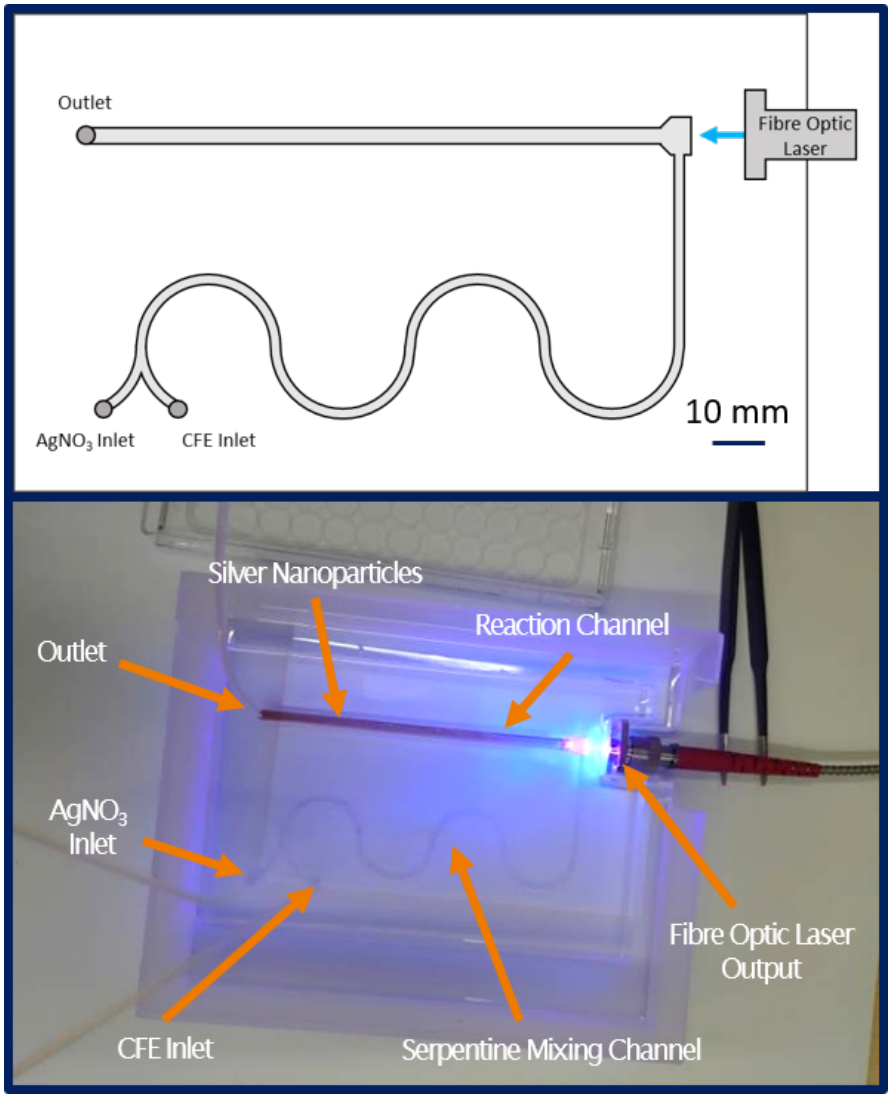

Figure 6.3: Schematic (A) and photograph (B) of Reactor 1 design. Two inlets supplied $AgNO_3$ and CFE. Mixing was increased through a serpentine section before the solutions entered the main reaction channel. A laser is aligned down the length of the main channel. Sample collection occurred via the outlet at the end of the main channel.

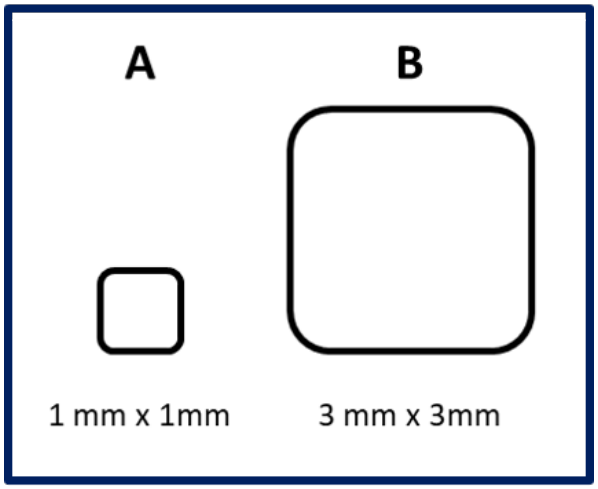

Figure 6.4: Reactor 1 channel cross sections. The mixing channel had a square cross section of 1 mm x 1mm and a length of 180 mm (A). The reaction channel had a larger square cross section of 3 mm x 3 mm and a length of 80 mm (B).

in samples collected decreased indicating lower concentrations of AgNPs were being produced.

It was observed that at the junction between the mixing channel and the reaction channel, immediately in front of the laser, gas bubbles had become trapped (Figure 6.6 C). Dislodging these bubbles proved challenging and neither adjustments to the TFR or massaging the reactor were effective in their removal. These bubbles were thought to have been introduced during the preparation and setup of the reactor, rather than generated by the reagents. Moreover, when the reaction was stopped and the reactor flushed with diH_2O, considerable discolouration of the normally clear PDMS device was observed (Figure 6.6 A & B). A brown residue was seen in the reaction channel.

The discolouration in the channel appeared to be most sever nearest the beginning of the reaction channel where the laser light was introduced. At this location, the intensity of light was the greatest and the concentrations of the reagents was highest. No similar staining was observed when previously prepared AgNPs were put in contact with PDMS. This suggests the particles are more susceptible to becoming associated with the PDMS surface during the synthesis process. The exact explanation for this remains to be fully understood. However, it may be due to either the roughness of the PDMS surface.[272] If unreacted Ag^+ ions became located in imperfections, such as crevasses, in the PDMS surface before being reduced and undergoing nucleation, the crystals may have grown too large to be easily removed from the PDMS simply by the flow of liquid (visualised in Figure 6.7). Further investigation, for example by scanning electron microscopy, is required to understand this observation. Another factor which may contribute to the coating of the channels is the electrostatic interactions of the nanoparticles and the channel walls. During the synthesis of Au nanoparticles, similar fouling was reported by Huang on PTFE tubing.[273] The mechanism

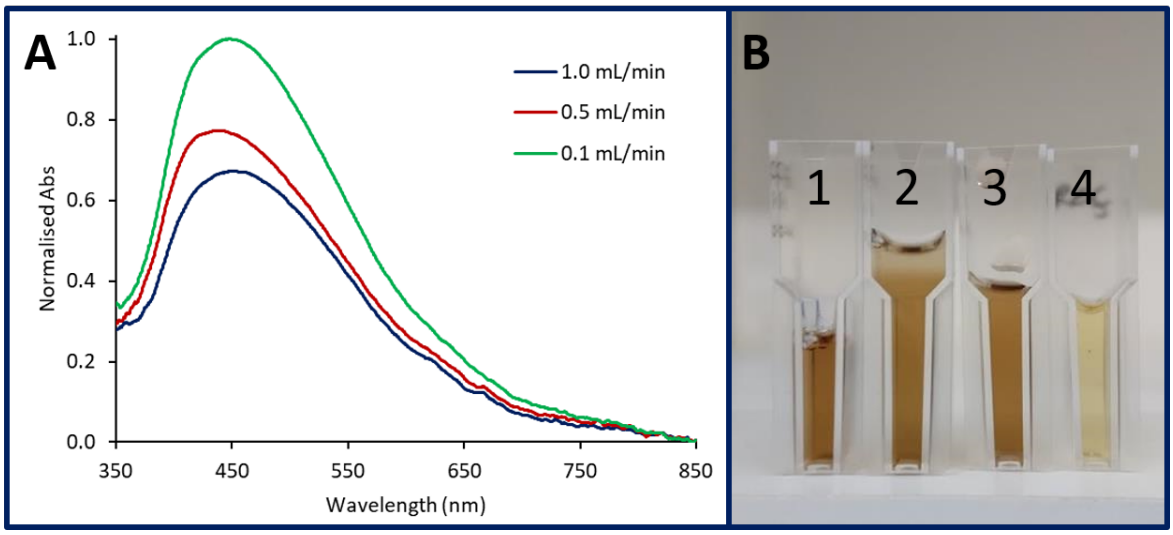

Figure 6.5: (A) UV-Vis spectra of AgNPs produced in Reactor 1 under different TFRs. (B) Photograph of crude AgNP samples from Reactor 1 produced at 1.0 mL min^{-1} (1), 0.5 mL min^{-1} (2), 0.1 mL min^{-1} (3), and unreacted CFE and $AgNO_3$ used as a reference (4).

was suggested to be electrostatic interactions between the negatively charged walls of the tubing and the positive citrate-Au precursors used in the synthesis. Further investigation, with particularly focus on the electrostatic interactions of the coatings of the AgNPs and the channel, is required to fully understand the cause of the fouling in the reactor used here.

The deposition of AgNPs on the walls of the channel is thought to have contributed to the decrease in reactor efficiency over a relatively short runtime. This is because the absorption peak of the AgNPs was broad and overlapped with the 405 nm laser light. This results in the absorption of much of the laser light before it can be used in the photochemical reaction, a key reason for opting for flow over batch reactions. Additionally, the difference in the channel dimensions between the mixing and reaction channels, particularly the height, led to a dead volume (a section of the channel with little or no flow velocity). The sharp step up from a 1 mm channel height to 3 mm meant that gas bubble present in the system would accumulate in the dead volume and become trapped, unaffected by the flow of the liquid below. These bubbles then caused increased diffraction and loss of light out of the reaction channel before it could be utilised.

Three possible solutions were discussed to resolve this. First, the device could be operated in a different orientation, such that the reactor outlet was the highest point in the reactor meaning the bubbles would be expelled. Alternatively, removing the step in the channel height to remove the dead volume and prevent the accumulation. Third, the channel could have been coated, for example with a hydrophobic silane, to reduce the interaction between the walls of the channel and the reagents. When considered in combination

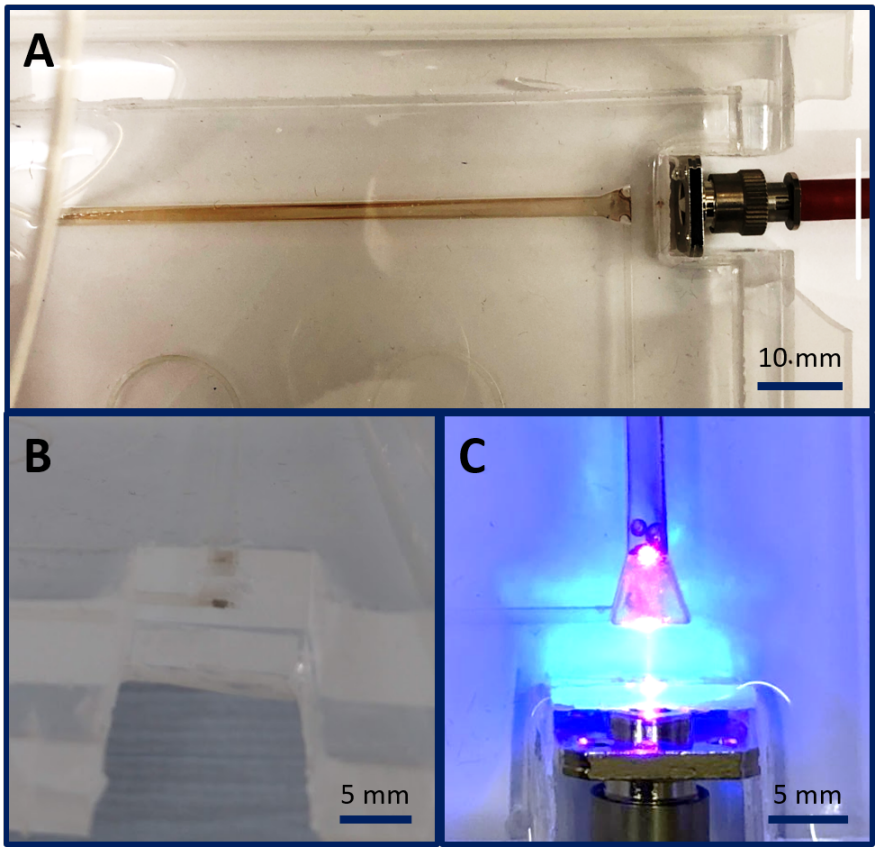

Figure 6.6: Fouling of Reactor 1 after use. AgNPs were deposited on the channel walls of Reactor 1 after use, as indicated by the dark brown discolouration (A). AgNPs still remained at the laser spot location after washing with 30% H_2O_2 (B). Bubbles were trapped at the beginning of the reaction channel (C). Photo Credits: (A and C) D. A. Cristaldi

with other desired design modifications, a reactor with a consistent single channel height was chosen.

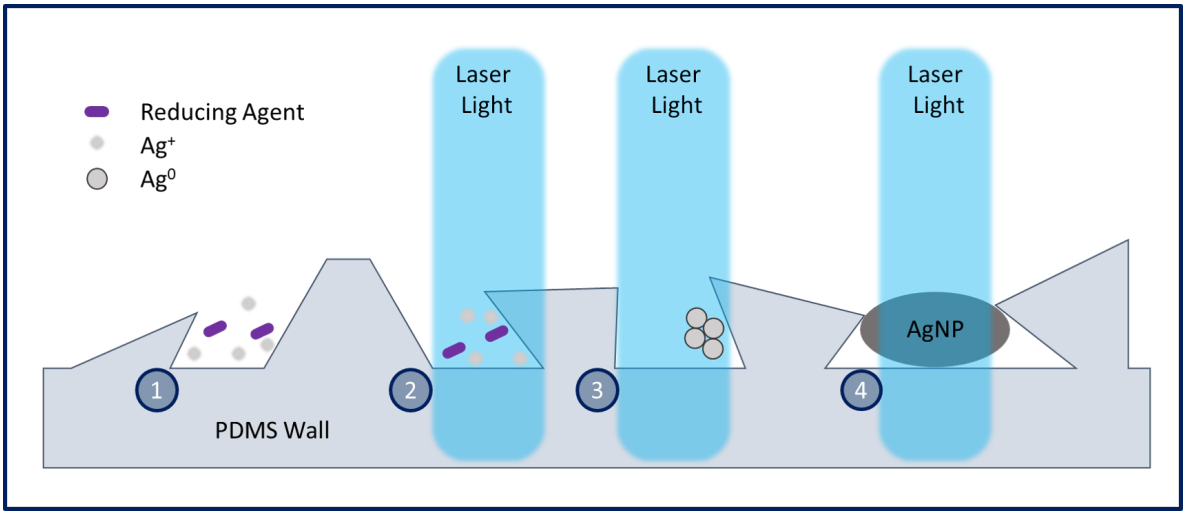

Figure 6.7: Possible mechanism for AgNP deposition on PDMS reactor walls. The reducing agent and Ag^+ ions entered small imperfections in the surface of the PDMS (1). These reagents were then exposed to the laser light and the photo-driven reduction of the Ag^+ occurred to form atoms (2) which underwent nucleation (3). Further reduction occurred and the newly formed AgNP grew and became trapped in the PDMS.

6.3.2 Reactor 2

The design of Reactor 2 was similar to the first but with two key differences; a schematic of Reactor 2 is shown in Figure 6.8. First, the channel dimensions were consistent throughout the whole device being 0.5 mm x 3.0 mm (H x W). This resolved the issue of bubbles becoming trapped in the dead volume where the channel height changed abruptly from 1 mm to 3 mm in Reactor 1. Second, the laser light was delivered in a different way. A lens was used to generate a line of light rather than a spot when interacting with the reactor. This meant reaction channel could be illuminated perpendicular to the flow, that is, from the top of the device.

This reduced absorption of the light by AgNPs allowing for a greater surface area for the photochemical reaction to occur. An additional benefit of this was the removal for the need of an orthogonal surface for the laser inlet to be designed into the plane of the device, creating a sharp 90°angle in the channel which further contributed to the uneven flow characteristics and the dead volume in Reactor 1. To facilitate this method of illumination through the lens, the reactor was operated on its side due to the constraints of the optics apparatus used (Figure 6.8 B).

While AgNPs were produced in Reactor 2, the method of delivering the light proved to be inefficient and gave low yields of AgNPs. The UV-Vis spectra showed the characteristic absorbance peak between

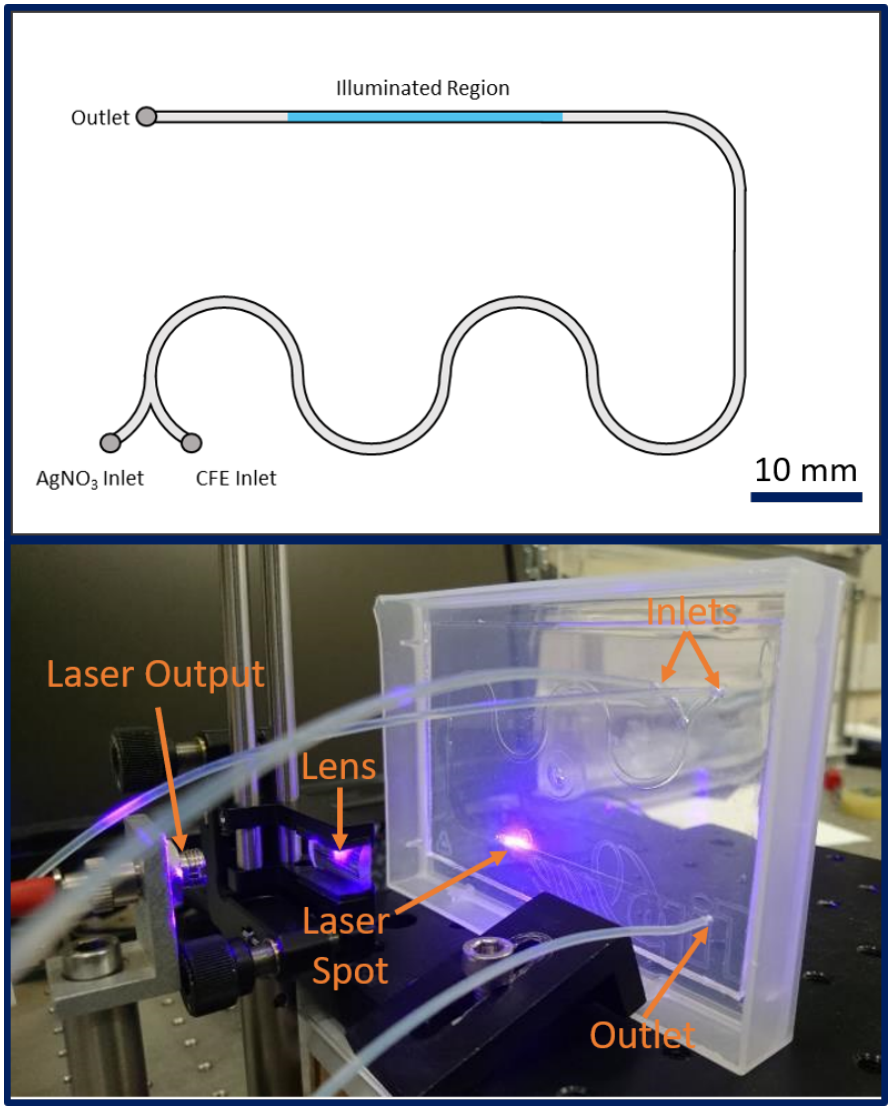

Figure 6.8: Schematic (A) and photograph (B) of the Reactor 2 design. The 90°turn at the beginning of the reaction channel in Reactor 1 was replace with a smooth curve. The laser was introduced perpendicular to the channel via a lens to increase the spot size along the channel length. The laser spot was estimated to be 10 mm x 3 mm and was adjustable by moving the lens.

400 nm and 450 nm, indicating Ag nanospheres were present. However, substantial production was not observed at TFR other than 0.01 mL min^{-1} (Figure 6.9 A). AgNP production was detected at 0.1 mL min^{-1}, but at a much lower amount. The particles produced gave a UV-Vis spectrum comparable in shape and position to those produced at 0.01 mL min^{-1}, suggesting the flow rate did not yield considerable difference in the shape and sizes of the particles produced (Figure 6.9).

The production efficiency of Reactor 2 was clearly inferior to Reactor 1. By changing from a laser spot in-line to the reaction channel to a perpendicular one, the area of the channel being illuminated was increased. However, the photon density was reduced as it was spread over this larger area. It was hoped that this reduction would be offset by the reduced effects of the absorption by the AgNPs as they formed, allowing for more production to occur; this was not the case. Compounding this decreased intensity, the photons which did not interact with reagents or AgNPs exited through the back of the reaction channel and were lost. In Reactor 1, due to the in-line delivery of the light, any photons that did not immediately interact travelled down the reaction channel giving more opportunities to be utilised. Improvements in performance could be made by adding a reflective backing to reactor to direct unused photons back to the channel. This was not tried and instead, returning to an in-line alignment was preferred.

6.3.3 Reactor 3

The photon efficiency of the setup used in Reactor 2 was poor. To ameliorate this, a fibre optic that could deliver the laser light as close as possible to the reagents and to a concentrated area was integrated into a new reactor.

Reactor 3, as shown in Figure 6.10 A & B, employed a serpentine mixing section (1 mm square), similar to Reactors 1 and 2, before the channel split in two (0.5 mm square). The two channels looped round to re-join in front of the fibre optic before continuing as a single channel (1 mm square) to the outlet, in-line with the laser.

The fibre optic required a perpendicular surface through which to shine to minimise the diffraction and loss of light. Without a 90°angle in the channel, like in Reactor 1, this cannot be easily achieved. However, the introduction of a 90°angle in the channel results in disrupted flow and a dead volume with reduced flow. The rationale behind the heart-shaped design was to allow the fibre optic to be aligned parallel with the reaction channel while minimising the dead volume. Though computational fluid dynamic (CFD) modelling is required to confirm this, it was hoped that by having symmetrical flow from both inlets either side of the fibre optic, the volume could be reduced, and with it, particle accumulation and coating of the walls.

The design also allowed for the fibre optic to be installed very close to the reaction channel (wall

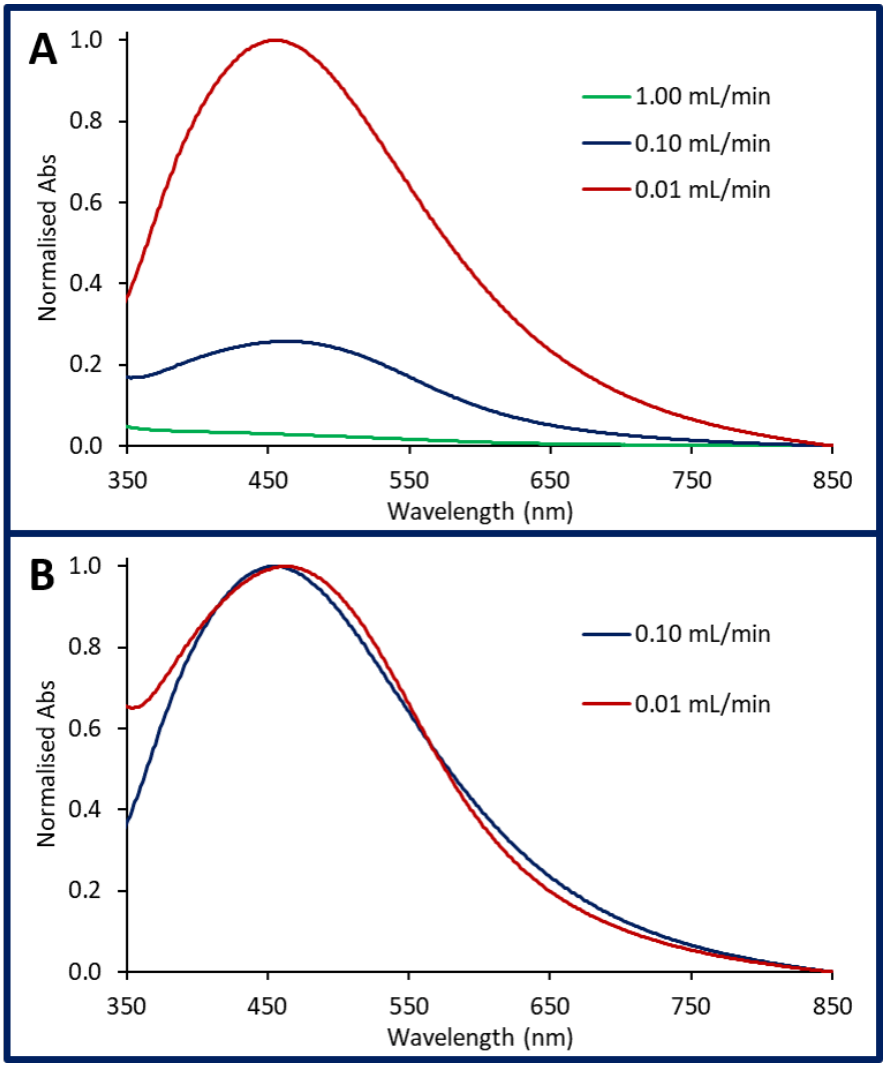

Figure 6.9: UV-Vis spectra of AgNPs produced in Reactor 2 at different TFRs (A). Comparison of normalised UV-Vis spectra of AgNPs produced in Reactor 2 at 0.1 mL min^{-1} and 0.01 mL min^{-1} (B)

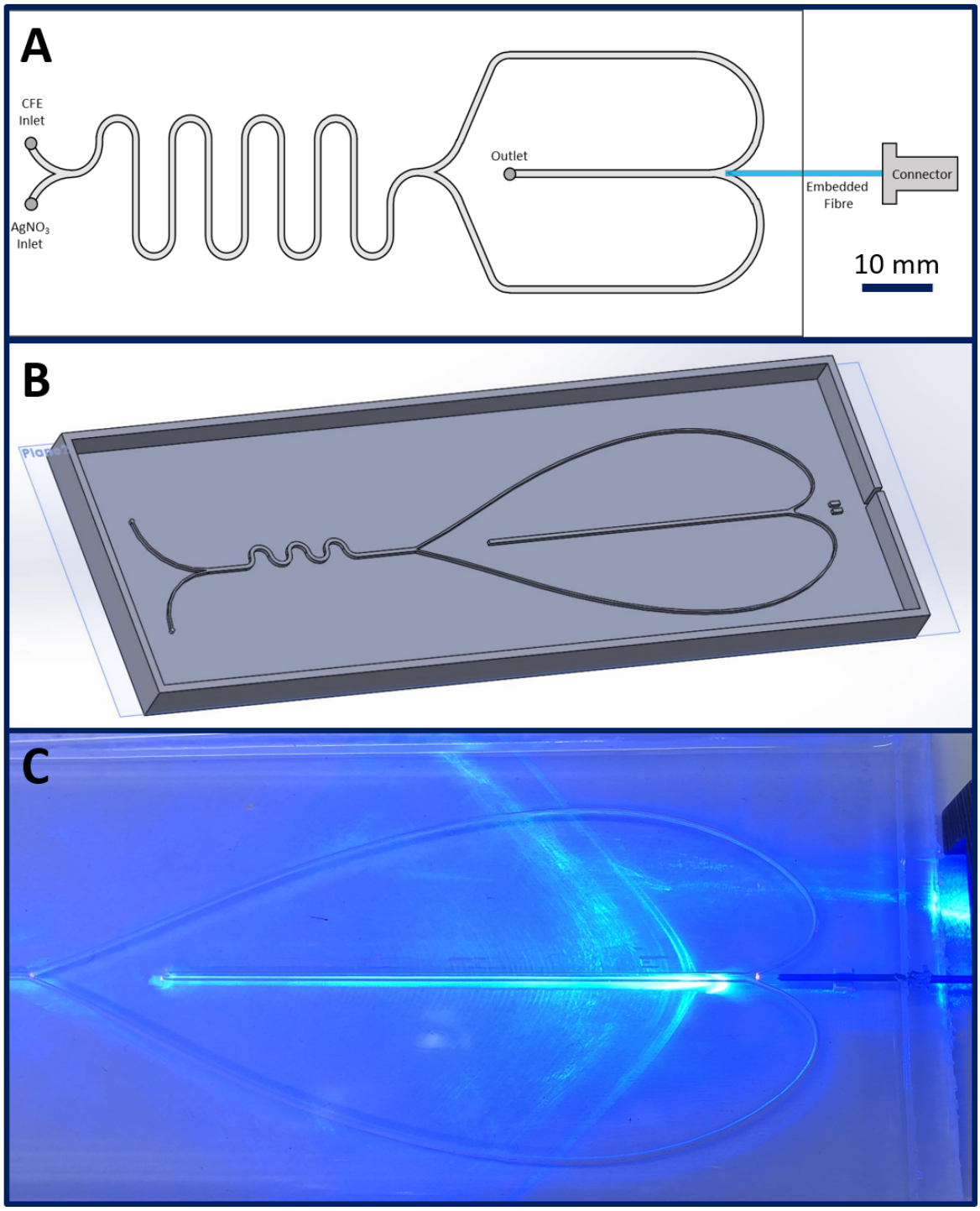

Figure 6.10: "Heart" design of Reactor 3. An initial design schematic of Reactor 3 with integrated fibre optic (A). As the laser was delivered to the channel by a fibre optic, the laser spot size was estimated to be very similar in size to the 1.06 mm fibre at the interface with the channel. CAD model used for 3D printing the mould into which the PDMS reactor was prepared (B); image kindly provided by D. A. Cristaldi. Photograph of Reactor 3 with 405 nm laser delivered by integrated fibre optic (C).

thickness < 1 mm) to reduced scattering by the PDMS, while having sufficient PDMS material to enable the successful bonding of the two halves of the reactor during manufacturing.

When operated, the reactor produced spherical AgNP with a λ_{max} of at 414 nm at 1 mL min^{-1} (Figure 6.11). However, the duration of operation was very short as particles, once again, accumulated in front of the laser beam inlet and led to reduce efficiency. This suggests that either the dead volume in front of the fibre optic was not sufficiently reduced, or that the accumulation on the surface of the channels cannot be resolved exclusively by flow optimisation. Instead, reactor material and channel coatings could be used to prevent the AgNP staining the device. The substantial reduction in efficiency over time made reliable spectroscopic measurements challenging and so should be interpreted cautiously.

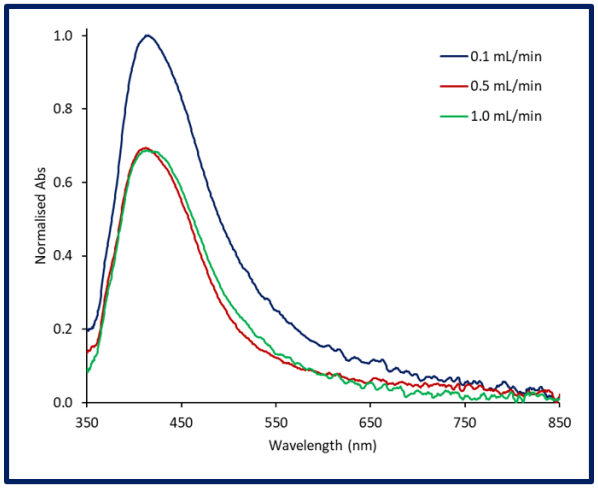

Figure 6.11: UV-Vis spectra of AgNPs produced in Reactor 3 at 0.1 mL min^{-1}, 0.5 mL min^{-1}, and 1.0 mL min^{-1}.

To explore how the PDMS of the channel walls was affecting the reactor fouling, (dodecyloxy)trimethylsilane was coated onto glass slides and the ends of polished glass fibres to test its effectiveness. Coated glass was observed to have reduced particle accumulation when AgNPs were dried onto the surface. Likewise, when fibre optics were submerged in reaction mixtures and used to produced AgNPs, the coated fibres performed better than non-coated. However, this enhanced performance was short lived and AgNP deposition on the surface of the fibres was observed after 1 min of illumination, as seen by a discolouration of the polished fibre end (Figure 6.12). Other surface coatings, such as hydrophilic or hydrophobic coatings, were not investigated and would be useful avenues for future work. Super hydrophobic surface coatings, for instance highly fluorinated silanes, or conversely, hydrophilic coatings such as polyimides or cyano-terminated silanes would be of particular interest.

Reactor 3 incorporated interesting design elements but was ultimately hindered in its performance by

the inability to illuminate a larger area of reagents for a sustained period of time. It was therefore decided to change to a different method of supplying light to the reagents.

To further investigate the effects of having the fibre optic deliver the light closer to the reagents, a hole was punched through the wall of Reactor 1 at the location where the laser was previously mounted on the external wall. An uncoated fibre optic was then inserted through the reactor wall directly into the reaction channel (Figure 6.12). The reactor (Reactor 1-FO) was then operated at 0.1 mL min^{-1} and the AgNPs collected for spectroscopy. The LSPR peak at 450 nm was present which suggested AgNPs were forming. However, production was very short lived as the end of the glass fibre rapidly became coated in particles within seconds of operating. The accumulation and coating of the fibre continued until the production efficiency appeared to be reduced and the reagent solution was undergoing only a very weak colour change to pale brown.

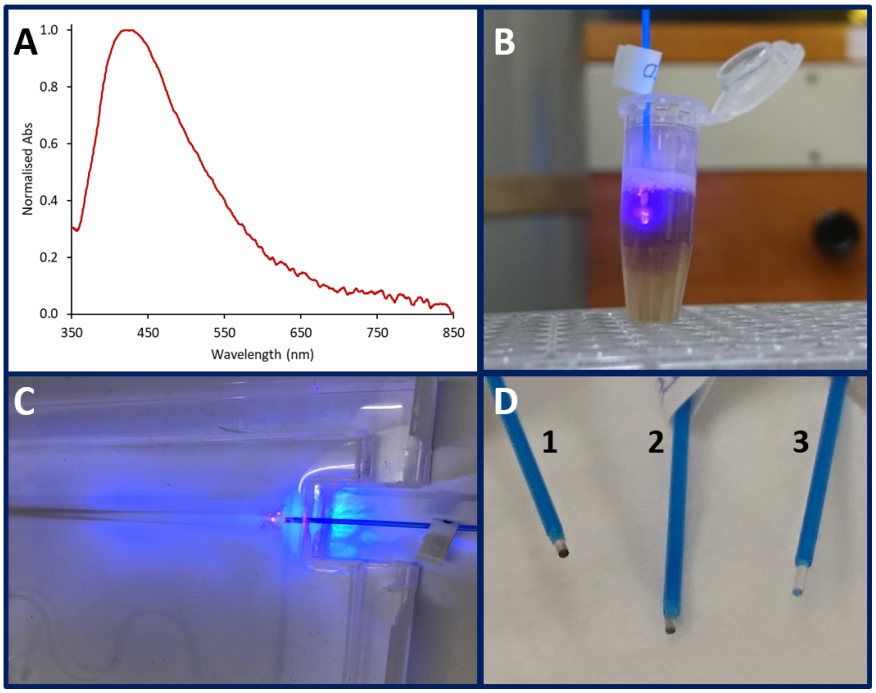

Figure 6.12: UV-Vis spectra of AgNPs produced in Reactor 1 with fibre optic (Reactor 1-FO) inserted into reaction channel to deliver 405 nm laser light (A). Test of laser-driven AgNP production in CFE with uncoated fibre optic (B). Fibre optic inserted in to the reaction channel of Reactor 1 delivering 405 nm laser light directly into the reaction solution (C). Photograph of the ends of glass fibre optics (D): uncoated glass fibre optic after AgNP production (1), and (dodecyloxy)trimethylsilane coated glass fibre optics after (300 s illumination) (2) and before (3) AgNP production.

6.3.4 Reactors 1 & 2 with UV Lamp

It was evident from the first 3 reactors that delivering sufficient light to the reaction via a laser was challenging. To overcome this, Reactor 1 was placed under a UV lamp such that the whole device was illuminated (Reactor 1-UV). The delivery of $AgNO_3$ and CFE remained the same, but the amount of AgNPs production was considerably greater than when the laser was used. The product was a very dark brown and when run at 0.1 mL min^{-1} became almost black. UV-Vis spectra of AgNPs produced at 1.0 mL min^{-1} and 0.1 mL min^{-1} indicated the presence of spherical particles (Figure 6.13).

Reactor 2 had a wider and shallower channel cross section (0.5 mm x 3 mm; H x W) than Reactor 1. The top-viewed surface area was therefore larger than that of Reactor 1 with the same total channel length. The shallower channel also reduced the amount of reagent material through which the light must have penetrated to be utilised. For these reasons, Reactor 2 was also operated under UV lamps (Reactor 2-UV). As shown in Figure 6.14, the characteristic LSPR band of Ag nanospheres was present with increasing intensity at lower flow rates, supporting all previous reactors.

When the product of Reactor 2-UV was imaged using TEM, the particles were observed to be spherical and quasi-spherical in morphology. The particles did not appear to differ considerably in appearance between those produced at 1 mL min and 0.1 mL min (Figure 6.15 A & C). Under a TFR of 1 mL min, very small particles were observed alongside a majority of larger particles (Figure 6.15 B). Additionally, at a slower TFR (0.1 mL min^{-1} vs 1.0 mL min^{-1}) clusters of AgNPs were observed. Approximately 100 nm in diameter, these clusters were quasi-spherical and distributed throughout the samples (6.15 C & D). The surfaces of the clusters were rough with the morphologies of the constituent AgNPs being visible in many cases. It was unclear from these observations whether the nanoparticles were simply in close proximity to one another, or if they had undergone coalescence at the crystal level to form a single larger particle.

This mode of light delivery showed great promise for improving the yield of AgNP production from a reactor and the UV lamp was chosen for future reactors. Now considerable AgNP production could be achieved under flow conditions, work focused on scaling the production up to a more viable level. To operate at a larger scale, the channel needed to be longer to allow for higher TFRs while maintaining the t_r.

6.3.5 Reactor 4

The smooth corners of Reactor 2 and Reactor 3 were useful at maintaining even flow through the reactors and the avoidance of dead volumes where bubbles and AgNPs could accumulate and deposit. Additionally, an increased duration of light exposure, through the use of a longer channel, was required to further

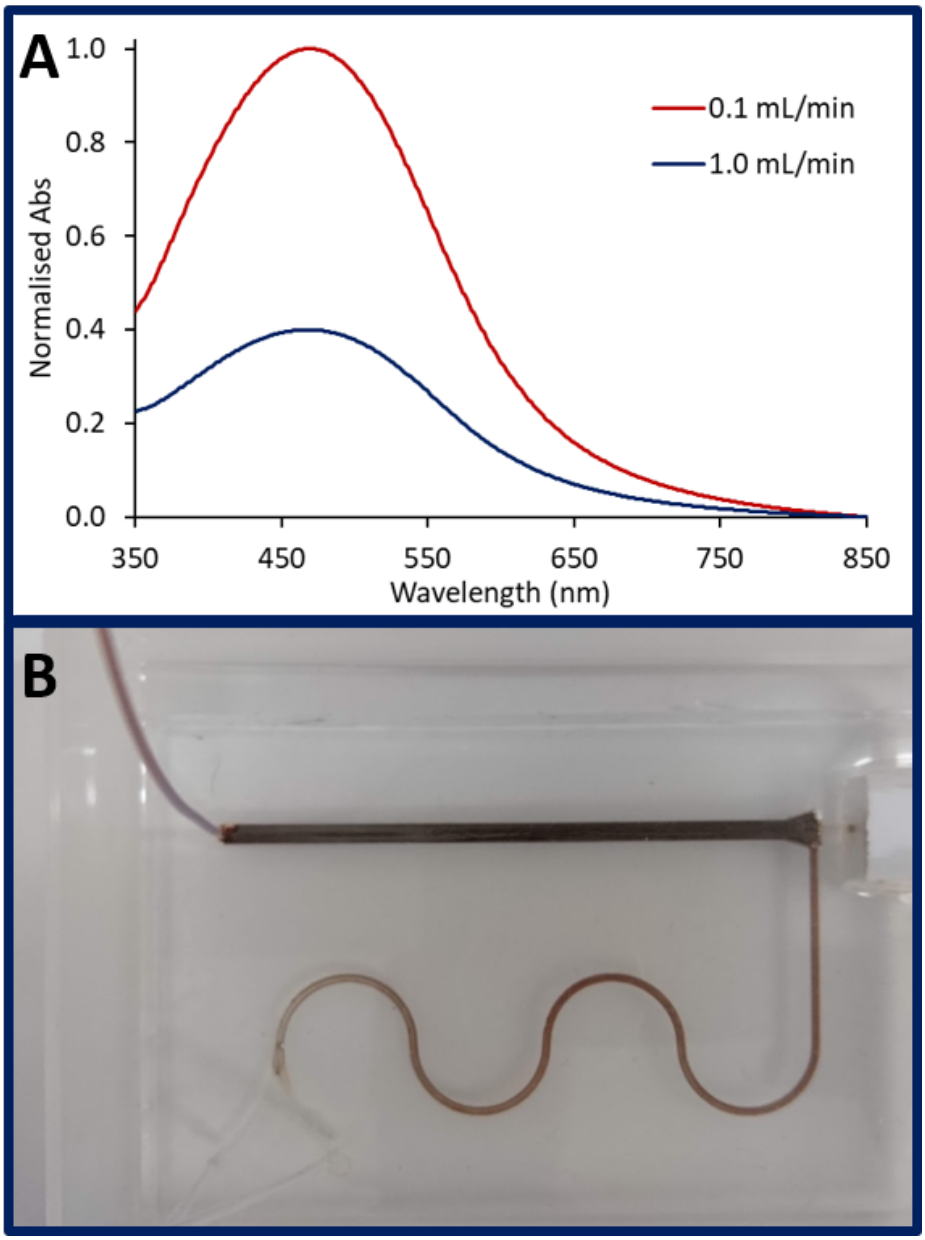

Figure 6.13: UV-Vis spectra of AgNPs produced in Reactor 1 under a UV lamp (Reactor 1-UV) at 0.1 mL min^{-1} and 1.0 mL min^{-1} (A) and a FRR of 1:1. Photograph of Reactor 1-UV after AgNP production under UV lamp (B).

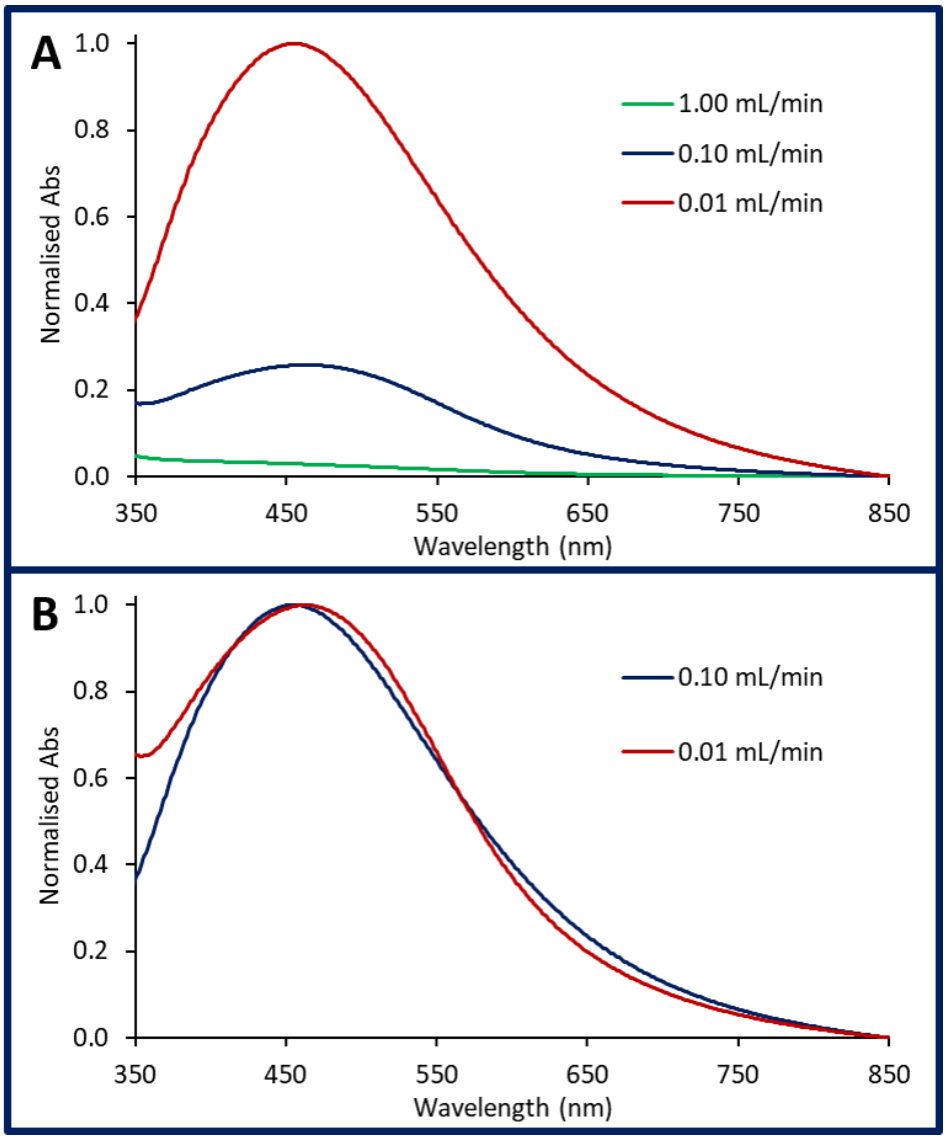

Figure 6.14: UV-Vis spectra of AgNPs produced in Reactor 2 under a UV lamp with different TFRs normalised across samples (A), and within samples (B). A FRR of 1:1 was used for all samples.

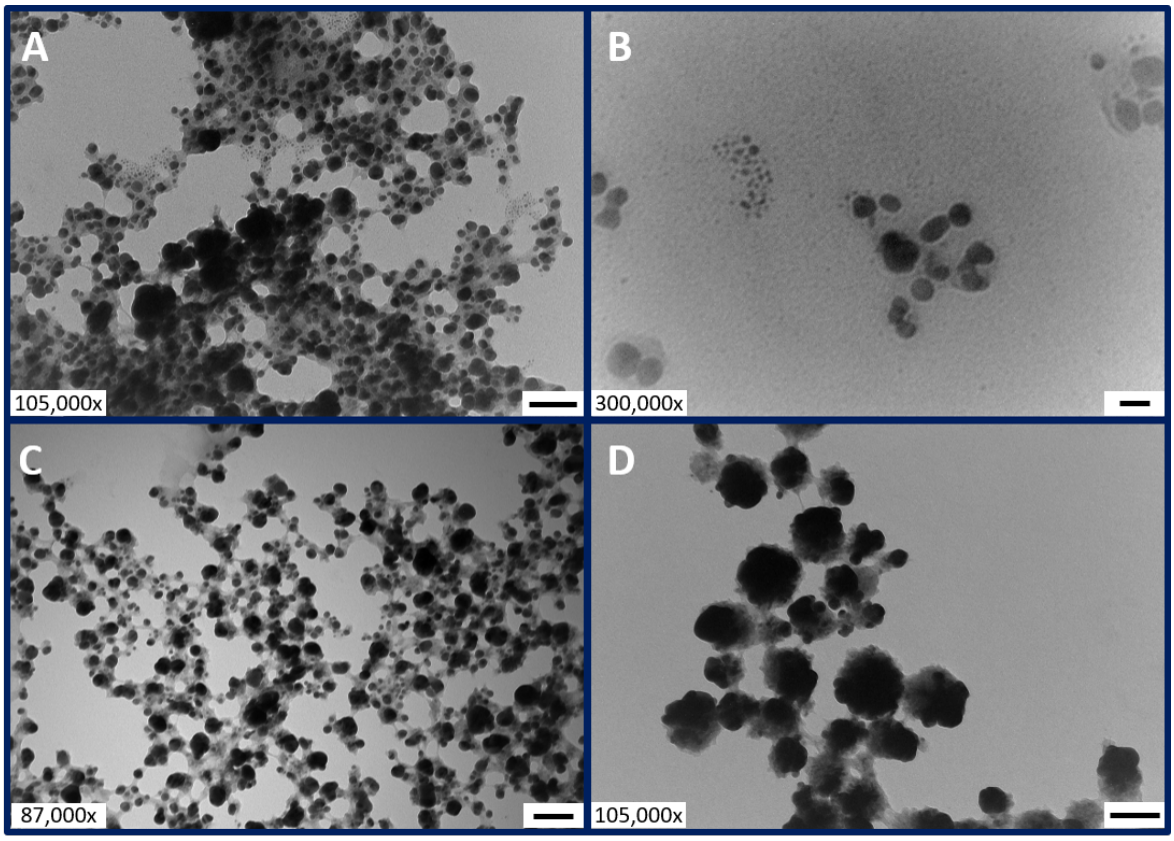

Figure 6.15: TEM images of AgNPs produced in Reactor 2 with TFRs of 1.0 mL min^{-1} (A & B) and 0.1 mL min^{-1} (C & D). A FRR of 1:1 was used for all samples. Scale bars: 100 nm (A), 20 nm (B), 100 nm (C), 100 nm (D).

improve the performance of the reactors. For this, a 1 m long channel comprising exclusively of serpentine curves was used. Initially developed by D. A Cristaldi to improve mixing in the chemical synthesis of Ag nanoprisms, this reactor was also a PDMS-PDMS device with a constant 1 mm x 1 mm square channel cross-section. As with the previous reactor, 2 inlets supplied CFE and $AgNO_3$.

The reactor was operated under a UV lamp at TFRs of 1.0 mL min^{-1}, 0.5 mL min^{-1}, 0.1 mL min^{-1}, and 0.01 mL min^{-1}. The UV-Vis spectra showed, in agreement with the previous reactors, that lower flow rates resulted in increased AgNP production (Figure 6.16 A & B). The spectra indicated Ag nanospheres had been formed with no marked differences in LSPR peak positions or the formation of additional spectra features at different TFRs.

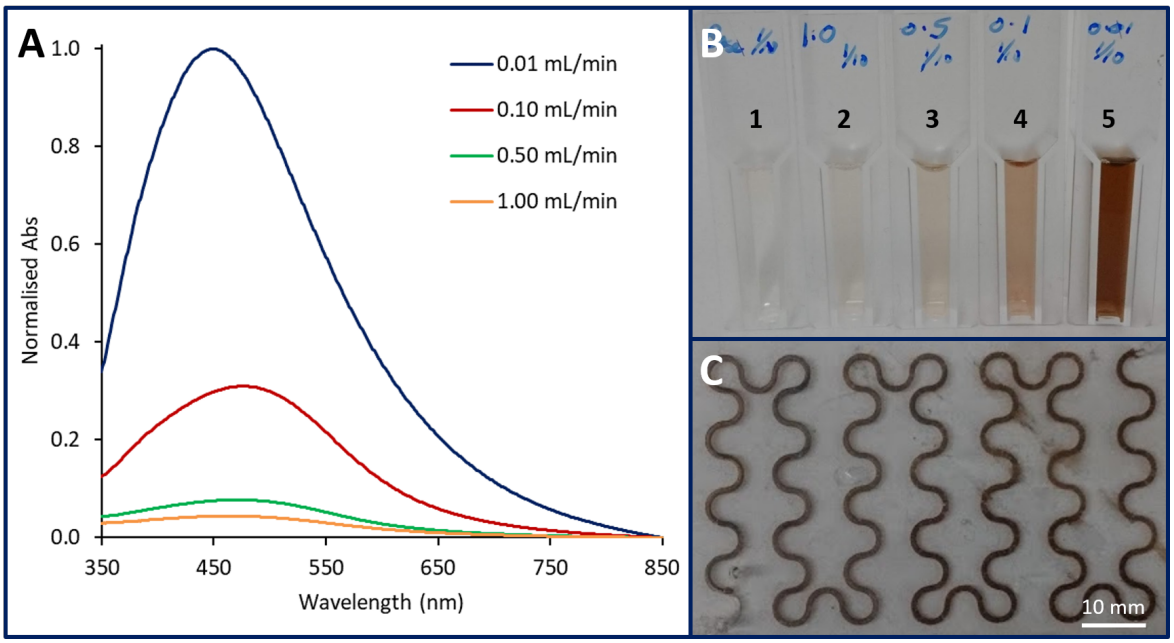

Figure 6.16: UV-Vis spectra of AgNPs produced in Reactor 4 (curved serpentine) with different TFRs (A) and a photograph of diluted samples sued for UV-Vis spectroscopy (B). Unreacted reference sample (1) and samples prepared at 1.0 mL min^{-1} (2), 0.5 mL min^{-1} (3), 0.1 mL min^{-1} (4), and 0.01 mL min^{-1} (5) were diluted 1 in 10 with diH_2O. After the reactor was washed with H_2O, AgNP deposition was observed on the channel walls (C).

As with the Reactor 1 and 2 operated under a UV lamp, substantial discolouration occurred on the walls of the channel throughout the reactor (Figure 6.16). The staining was observed very close to the two inlets which suggests mixing of the two reagents occurred rapidly on entry into the device, though CFD modelling is required to confirm this. The larger channel surface area through which light could enter, compared to the small spot when using lasers, meant that the decrease in production was not as fast and detrimental to the use of the reactor.

The increased channel length was a promising development, but the challenges posed by AgNP deposition onto the PDMS persisted. To resolve this, a new material out of which the reactor could be manufactured was required.

6.3.6 Reactor 5

Reactor 5 brought together design elements from the previous iterations to create a larger scale device capable of operating at higher TFRs. The reactor was comprised of 20 m of PTFE tubing in two 10 m coils. Each coil was formed on a reflective backed support and placed under a UV lamp (Figure 6.17). With an internal diameter of 1 mm, the total volume of the reactor exposed to the lamps was 15.7 mL (assuming complete penetration of light through the liquid depth), substantially larger than the previous designs. The use of coils removed sharp angles in the channels which could disrupt flow, and the chemical resistance and "non-stick" properties of PTFE were hoped would prevent or reduce AgNP deposition observed in PDMS.

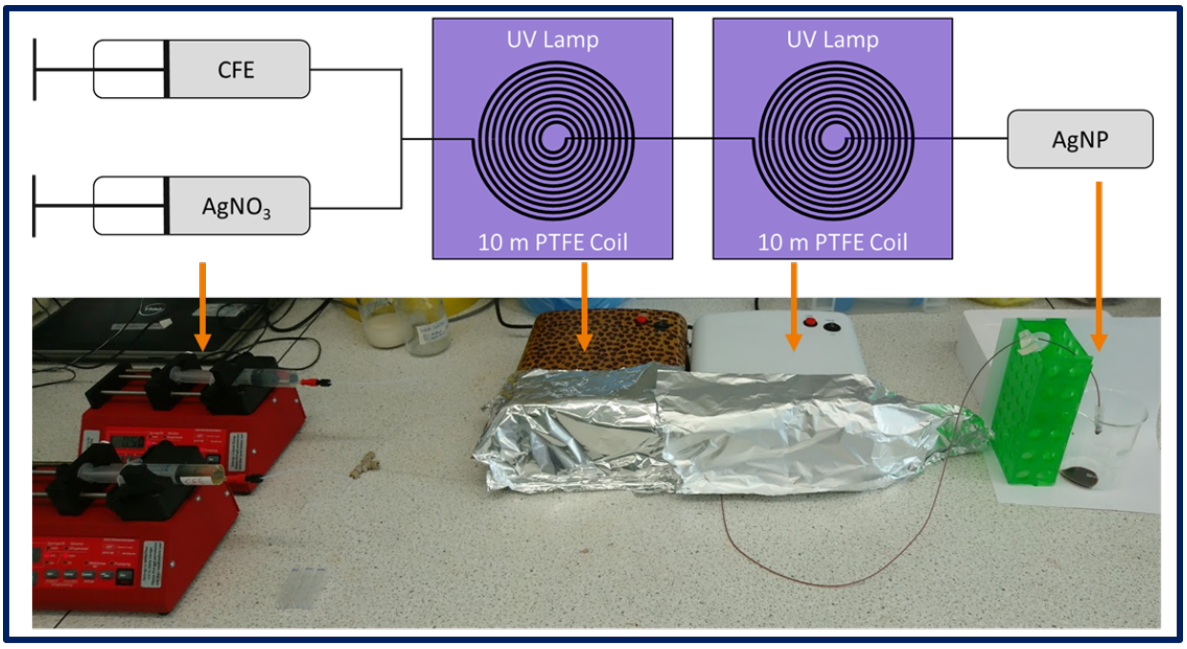

Figure 6.17: Design schematic of Reactor 5 (Coil Reactor), and photograph of corresponding apparatus below. $AgNO_3$ and CFE was supplied by syringe pumps to a T-mixer. The mixed reagents entered 2 x 10 m flat coils of PTFE tubing under UV lamps. The crude AgNP product was collected at the outlet

The outer diameter of the tubing was 1.6 mm, giving a wall thickness of 0.3 mm. A thin wall thickness was desired as PTFE has a milky-white translucent appearance due to its tendency to scatter visible light. In thin layers, PTFE has low absorbance to visible and UV light down to 200 nm. While not ideal, the optical

properties of PTFE were acceptable due to the other attractive properties of PTFE.

Initial tests showed considerable AgNP production with a very dark crude product collected (Figure 6.18 D). To determine the optimal operating conditions for Reactor 5, TFRs of 1.0 mL min^{-1}, 5 mL min^{-1}, 10 mL min^{-1}, and 20 mL min^{-1} were investigated at a FRR of 1:1. As with previous designs, the slowest flow rate (1.0 mL min^{-1}) produced the most AgNPs, as determined by the greatest LSPR peak intensity when analysed by UV-Vis spectroscopy (Figure 6.18 A & C). Production decreased with increasing flow rates, though the peak shapes did not change considerably. However, the positions of the peaks were distinctly different with 1.0 mL min^{-1} and 5 mL min^{-1} having λ_{max} of approximately 470 nm while 10 mL min^{-1} and 20 mL min^{-1} were located at 455 nm, suggesting that while the shapes of the nanoparticles produced did not differ substantially, the particles produced at lower flow rates were likely larger.

AgNPs produced at TFRs of 1 mL min^{-1}, 5 mL min^{-1}, and 10 mL min^{-1} were imaged by TEM (Figure 6.19). All of the particles observed had spherical or quasi-spherical morphologies. The mean diameters of the particles were 15.8 $\pm$ 16.9 nm, 13.2 $\pm$ 5.0 nm, and 6.7 $\pm$ 3.1 nm for 1 mL min^{-1}, 5 mL min^{-1}, and 10 mL min^{-1}, respectively (Figure 6.20). It is clear that the higher the flow rate, the narrower the distribution of nanoparticle sizes. Interestingly, clusters of particles, similar to those observed in Reactor 2 under a UV lamp, were observed at a flow rate of 1 mL min^{-1} supporting the general understanding that a longer t_r exposed to UV light may contribute to particle coalescence (Figure 6.19 B).

Shoulders can be seen in the histograms of both the 5 mL min^{-1} and 10 mL min^{-1} data. One possibility is that multiple populations of different sized particles exist in the samples, but because the size difference between the populations is too small to resolve as separate peaks, shoulders form. Additionally, they may be due to a measurement error. The ellipses used to measure the size of the particles were drawn by hand in ImageJ software. Therefore, there is an opportunity for human error or bias to introduce these features. To minimise these effects, a large number ($n => 3,000$) of particles were measured across multiple fields of view for each sample. Alternatively, they may be caused by the KDE used to produce the graph. KDE estimates the probability density at, in this case, a given particle size. While a histogram uses the absolute values from a bin, KDE approximates across a continuum allowing for a closer approximation of data from a continual scale (e.g. particle size in nm). As a result there is a compromise between the discrete absolute bins of a histogram and the continuous nature of KDE. More extensive TEM imaging to increase the total number of particle analysed and the development and use of an automated image analysis method to remove human error and subjectivity may benefit in resolving this.

To further optimise production in the reactor, FRRs of 1:10, 1:5, 1:2, 1:1, 2:1, 5:1, 10:1 ($AgNO_3$:CFE) were investigated. As shown in Figure 6.21 A, all of the UV-Vis spectra have similar shapes but have

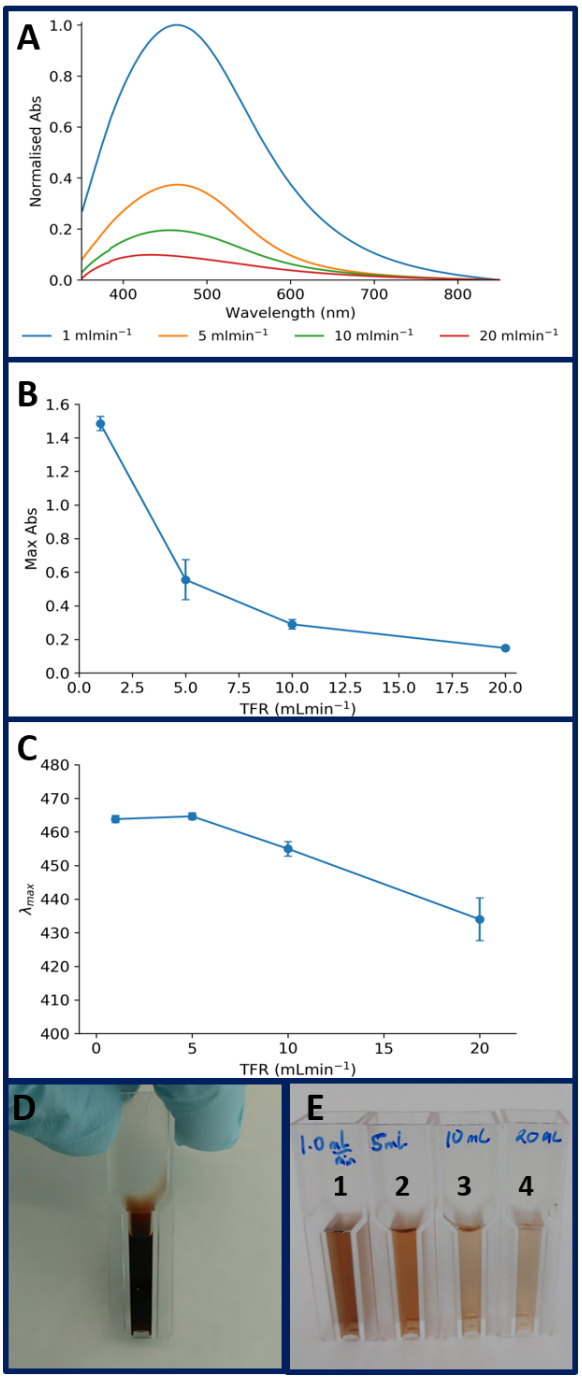

Figure 6.18: UV-Vis spectra of AgNPs produced in Reactor 5 (coil) under different TFRs (A) with the intensities (B) and positions (C) of the LSPR peaks. Photographs of neat crude (D) and diluted (1 in 10) AgNPs (E), as prepared for UV-Vis spectroscopy at 1.0 mL min^{-1}, 5 mL min^{-1}, 10 mL min^{-1}, and 20 mL min^{-1}.

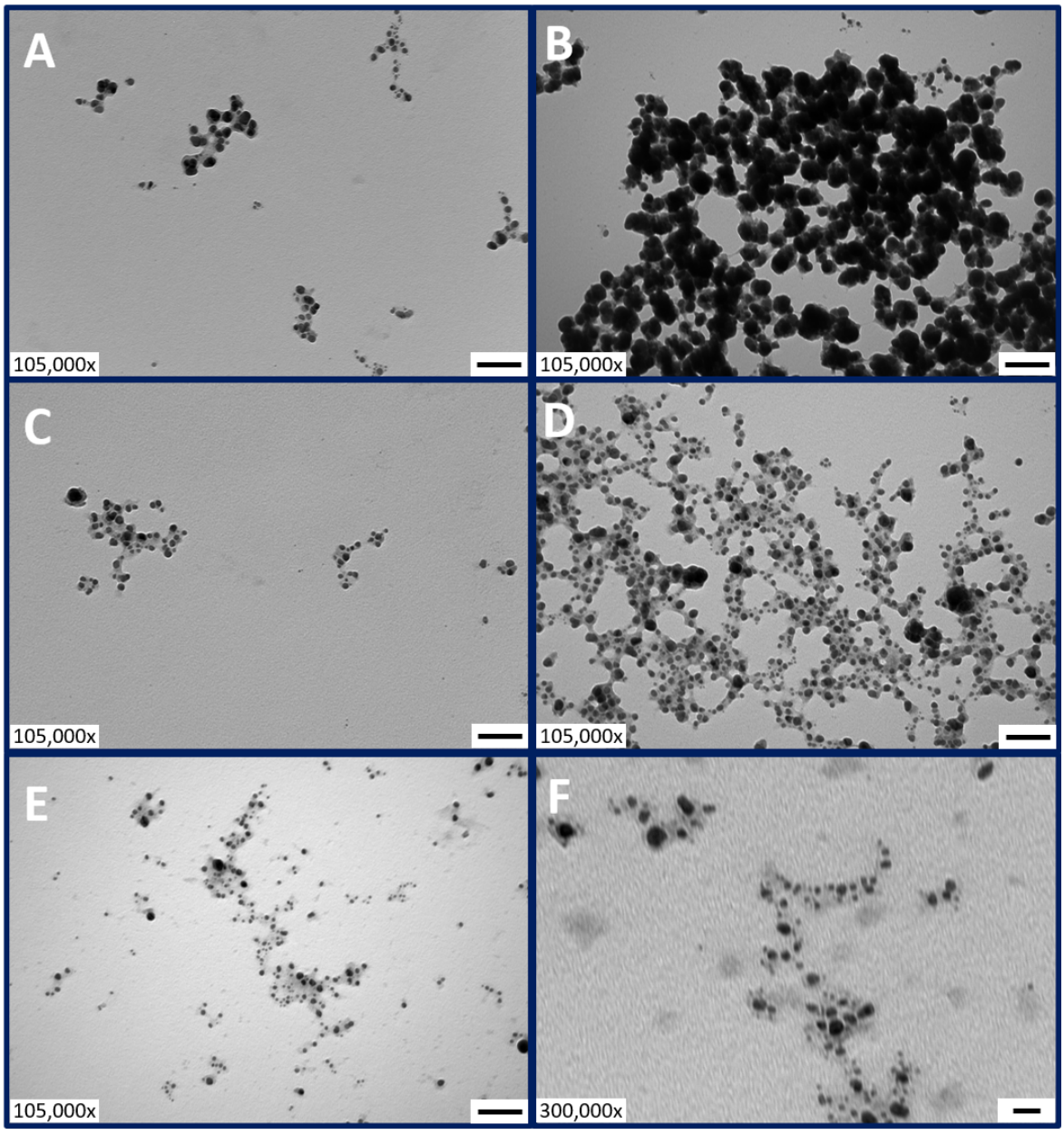

Figure 6.19: TEM images of AgNPs produced using Reactor 5 at 1 mL min^{-1} (A & B), 5 mL min^{-1} (C & D), and 10 mL min^{-1}(E & F). Scale bars: 100 nm (A - E), 20 nm (F).

markedly different intensities. The absorbance maxima showed a clear pattern between FRR and AgNP production (Figure 6.21 B). The optimal conditions appeared to be a slightly CFE dominant mixture at 1:2 ($AgNO_3$:CFE). Deviation away from this optimum lead to a decrease in peak intensity and AgNP production. The intensity of the peaks produced under FRRs of 1:5 and 2:1 were comparable, and 5:1 was substantially lower than the mirror ratio of 1:5.

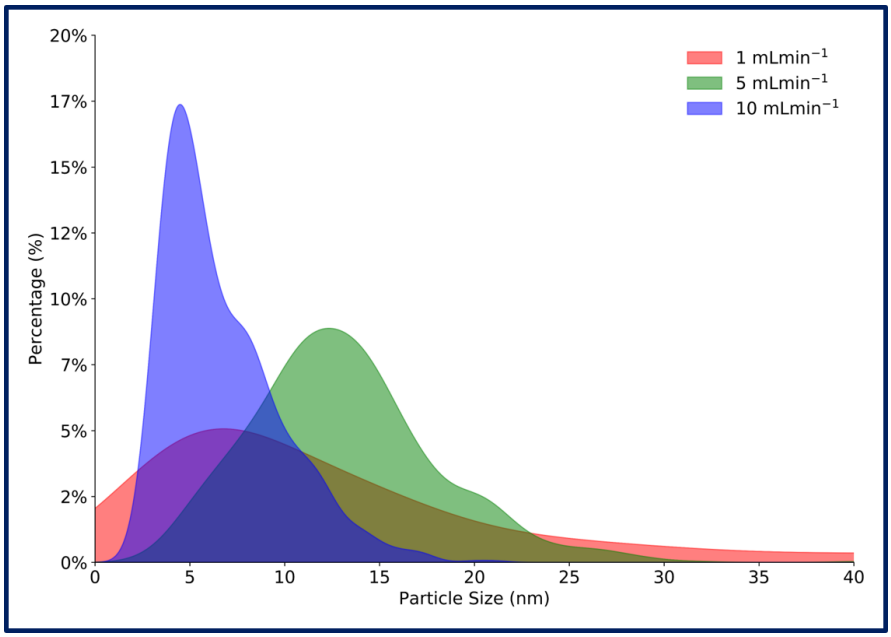

Figure 6.20: Size distributions of AgNPs produced at 1 mL min^{-1}, 5 mL min^{-1}, and 10 mL min^{-1}, as measured from TEM images.

Under the CFE-rich condition of 1:10, there was a high relative concentration of the reducing agent but low availability of Ag^+, resulting in fewer nucleation events and particles. Moreover, the concentration of the capping agent (likely proteins) was also higher, which may act to smother the seed particles as they form and limit their growth. However, the expected bathochromic shift in the λ_{max} associated with smaller particles was not observed, suggesting this was not the case. Under Ag^+-dominant FRRs, the opposite was the true, where a lack of the reducing agent likely hindered AgNP production. The positions of the peaks did not follow a discernible pattern with peak located between 430 nm and 450 nm (Figure 6.21 C).

During one experiment operating at 1 mL min^{-1}, the product turned black in colour and quickly precipitated when collected leaving a slightly grey clear liquid phase. This was thought to be Ag_2O which is highly insoluble in H_2O, explaining the precipitation.[274] Ag compounds are notoriously sensitive to UV light and liable to oxidise under certain conditions. An explanation for this phenomenon remains unclear, though it is possible the pH of the CFE used was higher than usual, resulting in the formation of AgOH when the

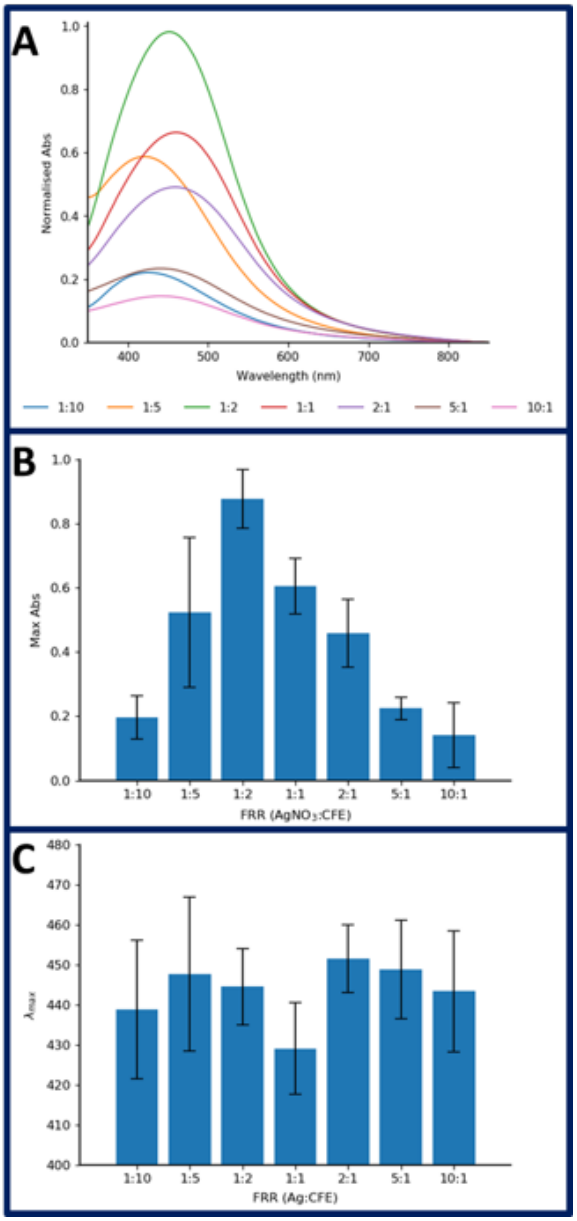

Figure 6.21: UV-Vis spectra of AgNPs produced in Reactor 5 (coil) under different FRRs (A) with the intensities (B) and positions (C) of the LSPR peaks.

$AgNO_3$ was introduced; AgOH then decomposes to Ag_2O.[274] While this was not observed in any other experiment, it highlights the need to consider the variability in biologically generated material when used in material synthesis.

PTFE is a highly fluorinated compound with a hydrophobic surface and a very low coefficient of friction.[275][276] Together these give PTFE its renowned non-stick properties. This was a key consideration when selecting PTFE for this reactor design. It was hoped these properties would prevent or reduce the deposition of AgNPs onto the surface of the channel, like that seen in all of the PDMS reactors.

PTFE has a milky-white translucent appearance (Figure 6.22 A), and during production the characteristic brown colour of biogenic AgNPs was clearly visible through the thin walls of the channel (Figure 6.22 B). However, after approximately 45 min of operating the channel appeared discoloured. Following a thorough rinse with diH_2O, a strong brown discolouration remained (Figure 6.22 C). As with the PDMS reactors, only flushing and soaking the reactor in 30 % H_2O_2 for 24 h was successful in fully removing the staining; HCl had a negligible cleaning effect on the reactor.

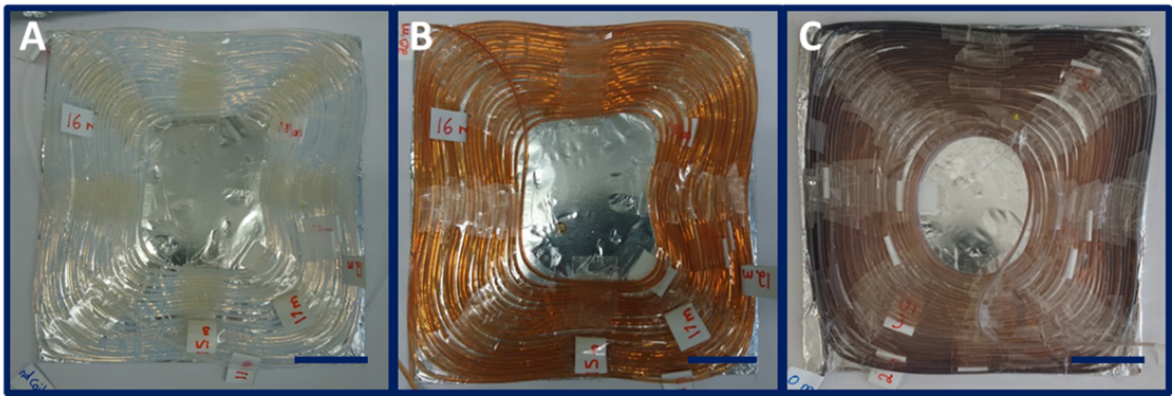

Figure 6.22: PTFE coils from Reactor 5 before (A) and during (B) AgNP production under UV lamps. The coil was visibly discoloured after AgNP production and washing with H_2O(C). All error bars show 20 mm.

Further to this, in-line UV-Vis spectroscopy was used to monitor the output of the reactor during its operation. The reactor was initially operated with the lamps switched off to fill the reactor and collect baseline measurements. As shown in Figure 6.23, when the lamps were switched on and the spectroscopy begun, production increased steadily as the AgNPs were being produced. As the reagents were already in the reactor, they experienced a linearly increasing t_r the earlier in the reactor they were located when the lamps were switched on the longer the t_r experienced which gave the increasing production. Once the reactor was operating normally and the t_r had reached the maximum production plateaued. After operating at 1 mL min^{-1} for 100 min, the production did not decrease notably.

It should be noted that the syringe pumps had a finite volume and so required refilling periodically. To

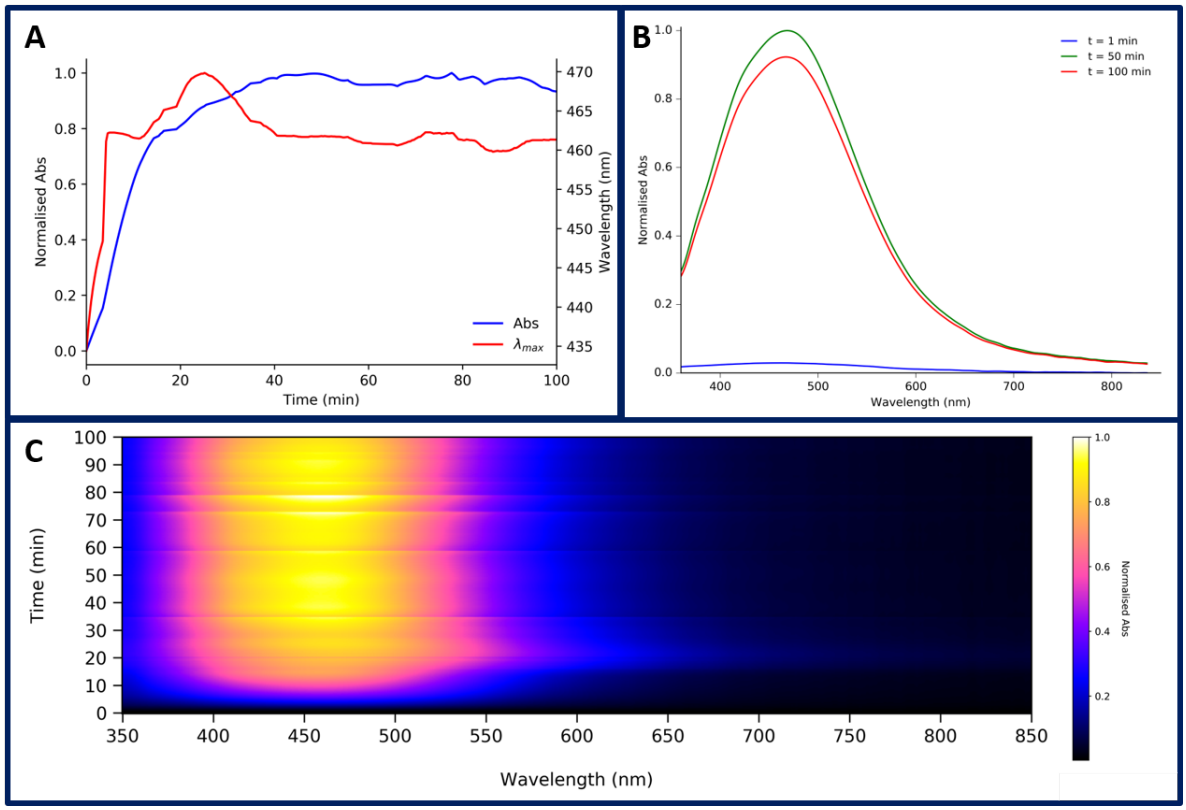

Figure 6.23: Output stability of Reactor 5 over time. The intensity (blue) and position (red) of the absorbance peak of AgNPs produced in Reactor 5 over 100 min of operation (A). UV-Vis spectra of AgNPs produced in Reactor 5 at 1 min, 50 min, and 100 min of operation (B). Heatmap of real-time spectra collected at the outlet of Reactor 5 over 100 min (C).

do this, the lamps were turned off and spectroscopy paused as the flow was stationary. The syringes were refilled and the pumps, lamps and spectroscopy restarted. This pausing in operation and opening of the system led to variation in the output of the reactor, detected as sudden peaks and troughs in the output, which were, at least in part, the result of gas bubbles in the line passing through the flow cuvette.

The coils were inspected after being flushed with diH_2O and they appeared discoloured as previously observed. The first coil was substantially more discoloured than the second coil. The lack of a decrease in production may suggest the loss of efficiency in the early stages of the reactor did not have a considerable overall effect on production and so the reaction is reaching completion before the end of the reactor with an excess of channel length when operating at 1.0 mL min^{-1}, the second coil may have had sufficient length to compensate for the loss in the efficiency of the first coil. If the reactor was operated longer and more deposition was allowed to occur further down the channel, a greater effect on AgNP production would likely have been observed.

6.3.7 Comparison of Reactors

A total of 5 reactors were developed and tested. Each had different design features for exploring and improving AgNP photobioproduction in a flow system. A comparison of the Reactors is made in Table 6.1 and the Appendix D.1.

The output production of the reactors with laser illumination was observed to be similar (Figure 6.24 A). Reactor 1 appears to have been the most efficient at producing AgNP and the insertion of the glass fibre optic into the reactor has little impact on production. The more direct light delivery might be expected to yield more AgNPs, but the rapid deposition of particles on the fibre optic surface likely impeded the performance of this mode of illumination. Reactor 3 had a narrower channel than Reactor 1 (1 mm x 1 mm vs 3 mm x 3 mm) and, with the same channel length, had a lower volume and t_r (Table 6.1). This likely explains the reduced performance of Reactor 3. Reactor 2 performed very poorly with respect to yield of AgNP production.

The peaks of Reactors 1 and 3 have very similar λ_{max} positions and morphologies suggesting the particles produced were alike in their shape, size, and distribution of sizes (Figure 6.24 B). This is interesting because Reactor 1 with the flush-mounted external fibre optic and Reactor 1 with an inserted fibre optic produced peak with similar intensities but differing peak positions and widths. Having the fibre optic inserted into the channel appears to have produced a broader distribution of particle sizes, based on the wider LSPR peak. The bathochromic peak position also shows the particles were larger with the inserted fibre optic. This may be explained by the close proximity of the laser output to the reagents delivering more

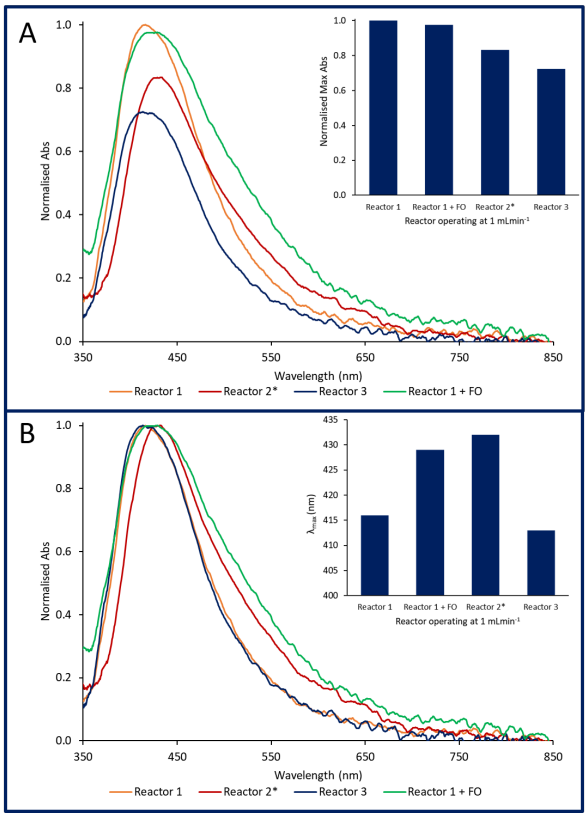

Figure 6.24: Comparison of UV-Vis spectra of AgNPs produced in flow reactors at 1 mL min^{-1} with laser light illumination. The intensities of the LSPR peaks in compared (A). Insert: Maximum absorbance intensity of the LSPR peak from each reactor. The positions and shapes of the LSPR peaks is compared (B). Insert: λ_{max} of the LSPR peaks from each reactor. *Reactor 2 was operated at 0.1 mL min^{-1} as negligible AgNP production was detect at 1 mL min^{-1}. FO: Fibre optic inserted into channel.

photons than when the laser light had to pass through the PDMS wall of the channel. This increase in light intensity would likely allow for more plasmonically driven growth of particles, resulting in the larger sizes and distribution.

Reactor 2 was operated at 0.1 mL min^{-1} as negligible production was observed when a higher TFR was used. Comparison of the LSPR peak intensity, therefore, carries little meaning. However, the position of the LSPR peak detected was at a considerably longer λ_{max} than Reactors 1 and 2. An explanation for this requires more experimental investigation, however, it is possible the diffused beam exposed the particles to a more consistent intensity of laser light for longer than those in the in-line laser reactors in which the high levels of AgNPs being produced were absorbing the laser light.

In UV illuminated reactors, Reactor 5 (PTFE coils) with its 20 m channel length was considerably more efficient at producing AgNPs at 1 mL min^{-1} compared with the other reactors (Figure 6.25 A). Interestingly, Reactor 1 produced more particles than Reactor 4 (1 m serpentine channel), despite the shorter t_r. This may be due to the larger reaction channel (3 mm x 3mm) in Reactor 1-UV, compared to the constant 1 mm x 1mm in Reactor 4. The larger channel may have been less susceptible to AgNP deposition on the channel walls, making it more efficient. Likewise, the small reactor volume meant operating the reactor to produce 1 mL of sample required less exposure time to the UV lamps, and so may also have resulted in less AgNP deposition.

The positions of the LSPR peaks in Reactors 1-UV, 4 (serpentine), and 5 (coil) were similar, but Reactor 2 had a notably hypsochromic peak position (Figure 6.25 B). The channel dimensions (0.5 mm x 1 mm) was the only difference with Reactor 1, and so likely explains this difference. The smaller channel volume resulted in a shorter t_r, which means the particles may not have had sufficient time to grow under the UV light to increase the LSPR position to be comparable with the other reactors.

When the peak intensities of LSPR peaks produced in all of the reactors were compared to their corresponding t_r, it was clear that a longer t_r results in more AgNPs, as expected (Figure 6.26 A). Interestingly, then the λ_{max} of the peaks were compared, the laser produced particles had shorter wavelength peak positions compared to the UV illuminated reactors (Figure 6.26 B). Moreover, the longer the t_r, the longer the λ_{max} wavelength tended to be. The broad emission on the UV lamps compared to the laser source, may explain why UV illuminated particles were larger, resulting in the red-shifted peaks. With a broad emission, the particles may have been able to utilise plasmonic growth mechanisms through a larger range of sizes. As the particles grow, the LSPR position increases, drifting further from the light source and so reducing the efficiency of plasmonic activity. With a broader light source, this drift can be further before it become less effective at driving crystal growth. Additionally, the laser reactors had shorter t_r than their

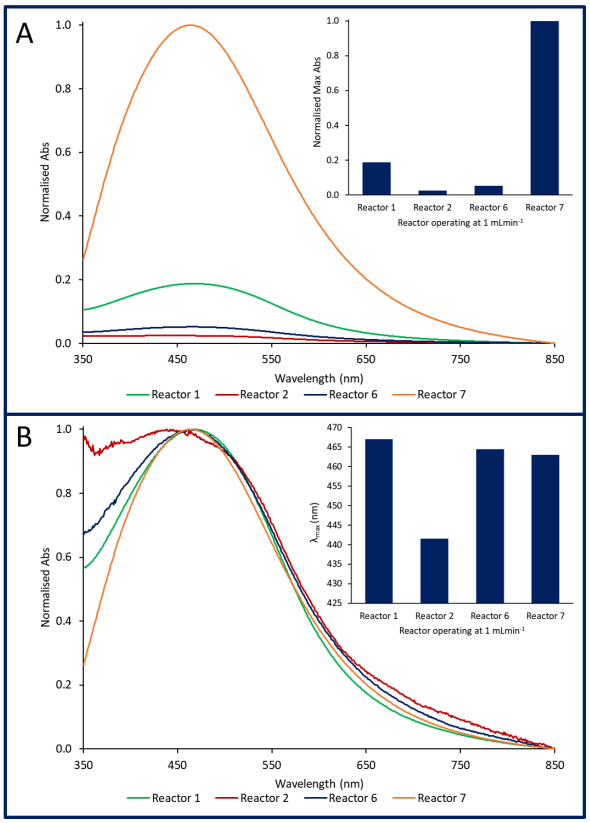

Figure 6.25: Comparison of UV-Vis spectra of AgNPs produced in flow reactors at 1 mL min^{-1} with UV lamp illumination. The intensities of the LSPR peaks in compared (A). Insert: Maximum absorbance intensity of the LSPR peak from each reactor. The positions and shapes of the LSPR peaks is compared (B). Insert: λ_{max} of the LSPR peaks from each reactor.

UV counterparts which would give less time for crystal growth and so likely contribute to the small particles associated with shorter wavelength LSPR positions.

Initial attempts of introducing light to the reactors from a laser source proved challenging as it could not be sufficiently delivered to enough of the reagent material at once to allow for higher TFRs. However, this controlled and restricted delivery method is a possible method to consider when a uniform product is required. At this stage in the development of the reactors, the path to increasing overall production of the particles and then to improve the product properties was taken, over the smaller scale production of a precise product and upscaling in the future; both rationales have their merits and shortcomings.

The use of UV lamps to illuminate the reactors proved highly effective increasing production at higher TFRs. The distributed illumination reduced the impact of AgNP deposition on the reactor walls and increased the surface area for reactions to occur. The culmination of the design elements into the coil design of Reactor 5 proved successful in producing a reactor capable of operating at much higher flow rates (up to

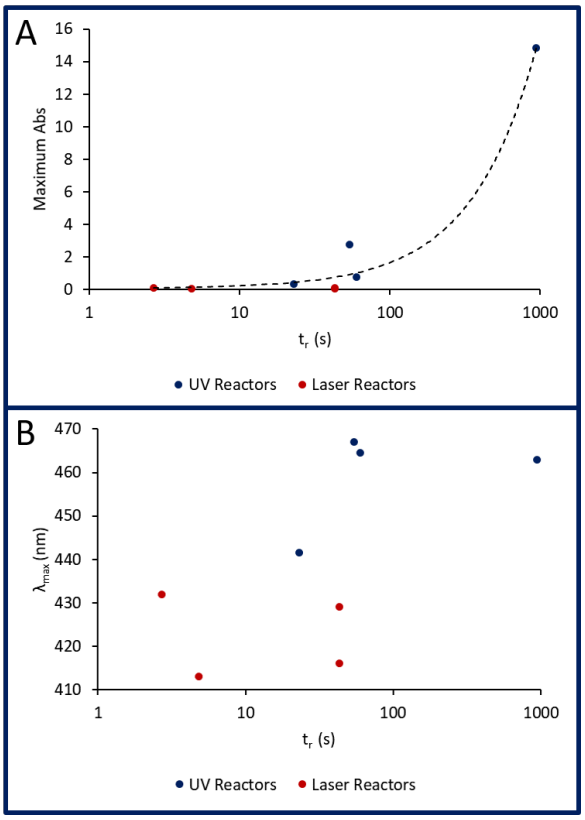

Figure 6.26: Comparison of the maximum absorbances with a linear trendline (A) and LSPR peak positions, as λ_{max},(B) of UV-Vis spectra of AgNPs produced in flow reactors at 1 mL min^{-1} relative to the residence time (t_r) of the reactor. Data from Reactor 2 operated at 0.1 mL min^{-1} were used as negligible AgNP production was detect at 1 mL min^{-1}.

20 mL min^{-1}) while generating considerable amounts of AgNPs. While Reactor 5 proved effective, further optimisation and design modifications could undoubtedly improve the operating scale and product quality.

PTFE tubing was selected for its chemical resistance and "non-stick" properties that result from its highly fluorinated surface. It was hoped that the AgNPs would not deposit on the walls of the channel and prevent a decrease in efficiency with continuous operation of the reactor, but this was not the case. Future investigations should focus on methods to reduce the deposition of AgNPs on the internal surfaces of the reactors, either through the use of surface coatings or reactor designs (e.g. annular flow).

Table 6.2: Summary of reactor achievements and limitations

Reactor	Design	Achievements	Limitations
1	Inline Laser	Continuous flow production was achieved	Liable to bubbles becoming trapped due to channel height change AgNPs deposited on the channel walls reducing the efficiency in a short space of time.
2	Perpendicular Laser	No accumulation of bubbles due to constant channel height and smooth curves	Very poor photo-efficiency as most of the light was lost out of the back of the reactor
3	Heart with Integrated Fibre Optic	Improved light delivery to reagents	Small reactor volume limits the production scale
1-FO	Reactor 1 with Inserted Fibre Optic	Maximum light delivery to the reagents	Very short-lived production as fibre was coated in AgNPs very quickly
1-UV	Reactor 1 Under UV Lamp	Concentrated product was generated	TFR limited by the reaction volume AgNPs coated the PDMS
2-UV	Reactor 2 Under UV Lamp	Consistent and shallow channel dimension allow for more even light distribution	TFR limited by the reaction volume AgNPs coated the PDMS
4	Curved Serpentine Under UV Lamp	Longer channel allows for higher flow rates while maintaining product concentration	Reactor volume limits scalability of TFR AgNPs coat PDMS
5	PTFE Coils Under UV Lamps	Larger volumes mean higher flow rates can be used while maintaining high product concentration Large surface area	Large volume means the operating time is short using syringe pumps AgNPs coat PTFE Uneven light distribution across coils

It is noteworthy that all assessments of production quantity of the reactors are based on UV-Vis absorbance. While the intensity of LSPR absorbance peaks is a good proxy for the concentration of AgNPs, it does not offer an absolute measurement, for example number of particles per mL or mass of particles per mL. Known standards could be used to generate a calibration curve against which the concentration of samples could be estimated. However, the poor uniformity of the particles produced here may pose a challenge in generating an accurate calibration curve. As the absorbance properties of AgNPs are sensitive to the shape and size of the particle, the molar attenuation coefficient of a colloid produced here would be different to a monodispersed standard. However, if the uniformity of the AgNPs produced here can be improved, this approach will offer a useful way to determine the concentration of particles. Alternatives, such as dry weight measurements and quantitative TEM, may also be beneficial when performed in conjunction with absorbance measurements. Accurate absolute yields would allow for better comparison of reactor performance.

6.3.8 Comparison with Previous Reactors

Biological Reactors

There is a paucity of research investigating the use of flow reactors for the biosynthesis of AgNPs. Of those which utilise biological material, most have explored the process from a chemical synthesis perspective, often using refined and purified biomolecules, rather than biomass or biological extracts.

Using *E. coli* DH5-α, Ghorbani et al.[157] developed a bench-scale reactor setup for the continual production of AgNPs. The setup included a reservoir for the culturing of *E. coli* and culture filtrate. This CFE was then added to a $AgNO_3$ and PVP solution in a glass reactor. Operating at 5°C and pH 5.5, the reactor produced Ag nanospheres with a mean diameter 121 nm with an impressively short t_r of 12 min. Through the use of atomic absorption spectroscopy, the conversion of Ag^+ to AgNPs was calculated to be 75%. Previous batch reactions with bacteria at 4°C have taken days and even weeks to produce AgNPs.[57] Moreover, batch production with *E. coli* DH5-αhas been reported, taking 24 h and favouring higher pH conditions (optimal = pH 10), considerably higher than pH 5.5.[99] How the designers of the bioreactor achieved such rapid production under these conditions and without external stimuli remains unclear.

Biological surfactants (oleic acid sophorolipid and stearic acid sophorolipid) have been used to produce spherical AgNPs in a thermally driven reaction.[50] The lipids acted as both the reducing and capping agents when mixed with $AgNO_3$ in a stainless-steel tube reactor at 90°C. At a TFR of 1 mL min^{-1}, particles with sizes 50 nm – 60 nm were produced compared with small 8 nm – 13 nm produced at 0.1 mL min^{-1}. The authors postulated that the difference in size distribution was the mixing dynamics in the spiral-shaped

reactor coil. The use of high temperatures to drive the reaction, while highly controllable in microscale reactors,[269] has downsides over the use of light used in this study including increased apparatus costs and energy usage, especially when scaled up.

In glass and stainless-steel coils, *Cinnamomum camphora* leaf biomass has been used to prepare AgNPs when reacted with $AgNO_3$ at 60°C or 90°C.[277] Being quasi-spherical with some irregular shapes, the particles produced has morphologies similar to those in this research when visualised by TEM. The particle sizes were typically larger than those produced in Reactor 5 here. However, when using stainless steel coil in a 90°C glycerine bath, the size distribution of particles was similar to that observed here when Reactor 5 was operated with a TFR of 5 mL min^{-1}. The authors reported that polyols in the biomass extract were crucial for the both the reduction of Ag^+ and coating of the AgNPs.

Similarly, operating at 200 µL to 600 µL, powdered *Cacumen platycladi* was reacted with $AgNO_3$ to produce AgNPs.[186] The average size of the AgNPs increased from 3.5 nm to 7.2 nm for 0.2 mL min^{-1} to 0.4 mL min^{-1} before decreasing to 5.2 nm and 3.0 nm for 0.5 mL min^{-1} and 0.6 mL min^{-1}, respectively. Higher concentrations of biomass extract resulted in increased AgNP production, but a widening of the LSPR peak accompanied by larger particles and wider distribution of sizes (4.7 ± 1.9 nm for 10 gL^{-1} and 15.0 ± 8.6 nm for 60 gL^{-1}). In comparison, when the FRRs of Reactor 5 were examined, the stoichiometry of the reaction appears to have been more balanced with the reservoir concentrations as only a change form 1:1 to 1:2 ($AgNO_3$:CFE) resulted in optimal production, but no pattern was observed in the LSPR peak positions, and thus the size of the AgNPs.

The algae *Chlorella vulgaris* was grown in a continually fed reactor vessel to produce AgNPs.[187] The particles were roughly spherical and 8 nm to 20 nm in size. The bioreactor in which the algae was grown was exposed to alternating 12 h light-dark cycles. As no controls with the reactor run in the dark were reported, it is unclear if the production was the result of a mechanism similar to the observed here, or the direct enzymatic activity of the algae. Nevertheless, the 15 L scale of the reactor holds promise for larger scale AgNP bioproduction.

Chemical Reactors

The synthesis of AgNPs in flow reactors is much more widely reported in chemical systems.[35,181–185]

Similar to Reactor 5 here, a PTFE capillary coil reactor has been used to produce Ag nanospheres with very narrow size distributions.[278] Using a 0.3 mm ID tube, smaller than the 1.0 mm used here, the reaction was performed at 160°C with Ag acetate and oleylamine as the reducing and capping agent; 1,2-dichlorobenzene was used as the solvent. The reactor was operated up to 70.7 µL min^{-1}, a t_r of 10

min, with the largest particles and highest production observed at the slowest flow rate of 14.2 µL min^{-} (t_r of 2 min); this aligns with the findings in this work. The effects of different diameter tubing were also investigated. Tubing with an ID of 0.5 mm showed comparable UV-Vis spectra of AgNPs at t_r of 2 min and 5 min with the 0.3 mm tubing. However, at a slower flow rate (t_r = 10 min) a red-shifted and wider peak was observed indicating larger and less monodispersed product. Conversely, 0.6 mm tubing produced AgNPs with a very narrow and consistent LSPR peak positions regardless of t_r. The different mixing regimes in the tubes were thought to be responsible for these differences through disruption to the crystal growth process. Moreover, laser light has been used to produce Ag nanoaggregates of 6 µm in size comprised of particle with diameters of 20 nm – 80 nm.[279] These clusters were considerably larger than those observed in Reactor 5 in this study.

The technology developed for manufacturing the PDMS reactors used here was originally used for chemical AgNPs synthesis and the production of liposomes.[272] The cost of manufacturing a reactor is estimated to be £5. The low price and relative ease of production makes these reactors a powerful tool for the rapid prototyping and testing of micro- and meso-fluidic reactors. PDMS has material properties which make it attractive for use in these reactors. First, it is transparent to visible and UV light. This is not only essential when performing photocatalysed reactions, but also allows for easy observation of the reaction channels. Through the use of *in situ* microscopic spectroscopy techniques, this allows for spatial spectroscopy to be performed at different location in the channel to gain an understanding of the production process;[280] this was not done here but would be a valuable line of investigation in future work. However, the properties of PDMS which result in the high tendency for reactor fouling through the deposition of AgNPs on to the channel walls require improvement to warrant its continued use in these reactors.

6.3.9 Future Developments

Reactor 5 demonstrates the potential for flow synthesis of biogenic AgNPs. However, further developments and design improvements can be made to improve both the yield production and the quality of the product.

Annular and Droplet Flow

A major challenge encountered with all the devices used in this work was the accumulation and deposition of AgNPs on the internal surfaces of the reactors. While a hydrophobic coating and PTFE were tested as a way of preventing this, no significant improvement was observed. An alternative to coating the channels of the reactors is to prevent the AgNPs coming into contact with the walls; this can be achieved by two-phase flow. In small scale microreactors, such flow patterns typically utilise two immiscible (or partially

miscible) fluids.[266] The reactor can be designed so that the aqueous phase is surrounded by the carrier phase meaning it has no direct contact with the walls of the channel.[281] Two common modes of liquid-liquid two-phase flow are annular flow (or core flow) and droplet trains. As demonstrated in Figure 6.27, annular flow maintains the continual flow characteristics of single-phase flow, whereas droplet trains partition the liquid into discrete compartments. While annular flow has been used in UV photochemistry,[282] a benefit of this compartmentalisation is the reduction in hydrodynamic dispersion experienced by the reagents and products due to parabolic flow velocities.[283][284] A more even flow velocity in the reagents yields more consistent residence times for reagent molecules in the reactors, resulting in improved uniformity of the product. As such, droplet flow may prove useful in reducing the dispersity observed in the samples produced under continuous flow here. Indeed, AgNP production has been demonstrated in droplets at flow rates up to 30 mLh^{-1}.[184] However, such systems, require considerable optimisation due to their increased complexity over single phase flow.[266]

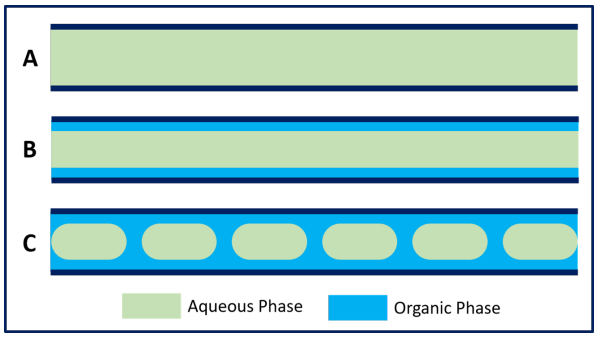

Figure 6.27: Diagram of annular and droplet flow. Single phase (A) has only one liquid and fills the whole channel. Annular flow (B) has a central core of aqueous phase solution surrounded by an organic phase so that the aqueous phase does not come into contact with the walls of the channel. Trains of droplets (C) have a similar pattern to annular flow, but the aqueous phase is partitioned into discrete droplets instead of a continual stream.

AgNP Isolation and Purification

Large amounts of a concentrated crude of AgNPs were produced using Reactor 5. However, the bottleneck in production is now the down-stream processing. The need to centrifuge material to isolate and wash the AgNPs from the CFE and any remaining Ag^{+} is time consuming and has limited volume capacity. Typically, the AgNPs were washed for a minimum of 3 x 30 min in 2 mL centrifuge tubes (with 24 slots, the centrifuge could process a total of 48 mL simultaneously). While continuous flow (ultra)centrifugation is possible, it is expensive as it requires a specialised centrifuge, rotors, and pumps, and is not true continuous flow as the product must periodically be collected from the rotor. Alternatively, "on-chip" separating methods

are possible, and may prove to be powerful tools in this pursuit.[285] These methods utilise a range of passive and active separation techniques; however, the small volume processing rates currently limit their application on an industrial scale.[285][286] Other in-line methods for AgNP isolation which can operate at larger scales are therefore preferred. Such a method should be able to operate at flow rates of at least those used in the production stage to allow for system integration. Of the technologies that have been utilised for AgNP separation, tangential flow filtration (TFF) is of interest for future reactor developments and investigations.

TFF utilises filter membranes across which the crude product is flowed tangentially. The particles can continue in the main flow and excess reagents are expelled through the membrane.[287][288] Further, TFF can be used to concentrate and apply size selection to AgNPs in flow.[289] In this case, the smaller CFE components can pass through the membrane leaving the larger AgNPs in the main flow phase. Additionally, the flow phase continually acts to remove material caught in the membrane, meaning the system is less prone to clogging and the development of "filter cakes" (material build up on the filter which prevents its effective function) in the same way direct flow filters suffer.[290] This benefit suits use in a flow system where continual operation would be challenging if the filter is easily blocked.

6.4 Conclusions

Continuous flow synthesis of AgNPs has been achieved using a photo-driven process. The development of a series of low-cost flow reactors allowed different design elements to be tested to optimise the production of AgNPs. Reactor 5 was capable of substantial AgNP production and forms the basis of future work into large scale AgNP bioproduction. Challenges remain regarding the deposition of AgNPs onto the surface of the channels in the reactors which will need to be overcome to further optimise the reactor. Continued investigation is required to explore in-line clean-up and processing to produce higher quality AgNPs.

Chapter 7

Non-Specific Binding of Proteins Form Coronae of Biogenic AgNPs Produced by *M. psychrotolerans*

7.1 Introduction

Biogenic AgNPs are widely reported to have a corona made of biomolecules, often proteins, coating their surface (Figure 7.1).[75,76,95,103,142] This coating is thought to be responsible for both the morphological and colloidal stability of biologically sourced AgNPs as it offers steric or electrosteric protection.[24,61,291] Understanding the corona is a crucial step in optimising the biosynthesis of AgNPs for industrial applications as its composition will affect how the particles interact with surrounding materials, such as a polymer support matrix, as well as their stability in different environments. Moreover, the composition of the corona may yield valuable insight into the biological mechanisms of AgNP bioproduction.

To date, the compositions of coronae have been primarily investigated using spectroscopic techniques including FTIR spectroscopy.[52,75,76,95,103,142] Most of these studies are in agreement that the coating contains peptides, presumed to be from proteins or protein fragments, though sugars and fatty acids have also been reported.[76,109,113] While spectroscopic techniques can identify the type of molecules in the corona, they cannot directly identify the specific compound or protein. The identities of the proteins in the corona of bacterially produced AgNPs have received very little attention and have not been described in the corona of AgNPs produced by *M. psychrotolerans*.

It is hoped that the mechanisms of AgNP production can be further elucidated by identifying which

proteins coat the AgNPs. Moreover, particle morphology has been driven by proteins in chemical synthesis settings.[292,293] It may, therefore, be possible to manipulate the corona by altering protein expression in the bacterium to help selectively produce AgNPs of specific shapes.

It remains to be determined if these proteins are specific, potentially serving as yet unknown functions beyond stabilisation, or whether an unspecific cacophony of peptides from the secretome are binding purely due to their affinity to Ag. Here, the protein composition of the corona was investigated using a proteomic approach.

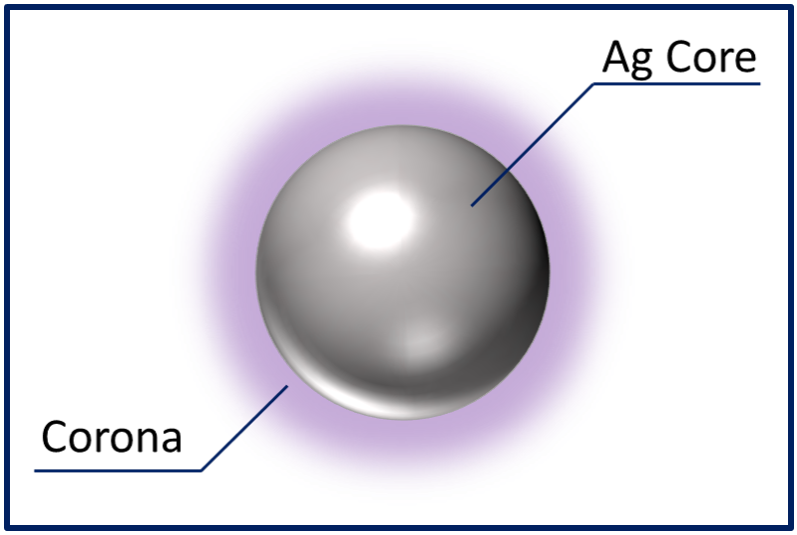

Figure 7.1: Diagram of a AgNP and Corona. The Ag core is coated in biomolecules such as protein to form the corona.

7.2 Methods

7.2.1 Preparation of AgNPs

M. psychrotolerans was grown in 100 mL volumes as describe previously in Chapter 3. $AgNO_3$ was added directly to the cultures with a final concentration of 9 mM and incubated at 22°C for 24 h in the dark. Following incubation, the culture was separated into two (45 mL each). Cells were removed by centrifugation at 3,000 x *g* for 20 min and the supernatant filtered (0.22 µm pore diameter syringe filters). The crude AgNP solution was then concentrated and washed using a total of four centrifugation steps (1 h at 21,100 x *g* at 4°C) after each of which the pellets were resuspended in smaller volumes of PBS so that after the last resuspension the total volume of the sample was ≈ 500 µL. Samples were transferred to new centrifuge tubes between each wash and kept on ice or at 4°C throughout.

7.2.2 Visualisation and Spectroscopic Analysis of Corona

TEM

TEM of washed AgNPs was performed using the same methods are previously described (Section 3.2.3).

FTIR

AgNPs were harvested from *M. psychrotolerans* culture by centrifugation and washed as before (see Section 7.2.1), except particles were washed using diH_2O instead of PBS. The washed AgNPs were then dried at 60°C overnight on glass slides; the slides were cleaned with 70% ethanol and rinsed thoroughly with diH_2O before use. The particles were then mixed with a small amount ($\approx$ 20 mg) KBr. The mixture was loaded into a pellet die and $\approx$ 7 tons of pressure applied. Pellets were stored in a desiccator with silica gel until analysis. The KBr pellets were checked for imperfections (e.g. cracks, opacity, and structural integrity) before being analysed using an FTIR spectrometer (Agilent Cary 660). The sample chamber was purged with nitrogen before samples were scanned from 800 cm^{-1} to 2200 cm^{-1}. Spectra were collected in triplicate from each sample and averaged. Baselines of blank KBr pellets were subtracted from each average. FTIR spectroscopy data collection and processing of prepared samples was kindly performed by Dave Rowe (ORC, University of Southampton).

Raman

AgNPs were produced, washed, and dried in the same way as FTIR samples. After drying, the particles were transferred to quartz cover slips for analysis. Raman spectroscopy data collection and processing of the prepared samples was kindly performed by Adam Lister (Faculty of Life Sciences, University of Southampton).

Raman spectra were collected using a home-built Raman micro-spectrometer system utilizing a Ti-E Nikon microscope for visualisation and locating samples on the quartz cover slips. The spectrometer consisted of a Shamrock303 spectrograph with an Andor iDus420 camera as the detector. A 785 nm variable power laser was used with a 60x water immersion objective.

For each measurement, 10 spectra (20 s collection) were collected from the sample and averaged. The peaks were identified using known positions of biological molecules.[294]

Fluorescence Microscopy

Fluorescence microscopy was used to detect residual stain bound to AgNPs. The staining procedure for all three stains used was the same. AgNPs were produced and washed as before (Section 7.2.1). After the final wash step, the particles were resuspended in 500 µL of diH_2O. To these samples 100 µL of Nile red (25 mM; λ_{Ex}: 552 λ_{Em}: 636), 100 µL SYPRO Ruby (neat as supplied, λ_{Ex}: 450 λ_{Em}: 610), or 5 µL Syto-9 (5 mM; λ_{Ex}: 485 λ_{Em}: 501) were added. All stained samples were incubated at room temperature for 15 min in the dark. The samples were then centrifuged at 17,000 x *g* for 20 min and the supernatant (containing unbound stain) was removed. The pellet was resuspended in 100 µL of diH_2O and centrifuged again with the same conditions to wash any residual unbound stain. The pellet was then dried onto a glass slide which had been cleaned with ethanol and diH_2O, as before, and examined using a episcopic differential interference contrast /epifluorescence microscopy with a 100x oil immersion objective(Best Scientific, UK).[295]

7.2.3 Gel Electrophoresis

Sodium dodecyl sulphate polyacrylamide gel electrophoresis (SDS PAGE) was used to separate proteins in the AgNP samples and samples of culture supernatant based on their molecular weight.

Washed and concentrated AgNPs prepared in Section 7.2.1 were used as AgNP samples. Culture supernatant samples were prepared by removing the cells from cultures by centrifugation (10,000 x *g* for 5 min) and syringe filtration of the collected supernatant (0.22 µm pore diameter).

Reagents

Pre-cast 12% bis-tris NuPAGE gels, lithium dodecyl sulphate (LDS) loading buffer concentrate (4x), and MES running buffer concentrate (20x, 50 mM 2-(N-morpholino) ethanesulfonic acid, 50 mM Tris Base, 0.1% SDS, 1 mM EDTA, pH 7.3), SYPRO Ruby stain, Novex Sharp pre-stained protein standard, and SimplyBlue Safe Stain (a Coomassie G-250 based stain) were purchased from ThermoFisher (USA). Glacial acetic acid and absolute methanol were purchased from Fisher Scientific (UK). Chemically synthesised PVP-coated Ag nanospheres were kindly synthesised and provided by D. A. Cristaldi of the same research group.

Sample Preparation and Gel Setup

LDS loading buffer concentrate (25 µL) was added to all samples (75 µL) and the samples heated to 90°C in a heating block for 5 min to denature the proteins. Samples were then loaded in to a gel along with a protein standard ladder (Novex Sharp). The gel was run for approximately 45 min with a potential of 200 V.

Staining and Imaging

After the gel had run, it was removed from the gel tank and the running buffer washed off with diH_2O. The gel was then stained with SYPRO Ruby according to the manufacturer's instructions. For this, the gel was fixed with a 50% methanol and 7% acetic acid solution twice for 30 min at room temperature. The fixing buffer was then removed and SYPRO Ruby added and incubated overnight. The gel was then transferred to a clean container and a wash buffer (10% methanol and 7% acetic acid) was used to remove excess stain for 30 min. The gel was then washed twice for 5 min with diH_2O to remove residual acid. All fixing, staining, and washing steps were performed at room temperature with gentle agitation by orbital mixing. The gel was imaged using a GBox gel imager with a UV light source.

Post-staining was performed using SimplyBlue Safe Stain. Gels were incubated with the stain for a minimum of 4 h before three 1 h washes in diH_2O. Gels were then imaged using a white-light backlit imaging system and a colour-camera.

7.2.4 Proteomic Analysis of Corona

To investigate the composition of the corona, 5 samples of AgNPs were produced and the proteins bound to the AgNPs identified using mass-spectrometry. An additional 5 samples of culture supernatant were produced (referred to as the controls) to identify proteins present in the extracellular environment prior to the addition of $AgNO_3$ for AgNP production.

The protocols used in this work were kindly provided by Paul Skipp and Adam Lester (Centre for Proteomic Research, University of Southampton). Facilities and all reagents used in the preparation of samples were kindly provided by the Centre for Proteomic Research, University of Southampton.

AgNP Sample Preparation

Washed and concentrated AgNPs were resuspended in 0.1 M ammonium bicarbonate. Reduction was achieved with 1 µg mL^{-1} of dithiothreitol (DTT) added to a 1 mL aliquot of each sample. Following incubation at 56°C for 1 h, iodoacetamide (IAA) was added to alkylate the samples with a final concentration of 0.5 µg mL^{-1}; the samples were incubated for 20 min at room temperature in the dark. A 0.5 µg mL^{-1} trypsin/Lys-C solution was prepared and a total of 1 µg of each enzyme added to each sample. Digestion was carried out at 37°C overnight. Following digestion, the AgNPs were removed by centrifugation (21,100 x *g* for 1 h at room temperature). The supernatant was collected and evaporated in a vacuum concentrator (45°C) until dry. The peptide sample was resuspended in 100 µL of 0.1% formic acid and stored at 4°C until clean up.

Control Secretome Preparation

Aliquots of 500 µL of culture were collected immediately before $AgNO_3$ was added and stored in 50% glycerol at -80°C until analysis. To prepare the secretome, the culture samples were centrifuged at 21,100 x *g* for 10 min to remove cells and debris. A 200 µL volume of supernatant was added to 600 µL of 100% methanol and 150 µL of chloroform to clean the protein sample by removing lipids and nucleic acids. The samples were mixed thoroughly by vortexing before centrifugation at 10,000 x *g* for 10 min. The aqueous layer was discarded and 450 µL methanol added to the remainder. The sample was mixed before being centrifuged at 13,000 x *g* for 5 min. The methanol was then removed, and the pellet dried at room temperature. The pellet was reuspsended in 100 µL of 6 M urea/Tris-HCl pH 8.0. To this, 5 mM DTT was added and incubated at 37°C for 1 h. 1 mM IAA was then added and incubated at room temperature in the dark. Trypsin/Lys C was added and incubated for 4 h at 37°C. To dilute the urea, 750 µL of Tris-HCl (pH 8.0) was then added and the samples further incubated overnight at 37°C. Digestion was terminated with the addition of 4 µL of trifluoroacetic acid (TFA) and the samples centrifuged at 13,000 x *g* for 10 min. The supernatants were collected for clean-up.

Sample Clean-up and Analysis

Following digestion, all protein samples were desalted and cleaned. For this, a Waters Oasis (USA) µElution plate was used according to the manufacturer's instructions. Briefly, the columns were conditioned with 100% acetonitrile and equilibrated with 0.1% TFA. Samples were then loaded onto the column and washed with 0.1% TFA and again with diH_2O. The peptides were then eluted from the column in 70% acetonitrile. All steps were performed using a vacuum manifold. The cleaned samples were dried under vacuum to remove the acetonitrile and resuspended in 10 µL of 0.1% formic acid (Buffer A).

A total of 15 samples of AgNPs and 15 corresponding sectretomes were produced. Due to the low amounts of protein expected, samples were combined into 5 pooled samples of 3 original samples prior to analysis. This was done for both sample type yielding 5 AgNP samples and 5 control supernatant samples. Samples were analysed by mass spectrometry by the Centre for Proteomic Research (University of Southampton).

Data Analysis

Initial data analysis to convert mass spectrometry results to protein-level results was kindly performed by Paul Skipp (Centre for Proteomic Research, University of Southampton).

This protein-level data was further analysed. Protein information was retrieved from the UniProt database

(https://www.uniprot.org) for each accession number.[296] Proteins were considered for analysis only if present in a minimum of 4 replicates (80%) of the same sample type. Proteins with a false positive rate of $\geq$1% were excluded from analysis.

Relative abundance was approximated within each replicate using top three matched peptide intensity sum (A_0) compared to the sum of all top three matched peptide intensity sum values (A_{total}), as shown in Eq. 7.1:

$$Abundance = \frac{A_0}{A_{total}} \times 100\% \quad \text{(Eq. 7.1)}$$

7.2.5 Determining Protease Activity

The presence of proteolytic enzymes in a sample can make analysis challenging. Therefore, protease activity was assessed in samples prior to the use of molecular biology techniques. If such activity is identified, protease inhibitors can be used to prevent degradation of the samples.

Skimmed milk powered was sourced from Sigma Aldrich (UK). Fresh skimmed cow's milk was purchased from a supermarket on the day of use. LB agar and broth with no added NaCl was prepared as in Chapter 3.

Effects of Supernatant on Protein Standards

Prior to denaturing, 5 µL of protein standard ladder (Novex Sharp) was added to *M. psychrotolerans* supernatant and incubated at room temperature for 30 min. The sample was then processed with LDS with all other SDS PAGE samples. A control of the ladder without supernatant was also denatured with LDS. Samples were then run on an SDS PAGE. Smearing of the ladder due to fragmentation of the protein standards can indicate the presence of proteolytic activity.

Milk Coagulation Test

The ability to coagulate milk was used as an indicator for the presence proteolytic enzymes. For this, 0.5 mL of supernatant was added to 4.5 mL of fresh skimmed milk (SM). The solution was then mixed thoroughly before incubation at room temperature for 24 h. Proteinase K (100 µg mL^{-1}) was used as a positive control, and diH_2O as a negative control. Sterile LB and chemically produced Ag nanospheres were also investigated. If proteases are present, the proteins in the milk will coagulate and precipitate observed as clearing of the milk solution.

SM Agar Tests

SM-agar was prepared by the addition of SM powder to LB agar (with no added NaCl) with a final concentration of 2% (w/v) SM. Wells were made in the centre of plates and 50 µL of CFE was added. The plates were then incubated for 24 h at room temperature. Proteinase K and sterile LB (no added NaCl) were used as controls. The presence of proteolytic activity can be observed as clearing of the white and turbid agar.

7.3 Results and Discussion

7.3.1 Visualising the Corona

When AgNPs were imaged by TEM, dark electron dense cores of Ag were clearly visible. However, a lower intensity area was clearly visible surrounding some particles. This material was considerably less electron dense than the Ag and was seen to encase both individual and small clusters of washed AgNPs (Figure 7.2 A & B). The composition of this material could not be determined by TEM; the X-ray spectroscopy techniques available could only give elemental composition and would require a larger sample to get a sufficiently strong signal. Moreover, the polymer coated grids used make identification of carbon containing molecules challenging. Despite this, the observed area was present after 3 washes in diH_2O and so was unlikely to be residual supernatant material or growth media components, but instead was thought to be the corona.

Of the three fluorescent stains used, only SYPRO Ruby was detectable by fluorescence microscopy. Staining revealed considerable red fluorescence, characteristic of SYPRO Ruby, which was dispersed throughout the sample, but the resolution of the microscope was insufficient to resolve individual particles (Appendix Figure E.3). While the visualisation of individual particles is not possible using conventional microscopes, the apparent staining suggested the presence of protein in the sample.

No fluorescence was observed when staining for lipids or nucleic acids. However, this cannot be used to rule out the presence of these materials. The method used here lack the reliability and confidence to be used for the detection of proteins, lipids, or nucleic acids. However, they may be useful as a confirmatory tool if such molecules are detected by other means first. In general, other more sensitive methods are more appropriate for this task and should be used with preference over fluorescent stains and this protocol in its current form without considerable optimisation.

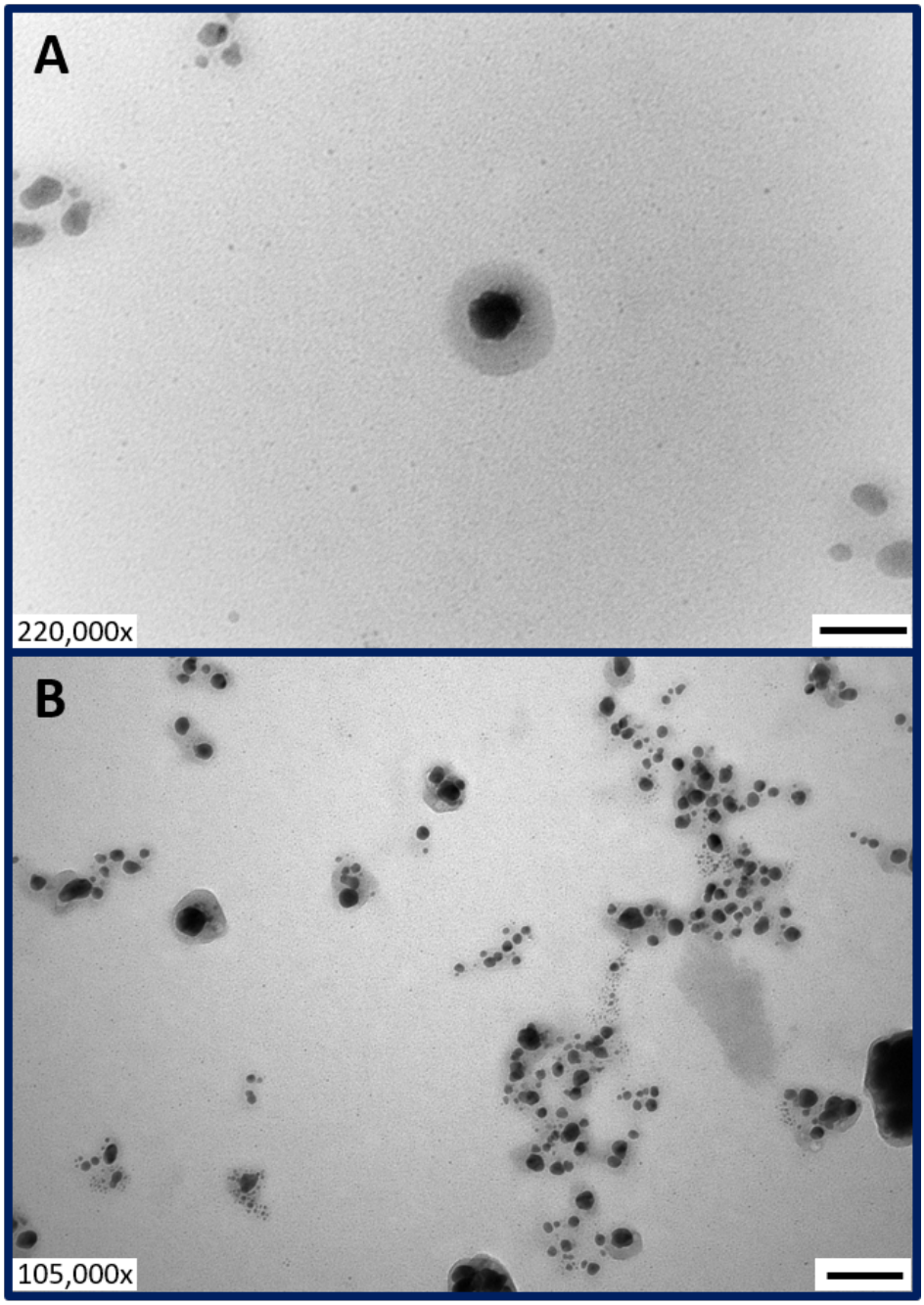

Figure 7.2: TEM images of AgNPs with low electron density coating. Low-density material can be observed surrounding an individual AgNP (A) and around grouped and loosely aggregated AgNPs (B). AgNPs were washed 3 times in diH_2O before imaging. Scale bars: 50 nm (A), 100 nm (B).

7.3.2 Spectroscopic Investigation of Corona

UV-Vis spectroscopy, Raman spectroscopy, and FTIR spectroscopy were used to determine the composition of the corona. Of these, UV-Vis spectroscopy proved the most successful. As shown in the typical spectra in Figure 7.3 A, characteristic peaks between 400 nm and 450 nm, which were attributed to Ag nanospheres, were observed in the spectra of washed AgNPs. However, a second peak was also visible at 300 nm. Protein can be detected by UV spectroscopy due to the absorption by the aromatic structures of tyrosine, tryptophan, and phenylalanine at 274 nm, 280 nm, and 250 nm, respectively.[297] The intensities of both peaks decreased with each subsequent wash; this was expected as complete sedimentation of the AgNPs could not be achieved under these centrifugation conditions. Interestingly, the intensity of the peak at 300 nm did not decrease at the same rate as the LSPR-associated peak at 400 nm - 450 nm (Figure 7.3 B) and the ratio of the two peaks approached 1.0 with each wash (Figure 7.3 D). Moreover, the position of the LSPR peak blue shifted with washes (Figure 7.3). It would be expected that the larger particles would sediment more efficiently meaning the average size of particles would increase after each wash, however, this would be associated with a red shift peak position. The reason for this blue shift remains unclear. However, a possible explanation is that cellular debris was being precipitated during washing. While the AgNPs were filtered (syringe filter with a pore diameter of 0.22 µm), it is possible that smaller cellular components may have been present in the samples. However, the centrifuging conditions (21,200 x *g* for 1 h) are lower than those reported for the pelleting of prokaryotic ribosomes (100,000 x *g* for 16 h) and protein sedimentation.[298,299] Therefore, it is unlikely that considerable amounts of cellular material was recovered after the washing steps and the absorbing material which remained was more likely associated with the AgNPs.

Despite being used to detect protein and nucleic acids, UV-Vis spectroscopy has very poor specificity and is not able to distinguish between two molecules which absorb at the same wavelength. Moreover, DNA and RNA absorb at 260 nm which could overlap with the protein absorbance bands. Additionally, atomic clusters of Ag have absorbance peaks between 290 nm and 325 nm;[300] the dissolution of AgNPs may result in these clusters forming and being detected. Therefore, although no definitive conclusions could be drawn from these results, they encouraged further investigation.

FTIR spectroscopy and Raman spectroscopy both offer vibrational bond information and can be used to identify chemical groups in a sample.[301,302] Both methods were used in this study but due to challenges discussed here, the results were unsatisfactory.

FTIR has routinely been used to identify the presence of peptides, assumed to be from protein or polypeptides, in biosynthesised AgNP samples.[52,75,76,95,103,142] Unfortunately, due to technical limitations,

the quality of the data collected in this study was not sufficient to be used for the identification of peptides. Challenges with the preparation of the KBr pellets and the instrumentation used meant significant amounts of noise were introduced in the recorded data, much of which was due to water and CO_2 contamination. While attempts to reduce this were made, such as by purging the spectrometer with nitrogen for long periods of time prior to collecting spectra and drying the pellets in a desiccator, they ultimately proved unsuccessful.

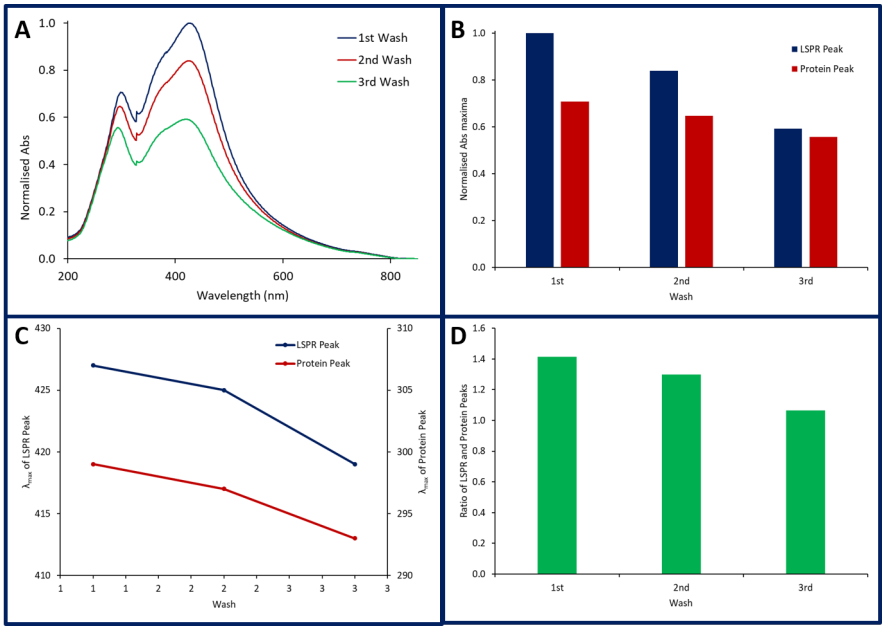

Figure 7.3: Typical UV-Vis spectra of AgNPs washed in diH_2O. (A) Spectra of the same sample were taken after each 1 h wash step at 21,100 x *g* at 4°C. (B) Normalised Abs maxima of LSPR peak (400 nm - 450 nm) and presumed protein peak (280 nm and 320 nm) after multiple wash steps. (C) Peak positions (λ_{max}) of LSPR and protein peak after multiple wash steps. (D) Ratio of LSPR and protein peak Abs maxima after multiple wash steps.

Raman spectroscopy suffered a similar fate with large amounts of fluorescence detected. The setup used a 650 nm laser but as the AgNPs investigated in this work scattered 650 nm very poorly due to their shape and size, the Raman signal was very weak. When examining *M. psychrotolerans* cells, those containing AgNPs gave a higher signal than those which did not contain particles (Appendix Figure E.1); this was thought to be due to surface enhanced Raman effects of molecules on the surface or in close proximity with the AgNPs. However, as the particles were inside the cells, the information was not that of the corona, but of any material in the cells near the particles. As a result, many different organic molecules were detected (Appendix Figure E.2).

7.3.3 Detection and Visualisation of Corona by Fluorescent Staining

Further attempts to characterise the composition of the corona were made using fluorescent stains, specifically SYPRO Ruby, Nile red, and Syto9 to stain protein, lipids, and nucleic acids, respectively. Both fluorescence microscopy and fluorescence spectroscopy were employed to detect the stained particles. The methodology and data are presented in Appendix E. In general, these methods proved unsuccessful as the scale of the material investigated was too low to be reliably detected and quantified using these approaches. Further optimisation of these techniques is required to be a useful tool in the characterisation of biogenic AgNPs.

7.3.4 Protease Activity

The proteins suspected of being on the surface of the particles were examined using molecular biology tools. However, before such methods could be used, the presence of proteases in the supernatant was assessed to ensure sample integrity prior to analysis. Many organisms including *Morganella morganii* are known to possess secretable proteases.[303,304]. Indeed, the genome of *M. psychrotolerans* contains the genes for numerous proteases (as determined by a search of the UniProt database using the keywords "*Morganella psychrotolerans*" and "protease"). To determine if the supernatant of *M. psychrotolerans* cultures exhibited proteolytic activity, a series of assays were used.

When CFE of *M. psychrotolerans* cultures was added to skimmed milk, there was no observed coagulation of the milk following an overnight incubation, nor was there any observable clearing or discolouration of SM agar plates on which CFE was added (Figure 7.4 B & H). Likewise, diH_2O and LB (with no added NaCl) showed the same result in milk solutions and SM agar (Figure 7.4 A, C & F).

Proteinase K, used as a positive control for protease activity, showed a clear zone around the central well of a SM agar plate and substantial precipitation and clearing of the SM solution (Figure 7.4 D & G). This indicates the hydrolysis of casein in the milk leading to the loss of the white colour and turbidity of the medium.[305] Together these results indicate no proteolytic activity was detectable. Moreover, the presence of chemogenic AgNPs did no induce visible precipitation or any observable effects in the SM solution (Figure 7.4 E).

When run on an SDS PAGE, the presence of clearly defined band ($\approx$ 43 kDa, 38 kDa, 36 kDa, and 31 kDa) in the AgNP samples suggested the samples contained intact or large peptide fragments (Figure 7.5 lanes 3, 5, & 7). When incubated with proteinase K prior to running, the bands were no longer visible and instead a very large and intense band was seen between 20 kDa and 30 kDa which corresponds with proteinase K (28.9 kDa), shown in lane 8 of Figure 7.5. Additionally, faint bands were observed between

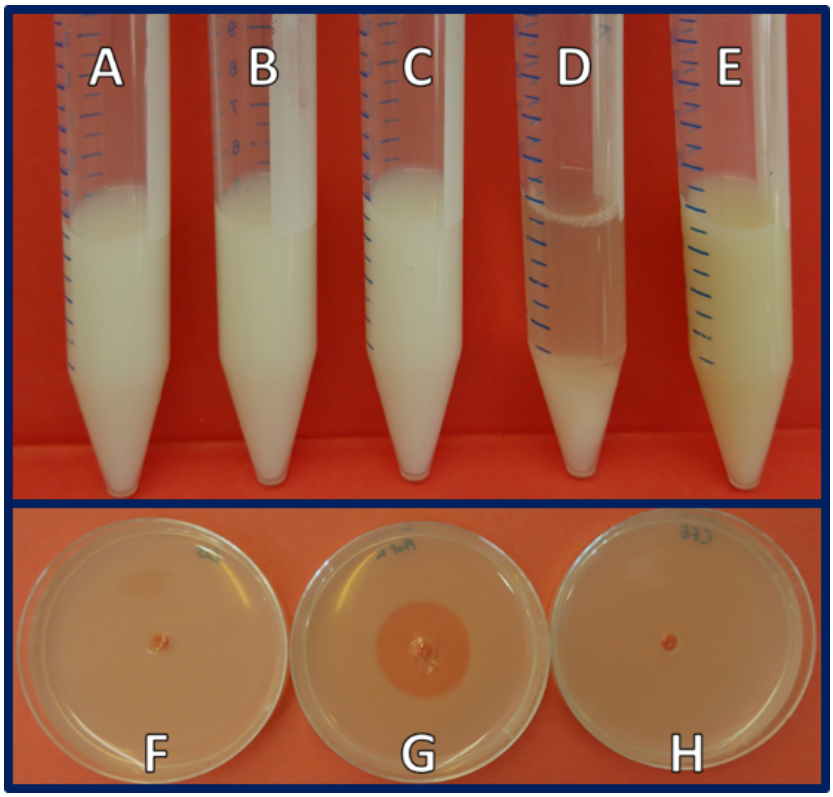

Figure 7.4: Skimmed milk assay for protease activity. No coagulation was observed after 24 h in LB (A), CFE (B), H_2O (C), or chemogenic Ag nanospheres (E) when added to fresh skimmed milk. However, precipitation occurred when proteinase K (D) was added. On SM-agar, a clear zone is visible when proteinase K was added (G), while no clearing was observed when LB (F) or CFE (H) was added.

10 kDa and 15 kDa; these are likely to have been fragments of the digested proteins. This shows that if proteases were present in the samples, fragmentation and smearing would likely have had been visible in the lower molecular weight region of the gels. Moreover, it suggested that the bands observed were protein and not AgNPs which had migrated into the gel.

Finally, when the supernatant of cultures was incubated with the protein standards used to generate the ladder of known molecular weights, no degradation of the bands was observed in the visualised gels (Figure 7.6 lanes 4 & 5). This further supports no protease activity was present in the supernatant.

Together, these results indicated than there was no detectable protease activity present in the samples. These simple and low-cost techniques offered a quick method for the detection of proteases. However, more advanced approaches, such as zymography, would likely be more sensitive and yield more information if proteolytic activity was detected. For this study, however, the approaches used were considered sufficient given the lack of activity detected and the quality of the banding achieved by SDS PAGE without the addition of protease inhibitors.

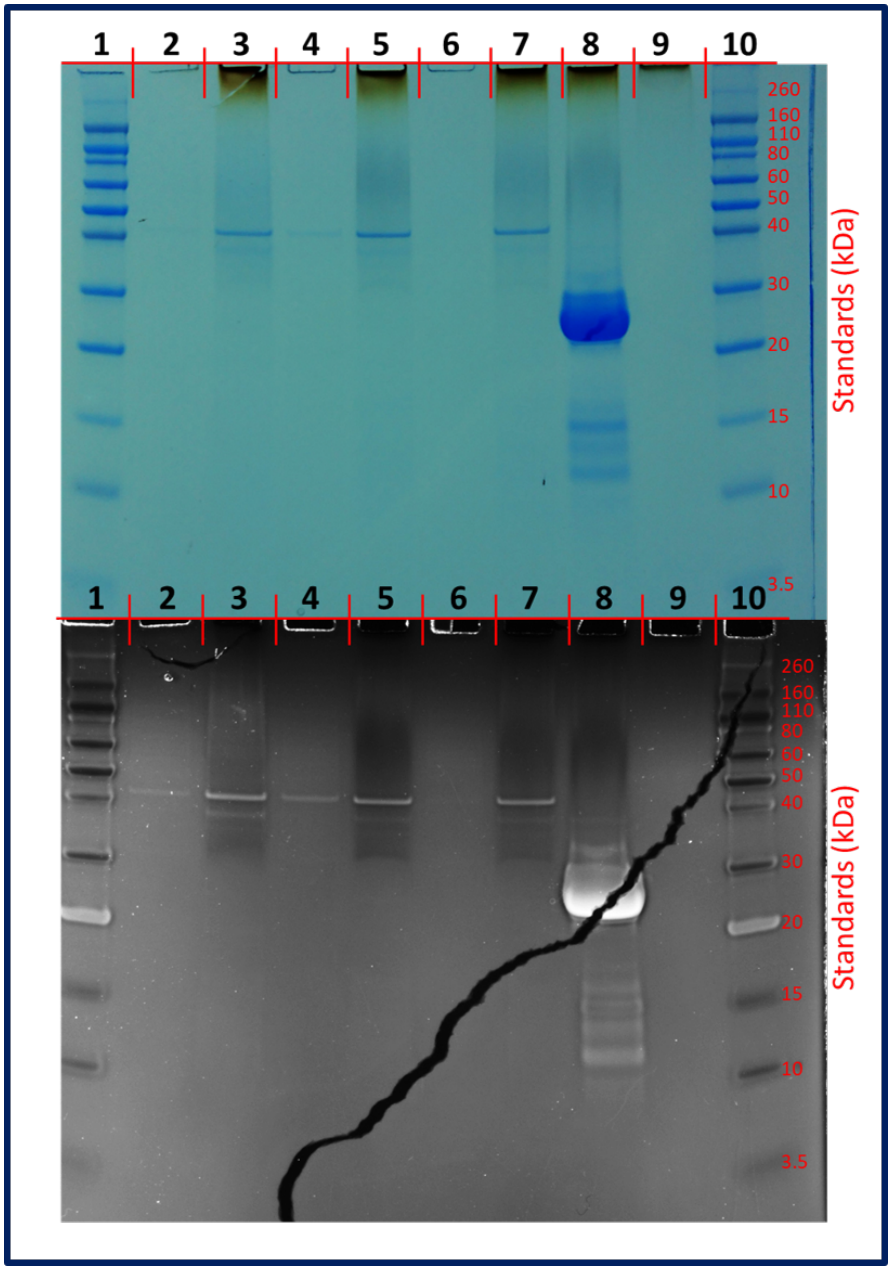

Figure 7.5: SDS PAGE of AgNPs produced by *M. psychrotolerans* stained with SimplyBlue (top) and SYPRO Ruby (bottom). Lanes: NovexSharp protein weight standards (1 & 10), the supernatant (2, 4, & 6) and AgNPs (3, 5, & 7) of 3 *M. psychrotolerans* cultures. An example of AgNPs incubated with proteinase K (8), and chemically produced Ag nanospheres (9).

7.3.5 Separation of Coronal Proteins by SDS PAGE

No bands were observed in the SDS PAGE lane containing the growth medium used (Figure 7.6 lane 2) signifying that there was no, or undetectable, amounts of oligopeptides or proteins in the yeast extract and tryptone mix used that could interfere with the visualisation of bacterial proteins in the gels. In contrast, considerable banding was observed in supernatant of *M. psychrotolerans* cultures (Figure 7.6 lane 3), as expected due to the secretion or proteins by the bacterium and through autolysis that occurs in stationary phase cultures. The banding was more visible when stained with the more sensitive SYPRO Ruby stain than when post-stained with Coomassie blue-based SimplyBlue (SYPRO Ruby has a higher sensitivity than SimplyBlue of 0.25 ng vs 7 ng of protein, as reported by the manufacturers).[306,307] The faintness of the bands suggests that the concentration of protein in the samples was low and near the detection limit of SimplyBlue in many cases. The manufacturer's instructions report that SimplyBlue is effective as a post-stain after SYPRO Ruby.

The storage and processing conditions of AgNPs were examined. AgNPs remain relatively stable in suspension for long periods of time at room temperature when stored in the dark (as discussed in Section 5.3.6). However, when a sample of AgNPs stored under these conditions for over 6 months was run on a SDS PAGE (Figure E.5 lane 5) no clear bands were observed using SimplyBlue staining but a very faint band at approximately 40 kDa – 43 kDa was observed when stained with SYPRO Ruby. Due to the faintness of the band and the long imaging exposure required to make it visible, the quality of the image was compromised making a clear identification of the band difficult. In addition to this band, a smear was observed at the top of the lane in both staining methods. This was attributed to the migration of small AgNPs into the gel. In contrast to the stored samples, freshly prepared samples (prepared less than 24 h before analysis) were observed to have clearly defined and visible bands indicating the presence of intact proteins in the samples. It should be noted that the protein loads were not normalised by concentration and so the differences in the intensities of the bands reflect the different processing and storage efficiencies. Freshly prepared samples were processed (collected, washed, and stored) at either room temperature ($\approx$ 24°C) or 4°C and on ice. AgNPs from the same production batch were processed under the two conditions. As shown in lanes 7 and 8 of Figure 7.6, bands were clearly visible in both staining methods in both lanes. However, the bands in the 4°C sample appear more intense which would indicate more protein being present in the bands. As the samples came from the same batch of AgNPs, this would suggest the 4°C processing method was more effective at collecting the proteins for analysis. However, no further quantification of protein concentrations was performed and would be required to validate this conclusion.

When the AgNP samples were separated by SDS PAGE, clear and distinct bands were observed (Fig-

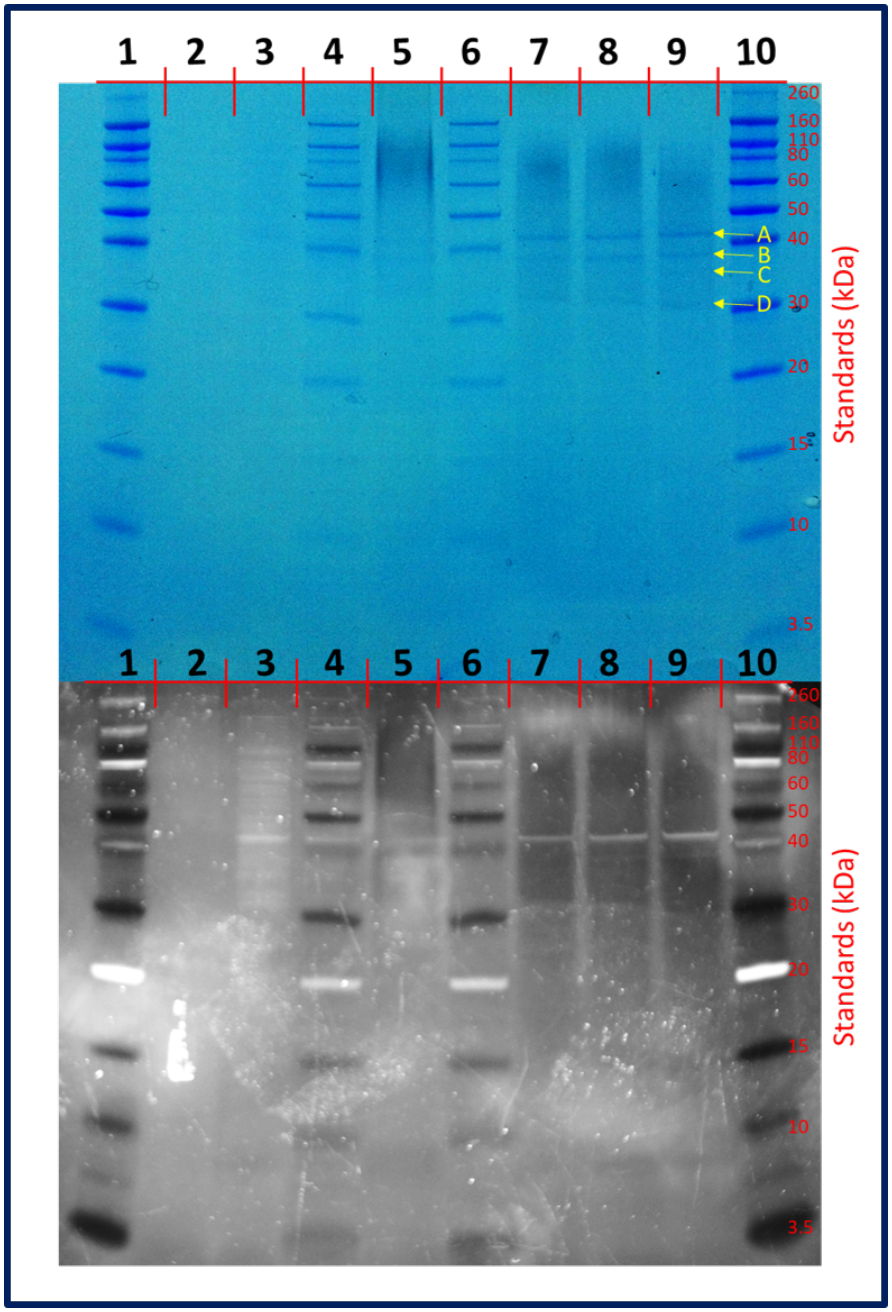

Figure 7.6: SDS PAGE of AgNPs processed under different conditions with SimplyBlue (top) and SYPRO Ruby fluorescence staining (bottom). Lanes: NovexSharp protein weight standards (1 & 10), LB (2), CFE from *M. psychrotolerans* culture (3), the protein standards incubated with CFE and loading buffer (4), AgNP sample stored at room temperature for approximately 6 months (5), the protein standards incubated with loading buffer (6), a fresh samples of AgNPs prepared at room temperature (7) and 4°C (8 & 9). Bands A - D are summarised in Table 7.1.

ure 7.5, tracks 3, 5, & 7). The intensity of these bands was, however, very weak suggesting there was a very low amount of protein present, although no quantification was performed. The bands were estimated to be approximately 43 kDa, 38 kDa, 36 kDa, and 31 kDa in mass for A – D, respectively (Table 7.1). The strongest band at 43 kDa was also clearly visible in the CFE sample (supernatant of bacterial culture not exposed to Ag) in tracks 2, 4, and 6 of Figure 7.5. Though it cannot be confirmed from this method as the same protein, this would indicate the protein responsible for the band present was in CFE and bound to the AgNPs to remain in the sample though the washing steps.

Table 7.1: SDS PAGE bands and possible proteins

Band	Estimated Mass (kDa)	Possible Proteins
A	43	Elongation factor Tu; Succinate–CoA ligase [ADP-forming] subunit β
B	38	Flagellin
C	36	Glyceraldehyde-3-phosphate dehydrogenase; Flagellar hook-associated protein 3; Transaldolase
D	31	Malate dehydrogenase

The AgNPs were still present in the samples when loaded in to the gels. After the SDS PAGE had been run, the wells containing AgNPs were discoloured with a brown/yellow residue (Figure 7.5 lanes 3, 5, & 7). This was thought to be due to the accumulation of AgNPs in the stacking gel; the brown colour corresponds to AgNPs observed in colloidal suspension, whereas the yellow is typical of a more size-uniform sample of AgNPs suggesting that the gel may be able to separate the AgNPs based on size. Moreover, discolouration and smearing were visible in the high weight region (110 kDa – 50 kDa) of the gels prior and after staining with both SYPRO Ruby and SimplyBlue stains. To determine if these smears could be caused by the AgNPs entering the running gel, to confirm this, chemically synthesised PVP-coated Ag nanospheres were also run in the gel. It can be seen in lane 9 of Figure 7.5 that the similar discolouration of the stacking gel is observed as with biogenic AgNPs. Additionally, smearing at the top of the lane in the running gel can be seen. This suggests that the smearing can be attributed, at least in part, to the presence of AgNPs in the gel.

The evidence from the SDS PAGE images supports previous reports of protein being present in the corona of AgNPs produced by bacteria.[52,75,76,95,103,142,308] Moreover, the multiple bands observed in AgNP samples indicates more than one polypeptide is present; this could be multiple different proteins or fragments of the same protein. This too supports previous work which identified multiple proteins bound to Ag_2S nanoparticles.[308]

In contrast to the 4 faint bands consistently observed in the AgNPs samples of this work, Voeikova et al. observed 11 distinct bands when the corona of *S. oneidensis*.[308] Moreover, in the case of *B. subtilis*, more

than 10 bands were observed from supernatant of the cultures while only one band was visible from the nanoparticle corona.[308] Contrary to this, it was observed in this study that similar banding patterns were present in both the supernatant samples and their corresponding AgNPs samples, as shown in lanes 3 & 4 of Figure 7.6.

7.3.6 Proteomic Investigation of Coronal Proteins

To identify the proteins bound to the AgNPs, proteomic analysis was performed using mass spectrometry where a total of 10 samples (5 AgNP samples and 5 supernatant control samples) were analysed. Across all samples, a total of 731 proteins were identified. When comparing replicates, 500 $\pm$ 71 proteins were identified in controls while 87 $\pm$ 48 were identified AgNP samples. Proteins identified in the controls appeared in 3.4 $\pm$ 1.7 replicates, whereas in AgNP samples, proteins appear in 2.5 $\pm$ 1.3 of replicates. A comparison is shown in Figure 7.7 of the distribution of proteins identified in each replicate in relation to its appearance in other replicates of the same sample type. It shows that 329 proteins were found in all 5 replicates of the control supernatant groups, whereas 20 were found in all 5 AgNP replicates. As a large number of proteins in both sample types were only present in one or two replicates, an occurrence threshold requiring proteins to be present in 4 out of the 5 replicates for each sample type to be considered. Following this, 37 proteins were identified bound to AgNPs and 409 proteins were identified in the supernatant. All of the 37 AgNP-bound proteins were also present in the supernatant; there were no proteins found to be unique to the AgNPs. For further analysis, the identified proteins were classified in to two groups: bound and unbound. The bound group consisted of the 37 proteins identified in the corona and the unbound group consisted of the 372 proteins present in the supernatant but not in the corona (Figure 7.8).

Far more proteins were identified by mass spectrometry in both AgNP samples and control supernatant samples than bands observed in SDS PAGE images. This is likely due to the superior sensitivity of mass spectrometry over SimplyBlue and SYPRO Ruby staining. Moreover, as the proteins were fully digested prior to proteomic analysis rather than being denatured for SDS PAGE, it is possible proteins remained adhered to the particles and so did not migrate into the gels. This illustrates a benefit of analysing the corona directly form the AgNPs over using excised gel bands.

Protein Abundance

The relative abundances of proteins in the corona and supernatant, and unbound proteins in the supernatant were calculated and are presented in Figures 7.9, 7.11, and 7.10, respectively.

With an abundance of 8.14 $\pm$ 4.74%, flagellin was the most abundant protein in the corona and super-

natant where it represented 3.85 $\pm$ 0.67% of total protein. The most abundant protein in the supernatant which was not present in the corona was glutamate/aspartate ABC transporter substrate binding protein (2.32 $\pm$ 0.15%) followed by cold shock protein as the second most abundant. These two proteins were the second and third most abundant proteins in the supernatant prior to the addition of $AgNO_3$. Moreover, of the 37 most abundant proteins in the supernatant before Ag^+ was introduced, 11 were found in the corona.

Protein Location and Function

When the subcellular locations of the proteins in the bound and unbound groups were examined, it was clear that the cytoplasm was the origin of the majority of the all of the proteins for which location data was available (Figure 7.12). In the bound proteins, only 10 have reported subcellular locations in the UniProt database. Two proteins were secreted into the extracellular environment and one was a membrane protein.

Based on gene ontology data reported in the UniProt database, the functions of the proteins identified could be classified (Figure 7.13). The largest group classified in the proteins bound to AgNPs translation related proteins; translation was also the most associated function of proteins found in the unbound group. Carbohydrate metabolism (including enzymes in the tricarboxylic acid cycle and glycolysis) was the second largest group in the bound proteins and was also a considerable proportion of the unbound proteins. Biosynthetic processes (synonymous with anabolic pathways) was a large proportion of unbound protein, but accounted for a smaller portion of bound proteins. It should be noted that the analysis does not take the abundance of each protein into consideration, but rather looks at all proteins identified equally.

Proteins Identified in the Corona

All 37 proteins identified on the surface of the AgNPs were also present in the control samples. This indicates that the proteins in the corona are expressed under the growth conditions used and were isolated through binding to the AgNPs during the washing and samples preparation processes. A full list of these proteins is given in Table 7.2. The two most abundant proteins in the corona (flagellin and a fragment of the elongation factor Tu) accounted for approximately 15% of the total protein coat.

Flagella are electro-chemical drive systems used by bacteria for motility. The organelles are typically comprised of 20 different proteins making up the trans-membrane motor and the extracellular filamentous propeller.[309] The propeller is a hollow helical structure made of up to 30,000 repeating monomers of flagellin.[309,310] The total flagellum can extend over to 10 μm in length (five time the cell length of *M. psychrotolerans*);[310,311] examples of *M. psychrotolerans*' can be seen in Figures 3.2 and 4.5 B. Because of the larger numbers of monomers used in the formation of a single flagellum, and that motile bacteria typically

produce 5 – 10 flagella across the cell surface, flagellin is one of the most abundant proteins expressed by such organisms.[312,313]

Flagellin was observed as the most abundant protein in the corona of AgNPs produced in this study by *M. psychrotolerans* accounting for 8.14 $\pm$ 4.74% (Figure 7.9), and was also observed in the coronae of *S. oneidensis* and *B. subtilis*, though the relative abundances were not reported.[308] In addition to flagellin, flagellar hook-associated proteins 2 and 3 were also observed in high abundance in the corona representing the fifth and sixth most abundant proteins in this study (3.90 $\pm$ 3.04% and 3.81 $\pm$ 1.35%, respectively); these proteins were not identified in the previous investigation into the corona of biogenic AgNPs.[308] Flagellin was the most abundant protein in the supernatant prior to the addition of $AgNO_3$ accounting for 3.85 $\pm$ 0.67% of all protein. A high abundance in the environment where the AgNPs form is likely the cause of the high abundance in the corona, as opposed to specific or target flagellin binding.

Elongation factor Tu is responsible for the delivery of amino acid-complexed tRNA to the ribosome during protein synthesis. As a result of its crucial role, it is known to be the most abundant protein expressed in *E. coli* accounting for 5% – 10% of total cell protein and had the highest copy number of all proteins when *E. coli* was grown in LB.[313,314] Indeed, ribosomal proteins and those involved in protein synthesis are known to be the most abundant proteins in the cytosol of *E. coli*.[315] This likely explains why such a large proportion of the corona was comprised of translation-related proteins, such as ribosomal subunits (Figure 7.13). As with flagellin, these proteins all appear in the control samples, with elongation factor Tu being the seventh most abundant. Therefore, they appear to have been enhanced disproportionally to the other proteins in the supernatant.

Both flagellin and elongation factor Tu were proposed as possible candidates for the banding observed in the SDS PAGE images due to their molecular weights (Table 7.1). The bands for which these were proposed were the most intense, especially in the case of elongation factor Tu. The high abundance of these proteins in the proteomic analysis supports this as higher amounts of protein in the gels corresponds with greater intensity of bands when stained. The band identified as flagellin in the corona of *B. subtilis* was also very intense which suggests it too was a highly abundant component of the corona; the investigation into *B. subtilis* used mass spectrometry only of intensely stained bands excised from PAGE gels making assessments of the abundance relative to the total corona not possible.[308]

The remaining 35 proteins identified in the corona are predominantly related to translation as either ribosomal proteins or being involved in translation, or carbohydrate metabolism (Figure 7.13). Neither flagella, ribosomes, nor carbohydrate metabolism have previously been observed or suggested to be involved in bacterial AgNP bioproduction. The proteins thought to be involved in the reduction of Ag^+ include

NAD(P)H-nitrate reductase, and the Sil family of proteins, particularly SilE, as discussed in Section 2.2.1. No Sil proteins were identified in any sample analysed in this study. A copper resistance protein was identified in the control samples, but in only one of the AgNP replicates, below the threshold for consideration. Limited functional information is available on this protein but it does not appear to be homologous to any of the Cus proteins.

Taken together, the results presented in this study suggest that while protein is a component of the corona, the functions of proteins appears to have little influence on their presence on the surface of the AgNPs. Instead, binding appears to be the result of the physiochemical properties of the proteins. The presence of these proteins does not infer functional activity on the surface of the particles. Indeed, many of the proteins identified are constituents of the translation pathways of protein synthesis. However, as Ag^+ is known to disrupt RNA, DNA, and protein synthesis, it is possible that these pathways are not functional.[47,316] It remains unclear, and ultimately the subject of future work, whether the proteins with catalytic functions remain active when in the corona. Moreover, the involvement of the proteins bound to the surface in AgNP production (i.e. Ag^+ reduction) is unclear. Previous reports have suggested NAD(P)H nitrate reductase as a crucial reducing component in the mechanism. Nitrate reductase subunit alpha was observed in all 5 supernatant replicates in this study (abundance = 0.05 $\pm$ 0.02%), but was not observed in any of the AgNP replicates.

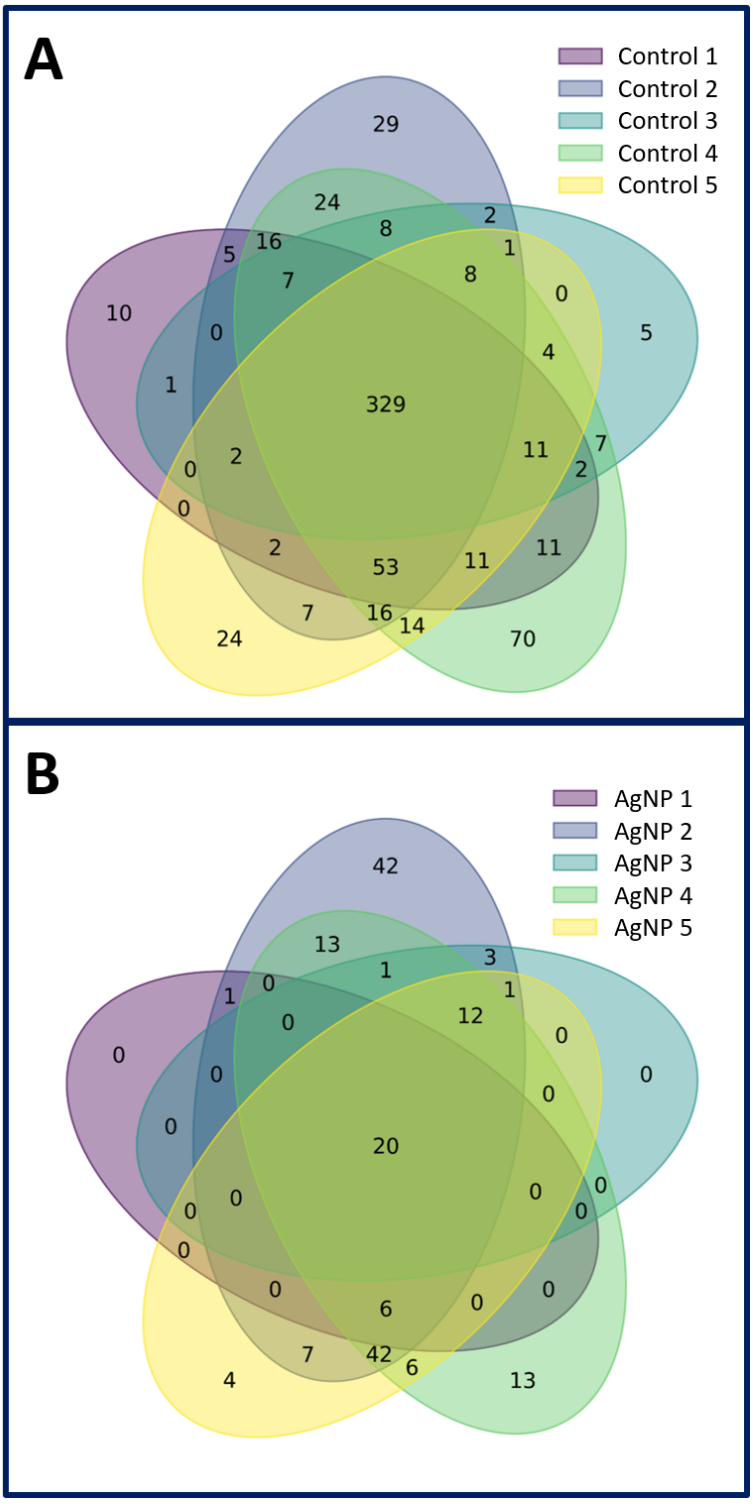

Figure 7.7: Comparison of number of proteins identified in replicates of supernatant control (A) and AgNP (B) samples. The 37 proteins identified in the AgNPs samples were considered the bound group and the 372 proteins present in the supernatant control were classified as the unbound group.

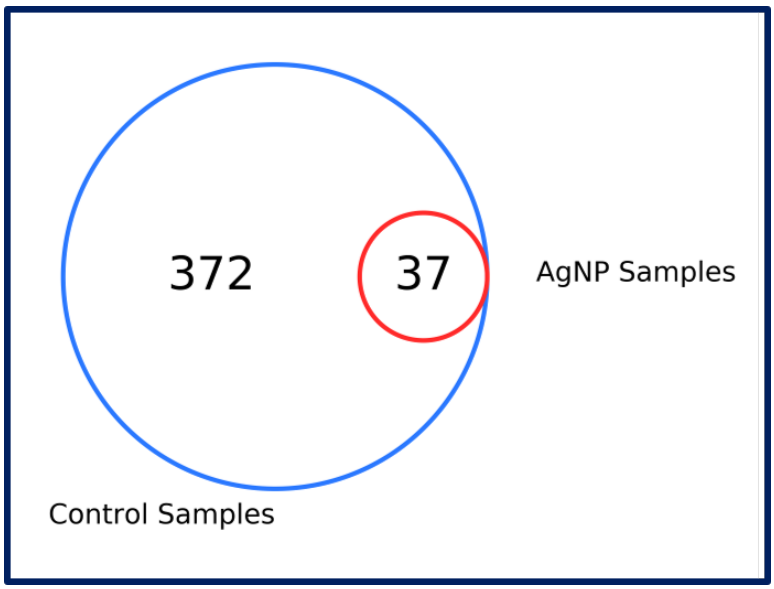

Figure 7.8: Comparison of number of proteins identified in at least 4 of the 5 replicates for AgNP (red circle) and supernatant control (blue circle) samples.

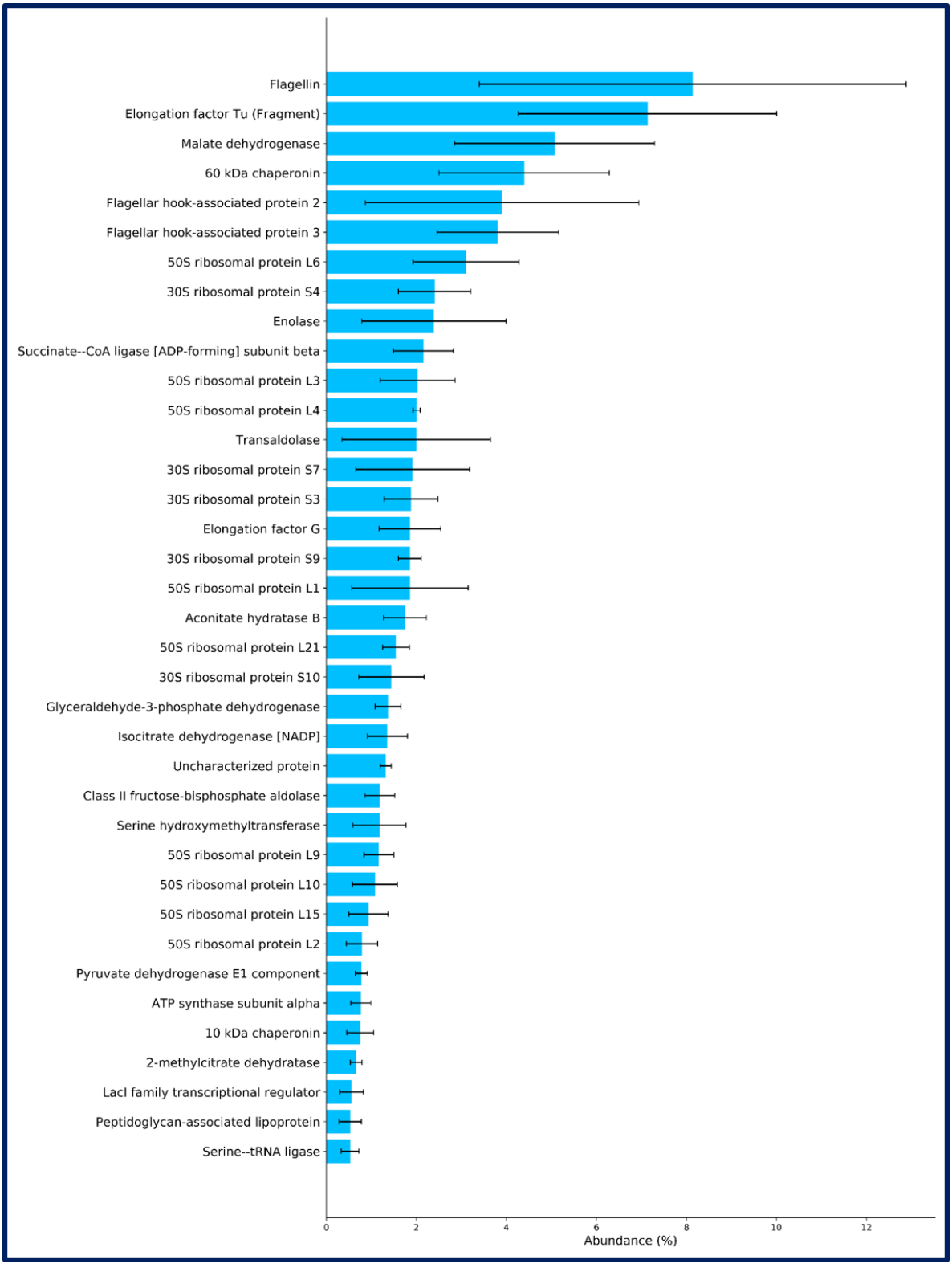

Figure 7.9: Abundance of all proteins bound to AgNPs present in at least 80% of replicates. Error bars show $\pm$ 1 SD.

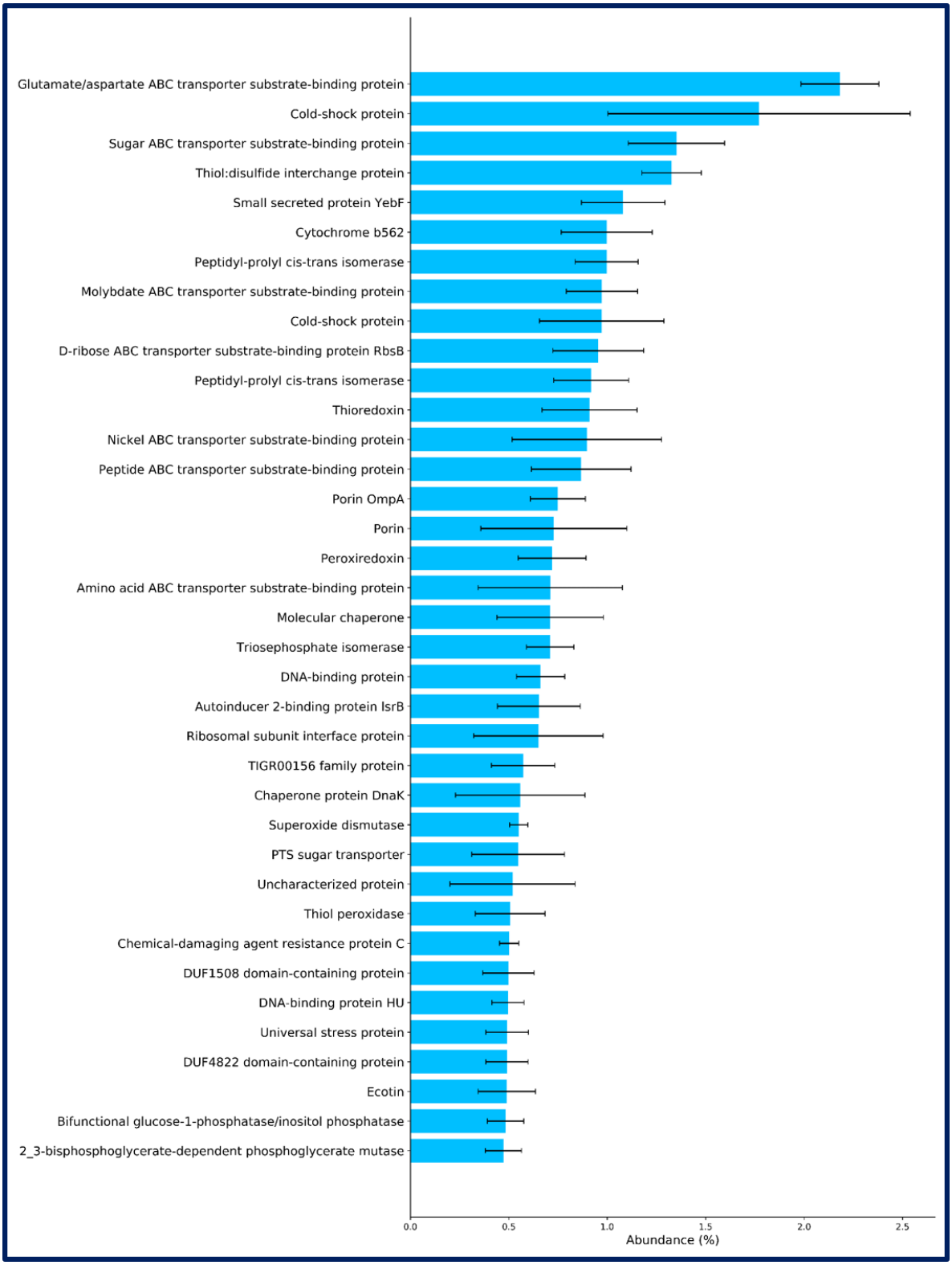

Figure 7.10: Abundance of the 37 most abundant proteins present in at least 80% of replicates that did not bind to AgNPs. Error bars show $\pm$ 1 SD.

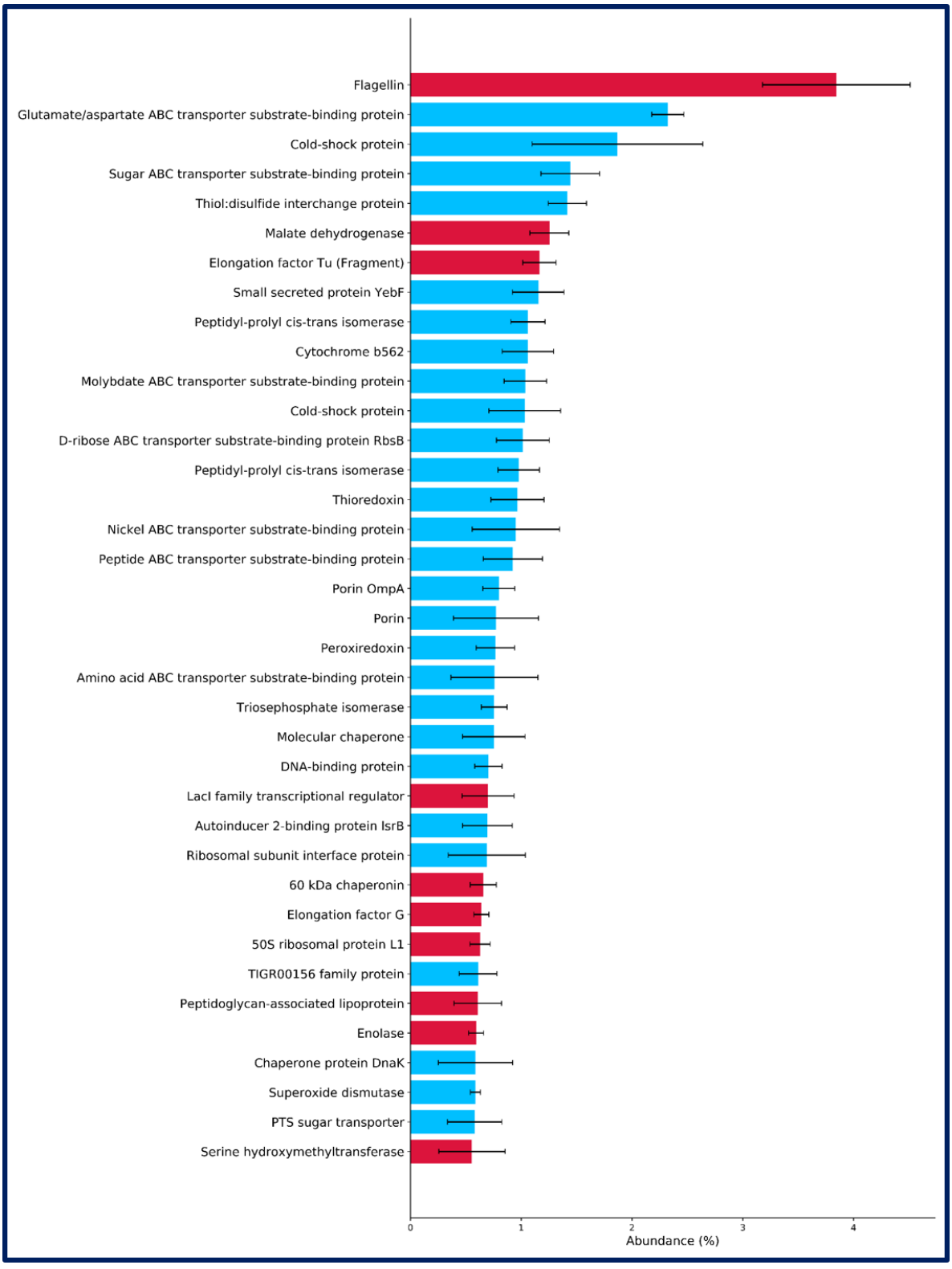

Figure 7.11: Abundance of the 37 most abundant proteins present in at least 80% of replicates in the supernatant of *M. psychrotolerans* cultures. Red bars indicate those proteins which were identified in the corona of AgNPs. Error bars show $\pm$ 1 SD.

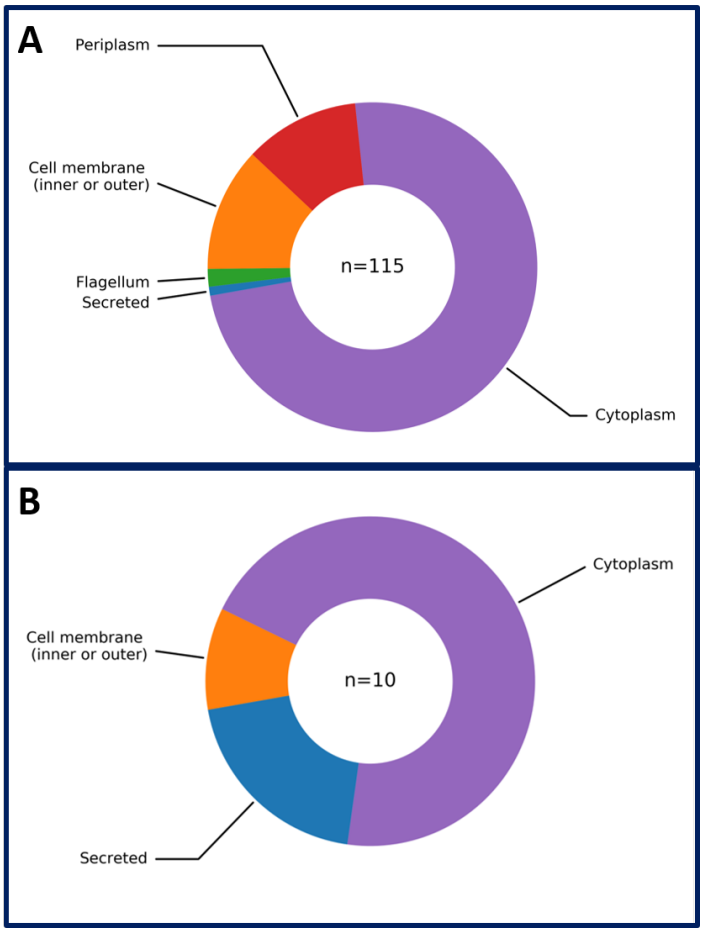

Figure 7.12: Subcellular locations of proteins bound (A) and that did not bind to AgNPs (B). n represents the number of proteins with reported subcellular locations in the UniProt database.

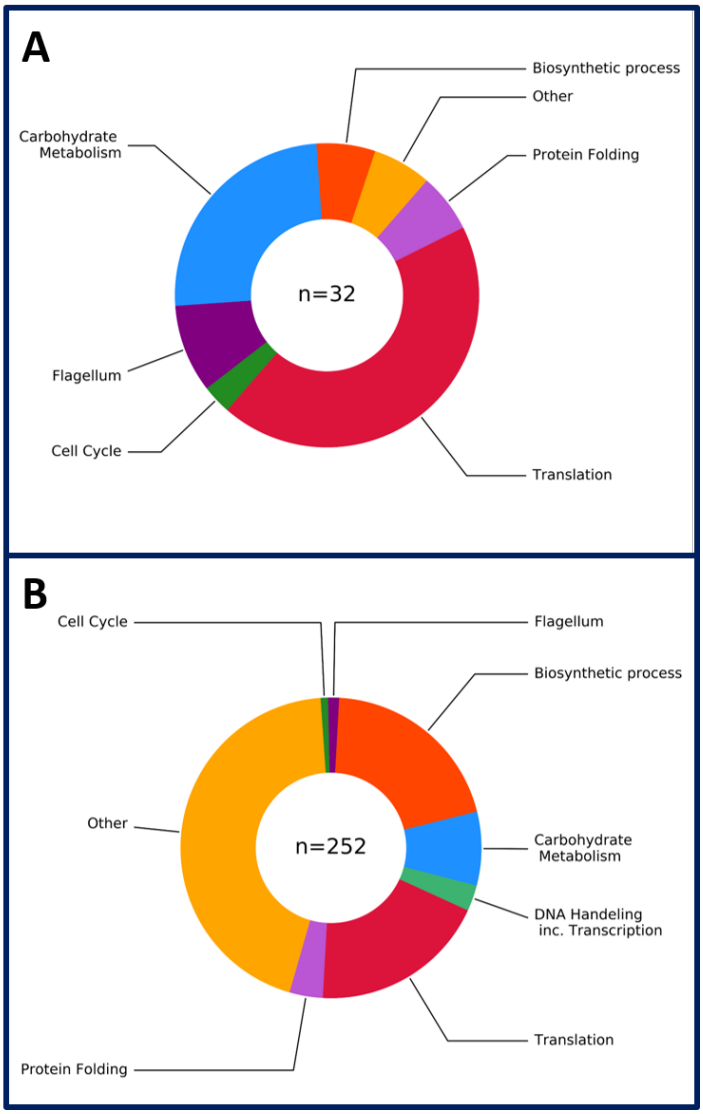

Figure 7.13: Functions of proteins bound (A) and unbound (B) to AgNPs identified by proteomic analysis. n represents the number of proteins in the samples with reported biological processes based on gene ontology in the UniProt database.

Table 7.2: Proteins identified in the corona of AgNPs produced by *M. psychrotolerans*

Name	Gene Name	Accession	Abundance (%)	Activity
Flagellin	AYY17_07560	A0A1B8H6R6_9GAMM	8.14±4.74	structural molecule activity
Elongation factor Tu (Fragment)	AYY17_20815	A0A1B8H862_9GAMM	7.13±2.87	GTP binding - GTPase activity - translation elongation factor activity
Malate dehydrogenase	mdh	A0A1B8HL30_9GAMM	5.07±2.22	L-malate dehydrogenase activity
60 kDa chaperonin	groL	A0A1B8HBZ6_9GAMM	4.39±1.89	ATP binding - unfolded protein binding
Flagellar hook-associated protein 2	AYY17_07550	A0A1B8H6R0_9GAMM	3.90±3.04	-
Flagellar hook-associated protein 3	AYY17_07370	A0A1B8H6M7_9GAMM	3.81±1.35	structural molecule activity
50S ribosomal protein L6	rplF	A0A1B8HBR1_9GAMM	3.10±1.18	rRNA binding - structural constituent of ribosome
30S ribosomal protein S4	rpsD	A0A1B8HCA4_9GAMM	2.41±0.81	rRNA binding - structural constituent of ribosome
Enolase	eno	A0A1B8HB79_9GAMM	2.39±1.60	magnesium ion binding - phosphopyruvate hydratase activity
Succinate–CoA ligase [ADP-forming] subunit beta	sucC	A0A1B8HDK7_9GAMM	2.16±0.67	ATP binding - magnesium ion binding - succinate-CoA ligase (ADP-forming) activity
50S ribosomal protein L3	rplC	A0A1B8HKX5_9GAMM	2.03±0.83	rRNA binding - structural constituent of ribosome
50S ribosomal protein L4	rplD	A0A1B8HBS4_9GAMM	2.01±0.08	rRNA binding - structural constituent of ribosome
Transaldolase	tal	A0A1B8H1J7_9GAMM	2.00±1.65	sedoheptulose-7-phosphate
30S ribosomal protein S7	rpsG	A0A1B8H1V9_9GAMM	1.92±1.26	rRNA binding - structural constituent of ribosome - tRNA binding
30S ribosomal protein S3	rpsC	A0A1B8HC74_9GAMM	1.88±0.60	mRNA binding - rRNA binding - structural constituent of ribosome
Elongation factor G	fusA	A0A1B8H3A5_9GAMM	1.86±0.68	GTP binding - GTPase activity - translation elongation factor activity
30S ribosomal protein S9	rpsI	A0A1B8HNY5_9GAMM	1.86±0.25	structural constituent of ribosome
50S ribosomal protein L1	rplA	A0A1B8HCD1_9GAMM	1.86±1.29	rRNA binding - structural constituent of ribosome - tRNA binding
Aconitate hydratase B	AYY17_13580	A0A1B8GZ93_9GAMM	1.75±0.48	2-methylisocitrate dehydratase activity - 4 iron, 4 sulphur cluster binding - aconitate hydratase activity - metal ion binding
50S ribosomal protein L21	rplU	A0A1B8GZM3_9GAMM	1.55±0.30	rRNA binding - structural constituent of ribosome
30S ribosomal protein S10	rpsJ	A0A1B8HKR9_9GAMM	1.45±0.73	structural constituent of ribosome - tRNA binding
Glyceraldehyde-3-phosphate dehydrogenase	AYY17_01400	A0A1B8HQ80_9GAMM	1.37±0.29	NAD binding - NADP binding - oxidoreductase activity, acting on the aldehyde or oxo group of donors, NAD or NADP as acceptor
Isocitrate dehydrogenase [NADP]	AYY17_12725	A0A1B8H095_9GAMM	1.36±0.44	isocitrate dehydrogenase (NADP+) activity - magnesium ion binding - NAD binding
Uncharacterized protein	AYY16_12955	A0A1B8H6F6_9GAMM	1.32±0.12	-
Class II fructose-bisphosphate aldolase	AYY17_06635	A0A1B8HB86_9GAMM	1.19±0.33	fructose-bisphosphate aldolase activity - zinc ion binding
Serine hydroxymethyltransferase	glyA	A0A1B8HEX7_9GAMM	1.18±0.59	glycine hydroxymethyltransferase activity - methyltransferase activity - pyridoxal phosphate binding
50S ribosomal protein L9	rplI	A0A1B8HL37_9GAMM	1.17±0.33	rRNA binding - structural constituent of ribosome
50S ribosomal protein L10	rplJ	A0A1B8HCE6_9GAMM	1.08±0.50	large ribosomal subunit rRNA binding - structural constituent of ribosome
50S ribosomal protein L15	rplO	A0A1B8HKT9_9GAMM	0.94±0.44	rRNA binding - structural constituent of ribosome
50S ribosomal protein L2	rplB	A0A1B8HBM7_9GAMM	0.79±0.35	rRNA binding - structural constituent of ribosome - transferase activity
Pyruvate dehydrogenase E1 component	AYY17_13560	A0A1B8GYZ1_9GAMM	0.78±0.14	metal ion binding - pyruvate dehydrogenase (acetyl-transferring) activity
ATP synthase subunit alpha	atpA	A0A1B8HL79_9GAMM	0.76±0.22	ATP binding - proton-transporting ATP synthase activity, rotational mechanism
10 kDa chaperonin	groES	A0A1B8HC09_9GAMM	0.75±0.30	ATP binding
2-methylcitrate dehydratase	AYY17_08625	A0A1B8H792_9GAMM	0.66±0.13	2 iron, 2 sulphur cluster binding - 2-methylcitrate dehydratase activity
LacI family transcriptional regulator	AYY17_01015	A0A1B8HPE4_9GAMM	0.56±0.26	-
Peptidoglycan-associated lipoprotein	AYY16_16725	A0A1B8HRV7_9GAMM	0.53±0.25	-
Serine–tRNA ligase	serS	A0A1B8H543_9GAMM	0.53±0.20	ATP binding - serine-tRNA ligase activity

* Activity information derived from UniProt entries.

7.3.7 Coronae of Other Organisms

Few studies have been published which have identified the proteins in the corona of biogenic AgNPs. The proteins which have been identified to date are shown in Table 7.3. As discussed, the coronae of AgNPs produced by *S. oneidensis* MR-1, *E. coli* K12, and *B. subtilis* 168 have been interrogated by mass spectrometry.[308] Bands were excised from a polyacrylamide gel and analysed as discrete samples; this is in contrast to the holistic approach used in this work. All of the proteins identified were shown to be associated with the outer or cytoplasmic membranes.[308] While a small proportion of the proteins identified in the corona of AgNPs from *M. psychrotolerans* were associate with either the outer cell membrane or the periplasmic membrane, the vast majority are typically found in the cytoplasm.

Porin OmpA was abundant in the supernatant of *M. psychrotolerans* supernatant in this study, but not identified in the corona of AgNPs. In contrast, OmpA and other porins were observed in the coronae of AgNPs from both *E. coli* and *S.oneidensis*. This highlights the apparent species-dependent composition of coronae.

The surface coverage of the nanoparticles was estimated to be 12%, 22%, and 1% for *S. oneidensis*, *B. subtilis*, and *E. coli*, respectively.[308] This was estimated from the calculated average surface area of the nanoparticles and the amount of protein bound to the nanoparticles. Assuming a protein size based from the average molecular weight of the proteins, the surface coverage and number of protein molecules bound to each particle were estimated. This allows for differences in protein adhesion to be compared between the species investigate. This could not be done in this work as the amount of bound protein was not determined (discussed in more detail below). However, it could provide a usefulness to gain insight into how different conditions affect the formation and composition of the corona over time.

In addition to the 3 bacterial species investigated, AgNPs produced by the fungus *Aspergillus tubingensis* have been examined.[248] A small number of proteins were identified on the surface of the particles but these, in contrast to those produced in the previously reported bacteria, were not membrane associated proteins. The proteins, namely acid phosphatase, glycosidase, serine carboxipeptidase, and glucanosyltransferase, are parts of metabolic pathways relating to carbon, phosphorus, and nitrogen uptake and fungal growth.[248] Additionally, all of the proteins were acidic with isoelectric points between 4.0 and 5.1, and varied in molecular weight from 39 to 65.5 kDa, this is comparable to the 39.1 $\pm$ 24.1 kDa of bound proteins observed in this study. In contrast to Parikh et al., the binding of proteins to the surfaces of the AgNPs was thought to be through thiol groups, rather than aromatic carbon atoms, as determined by FTIR spectroscopy.[52,248]. Further analysis into the binding of the proteins onto the AgNPs using X-ray photoelectron spectroscopy, as used by Parikh et al. may be a useful avenue of future research.[52]

Table 7.3: Comparison of proteins identified in the corona of AgNPs produced by other organisms in previous studies.

Proteins identified in coronae of AgNPs
***Shewanella oneidensis* MR-1**
Arg R-regulated TonB-dependent receptor
TonB-dependent siderophore receptor
TonB-dependent heme/hemoglobin receptor
TonB-dependent vitamin B12 receptor
FadL family outer membrane receptor
Global secretion system secretin TolC
Outer membrane porin
Outer membrane porin Omp35
Flagellin FliC
Protein of the outer membrane OmpK
Protein of the outer membrane OmpW
Protein of the outer membrane A
Outer membrane porin OmpK
***Escherichia coli* K12**
Maltoporin
Outer membrane porin OmpC
Outer membrane porin OmpA
Outer membrane porin OmpX
***Bacillus subtilis* 168**
Flagellin
Aspergillus tubingensis
Hypothetical protein An01g11010 (Glycosidase)
Preproglucoamylase G2
Hypothetical protein An04g08730 (Unknown function)
Acid phosphatase
Glucoamylase G1
Hypothetical protein An03g05200 (Serine carboxypeptidase)
Hypothetical protein An09g00670 (Glucanosyltransferase)

The data from *S. oneidensis*, *E. coli* and *B. subtilis* were reported by Voeikova et al.[308] The data from *Aspergillus tubingensis* were reported by Ballottin et al.[248]

7.3.8 Considerations and Limitations

Soft Corona vs Hard Corona

Hitherto, much of the research on the coronae of AgNPs has come from the field of toxicology where chemogenic AgNPs are introduced to a tissue samples (e.g. serum or cell cultures) and the proteins from the host which bind onto the particles are analysed for insights into the effects of the AgNPs.[291,317,318] From this work, the corona is considered to be comprised of two main parts: the hard corona and the soft corona.[318,319] The hard corona is a layer of strongly bound protein in direct contact with the surface of the particles, whereas the soft corona is made of more loosely bound proteins with lower bindings affinities to the particles. A meta-stable coating is proposed to initially form of high abundance proteins.[320] This coating is under equilibrial flux with unbound proteins in the surrounding environment which have higher binding affinities but lower abundances that replace coronal proteins with lower binding affinities. This process can take several hours depending on the conditions such as temperature, the proteins present, and particle properties.[319–322]

In this work, the AgNPs were washed multiple times in PBS. Due to the high variation in protein dissociation rates, the proteins identified on the particles may be susceptible to differences in the methods used for isolation and analysis with multiple washing steps likely removing proteins with low binding affinities.[323] The results presented in this study are, therefore, likely to be representative of the hard corona. It is unclear, however, if the soft corona was completely removed, and to what extend it remained if it was not. Analysing the soft corona remains challenging as it must be preserved sufficiently while unbound material, such as secreted proteins and growth medium components, are removed, though using size affinity chromatography has been proposed as a possible approach. Understanding how the corona of AgNPs produced by *M. psychrotolerans* evolves overtime may be valuable when considering the stability of particles in commercial applications.

Intracellular and Extracellular AgNPs

This study only examined AgNPs isolated from the extracellular environment. As the CFE of *M. psychrotolerans* cultures possesses the ability to reduce Ag^{+} and form AgNPs, many of these particles are likely to have formed outside of the cells. However, it is also clear from TEM imaging of cells exposed to Ag^{+} (e.g. Figure 4.5) that particles form inside or in very close proximity to the cells; previous reports support this with AgNPs present inside *P. stuzeri*, *Rhodococcus* spp., and *Bacillus* sp.[43,121,324] The differentiation of intracellular and extracellular AgNPs has received little attention. However, the different local conditions and protein abundances experienced in the cytoplasm or periplasm compared to the culture supernatant

would likely have considerable impact on the composition of coronal. While an extraction method has been developed to isolate intracellular nanoparticles, this approach would likely disrupt the corona due to the use of chloroform and ethanol washing steps.[325] Extracting these AgNPs without disrupting the corona may prove challenging, but comparing the coronal compositions of the intracellular and extracellular AgNPs would likely be of great interest, especially considering the higher tendency to find non-spherical and larger particles in the intracellular environment. Any differences may shed light on the mechanisms at play.

Quantification of Protein and AgNPs

Although the relative abundances of proteins were estimated, a quantitative approach was not taken throughout this work; the protein concentrations in the supernatant samples and the amount of protein bound to the nanoparticles were not determined. Additionally, protein loads were not normalised prior to SDS PAGE, as is often done.

The quantification of protein bound to AgNPs is challenging, though efforts have been made to develop a reliable method, albeit with their own limitations.[326,327] Challenges emerge due to the small sample size and the limited sensitivity of the most commonly used colorimetric assays. Additionally, the requirement of washing the nanoparticles prior to analysis in these assays likely leads to losses of loosely bound proteins. Caution should also be taken when considering using colorimetric or fluorescence-based assays as the optical properties of the AgNPs can interfere with the chromophores or fluorophores, for instance by absorbing at the excitation or emission wavelengths of a fluorophore.

Knowing the amount of protein present is valuable if the size and concentration of AgNPs in the sample is also known as it would allow the available surface area of the nanoparticles to be calculated, and from this, the protein coverage could be estimated; such a approach has previously reported.[308,321,326] The protein coverage could be used to assess the stability of the corona under different condition. Therefore, future work would benefit from the measuring of absolute protein and AgNP concentrations.

Determining the concentration of AgNPs presents its own challenge. As AgNPs follow the Beer-Lambert law which states that the absorption of a substrate is proportional to its concentration, a simple calibration curve can be generated using known standards. However, the absorption is also dependent on the molar extinction coefficient (ε). The $\varepsilon$of AgNPs is in turn dependent on the optical properties, and thus the shape and size, of the particles; this includes the polydispersity of the samples as a more dispersed sample typically exhibits a broader LSPR absorbance peak. Therefore, generating known standard with the same $\varepsilon$is challenging. The use of a standard with similar, but not identical properties, may be used with the compromise of a loss in accuracy. Nanoparticle tracking analysis (i.e. NanoSight) was unsuccessfully

attempted in this work; the scattering properties of the AgNPs used were not comparable with the laser source available.

It would also be valuable to know if any protein remained bound to the particles after digestion during the preparation of samples for proteomic analysis. This was not done here but it is possible proteins or peptide fragments remained bound to the particles were removed from the samples. Peptides with strong affinities to the particles may be more likely to remain bound and their losses may skew the reported findings. Employing a matrix-assisted laser desorption/ionisation (MALDI) as a method for generating ions may allow for the proteins to be ionised directly from the surface of the particles. However, analysis of the data generated would be more challenging without the predictable digestion with trypsin.

While this would undoubtedly add value to the results presented herein if the protein concentrations and coverages were known, it was not deemed essential for this project but should be a consideration in future investigations.

Cell Viability and Corona Formation

Ag^+ is toxic to bacterial cells. Attempts to re-culture *M. psychrotolerans* after long (24 h) incubations with Ag were unsuccessful. Although more detailed investigations into the fate of the cells were not undertaken, it would suggest that the cells are metabolically active at normal levels for the whole period. Therefore, questions remain regarding how much of an effect on protein expression Ag^+ at the concentration used had. Investigations into the viability and activity of the cells during the AgNP production process would shed light on this question. Tools including time-resolved transcriptomics and proteomics would show how the cells respond to the stress of Ag^+.

7.3.9 Future Work

Binding Affinities of Proteins to AgNPs

The physical and chemical properties of the proteins were interrogated in this study to elucidate the reasons behind the different apparent binding affinities of proteins with the AgNPs (See Appendix E.3). However, due to challenges in the methodology used, low confidence was held in the results. Consequently, such analysis is still required to understand the formation of the corona and is ongoing and the subject of future work.

Proteomes in Response to Ag^+ and AgNP

Comparison between the native secretome of *M. psychrotolerans* and the protein excretion after the production of AgNPs is of particular importance as it will not only reveal if the protein binding is specific, but will also likely shed light on the mechanisms involved in AgNP production and Ag^+ resistance. Such work has been performed in *P. aeruginosa* and *B. thuringiensis*, but to date has not been reported in *M. psychrotolerans*.[328,329]

Protein-driven Crystal Growth

A number of proteins have been added to chemogenic AgNPs to improve the stability; albumin for instance is known to reduce the agglomeration of AgNPs.[24] However, proteins can also influence the shapes of AgNP produced. Chakraborty et al. demonstrated that catalase could drive the growth of citric acid coated seed AgNPs to prismatic geometries while lysozyme resulted in more spherical particles.[292] The non-spherical growth of the particles was attributed to the number of accessible lysine residues present in the proteins. In a separate study, Pu et al. reported that the LSPR properties of AgNPs produced by the UV-driven degradation of AgCl could be affected by different proteins present during the reaction.[293] While the morphologies were not as anisotropic as the previous report, the results show that different proteins can influence crystal growth. Therefore, it may be possible to control the morphologies of particles during production in a bacterial system by altering the proteins present, for instance by up-regulating the expression of catalase.

7.3.10 Corona of Other Species

From the limited data available and the different methodologies used in the literature, it is difficult to assess how generalisable the results presented in this work are to other bacterial species.[248,308] By characterising the coronae of other species, it may be possible to gain a better understanding of the mechanisms through which they form. Moreover, it would allow for consistent trends to be identified which would make identifying key protein of interest easier. This could be useful in controlling coronae in the optimisation of production processes for different applications.

7.4 Conclusions

The presence of protein on the surface of bacterially produced AgNPs is of great interest when considering the applications of such materials. Here, the coronae of AgNPs produced by *M. psychrotolerans* was

investigated. SDS PAGE revealed multiple proteins present in the corona. Proteomic analysis identified 37 proteins in the corona. All of which were also present in the culture supernatant prior to the addition of $AgNO_3$. The binding of proteins to the AgNPs appears to have been driven by the abundance of and physiochemical properties of the proteins rather than selective binding for functional activity. Gaining a better understanding of the mediating factors involved in protein-AgNP binding would be required.

When compared with the proteins identified in the coronae of other organisms, it is clear that there is little overlap. This highlights the need to characterise the coronae of AgNPs produced by multiple species to be able to gain a better understanding of the factors affecting the coronae during formation. Moreover, the dynamic nature of the corona makes it important to consider the processing methods and analytical tools used.

Chapter 8

Discussion and Conclusions

8.1 Project Summary

AgNPs hold great potential in applications ranging from medical wound dressings to prevent infection, to optical coatings on vehicles. However, persisting challenges with the production of this material in chemical or physical processes are hindering their widespread use on industrial scales. Bacterial synthesis of AgNPs offers a possible alternative production route with a more environmentally friendly process for producing stable particles. This project aimed to develop a production method for these stable particles using bacteria and to explore ways in which the process could be optimised for larger scale production. Alongside this, insights into the mechanisms underpinning the biology and chemistry of the results observed was gained.

8.2 Summary of Key Findings

Effects of Reaction Conditions

A series of reaction conditions were explored for their effects on AgNP bioproduction. It was evident that while some conditions, namely reaction duration, concentration of Ag^{+}, and pH, had an impact on the amount of production observed, the absorption spectra of the particles produced under the different conditions did not change. This suggested that the particles being produced were morphologically similar. The ability to change the shape of the particles away from spherical or quasi-spherical does not appear to be achievable by simply changing the reaction conditions examined. An interesting and somewhat serendipitous observation of enhanced production was observed when samples were exposed to sunlight. With a substantial increase in production yield, the effects of light on production were examined further.

Photo-Enhanced AgNP Bioproduction

In chapter 4, LED light was used to enhance AgNP production. By utilising LED lighting over halogen, tungsten, or xenon lamps, meant the energy usage and heating could be minimised. Production was seen to greatly increase on exposure to white light and through examination of different filters and a UV lamp, it was evident that production favoured shorter wavelengths of light with blue and UV light yielding the greatest amount of AgNPs. The mechanism for this activity is thought to be the result of photo-induced fragmentation of small molecules such as amino acids. Indeed, considerable production was observed in sterile growth media when exposed to light. Though, importantly, the stability of the AgNPs produced in LB was lower than those produced in the presence of *M. psychrotolerans* cells.

Rapid AgNP Production Enhanced by Laser Light

Following the use of LED lights and UV lamps for AgNP production, lasers were investigated (Chapter 5). The high intensity of laser light allowed for the rapid production of AgNPs to be achieved on a time scale of seconds, rather than hours or days. The particles produced were spherical or quasi-spherical with smaller and more uniformly distributed sizes when prepared in CFE than whole cell cultures. By measuring the temperature throughout the production, it was concluded that heating was likely not responsible for the observed results, and rather it was a photo-catalytic mechanism. The particles produced were stable for 150 days with little change in the UV-Vis spectra.

Photo-Driven AgNP Bioproduction in Flow

The translation of batch reactions of photo-driven AgNP bioproduction to flow reactors proved successful in Chapter 6. Through the use of low-cost and easily manufactured prototypes, bespoke reactors were used to test a series of design elements to ultimately develop a viable flow system. Challenges regarding reactor fouling with the deposition of AgNPs on the internal surfaces of the reactors remains to be overcome. Investigations into reactor materials, surface coatings, and flow patterns are required for further optimisation.

Investigation of Corona Composition

Many previous reports have suggested the presence of protein on the surface of biogenic nanoparticles; the findings of Chapter 7 support these. Due to the small size of the corona, it proved challenging to interrogate its composition by spectroscopic techniques. However, TEM imaging revealed a possible visual

confirmation of the corona. When separated by SDS-PAGE, a number of bands were clearly visible indicating the presence of multiple protein or protein fragments. Following this, proteomic analysis was used to identify these proteins. A total of 37 proteins were identified in the coronae of AgNPs. The proteins tended to be in high abundance in the supernatant of cultures which had not been exposed to Ag. Therefore, it was concluded that the protein corona is made of abundant proteins which bind strongly to the AgNPs, rather than proteins with specific functions in nanoparticle synthesis.

8.3 Review of Project Aims and Objectives

The primary aim of this project was to develop an environmentally friendly and scalable method for the production of stable AgNPs through the use of bacteria. This was achieved as AgNPs have been produced by biologically sourced reducing agents which omits the need for more hazardous chemicals, such as sodium borohydride. The development of a flow reactor which is capable of producing AgNPs continually allows for this method to be scaled with relative ease.

The ability to control the morphologies of the particles produced in bacteria is yet to be obtained. Although some non-spherical particles were observed, the reasons behind their formation are unknown. Despite efforts to reproduce them and replicate the work of others, they could not be formed with the apparent relative ease reported in previous work.[57]

8.4 Potential Applications of the AgNPs Produced in this Project

The purpose of this project was to develop a method for producing AgNPs which could ultimately be used in real-world applications. Initial intentions were focused on the shape-specific uses in optically-active surface coating, for example low observable materials or energy saving glazing. However, as the ability to produce prismatic particles was not achieved, this remains a future goal. The particles synthesised in this study may see use in applications which do not require strict optical properties, for instance antimicrobial coatings, or chemical catalysts. The commercial viability of biogenic AgNPs remains to be determined but increasing production yields through the use of flow reactors will likely make it a more competitive material.

8.5 Shortcomings and Limitations of this Project

While efforts were taken throughout to maximise the power of the reported results, some limitations should be taken into consideration when interrupting the conclusions herein:

- *M. psychrotolerans* was use throughout this project. While *E. coli* and *P. fluorescens* were briefly investigated, no other organisms were studied. This limits how the findings, especially those pertaining to the biological aspects of the project, can be generalised across all bacteria. Further investigations into other organisms will be required to see if the results can be transferred. The Sil genes are known to exist in the PMG101 plasmid, and are found in multiple species. Likewise, NAD(P)H reducatases are ubiquitous in bacteria. It is possible, therefore, that the mechanism of AgNP production is similar in many of the reported strains. How the corona composition varies between species is unclear and will require further proteomic analysis to be determined.

- UV-Vis spectroscopy was used extensively throughout this project as the primary tool of detecting AgNPs and estimating the morphologies of the particles. While this is a routinely used method, minority populations of non-spherical particles may not be detected. For examples, TEM revealed a small number of triangular particles in this project but there was no spectroscopic evidence to support their presence. Ideally, TEM would be used to examine every sample produced in detail, but this would be prohibitively time consuming and expensive.

- This project used UV-Vis spectroscopy to estimate the relative amounts of AgNPs in samples. As discussed in Section 2.3, UV-Vis spectroscopy utilised the Beer-Lambert law to relate the absorbance at a given wavelength to the concentration of an analyte. However, this linear relationship only exists between given absorbance values which are dependent of the analyte of interest, the spectrometer, and the software used to collect data and control the machine.

  As shown in Appendix Figure C.4, the concentration range of AgNPs in the Lambda 35 spectrometer (PerkinElmer) use in this work was linear up to an absorbance of 2.5. Beyond this limit, errors could be introduced into the data. If absorbance values were recorded above this limit, samples were diluted to reduce the absorbance and then the values were scaled by the dilution factor. Ideally, all sample would be diluted equally, but due to the high variation between samples, especially in experiments using light exposure, this was not always possible as some samples had very low concentrations and diluting further would introduce considerable noise into the signal.

- The composition of the nanoparticles has been assumed to be Ag throughout this project. This was because the UV-Vis spectra of these particles matched what is expected from AgNPs. However, without elemental composition and crystallographic analysis, the particles cannot be completely identified. Ag oxide, Ag chloride, and Ag sulphide nanoparticles have been reported and often have similar absorption properties.[153] It is important to confirm the composition of these nanoparticles in future

work as their behaviour may differ and impact their use in certain applications.

- Throughout this project, LB with no added NaCl was used to culture *M. psychrotolerans*. While this modified LB is routinely in similar studies,[51,52,57,99] its use should be reported with the caveat that it may not be consistent between studies, or experiments as it is not a chemically defined medium. The variation comes from the non-standardised sources of the ingredients as it is comprised of 10% tryptone and 5% yeast extract. Tryptone is produced as the enzymatic digest of pancreas, whereas yeast extract is produced from the autodigestion of *Saccharomyces cerevisiae*. These are not perfectly defined sources as the nutritional compositions are not precisely controlled. As a result, there can be considerable batch-to-batch variation. The differences in medium composition may explain some of the conflicting or different results observed in the literature and this study.[51,57]

  Most nutritionally-rich media, such as LB, MHB, and tryptic soy broth, contain ill-defined components. Their widespread use is permitted due to their convenience and effectiveness with the trade-off of less controlled composition. Avoiding these media in place of better-defined minimal media, such as M9, that do not contain digests or extracts of biological materials, may help to improve the inter-experiment comparisons in this field. Special considerations also need to be made, however, for the use of halides, especially chlorides, in the media due to the involvement of Ag^{+} and its tendency to form insoluble precipitates.

8.6 Remaining Research Questions and Proposed Future Work

Biological Mechanism

The biochemical mechanisms underpinning AgNP bioproduction remains to be fully elucidated. While efforts have been made to identify the key components of any such pathways, large gaps remain.[4,6,62] Questions also remain over the generalisability and specificity of some of the previously reported mechanisms. NAD(P)H-dependent nitrate reductases have been cited as contributors to fungal and bacterial AgNP production. However, limited evidence exists to suggest this is an exclusive pathway, and indeed, additional mechanisms likely exist and operate in parallel.

To expand this understanding, molecular biology and “omics” techniques would likely be valuable. Investigations which explore how global gene and protein expression levels change with the addition of sub-bactericidal concentrations of Ag^{+} in the context of AgNP production would be insightful to gain an understating of not only a possible AgNP synthesis mechanism, but also the overarching Ag resistance systems, no doubt useful in medical applications for Ag-based antimicrobials.

Morphology Control of AgNP Bioproduction

Non-spherical AgNPs were observed in TEM images, though they were very rare and elusive. The source of these particles remains a mystery and the inability to reproduce it was frustrating. Nevertheless, it shows that non-spherical morphologies are possible in bacteria systems, supporting previous findings.[43,57,65,75,108,120]

The corona of the nanoparticles plays an important role in stability of colloids, but also the morphological stability of the particles by protecting the surface from oxidisation and etching.[319] This protection is one of the appeals of biosynthetic production routes. However, this protection also appears to act as a double-edge sword. The particles are too stable and resistant to surface alterations which makes morphological control during or after the growth stage challenging. The effectiveness of citrate as a capping agent to preferentially drive facet-selective crystal growth in chemogenic synthesis is due to the binding affinity of citrate to the 100 facet being higher than to the 111 facet.[21] If a protein could be identified which exhibits similar preference for a crystal facet, it may be possible to use to grow non-spherical AgNPs with much higher efficiency than observed in this project. This has been achieved in a chemical system, but translating this to a biological system may be challenging.[292] If these methods do prove successful at driving particle growth towards non-spherically shaped particles, their translation into a flow system will be a critical achievement for larger scale production.

Mechanism of Photo-assisted AgNP production

The mechanism of AgNP production in CFE and growth media is thought to involve the photo-fragmentation of small molecules such as tyrosine and tryptophan. By knowing the which ingredients in the growth media are critical, the reaction mixture can be simplified and optimised. This would not only reduce the costs, but it would likely result in a more uniform product as any minor reactions and interactions could be removed allowing for a single mechanism to dominate production.

Moreover, if a specific protein can be identified as being crucial to the stability of the nanoparticle, it may be possible to use a reaction mixture consisting of just three reagents: the photo-reducing agents (e.g. tyrosine), the stabilising protein as a capping agent, and $AgNO_3$. This mimics chemical reduction reactions for AgNPs and substantially simplifies the process. When considering large scale production, the simplicity of a process is attractive as it reduces the cost of reagents and the complexity and costs of reactors.

Flow Improvements

Future research with the reactors developed in this project, especially Reactor 5, would likely benefit from pumps which utilise a continuous mode of operation (i.e. drawing from an open reservoir), rather than the finite volumes of syringe pumps. Continuous cycle syringe pumps would offer the benefits of high-pressure outputs, required for the large reactor volumes, and the precise flow rate control, while overcoming the issue of finite reservoir volumes. Peristaltic pumps offer good control over flow rates and can draw from large and refillable reservoirs, but often struggle to supply the required output pressures of larger reactors. Additional benefits could be gained if in-line product clean-up and particle size isolation could be developed. This would be critical to becoming competitive with existing production methods.

Metals Beyond Silver

Nanoparticles have been made using a wide range of metals and non-metals. Indeed, *M. psychrotolerans* has previously been reported to produce Cu nanoparticles in a similar fashion to AgNP production here.[239] Exploring whether the photo-enhanced production methods reported here can be applied to produced nanoparticles of other metals, non-metals, or alloys would be an exciting avenue of research, especially if translatable into a flow system.

8.7 Concluding Remarks

The limitations of conventional production methods are restricting the exciting potential of AgNPs in a myriad of applications. Biological routes to producing AgNPs may be a useful tool in the future. However, the ability to control the geometries of particles in biological systems remains to be achieved. Nevertheless, in applications where the shape of particles is less important, such methods present exciting avenues of investigation and will likely see real-world use before the higher precision particles. The viability of future use will flow from the use of reactors to continually produce large volumes of products. To contend on an industrial scale with existing technologies for lower-quality products, the benefits of biosynthetic AgNPs must be financially competitive.

Appendices

Appendix A

Effects of Reaction Conditions on AgNP Bioproduction

A.1 *Culturing of M. psychrotolerans*

A.1.1 Cell Counts and Viability

The cell density of cultures was determined using turbidity measurements at 600 nm (OD_{600}) measured using a PerkinElmer Lambda 35 UV-Vis spectrometer. Cell counts were performed via colony-forming unit (CFU) plates prepared with 30 μL of serially diluted culture in PBS plated on LB agar and incubated at 22°C for 4 days.

A.1.2 Growth Kinetics

The growth of *M. psychrotolerans* was measured by CFU counts and the data shown in Figure A.1. Cultures took approximately 3 days to reach stationary phase when grown aerobically in LB with no added NaCl at 22°C.

A.2 Assessment of AgNP production by *E. coli* and *P. fluorescens*

E. coli and *P. fluorescens* were cultured aerobically in LB (no added NaCl) for 24 h at 37°C with orbital shaking (150 RPM). $AgNO_3$ was added directly to cultures to a final concentration of 9 mM. Samples were then incubated for a further 24 h under the same conditions with protection from light. Cells and

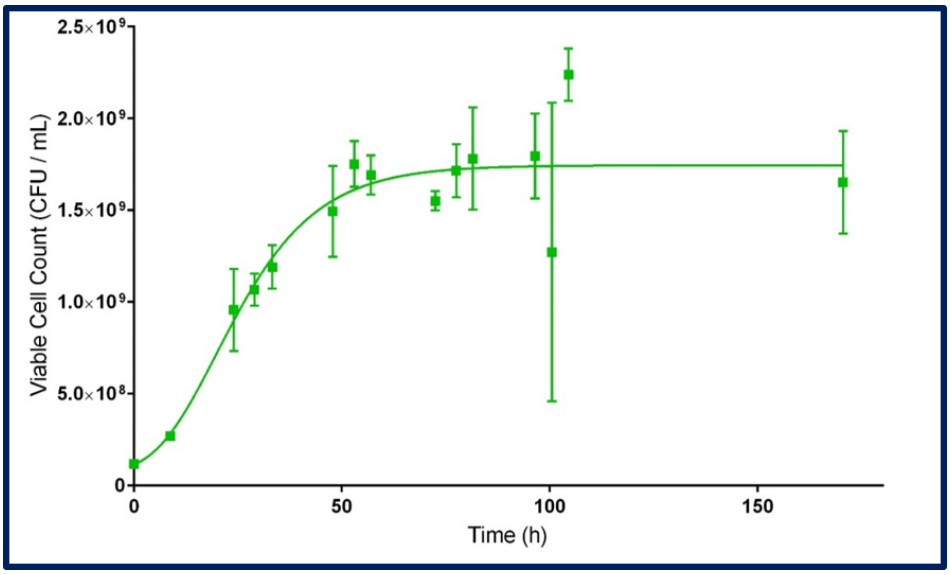

Figure A.1: Growth Curve of *M. psychrotolerans* grown aerobically in LB with no NaCl at 22°C.

debris was then removed by centrifugation (10,000 x *g* for 5 min) and the supernatant analysed by UV-Vis spectroscopy.

E. coli samples changed from pale yellow to brown, accompanied by an absorbance peak between 400 nm and 450 nm (Figure A.2). This indicated the formation of spherical AgNPs had occurred. No evidence of AgNP production was observed by *P. fluorescens*.

A.3 Sectioned TEM Imaging of *M. psychrotolerans*

To investigate the location of nanoparticles on or in cells, ultra-thin stained sectioned samples were prepared. For this, Cultures were centrifuged at 7500 RPM for 10 min and the supernatant discarded. The pellet was then resuspended in the fixative solution [4% formaldehyde, 0.1% glutaraldehyde, 0.1% 1,4 piperazinediethanesulfonic acid (PIPES) buffer] at room temperature for 1 h. The fixed cells were added to alginate and rinsed in PIPES buffer. Osmium tetroxide was used as a post-fixative and uranyl acetate was added as a contrast agent followed by graduated dehydration with ethanol. A 50:50 acetonitrile:Spurr resin solution was then used to start embedding the sample overnight. Following this, the specimen was embedded in 100% Spurr resin overnight at 60°C. Ultra-thin sections (≈50-80 nm) where then cut using an ultra-microtome and supported on a copper grid. Reynold's lead solution was used to stain the grids prior to imaging using an FEI Tecnai T12 microscope, as in Section 3.2.3.

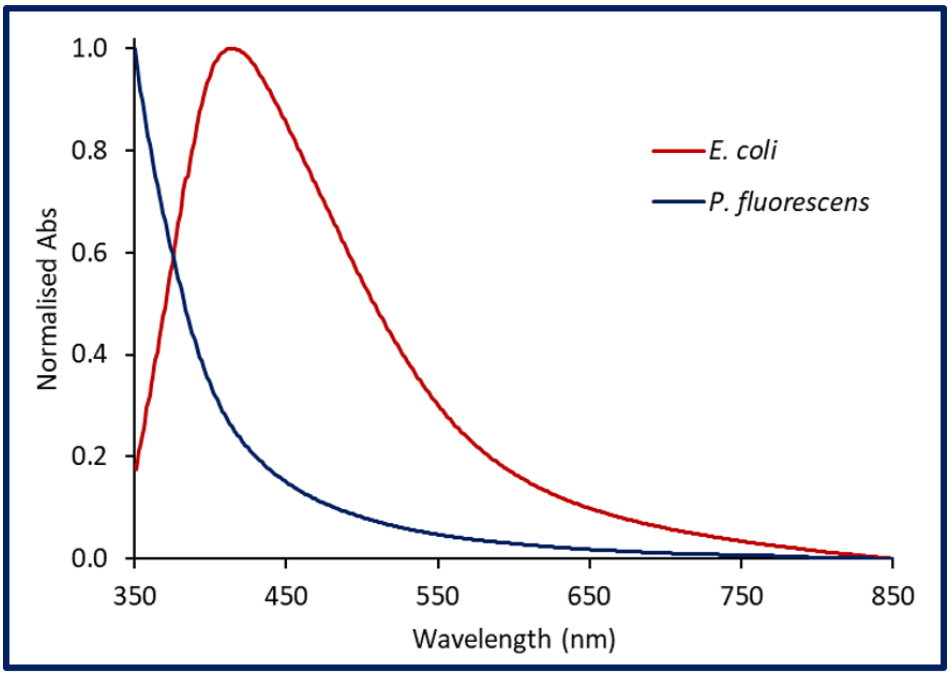

Figure A.2: UV-Vis spectra of *E. coli* and *P. fluorescens* culture supernatant following 24 h incubation with $AgNO_3$

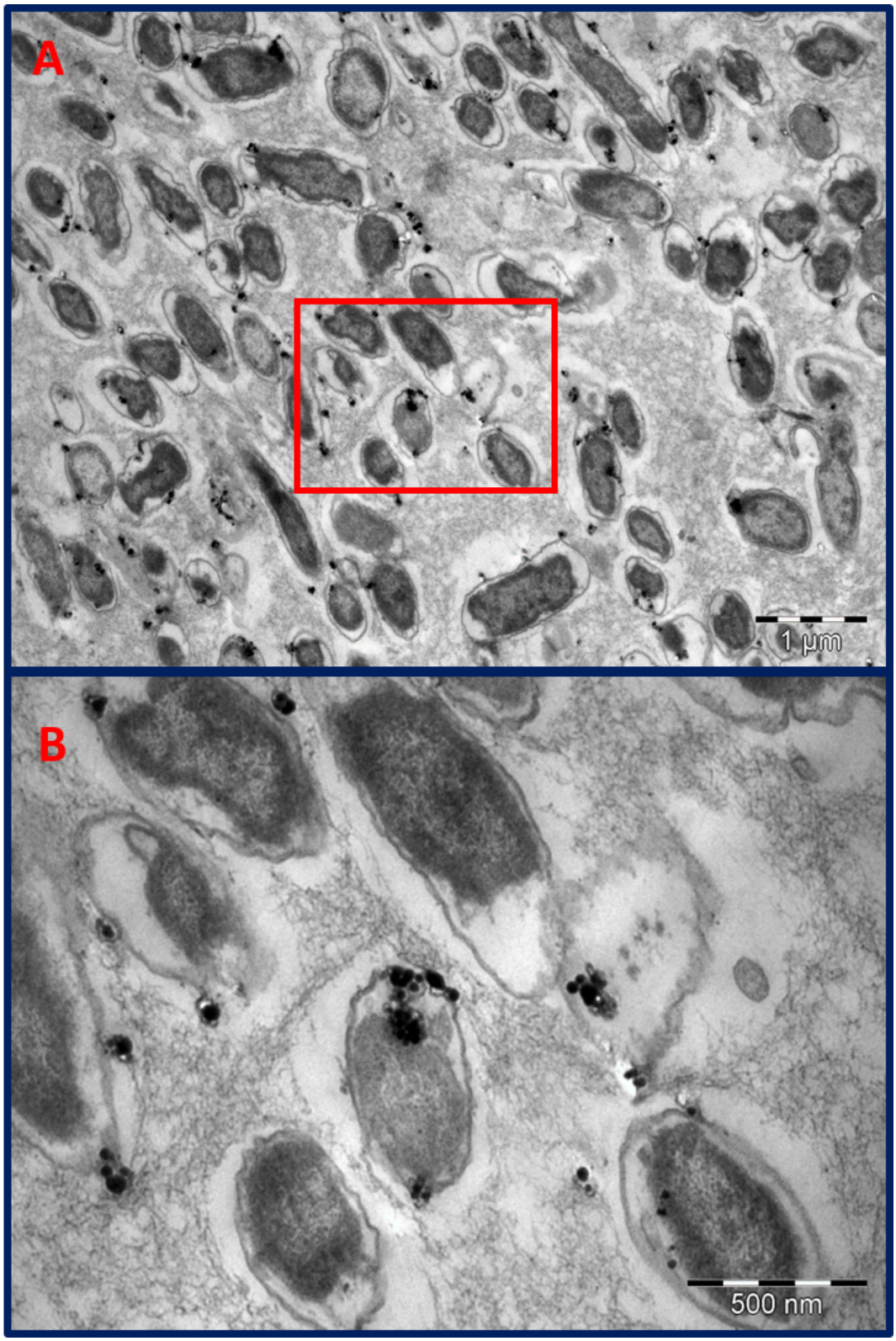

Figure A.3: TEM images of sectioned *M. psychrotolerans* after incubation with Ag^{+}. Image (B) shows the red box in image (A) at a higher magnification. Scale bars: 1 µm (A) and 500 nm (B).

Appendix B

Visible and ultraviolet light enhances AgNP synthesis by *M. psychrotolerans*

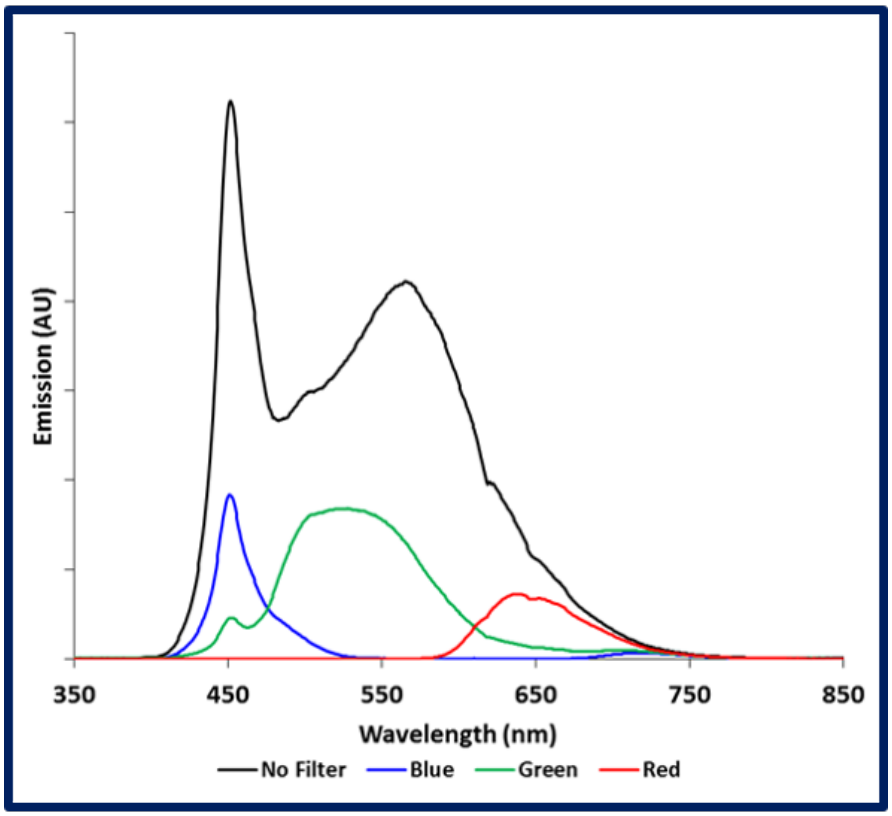

Figure B.1: Emission spectra of LED bulb with coloured filters.

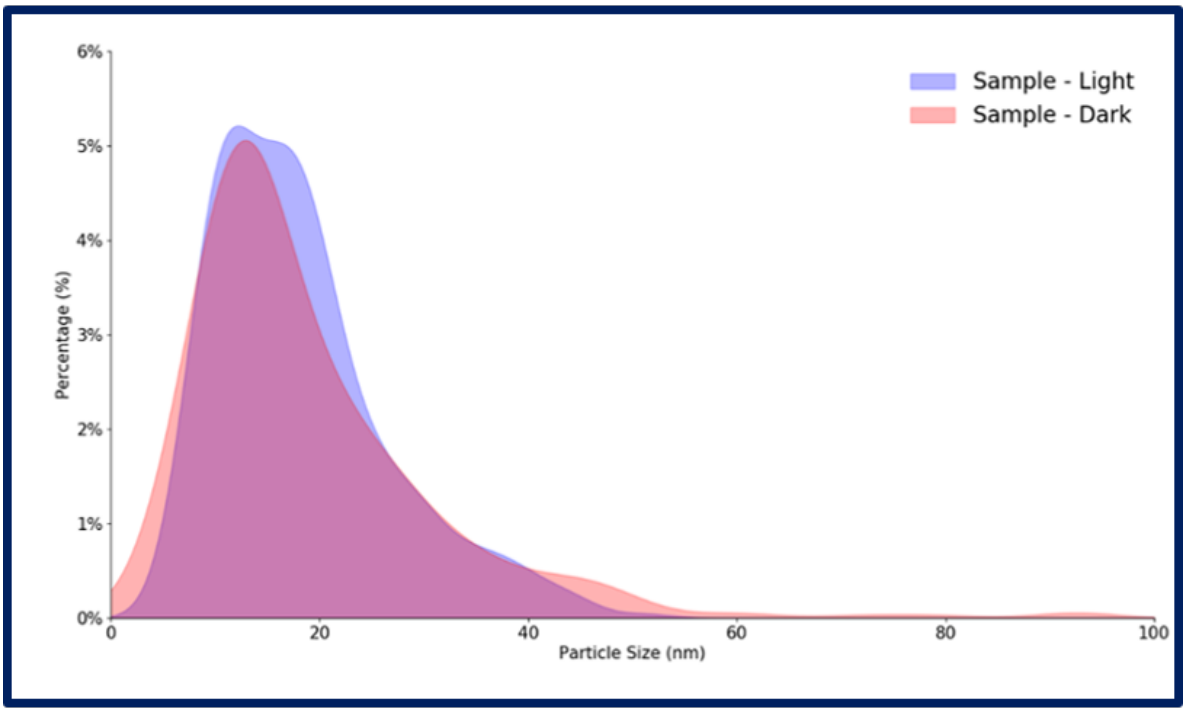

Figure B.2: Size distributions of AgNPs associated with *M. psychrotolerans* cells in dark conditions and exposed to white light.

Appendix C

A Rapid Green Process for AgNP Production Through Laser-Assisted Photoreduction

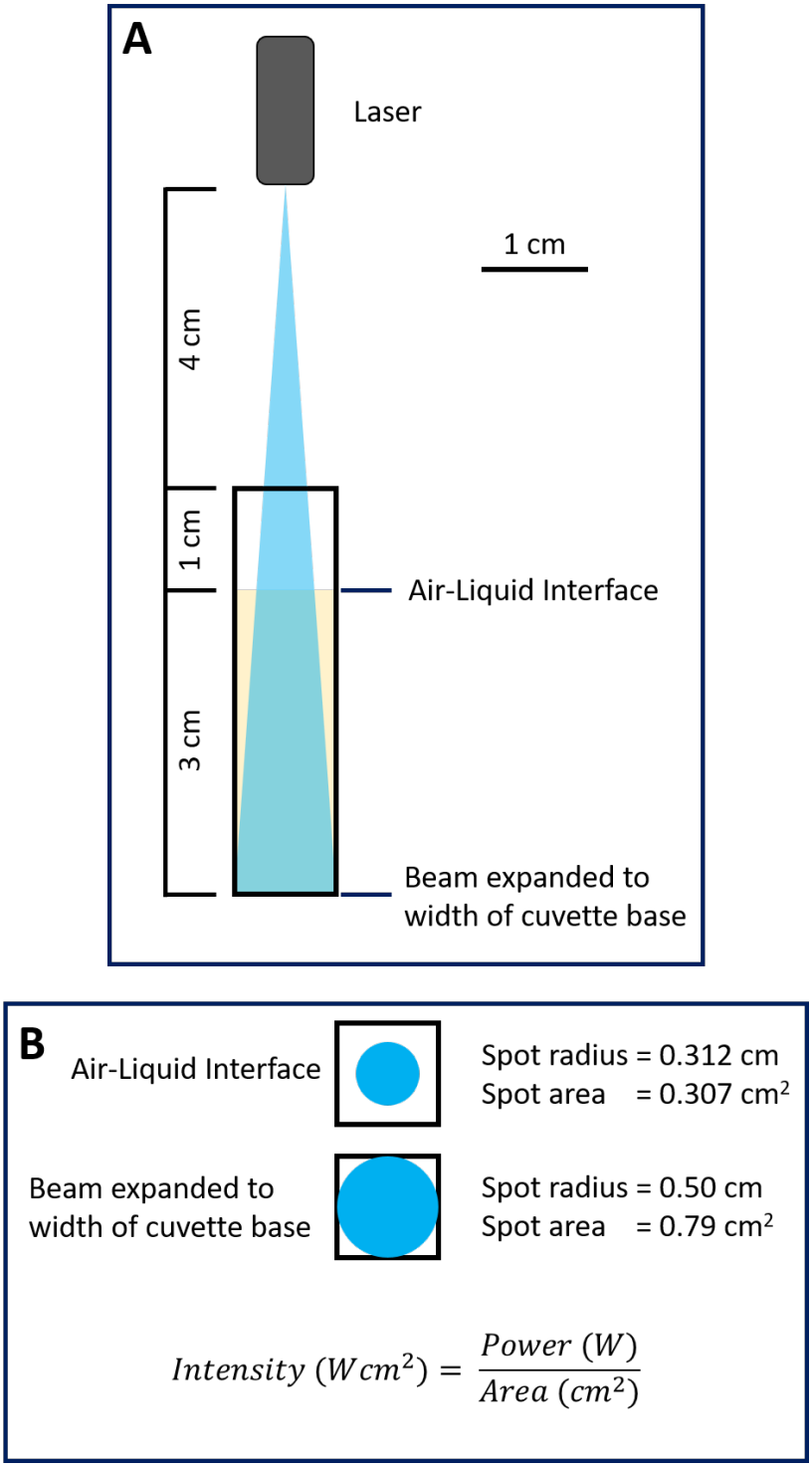

Figure C.1: Calculations for laser intensity. (A) The laser was held approximately 4 cm above the cuvette and adjusted so the beam was expanded to cover the bottom surface. (B) The surface area of the laser spot at the air-liquid interface was calculated and used for intensity calculations.

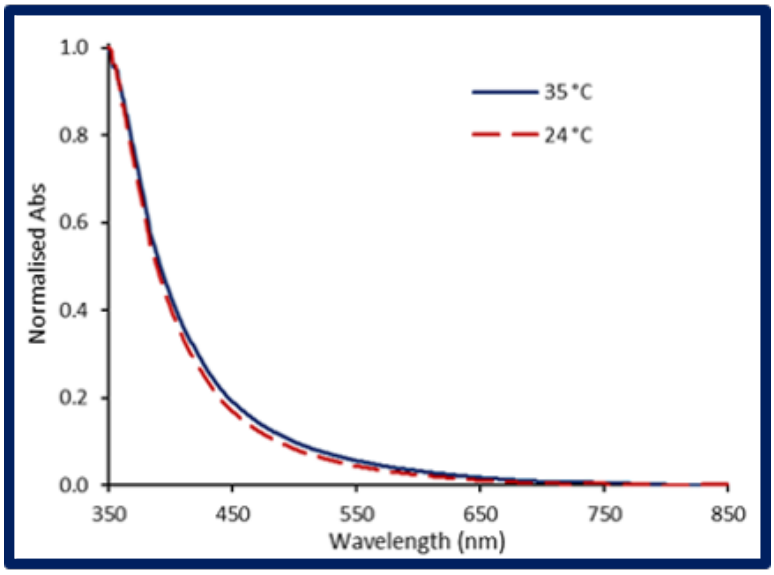

Figure C.2: UV-Vis spectra of supernatant of by *M. psychrotolerans* challenged with $AgNO_3$ in the dark at 24°C and 35°C after 10 min.

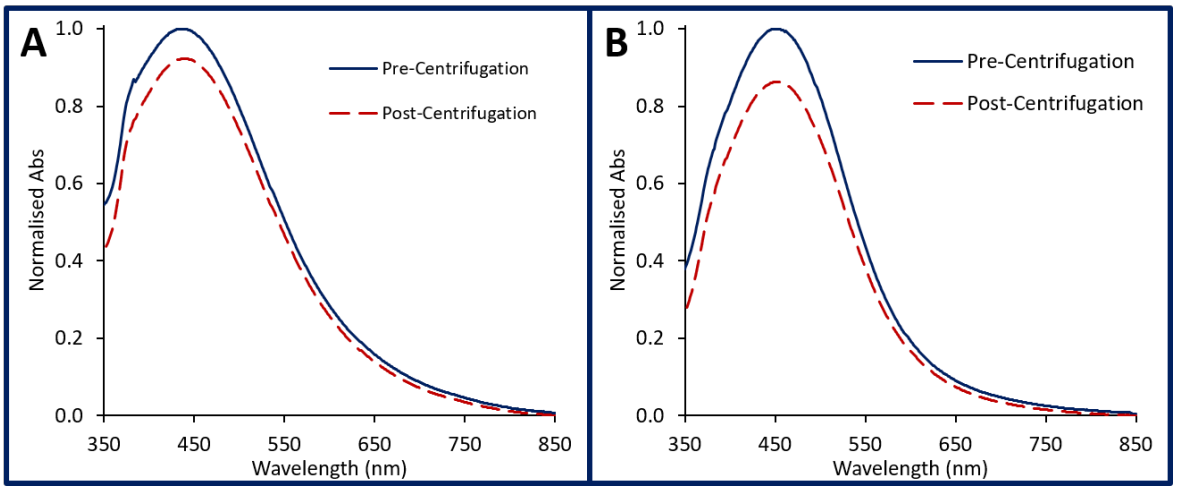

Figure C.3: UV-Vis spectra of AgNPs produced in the presence of CFE (A) and sterile growth medium (B), before and after centrifugation.

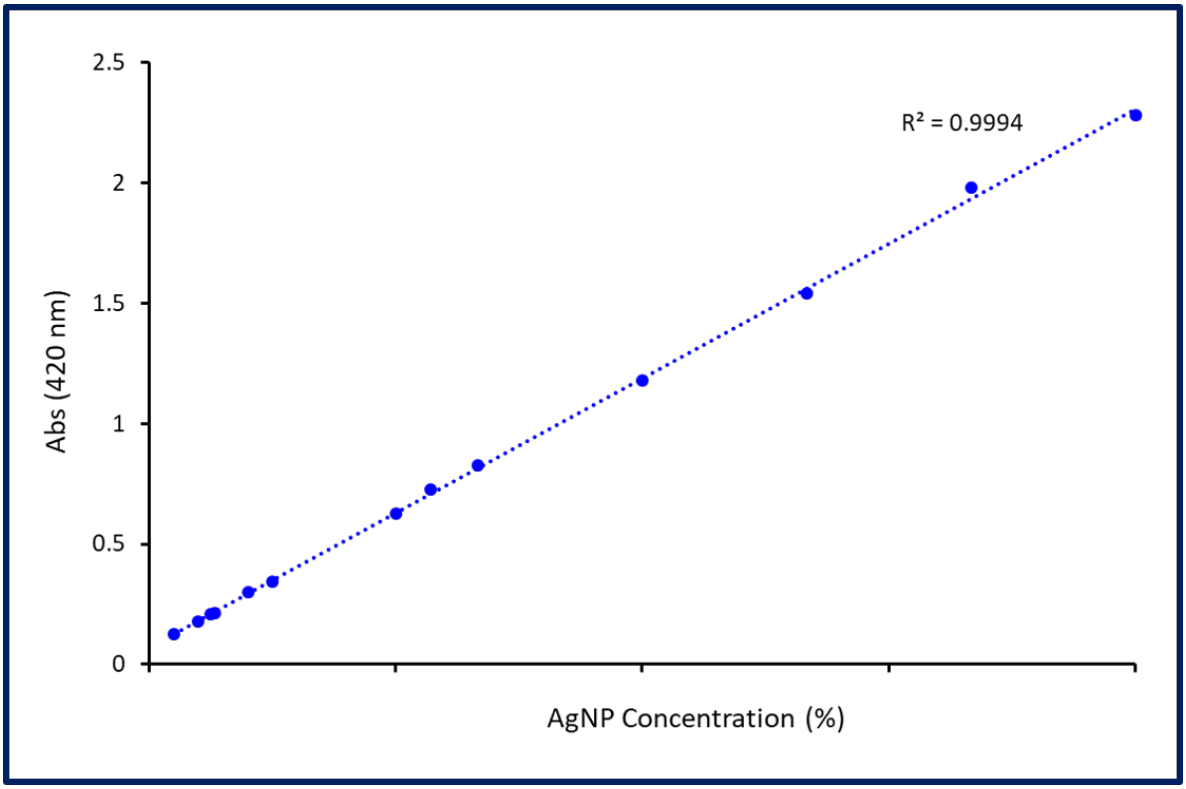

Figure C.4: Relationship between concentration of AgNPs and absorbance at 420 nm measured on a PerkinElmer Lambda 35 UV-Vis spectrometer. Particles diluted in diH_2O.

Appendix D

Photo-Assisted Biosynthesis of AgNPs Using Cell-free Extract in Flow Reactors

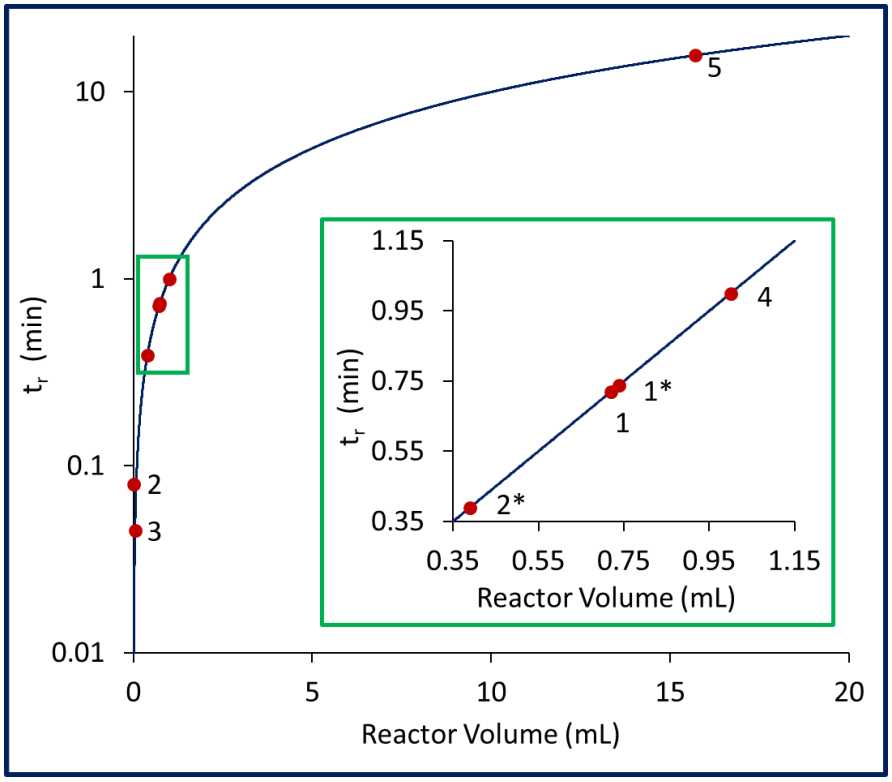

Figure D.1: Comparison t_r in reactors at a TFR of 1 mL min^{-1}. Insert: Magnified view of the selected area in the green box. Numbers are of Reactors as shown in Table D.1.

Table D.1: Comparison of residence times of flow reactors used for AgNP production

Reactor	Type	t_r at Flow Rates (s)						
		0.01 mL min^{-1}	0.1 mL min^{-1}	0.5 mL min^{-1}	1 mL min^{-1}	5 mL min^{-1}	10 mL min^{-1}	20 mL min^{-1}
1	Laser Inline	4320	432	86	43	8.6	4.3	2.2
2	Laser Perpendicular	270	27	5.4	2.7	0.54	0.27	0.14
3	Heart	48	4.8	0.96	0.48	0.10	0.05	0.02
1	1 + UV Lamp	4428	443	89	43	8.9	4.4	2.2
2	2 + UV Lamp	2340	234	47	23	4.7	2.3	1.2
4	Serpintine	6000	600	120	60	12	6.0	3.0
5	Coil	94248	9425	1885	942	188	94	47

Appendix E

Non-Specific Binding of Proteins Form Coronae of Biogenic AgNPs Produced by *M. psychrotolerans*

E.1 Spectroscopic Investigations of the Corona of AgNPs produced by *M. psychrotolerans*

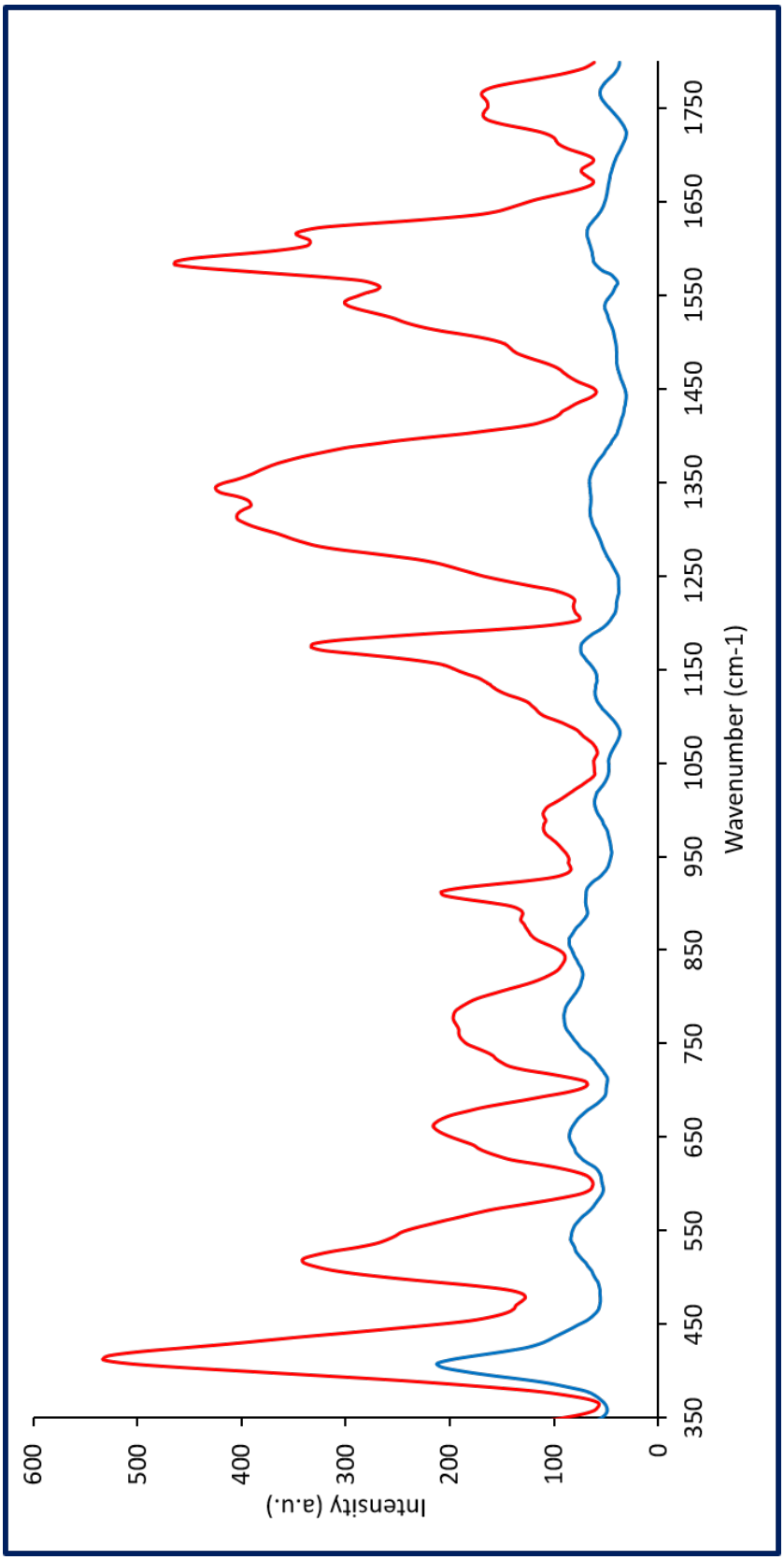

Figure E.1: Raman Spectra of *M. psychrotolerans* cells with and without AgNPs.

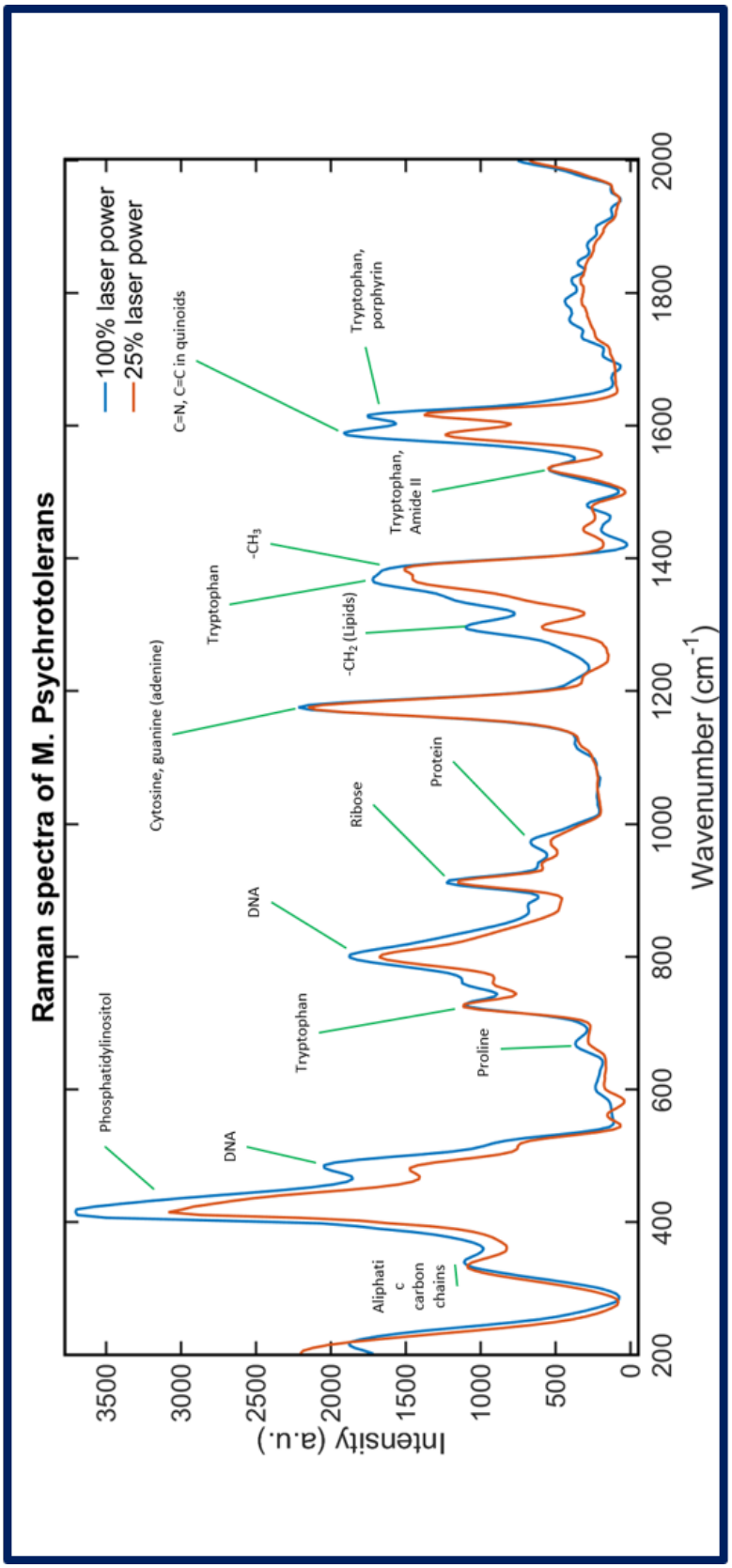

Figure E.2: Annotated Raman Spectra of *M. psychrotolerans* cells containing AgNPs at different laser intensities.

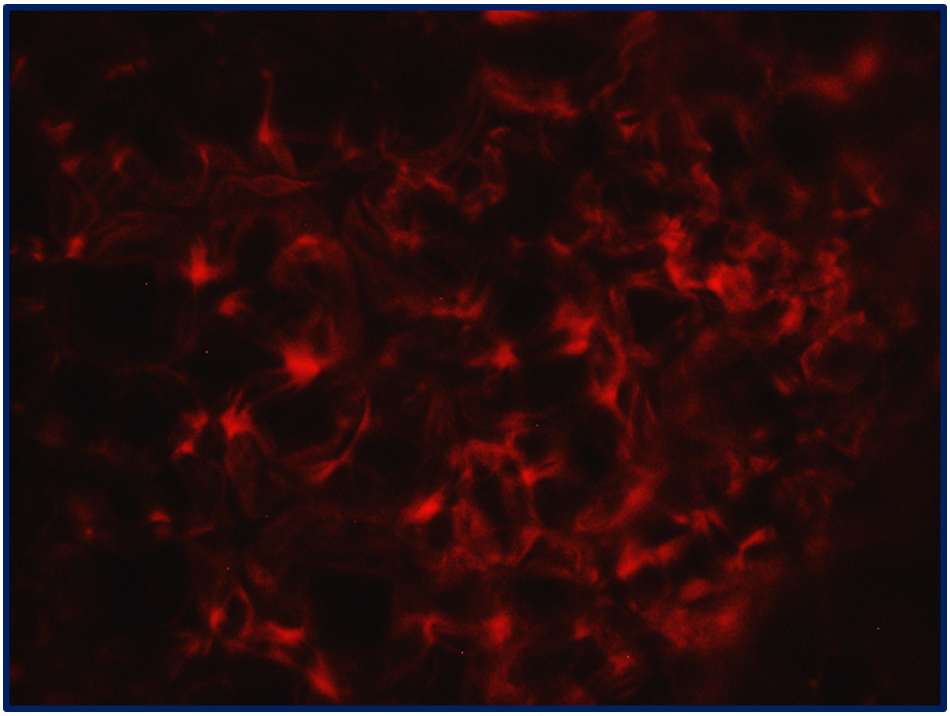

Figure E.3: AgNPs stained with SYPRO Ruby.

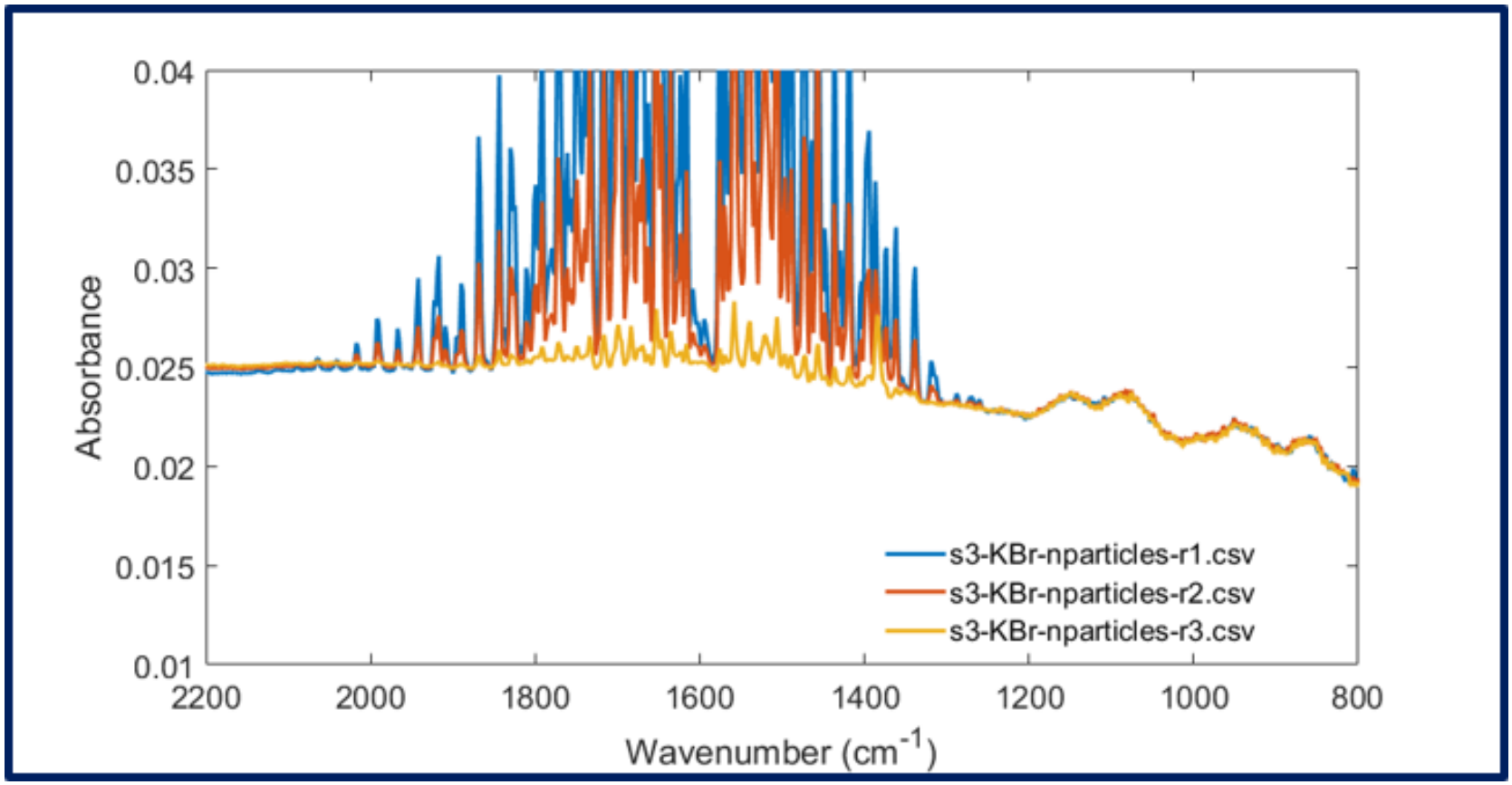

Figure E.4: FTIR Spectra of AgNPs in KBr Pellets. Repeat measurements of the same sample with continued purging with nitrogen. Water vapour and carbon dioxide interference made data collection challenging.

E.2 SDS PAGE of AgNP Proteomics Samples

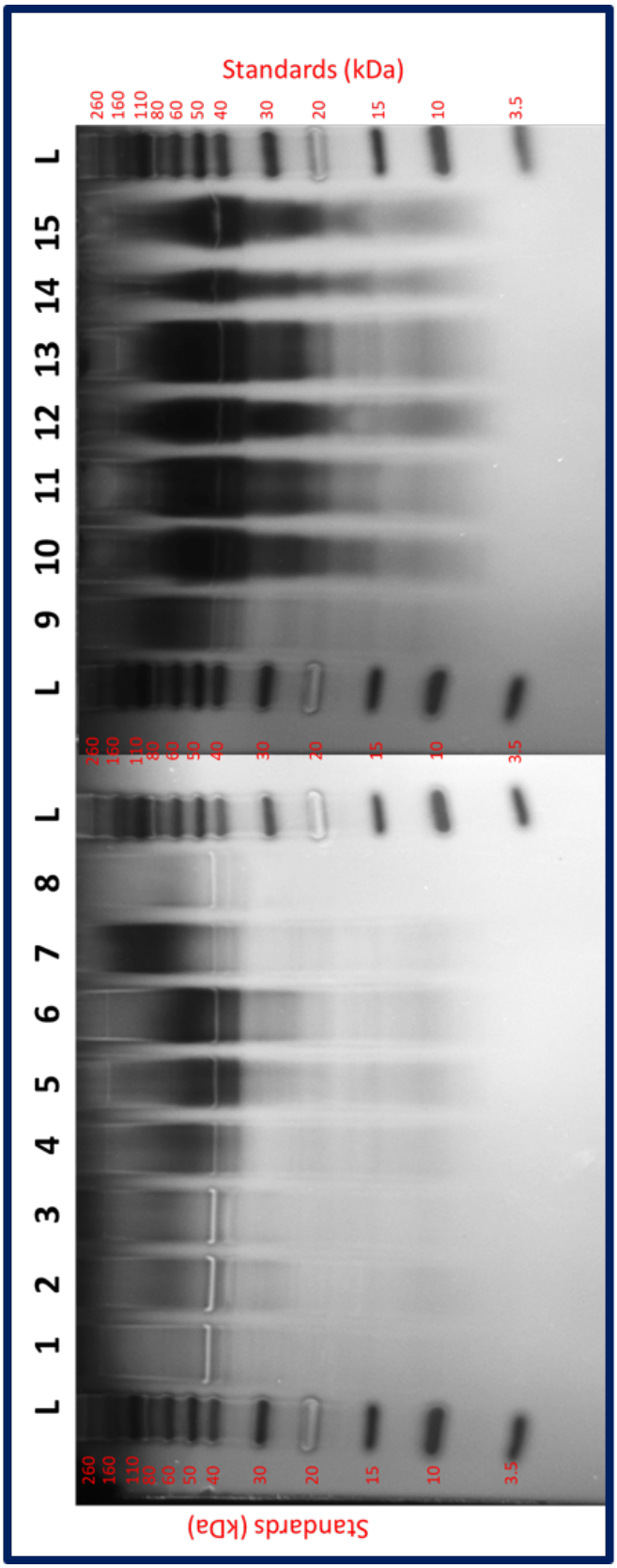

Figure E.5: SDS-PAGE of unpooled AgNP proteomic samples (1-15) imaged with SYPRO Ruby stain. Outer most lanes contain protein standards (L).

E.3 Analysis of Protein Properties

As discussed in Section 7.3.9, analysis of the properties of the proteins in the corona and supernatant was attempted. However, the confidence in the presented results is low and caution should be taken when interpreting. The uncertainty comes from the apparent discrepancy between the statistical results and the graphical representations.

E.3.1 Methods

The physical-chemical properties of the proteins (isoelectric point, grand average of hydropathy (GRAVY) value, instability index, and aromaticity) were calculated from the amino acid sequence of each protein using the BioPython library.[330] Amino acid residue composition was determined by the frequency of each amino acid (n) as a percentage of the sequence length (L), as shown in Eq. E.1. When comparing amino acid groups, the combined frequency of all amino acids in the group was used.

$$Composition = \frac{n}{L} \times 100\% \qquad \text{(Eq. E.1)}$$

Two-sample Kolmogorov-Smirnov tests were used to check for differences in the distribution of the data in each group. Parametric data were then compared using un-paired t-test. Levene test was used to assess the homogeneity of variance and Welch's t-test used if the variance of each group were significantly different. Non-parametric data were compared using Mann-Whitney U test. A p-value of less than 0.05 was considered significant. Statistical analysis were performed using SciPy.[252]

Physical and Chemical Properties of Proteins

Only 9% of proteins present in the supernatant were observed to be bound to the AgNPs. To explore possible reasons for this discrepancy in protein binding, the physical and chemical properties of the proteins were examined.

The molecular weight of each protein was calculated from the sequence data. The mean molecular weight of bound protein was 39.2 $\pm$ 24.0 kDa and the unbound proteins had a similar molecular weight of 39.1 $\pm$ 24.1 kDa. The distributions of the molecular weights were also near identical. This reveals the size of the proteins does not have an effect on the preference for binding to the particles.

Based on the molecular weights of the proteins identified on the surface of the AgNPs, possible proteins which may be responsible for the bands observed in the SDS PAGE experiments were proposed (Table

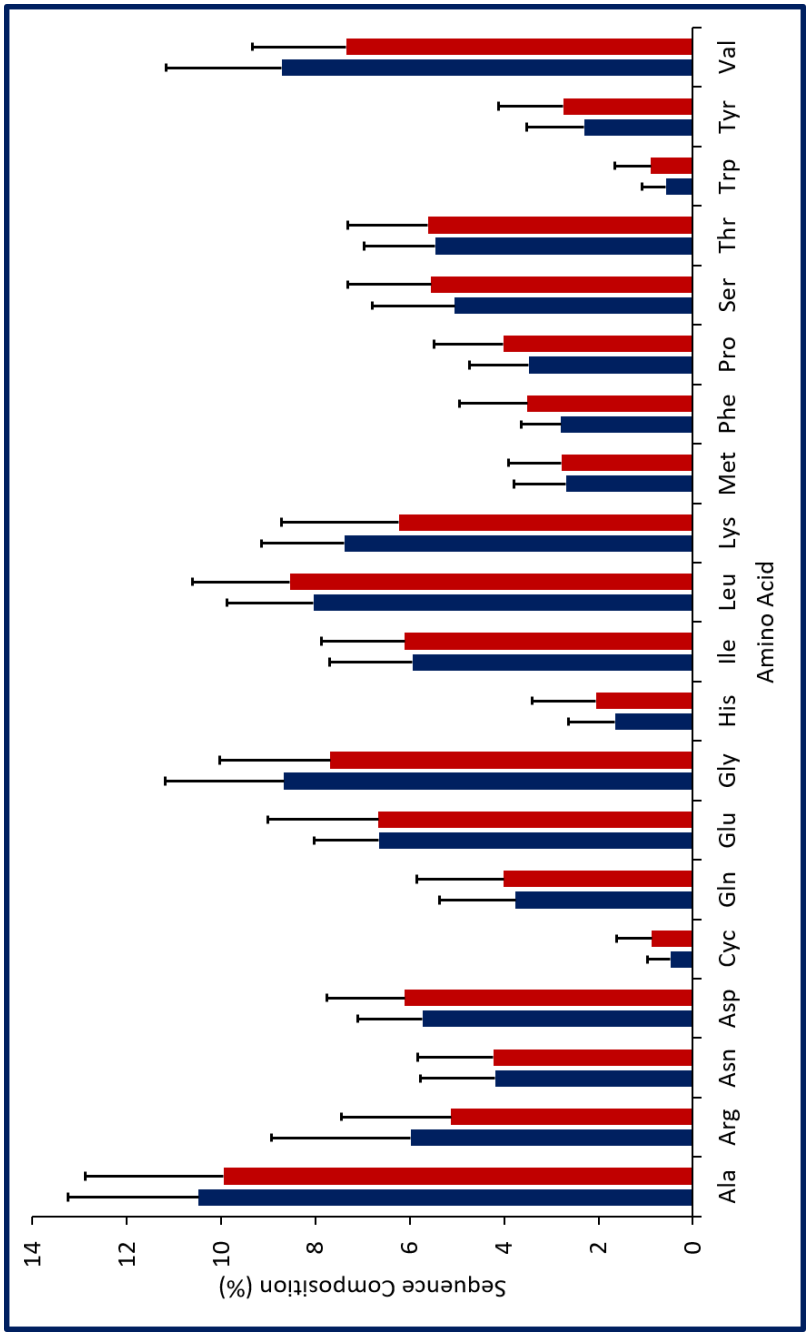

Figure E.6: Amino acid compositions in sequences of bound and unbound proteins

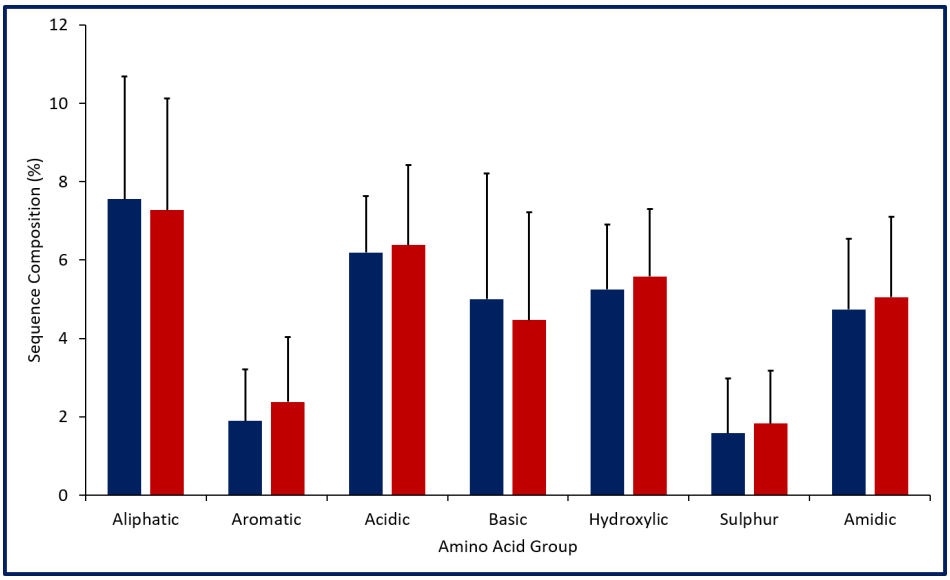

Figure E.7: Amino acids grouped by properties of proteins unbound and bound to AgNPs. (A) Basic (arginine, histidine, and lysine), (B) acidic (aspartic acid, glutamic acid), (C) aromatic (phenylalanine, tyrosine, and tryptophan), (D) aliphatic (alanine, glycine, isoleucine, leucine, proline, and valine), (E) amidic (asparagine, glutamine), (F) hydroxylic (serine, and threonine), and (G) sulphur-containing (cystine, methionine) residues were analysed.

7.1). The positions of the bands relative to the known standards were used to estimate the molecular weight of the stained peptides. Identified coronal proteins with molecular weights were then selected using a tolerance of $\pm$ 2,000 kDa.

The amino acid composition of the protein sequences were analysed, as shown in Figure E.6 and Table E.1. In addition to individual amino acids, the properties of the amino acids were investigated (Figure E.7). Significant differences were observe in the compositions of most residues. However, the apparent statistically significant results is not reflected in the graphical representation of the data. It is clear that further analysis and investigation is required. A summary of the statistical results is presented in Table E.1.

Properties for the proteins could be estimated from the amino acid sequences. As shown in Figure E.8 A, the mean isoelectric point for bound proteins was 7.2 $\pm$ 2.2 and 6.2 $\pm$ 1.6 for unbound proteins. The isoelectric point is the pH where a protein has no overall electric charge. The isoelectic point can be used to approximate how acidic or basic a protein is as acidic proteins require a lower pH to have a net charge of 0, while basic proteins require a higher pH. Based on the calculated isoelectric points of the two groups of proteins in this work, the neutral and slightly basic conditions of the isoelectric points suggest the proteins were not strongly acidic or strongly basic.

The GRAVY value represents the sum of the hydropathy values for every amino acid in a sequence divided by the total length of the sequence using the scale developed by Kyte and Doolittle.[331] A positive

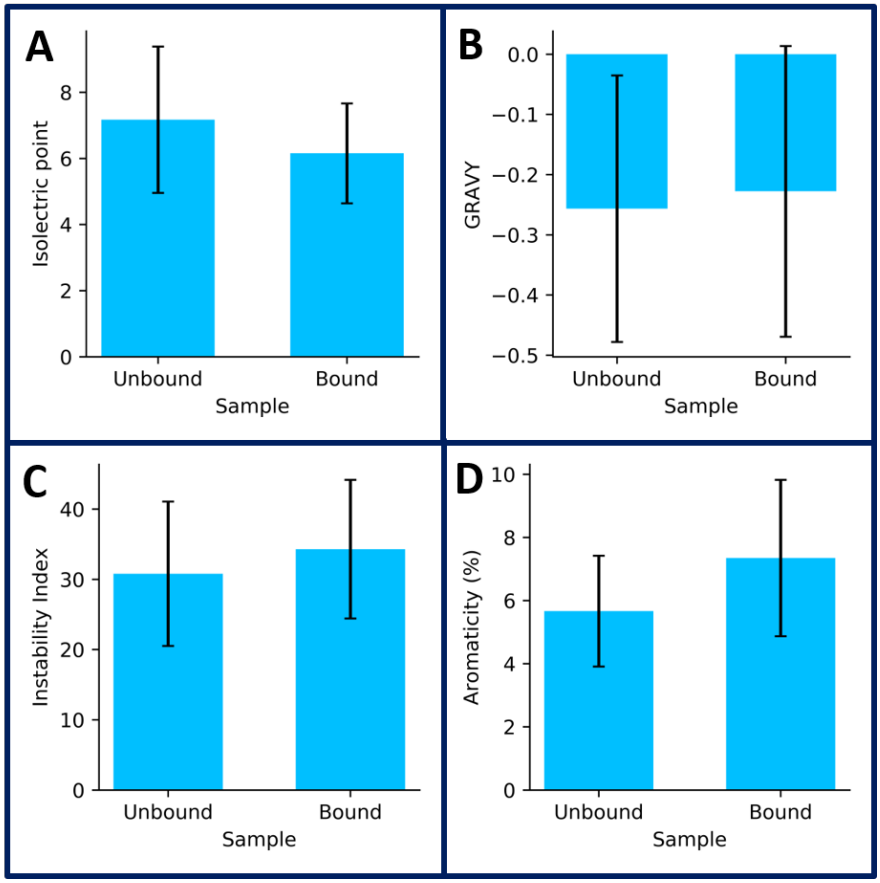

Figure E.8: Physiochemical properties of proteins bound and unbound to AgNPs. The isoelectric point (A), GRAVY value (B), instability index (C), and aromaticity (D) were estimated from the protein sequence data of proteins which did and did not bind to the AgNPs from the supernatant.

GRAVY value suggests the protein is hydrophobic whereas a negative value suggests the protein is hydrophilic. For example, membrane-embedded hydrophobic proteins tend to have higher GRAVY scores.[331] In this work, the GRAVY scores were calculated to be -0.3 $\pm$ 0.2 and -0.2 $\pm$ 0.2 for bound and unbound proteins, respectively (Figure E.8 B). The negative average GRAVY values in both protein groups suggests that the proteins tended to be hydrophilic rather than hydrophobic, though the large standard deviation demonstrated a high degree of variation in the proteins.

Based on the work by Guruprasad et al.[332], the instability index of a protein can be estimated. By examining the frequency of dipeptides within the protein sequence and estimating the stability of the bonds, a value representing the instability of the whole protein can be calculated. Proteins with an instability index of $>$40 tend to be unstable, where as stable proteins typically have instability index values of $<$40.[332] In the corona of AgNPs, the instability index was 30.9 $\pm$ 10.3 indicating that the proteins were stable (Figure E.8 C); proteins supernatant tended to be less stable in an instability index of 34.4 $\pm$ 9.9. As the AgNPs were washed prior to analysis, it is possible that unstable protein was lost resulting in an deflated instability index.

Parikh et al. have previously shown that aromatic rings in the proteins bound to AgNPs are in direct contact with the Ag surface.[52] To explore if this had influenced the protein binding in this study, the aromaticity of the proteins was calculated (Figure E.8 D). The relative frequency of the aromatic amino acid residues (phenylalanine, tyrosine, and tryptophan) was calculated; a higher value represent more aromatic residues present the protein.[333] Unbound proteins had 7.1 $\pm$ 2.5% aromatic residues, whereas bound proteins were 5.7 $\pm$ 1.8% aromatic.

Further analysis and investigation into the proteins bound and not bound to the AgNPs is required to gain an clearer understanding of the mechanism behind corona formation.

Table E.1: Amino acid compositions in bound and unbound proteins

Amino Acid	Bound (%)	Unbound (%)	P-Value
Ala	10.5 ± 2.77	9.9 ± 2.94	0.020
Arg	6 ± 2.95	5.1 ± 2.32	<0.001
Asn	4.2 ± 1.59	4.2 ± 1.59	0.266
Asp	5.7 ± 1.37	6.1 ± 1.66	0.001
Cys	0.5 ± 0.48	0.9 ± 0.74	0.000
Gln	3.8 ± 1.62	4 ± 1.84	0.040
Glu	6.7 ± 1.36	6.7 ± 2.34	0.987
Gly	8.7 ± 2.52	7.7 ± 2.35	0.000
His	1.6 ± 0.99	2 ± 1.36	0.000
Ile	5.9 ± 1.76	6.1 ± 1.77	0.252
Leu	8 ± 1.83	8.5 ± 2.08	0.001
Lys	7.4 ± 1.76	6.2 ± 2.48	<0.001
Met	2.7 ± 1.1	2.8 ± 1.13	0.284
Phe	2.8 ± 0.84	3.5 ± 1.44	<0.001
Pro	3.5 ± 1.26	4 ± 1.46	<0.001
Ser	5 ± 1.76	5.5 ± 1.76	0.001
Thr	5.5 ± 1.5	5.6 ± 1.7	0.223
Trp	0.6 ± 0.51	0.9 ± 0.76	<0.001
Tyr	2.3 ± 1.22	2.7 ± 1.37	<0.001
Val	8.7 ± 2.44	7.3 ± 1.99	<0.001
Aliphatic	7.6 ± 3.12	7.3 ± 2.85	0.003
Aromatic	1.9 ± 1.31	2.4 ± 1.65	<0.001
Acidic	6.2 ± 1.45	6.4 ± 2.05	0.099
Basic	5 ± 3.2	4.5 ± 2.76	<0.001
Hydroxylic	5.3 ± 1.65	5.6 ± 1.73	0.001
Sulphur	1.6 ± 1.4	1.8 ± 1.35	0.002
Amidic	4.7 ± 1.8	5.1 ± 2.04	0.003

References

1. Lu, X., Rycenga, M., Skrabalak, S. E., Wiley, B. & Xia, Y. Chemical Synthesis of Novel Plasmonic Nanoparticles. *Annu Rev Phys Chem* **60,** 167–192 (2009).
2. Millstone, J. E., Hurst, S. J., Metraux, G. S., Cutler, J. I. & Mirkin, C. A. Colloidal Gold and Silver Triangular Nanoprisms. *Small* **5,** 646–664 (2009).
3. Syafiuddin, A., Salim, M. R., Beng Hong Kueh, A., Hadibarata, T. & Nur, H. A Review of Silver Nanoparticles: Research Trends, Global Consumption, Synthesis, Properties, and Future Challenges. *Journal of the Chinese Chemical Society* **64,** 732–756 (2017).
4. Sintubin, L., Verstraete, W. & Boon, N. Biologically Produced Nanosilver: Current State and Future Perspectives. *Biotechnology and Bioengineering* **109,** 2422–2436 (2012).
5. Singh, P., Kim, Y.-J., Zhang, D. & Yang, D.-C. Biological Synthesis of Nanoparticles from Plants and Microorganisms. *Trends in biotechnology* **34,** 588–599 (2016).
6. Mabey, T., Andrea Cristaldi, D., Oyston, P., Lymer, K. P., Stulz, E., Wilks, S., William Keevil, C. & Zhang, X. Bacteria and Nanosilver: The Quest for Optimal Production. *Critical reviews in biotechnology* **39,** 272–287 (2019).
7. Iravani, S., Korbekandi, H., Mirmohammadi, S. V. & Zolfaghari, B. Synthesis of Silver Nanoparticles: Chemical, Physical and Biological Methods. *Research in pharmaceutical sciences* **9,** 385 (2014).
8. Cao, G. & Wang, Y. *Nanostructures and Nanomaterials: Synthesis, Properties, and Applications* ISBN: 9789814322508 (2011).
9. Iravani, S. Bacteria in Nanoparticle Synthesis: Current Status and Future Prospects. *International Scholarly Research Notices* **2014,** 18 (2014).
10. Haber, J. & Sokolov, K. Synthesis of Stable Citrate-capped Silver Nanoprisms. *Langmuir* **33,** 10525–10530 (2017).

11. Kelly, K. L., Coronado, E., Zhao, L. L., Schatz, G. C., *et al.* The Optical Properties of Metal Nanoparticles: The Influence of Size, Shape, and Dielectric Environment. *Journal of Physical Chemistry B-Condensed Phase* **107,** 668–677 (2003).

12. Petryayeva, E. & Krull, U. J. Localized Surface Plasmon Resonance: Nanostructures, Bioassays and Biosensing - A Review. *Analytica Chimica Acta* **706,** 8–24 (2011).

13. Willets, K. A. & Van Duyne, R. P. Localized Surface Plasmon Resonance Spectroscopy and Sensing. *Annu. Rev. Phys. Chem.* **58,** 267–297 (2007).

14. Kapoor, S. Preparation, Characterization, and Surface Modification of Silver Particles. *Langmuir* **14,** 1021–1025 (1998).

15. Mulvaney, P. Surface Plasmon Spectroscopy of Nanosized Metal Particles. *Langmuir* **12,** 788–800 (1996).

16. Jin, R., Cao, Y., Mirkin, C. A., Kelly, K., Schatz, G. C. & Zheng, J. Photoinduced Conversion of Silver Nanospheres to Nanoprisms. *science* **294,** 1901–1903 (2001).

17. Tsuji, T., Iryo, K., Watanabe, N. & Tsuji, M. Preparation of Silver Nanoparticles by Laser Ablation in Solution: Influence of Laser Wavelength on Particle Size. *Applied Surface Science* **202,** 80–85 (2002).

18. Zaarour, M., El Roz, M., Dong, B., Retoux, R., Aad, R., Cardin, J., Dufour, C., Gourbilleau, F., Gilson, J.-P. & Mintova, S. Photochemical Preparation of Silver Nanoparticles Supported on Zeolite Crystals. *Langmuir* **30,** 6250–6256 (2014).

19. Lee, G. P., Shi, Y., Lavoie, E., Daeneke, T., Reineck, P., Cappel, U. B., Huang, D. M. & Bach, U. Light-driven Transformation Processes of Anisotropic Silver Nanoparticles. *ACS nano* **7,** 5911–5921 (2013).

20. Zhang, X.-F., Liu, Z.-G., Shen, W. & Gurunathan, S. Silver Nanoparticles: Synthesis, Characterization, Properties, Applications, and Therapeutic Approaches. *International Journal of Molecular Sciences* **17,** 1534 (2016).

21. Zhang, Q., Li, N., Goebl, J., Lu, Z. & Yin, Y. A Systematic Study of the Synthesis of Silver Nanoplates: Is Citrate a “magic” Reagent? *Journal of the American Chemical Society* **133,** 18931–18939 (2011).

22. Pinto, V. V., Ferreira, M. J., Silva, R., Santos, H. A., Silva, F. & Pereira, C. M. Long Time Effect on the Stability of Silver Nanoparticles in Aqueous Medium: Effect of the Synthesis and Storage Conditions. *Colloids and Surfaces A: Physicochemical and Engineering Aspects* **364,** 19–25 (2010).

23. Korshed, P., Li, L., Wang, T., *et al.* Effect of Storage Conditions on the Long-Term Stability of Bactericidal Effects for Laser Generated Silver Nanoparticles. *Nanomaterials* **8,** 218 (2018).

24. Valenti, L. E. & Giacomelli, C. E. Stability of Silver Nanoparticles: Agglomeration and Oxidation in Biological Relevant Conditions. *Journal of Nanoparticle Research* **19,** 156 (2017).

25. Khodashenas, B. & Ghorbani, H. R. Synthesis of Silver Nanoparticles with Different Shapes. *Arabian Journal of Chemistry* (2015).

26. Raza, M., Kanwal, Z., Rauf, A., Sabri, A., Riaz, S. & Naseem, S. Size-and Shape-Dependent Antibacterial Studies of Silver Nanoparticles Synthesized by Wet Chemical Routes. *Nanomaterials* **6,** 74 (2016).

27. Sanyal, U. & Jagirdar, B. R. Metal and Alloy Nanoparticles by Amine-Borane Reduction of Metal Salts by Solid-Phase Synthesis: Atom Economy and Green Process. *Inorganic chemistry* **51,** 13023–13033 (2012).

28. Bhattarai, B., Zaker, Y. & Bigioni, T. P. Green Synthesis of Gold and Silver Nanoparticles: Challenges and Opportunities. *Current Opinion in Green and Sustainable Chemistry* **12,** 91–100 (2018).

29. Bhattarai, B., Chakraborty, I., Conn, B. E., Atnagulov, A., Pradeep, T. & Bigioni, T. P. High-Yield Paste-Based Synthesis of Thiolate-Protected Silver Nanoparticles. *The Journal of Physical Chemistry C* **121,** 10964–10970 (2017).

30. Kim, T. Y., Cha, S.-H., Cho, S. & Park, Y. Tannic Acid-Mediated Green Synthesis of Antibacterial Silver Nanoparticles. *Archives of pharmacal research* **39,** 465–473 (2016).

31. Korshed, P., Li, L., Liu, Z. & Wang, T. The Molecular Mechanisms of the Antibacterial Effect of Picosecond Laser Generated Silver Nanoparticles and their Toxicity to Human Cells. *PLoS One* **11,** e0160078 (2016).

32. Dell'Aglio, M, Mangini, V, Valenza, G, De Pascale, O, De Stradis, A, Natile, G, Arnesano, F & De Giacomo, A. Silver and Gold Nanoparticles Produced by Pulsed Laser Ablation in Liquid to Investigate their Interaction with Ubiquitin. *Applied Surface Science* **374,** 297–304 (2016).

33. Jendrzej, S., Gökce, B., Epple, M. & Barcikowski, S. How Size Determines the Value of Gold: Economic Aspects of Wet Chemical and Laser-Based Metal Colloid Synthesis. *ChemPhysChem* **18,** 1012–1019 (2017).

34. Barman, B., Dhasmana, H., Verma, A., Kumar, A., Chaudhary, S. P. & Jain, V. Formation of Plasmonic Silver Nanoparticles Using Rapid Thermal Annealing at Low Temperature and Study in Reflectance Reduction of Si Surface. *Advances in Natural Sciences: Nanoscience and Nanotechnology* **8,** 035010 (2017).

35. Lin, X. Z., Terepka, A. D. & Yang, H. Synthesis of Silver Nanoparticles in a Continuous Flow Tubular Microreactor. *Nano Letters* **4,** 2227–2232 (2004).

36. Rycenga, M., McLellan, J. M. & Xia, Y. Controlling the assembly of silver nanocubes through selective functionalization of their faces. *Advanced Materials* **20,** 2416–2420 (2008).

37. Zhang, J., Langille, M. R. & Mirkin, C. A. Photomediated synthesis of silver triangular bipyramids and prisms: the effect of pH and BSPP. *Journal of the American Chemical Society* **132,** 12502–12510 (2010).

38. Zhao, X., Zhou, L., Riaz Rajoka, M. S., Yan, L., Jiang, C., Shao, D., Zhu, J., Shi, J., Huang, Q., Yang, H. & Jin, M. Fungal Silver Nanoparticles: Synthesis, Application and Challenges. *Critical Reviews in Biotechnology* **38,** 817–835 (2018).

39. Quester, K., Avalos-Borja, M & Castro-Longoria, E. Biosynthesis and Microscopic Study of Metallic Nanoparticles. *Micron* **54,** 1–27 (2013).

40. Siddiqi, K. S., Husen, A. & Rao, R. A. K. A Review on Biosynthesis of Silver Nanoparticles and Their Biocidal Properties. *Journal of Nanobiotechnology* **16,** 14 (2018).

41. Barros, C., Fulaz, S., Stanisic, D. & Tasic, L. Biogenic Nanosilver Against Multidrug-resistant Bacteria (MDRB). *Antibiotics* **7,** 69 (2018).

42. Singh, R., Shedbalkar, U. U., Wadhwani, S. A. & Chopade, B. A. Bacteriagenic Silver Nanoparticles: Synthesis, Mechanism, and Applications. *Applied Microbiology and Biotechnology* **99,** 4579–4593 (2015).

43. Klaus, T., Joerger, R., Olsson, E. & Granqvist, C.-G. Silver-based Crystalline Nanoparticles, Microbially Fabricated. *Proceedings of the National Academy of Sciences* **96,** 13611–13614 (1999).

44. Alexander, J. W. History of the Medical Use of Silver. *Surgical infections* **10,** 289–292 (2009).

45. Mijnendonckx, K., Leys, N., Mahillon, J., Silver, S. & Van Houdt, R. Antimicrobial Silver: Uses, Toxicity and Potential for Resistance. *BioMetals* **26,** 609–621 (2013).

46. Prabhu, S. & Poulose, E. K. Silver Nanoparticles: Mechanism of Antimicrobial Action, Synthesis, Medical Applications, and Toxicity Effects. *International Nano Letters* **2,** 32 (2012).

47. Randall, C. P., Oyama, L. B., Bostock, J. M., Chopra, I. & O'Neill, A. J. The Silver Cation (Ag^{+}): Antistaphylococcal Activity, Mode of Action and Resistance Studies. *The Journal of antimicrobial chemotherapy* **68,** 131–138 (2013).

48. Jung, W. K., Koo, H. C., Kim, K. W., Shin, S., Kim, S. H. & Park, Y. H. Antibacterial Activity and Mechanism of Action of the Silver Ion in *Staphylococcus aureus* and *Escherichia coli*. *Appl Environ Microbiol* **74,** 2171–2178 (2008).

49. Bao, H., Yu, X., Xu, C., Li, X., Li, Z., Wei, D. & Liu, Y. New Toxicity Mechanism of Silver Nanoparticles: Promoting Apoptosis and Inhibiting Proliferation. *PLoS One* **10,** e0122535 (2015).

50. Kumar Pandian, S. R., Deepak, V., Kalishwaralal, K., Viswanathan, P. & Gurunathan, S. Mechanism of Bactericidal Activity of Silver Nitrate – a Concentration Dependent Bi-functional Molecule. *Brazilian Journal of Microbiology* **41,** 805–809 (2010).

51. Parikh, R. Y., Ramanathan, R., Coloe, P. J., Bhargava, S. K., Patole, M. S., Shouche, Y. S. & Bansal, V. Genus-wide Physicochemical Evidence of Extracellular Crystalline Silver Nanoparticles Biosynthesis by *Morganella* spp. *PLoS One* **6,** e21401 (2011).

52. Parikh, R. Y., Singh, S., Prasad, B. L., Patole, M. S., Sastry, M. & Shouche, Y. S. Extracellular Synthesis of Crystalline Silver Nanoparticles and Molecular Evidence of Silver Resistance From *Morganella* sp.: Towards Understanding Biochemical Synthesis Mechanism. *Chembiochem: A European journal of chemical biology* **9,** 1415–1422 (2008).

53. Gupta, A., Matsui, K., Lo, J. F. & Silver, S. Molecular Basis for Resistance to Silver Cations in Salmonella. *Nature Medicine* **5,** 183–188 (1999).

54. Silver, S., Phung le, T. & Silver, G. Silver as Biocides in Burn and Wound Dressings and Bacterial Resistance to Silver Compounds. *Journal of industrial microbiology and biotechnology* **33,** 627–634 (2006).

55. Franke, S., Grass, G., Rensing, C. & Nies, D. H. Molecular Analysis of the Copper-transporting Efflux System CusCFBA of *Escherichia coli*. *Journal of Bacteriology* **185,** 3804–3812 (2003).

56. Su, C. C., Long, F. & Yu, E. W. The Cus Efflux System Removes Toxic Ions via a Methionine Shuttle. *Protein Science* **20,** 6–18 (2011).

57. Ramanathan, R., O'Mullane, A. P., Parikh, R. Y., Smooker, P. M., Bhargava, S. K. & Bansal, V. Bacterial Kinetics-controlled Shape-directed Biosynthesis of Silver Nanoplates Using *Morganella psychrotolerans*. *Langmuir* **27,** 714–719 (2011).

58. Randall, C. P., Gupta, A., Jackson, N., Busse, D. & O'Neill, A. J. Silver Resistance in Gram-negative Bacteria: A Dissection of Endogenous and Exogenous Mechanisms. *Journal of Antimicrobial Chemotherapy* **70,** 1037–1046 (2015).

59. Xiu, Z. M., Zhang, Q. B., Puppala, H. L., Colvin, V. L. & Alvarez, P. J. Negligible Particle-specific Antibacterial Activity of Silver Nanoparticles. *Nano Letters* **12,** 4271–4275 (2012).

60. Sintubin, L., De Windt, W., Dick, J., Mast, J., van der Ha, D., Verstraete, W. & Boon, N. Lactic Acid Bacteria as Reducing and Capping Agent for the Fast and Efficient Production of Silver Nanoparticles. *Applied microbiology and biotechnology* **84,** 741–749 (2009).

61. Durán, N., Marcato, P. D., Alves, O. L., De Souza, G. I. H. & Esposito, E. Mechanistic Aspects of Biosynthesis of Silver Nanoparticles by Several *Fusarium oxysporum* Strains. *Journal of Nanobiotechnology* **3** (2005).

62. Durán, N., Marcato, P. D., Durán, M., Yadav, A., Gade, A. & Rai, M. Mechanistic Aspects in the Biogenic Synthesis of Extracellular Metal Nanoparticles by Peptides, Bacteria, Fungi, and Plants. *Appl Microbiol Biotechnol* **90,** 1609–1624 (2011).

63. Coelho, C. & Romao, M. J. Structural and Mechanistic Insights on Nitrate Reductases. *Protein Science* **24,** 1901–1911 (2015).

64. Anil Kumar, S., Abyaneh, M. K., Gosavi, S. W., Kulkarni, S. K., Pasricha, R., Ahmad, A. & Khan, M. I. Nitrate Reductase-mediated Synthesis of Silver Nanoparticles From $AgNO_3$. *Biotechnology letters* **29,** 439–445 (2007).

65. Saifuddin, N., Wong, C. W. & Yasumira, A. A. N. Rapid Biosynthesis of Silver Nanoparticles Using Culture Supernatant of Bacteria With Microwave Irradiation. *E-Journal of Chemistry* **6,** 61–70 (2009).

66. Shahverdi, A. R., Minaeian, S., Shahverdi, H. R., Jamalifar, H. & Nohi, A. A. Rapid Synthesis of Silver Nanoparticles Using Culture Supernatants of Enterobacteria: A Novel Biological Approach. *Process Biochemistry* **42,** 919–923 (2007).

67. Asiani, K. R., Williams, H., Bird, L., Jenner, M., Searle, M. S., Hobman, J. L., Scott, D. J. & Soultanas, P. SilE is an Intrinsically Disordered Periplasmic "Molecular Sponge" Involved in Bacterial Silver Resistance. *Molecular Microbiology* **101,** 731–742 (2016).

68. Srivastava, P., Braganca, J., Ramanan, S. R. & Kowshik, M. Synthesis of Silver Nanoparticles Using Haloarchaeal Isolate *Halococcus salifodinae* BK3. *Extremophiles: life under extreme conditions* **17,** 821–831 (2013).

69. Korbekandi, H., Iravani, S. & Abbasi, S. Optimization of Biological Synthesis of Silver Nanoparticles Using *Lactobacillus casei* Subsp Casei. *Journal of Chemical Technology and Biotechnology* **87,** 932–937 (2012).

70. Durán, M., Silveira, C. P. & Durán, N. Catalytic Role of Traditional Enzymes for Biosynthesis of Biogenic Metallic Nanoparticles: A Mini-review. *IET Nanobiotechnology* **9,** 314–323 (2015).

71. Oves, M., Khan, M. S., Zaidi, A., Ahmed, A. S., Ahmed, F., Ahmad, E., Sherwani, A., Owais, M. & Azam, A. Antibacterial and Cytotoxic Efficacy of Extracellular Silver Nanoparticles Biofabricated From Chromium Reducing Novel OS4 Strain of *Stenotrophomonas maltophilia*. *PLoS One* **8,** e59140 (2013).

72. Javani, S., Marín, I., Amils, R. & Abad, J. P. Four Psychrophilic Bacteria From Antarctica Extracellularly Biosynthesize at Low Temperature Highly Stable Silver Nanoparticles With Outstanding Antimicrobial Activity. *Colloids and Surfaces A: Physicochemical and Engineering Aspects* **483,** 60–69 (2015).

73. Saravanan, C., Rajesh, R., Kaviarasan, T., Muthukumar, K., Kavitake, D. & Shetty, P. H. Synthesis of Silver Nanoparticles Using Bacterial Exopolysaccharide and Its Application for Degradation of Azo-dyes. *Biotechnology reports (Amsterdam, Netherlands)* **15,** 33–40 (2017).

74. Mokhtari, N., Daneshpajouh, S., Seyedbagheri, S., Atashdehghan, R., Abdi, K., Sarkar, S., Minaian, S., Shahverdi, H. R. & Shahverdi, A. R. Biological Synthesis of Very Small Silver Nanoparticles by Culture Supernatant of *Klebsiella pneumonia*: The Effects of Visible-light Irradiation and the Liquid Mixing Process. *Materials Research Bulletin* **44,** 1415–1421 (2009).

75. Priyadarshini, S., Gopinath, V., Meera Priyadharsshini, N., MubarakAli, D. & Velusamy, P. Synthesis of Anisotropic Silver Nanoparticles Using Novel Strain, *Bacillus flexus* and Its Biomedical Application. *Colloids and surfaces. B, Biointerface* **102,** 232–237 (2013).

76. Rudakiya, D. M. & Pawar, K. Bactericidal Potential of Silver Nanoparticles Synthesized Using Cell-free Extract of *Comamonas acidovorans*: *In vitro* and *in silico* Approaches. *3 Biotech* **7,** 92 (2017).

77. Fu, M., Li, Q., Sun, D., Lu, Y., He, N., Deng, X., Wang, H. & Huang, J. Rapid Preparation Process of Silver Nanoparticles by Bioreduction and Their Characterizations. *Chinese Journal of Chemical Engineering* **14,** 114–117 (2006).

78. Zhang, H., Li, Q., Wang, H., Sun, D., Lu, Y. & He, N. Accumulation of Silver(i) Ion and Diamine Silver Complex by *Aeromonas* SH10 Biomass. *Appl Biochem Biotechnol* **143,** 54–62 (2007).

79. Abd-Elnaby, H. M., Abo-Elala, G. M., Abdel-Raouf, U. M. & Hamed, M. M. Antibacterial and Anticancer Activity of Extracellular Synthesized Silver Nanoparticles From Marine *Streptomyces rochei* MHM13. *The Egyptian Journal of Aquatic Research* **42,** 301–312 (2016).

80. Ali, D. M., Sasikala, M, Gunasekaran, M & Thajuddin, N. Biosynthesis and Characterization of Silver Nanoparticles Using Marine Cyanobacterium, *Oscillatoria willei* NTDM01. *Digest Journal of Nanomaterials and Biostructures* **6,** 385–390 (2011).

81. Bai, H. J., Yang, B. S., Chai, C. J., Yang, G. E., Jia, W. L. & Yi, Z. B. Green Synthesis of Silver Nanoparticles Using *Rhodobacter sphaeroides*. *World Journal of Microbiology and Biotechnology* **27,** 2723–2728 (2011).

82. Barud, H. S., Barrios, C., Regiani, T., Marques, R. F. C., Verelst, M., Dexpert-Ghys, J., Messaddeq, Y. & Ribeiro, S. J. L. Self-supported Silver Nanoparticles Containing Bacterial Cellulose Membranes. *Materials Science and Engineering C-Biomimetic and Supramolecular Systems* **28,** 515–518 (2008).

83. Baygar, T. & Ugur, A. Biosynthesis of Silver Nanoparticles by *Streptomyces griseorubens* Isolated From Soil and Their Antioxidant Activity. *IET Nanobiotechnology* **11,** 286–291 (2017).

84. Bhople, S., Gaikwad, S., Deshmukh, S., Bonde, S., Gade, A., Sen, S., Brezinska, A., Dahm, H. & Rai, M. Myxobacteria-mediated Synthesis of Silver Nanoparticles and Their Impregnation in Wrapping Paper Used for Enhancing Shelf Life of Apples. *IET Nanobiotechnology* **10,** 389–394 (2016).

85. Busi, S., Rajkumari, J., Ranjan, B. & Karuganti, S. Green Rapid Biogenic Synthesis of Bioactive Silver Nanoparticles (AgNPs) Using *Pseudomonas aeruginosa*. *IET Nanobiotechnology* **8,** 267–274 (2014).

86. Chai, C.-J. & Bai, H.-J. Biosynthesis of Silver Nanoparticles Using the Phototrophic Bacteria *Rhodopseudomonas palustris* and Its Antimicrobial Activity Against *Escherichia coli* and *Staphylococcus aureus*. *Microbiology/Weishengwuxue Tongbao* **37,** 1798–1804 (2010).

87. Chandrakasan, G., Seetharaman, P., Gnanasekar, S., Kadarkarai, M. & Sivaperumal, S. *Xenorhabdus stockiae* KT835471-mediated Feasible Biosynthesis of Metal Nanoparticles for Their Antibacterial and Cytotoxic Activities. *Artificial cells, nanomedicine, and biotechnology,* 1–10 (2017).

88. Das, V. L., Thomas, R., Varghese, R. T., Soniya, E. V., Mathew, J. & Radhakrishnan, E. K. Extracellular Synthesis of Silver Nanoparticles by the *Bacillus* Strain CS 11 Isolated From Industrialized Area. *3 Biotech* **4,** 121–126 (2014).

89. Debabov, V. G., Voeikova, T. A., Shebanova, A. S., Shaitan, K. V., Emel'yanova, L. K., Novikova, L. M. & Kirpichnikov, M. P. Bacterial Synthesis of Silver Sulfide Nanoparticles. *Nanotechnologies in Russia* **8,** 269–276 (2013).

90. Deepa, S, Kanimozhi, K & Panneerselvam, A. Antimicrobial Activity of Extracellularly Synthesized Silver Nanoparticles From Marine Derived Actinomycetes. *International journal of current microbiology and applied sciences* **2,** 223–230 (2013).

91. Deljou, A. & Goudarzi, S. Green Extracellular Synthesis of the Silver Nanoparticles Using Thermophilic *Bacillus* Sp. Az1 and Its Antimicrobial Activity Against Several Human Pathogenetic Bacteria. *Iranian journal of biotechnology* **14,** 25–32 (2016).

92. El-Batal, A., Amin, M., Shehata, M. M. & Hallol, M. M. Synthesis of Silver Nanoparticles by *Bacillus stearothermophilus* Using Gamma Radiation and Their Antimicrobial Activity. *World Applied sciences Journal* **22,** 1–16 (2013).

93. El-Shanshoury, A. E.-R. R., ElSilk, S. E. & Ebeid, M. E. Extracellular Biosynthesis of Silver Nanoparticles Using *Escherichia coli* Atcc 8739, *Bacillus subtilis* ATCC 6633, and *Streptococcus thermophilus* ESH1 and Their Antimicrobial Activities. *ISRN Nanotechnology* **2011,** 1–7 (2011).

94. Faghri Zonooz, N. & Salouti, M. Extracellular Biosynthesis of Silver Nanoparticles Using Cell Filtrate of *Streptomyces* Sp. Eri-3. *Scientia Iranica* **18,** 1631–1635 (2011).

95. Fouad, H., Hongjie, L., Yanmei, D., Baoting, Y., El-Shakh, A., Abbas, G. & Jianchu, M. Synthesis and Characterization of Silver Nanoparticles Using *Bacillus amyloliquefaciens* and *Bacillus subtilis* to Control Filarial Vector *Culex pipiens* Pallens and Its Antimicrobial Activity. *Artificial cells, nanomedicine, and biotechnology* **45,** 1369–1378 (2017).

96. Ghorbani, H. R. Biosynthesis of Silver Nanoparticles by *Escherichia coli*. *Asian Journal of Chemistry* **25,** 1247–1249 (2013).

97. Gou, Y., Zhang, F., Zhu, X. & Li, X. Biosynthesis and Characterisation of Silver Nanoparticles Using *Sphingomonas paucimobilis* Sp. BDS1. *IET Nanobiotechnology* **9,** 53–57 (2015).

98. Govindaraju, K., Basha, S. K., Kumar, V. G. & Singaravelu, G. Silver, Gold and Bimetallic Nanoparticles Production Using Single-cell Protein (*Spirulina platensis*) Geitler. *Journal of Materials Science* **43,** 5115–5122 (2008).

99. Gurunathan, S., Kalishwaralal, K., Vaidyanathan, R., Venkataraman, D., Pandian, S. R., Muniyandi, J., Hariharan, N. & Eom, S. H. Biosynthesis, Purification and Characterization of Silver Nanoparticles Using *Escherichia coli*. *Colloids and surfaces. B, Biointerfaces* **74,** 328–335 (2009).

100. Jain, D., Kachhwaha, S., Jain, R., Srivastava, G. & Kothari, S. Novel Microbial Route to Synthesize Silver Nanoparticles Using Spore Crystal Mixture of *Bacillus thuringiensis* (2010).

101. Juibari, M. M., Abbasalizadeh, S, Jouzani, G. S. & Noruzi, M. Intensified Biosynthesis of Silver Nanoparticles Using a Native Extremophilic *Ureibacillus thermosphaericus* Strain. *Materials Letters* **65,** 1014–1017 (2011).

102. Kalimuthu, K., Babu, R. S., Venkataraman, D., Bilal, M. & Gurunathan, S. Biosynthesis of Silver Nanocrystals by *Bacillus licheniformis*. *Colloids and Surfaces B: Biointerfaces* **65,** 150–153 (2008).

103. Kalishwaralal, K., Deepak, V., Ram Kumar Pandian, S., Kottaisamy, M., BarathmaniKanth, S., Kartikeyan, B. & Gurunathan, S. Biosynthesis of Silver and Gold Nanoparticles Using *Brevibacterium casei*. *Colloids and surfaces. B, Biointerfaces* **77,** 257–262 (2010).

104. Karthik, C. & Radha, K. V. Biosynthesis and Characterization of Silver Nanoparticles Using *Enterobacter aerogenes*: A Kinetic Approach. *Digest Journal of Nanomaterials and Biostructures* **7,** 1007–1014 (2012).

105. Karunakaran, G., Jagathambal, M., Gusev, A., Minh, N. V., Kolesnikov, E., Mandal, A. R. & Kuznetsov, D. *Nitrobacter* Sp. Extract Mediated Biosynthesis of Ag_2O NPs With Excellent Antioxidant and Antibacterial Potential for Biomedical Application. *IET Nanobiotechnology* **10,** 425–430 (2016).

106. Krishnaraj, R. N. & Berchmans, S. *In vitro* Antiplatelet Activity of Silver Nanoparticles Synthesized Using the Microorganism *Gluconobacter Roseus*: an AFM-based Study. *Rsc Advances* **3,** 8953–8959 (2013).

107. Law, N., Ansari, S., Livens, F. R., Renshaw, J. C. & Lloyd, J. R. Formation of Nanoscale Elemental Silver Particles via Enzymatic Reduction by *Geobacter sulfurreducens*. *Appl Environ Microbiol* **74,** 7090–7093 (2008).

108. Lengke, M. F., Fleet, M. E. & Southam, G. Biosynthesis of Silver Nanoparticles by Filamentous Cyanobacteria From a Silver(i) Nitrate Complex. *Langmuir* **23,** 2694–2699 (2007).

109. Mageswari, A., Subramanian, P., Ravindran, V., Yesodharan, S., Bagavan, A., Rahuman, A. A., Karthikeyan, S. & Gothandam, K. M. Synthesis and Larvicidal Activity of Low-temperature Stable Silver Nanoparticles From Psychrotolerant *Pseudomonas mandelii*. *Environmental science and pollution research international* **22,** 5383–5394 (2015).

110. Mahanty, A., Bosu, R., Panda, P., Netam, S. P. & Sarkar, B. Microwave Assisted Rapid Combinatorial Synthesis of Silver Nanoparticles Using *E. coli* Culture Supernatant. *International journal of pharmacy and biological sciences* **4,** 1030–1035 (2013).

111. Maharani, V., Sundaramanickam, A. & Balasubramanian, T. *In vitro* Anticancer Activity of Silver Nanoparticle Synthesized by *Escherichia coli* VM1 Isolated From Marine Sediments of Ennore Southeast Coast of India. *Enzyme and microbial technology* **95,** 146–154 (2016).

112. Manivasagan, P., Venkatesan, J., Senthilkumar, K., Sivakumar, K. & Kim, S. K. Biosynthesis, Antimicrobial and Cytotoxic Effect of Silver Nanoparticles Using a Novel *Nocardiopsis* Sp. MBRC-1. *Biomed Res Int* **2013,** 287638 (2013).

113. Mehta, A., Sidhu, C., Pinnaka, A. K. & Roy Choudhury, A. Extracellular Polysaccharide Production by a Novel Osmotolerant Marine Strain of *Alteromonas macleodii* and Its Application Towards Biomineralization of Silver. *PLoS One* **9,** e98798 (2014).

114. Mishra, S., Singh, B. R., Naqvi, A. H. & Singh, H. B. Potential of Biosynthesized Silver Nanoparticles Using *Stenotrophomonas* Sp. BHU-S7 (MTCC 5978) for Management of Soil-borne and Foliar Phytopathogens. *Scientific reports* **7,** 45154 (2017).

115. Mohammed Fayaz, A., Girilal, M., Rahman, M., Venkatesan, R. & Kalaichelvan, P. T. Biosynthesis of Silver and Gold Nanoparticles Using Thermophilic Bacterium *Geobacillus stearothermophilus*. *Process Biochemistry* **46,** 1958–1962 (2011).

116. Morsy, F. M. Toward Revealing the Controversy of Bacterial Biosynthesis Versus Bactericidal Properties of Silver Nanoparticles (AgNPs): Bacteria and Other Microorganisms Do Not Per Se Viably Synthesize AgNPs. *Archives of microbiology* **197,** 645–655 (2015).

117. Nair, B. & Pradeep, T. Coalescence of Nanoclusters and Formation of Submicron Crystallites Assisted by *Lactobacillus* Strains. *Crystal Growth and Design* **2,** 293–298 (2002).

118. Namasivayam, S. K. R., Kumar, E. G. & Reepika, R. Synthesis of Silver Nanoparticles by *Lactobaciluus acidophilus* 01 Strain and Evaluation of its *in vitro* Genomic DNA Toxicity. *Nano-Micro Letters* **2,** 160–163 (2010).

119. Nanda, A. & Saravanan, M. Biosynthesis of Silver Nanoparticles From *Staphylococcus aureus* and its Antimicrobial Activity Against MRSA and MRSE. *Nanomedicine: nanotechnology, biology, and medicine* **5,** 452–456 (2009).

120. Narayanan, K. B. & Sakthivel, N. Biosynthesis of Silver Nanoparticles by *Phytopathogen xanthomonas oryzae* Pv. oryzae Strain BXO8. *Journal of microbiology and biotechnology* **23,** 1287–1292 (2013).

121. Otari, S. V., Patil, R. M., Nadaf, N. H., Ghosh, S. J. & Pawar, S. H. Green Synthesis of Silver Nanoparticles by Microorganism Using Organic Pollutant: Its Antimicrobial and Catalytic Application. *Environmental science and pollution research international* **21,** 1503–1513 (2014).

122. Oves, M., Qari, H. A., Felemban, N. M., Khan, M. Z., Rehan, Z. A. & Ismail, I. M. I. Marinobacter Lipolyticus From Red Sea for Lipase Production and Modulation of Silver Nanomaterials for Anticandidal Activities. *IET Nanobiotechnology* **11,** 403–410 (2017).

123. Pourali, P., Baserisalehi, M., Afsharnezhad, S., Behravan, J., Alavi, H. & Hosseini. Biological Synthesis of Silver and Gold Nanoparticles by Bacteria in Different Temperatures (37°C and 50°C). *Journal of Pure and Applied Microbiology* **6,** 757–763 (2012).

124. Pourali, P., Baserisalehi, M., Afsharnezhad, S., Behravan, J., Ganjali, R., Bahador, N. & Arabzadeh, S. The Effect of Temperature on Antibacterial Activity of Biosynthesized Silver Nanoparticles. *Biometals* **26,** 189–196 (2013).

125. Pourali, P., Razavian Zadeh, N. & Yahyaei, B. Silver Nanoparticles Production by Two Soil Isolated Bacteria, *Bacillus thuringiensis* and *Enterobacter cloacae*, and Assessment of Their Cytotoxicity and Wound Healing Effect in Rats. *Wound repair and regeneration* **24,** 860–869 (2016).

126. Prabhawathi, V., Sivakumar, P. M. & Doble, M. Green Synthesis of Protein Stabilized Silver Nanoparticles Using *Pseudomonas fluorescens*, a Marine Bacterium, and its Biomedical Applications When Coated on Polycaprolactam. *Industrial and Engineering Chemistry Research* **51,** 5230–5239 (2012).

127. Prakash, A., Sharma, S., Ahmad, N., Ghosh, A. & Sinha, P. Bacteria Mediated Extracellular Synthesis of Metallic Nanoparticles. *International journal of bio-technology and research* **1,** 71–79 (2010).

128. Prakasham, R. S., Buddana, S. K., Yannam, S. K. & Guntuku, G. S. Characterization of Silver Nanoparticles Synthesized by Using Marine Isolate *Streptomyces albidoflavus*. *Journal of microbiology and biotechnology* **22,** 614–621 (2012).

129. Rajeshkumar, S, Malarkodi, C, Paulkumar, K, Vanaja, M, Gnanajobitha, G & Annadurai, G. Intracellular and Extracellular Biosynthesis of Silver Nanoparticles by Using Marine Bacteria Vibrio Alginolyticus. *Nanoscience and Nanotechnology* **3,** 21–25 (2013).

130. Rajora, N., Kaushik, S., Jyoti, A. & Kothari, S. L. Rapid Synthesis of Silver Nanoparticles by *Pseudomonas stutzeri* Isolated From Textile Soil Under Optimised Conditions and Evaluation of Their Antimicrobial and Cytotoxicity Properties. *IET Nanobiotechnology* **10,** 367–373 (2016).

131. Rostami, H., Khosravi, F., Mohseni, M. & Rostami, A. A. Biosynthesis of Ag Nanoparticles Using Isolated Bacteria From Contaminated Sites and Its Application as an Efficient Catalyst for Hydrazine Electrooxidation. *International journal of biological macromolecules* **107,** 343–348 (2018).

132. Sadhasivam, S., Shanmugam, P. & Yun, K. Biosynthesis of Silver Nanoparticles by *Streptomyces hygroscopicus* and Antimicrobial Activity Against Medically Important Pathogenic Microorganisms. *Colloids and surfaces. B, Biointerfaces* **81,** 358–362 (2010).

133. Samundeeswari, A., Dhas, S. P., Nirmala, J., John, S. P., Mukherjee, A. & Chandrasekaran, N. Biosynthesis of Silver Nanoparticles Using Actinobacterium *Streptomyces albogriseolus* and its Antibacterial Activity. *Biotechnol Appl Biochem* **59,** 503–507 (2012).

134. Seshadri, S., Prakash, A. & Kowshik, M. Biosynthesis of Silver Nanoparticles by Marine Bacterium, *Idiomarina* sp PR58-8. *Bulletin of Materials Science* **35,** 1201–1205 (2012).

135. Sharma, S., Ahmad, N., Prakash, A., Singh, V. N., Ghosh, A. K. & Mehta, B. R. Synthesis of Crystalline Ag Nanoparticles (AgNPs) From Microorganisms. *Materials Sciences and Applications* **1,** 1 (2010).

136. Shivaji, S., Madhu, S. & Singh, S. Extracellular Synthesis of Antibacterial Silver Nanoparticles Using Psychrophilic Bacteria. *Process Biochemistry* **46,** 1800–1807 (2011).

137. Singh, R., Wagh, P., Wadhwani, S., Gaidhani, S., Kumbhar, A., Bellare, J. & Chopade, B. A. Synthesis, Optimization, and Characterization of Silver Nanoparticles From *Acinetobacter calcoaceticus* and Their Enhanced Antibacterial Activity When Combined With Antibiotics. *International journal of nanomedicine* **8,** 4277–4290 (2013).

138. Siva Kumar, K., Kumar, G., Prokhorov, E., Luna-Bácenas, G., Buitron, G., Khanna, V. G. & Sanchez, I. C. Exploitation of Anaerobic Enriched Mixed Bacteria (AEMB) for the Silver and Gold Nanoparticles Synthesis. *Colloids and Surfaces A: Physicochemical and Engineering Aspects* **462,** 264–270 (2014).

139. Sneha, K., Sathishkumar, M., Mao, J., Kwak, I. S. & Yun, Y. S. Corynebacterium Glutamicum-mediated Crystallization of Silver Ions Through Sorption and Reduction Processes. *Chemical Engineering Journal* **162,** 989–996 (2010).

140. Sudha, S. S., Rajamanickam, K. & Rengaramanujam, J. Microalgae Mediated Synthesis of Silver Nanoparticles and Their Antibacterial Activity Against Pathogenic Bacteria. *Indian journal of experimental biology* **51,** 393–399 (2013).

141. Suresh, A. K., Pelletier, D. A., Wang, W., Moon, J. W., Gu, B., Mortensen, N. P., Allison, D. P., Joy, D. C., Phelps, T. J. & Doktycz, M. J. Silver Nanocrystallites: Biofabrication Using *Shewanella oneidensis*, and an Evaluation of Their Comparative Toxicity on Gram-negative and Gram-positive Bacteria. *Environmental science and technology* **44,** 5210–5215 (2010).

142. Tamboli, D. P. & Lee, D. S. Mechanistic Antimicrobial Approach of Extracellularly Synthesized Silver Nanoparticles Against Gram Positive and Gram Negative Bacteria. *Journal of hazardous materials* **260,** 878–884 (2013).

143. Thamilselvi, V. & Radha, K. V. Synthesis of Silver Nanoparticles From *Pseudomonas putida* NCIM 2650 in Silver Nitrate Supplemented Growth Medium and Optimization Using Response Surface Methodology. *Digest Journal of Nanomaterials and Biostructures* **8,** 1101–1111 (2013).

144. Thomas, R., Jasim, B, Mathew, J. & Radhakrishnan, E. Extracellular Synthesis of Silver Nanoparticles by Endophytic *Bordetella* Sp. Isolated From *Piper nigrum* and Its Antibacterial Activity Analysis. *Nano Biomedicine and Engineering* **4** (2012).

145. Zhang, H. R., Li, Q. B., Lu, Y. H., Sun, D. H., Lin, X. P., Deng, X., He, N. & Zheng, S. Z. Biosorption and Bioreduction of Diamine Silver Complex by *Corynebacterium*. *Journal of Chemical Technology and Biotechnology* **80,** 285–290 (2005).

146. Huerta-Cepas, J., Serra, F. & Bork, P. Ete 3: Reconstruction, Analysis, and Visualization of Phylogenomic Data. *Molecular Biology and Evolution Society* **33,** 1635–1638 (2016).

147. Lin, I. W. S., Lok, C. N. & Che, C. M. Biosynthesis of Silver Nanoparticles From Silver(i) Reduction by the Periplasmic Nitrate Reductase C-type Cytochrome Subunit NapC in a Silver-resistant *E. coli*. *Chemical Science* **5,** 3144–3150 (2014).

148. Ghorbani, H. R. Biosynthesis of Silver Nanoparticles Using *Salmonella typhirium*. *Journal of Nanostructure in Chemistry* **3,** 29 (2013).

149. Liu, L., Liu, T., Tade, M., Wang, S., Li, X. & Liu, S. Less Is More, Greener Microbial Synthesis of Silver Nanoparticles. *Enzyme and microbial technology* **67,** 53–58 (2014).

150. El-Naggar Nel, A. & Abdelwahed, N. A. Application of Statistical Experimental Design for Optimization of Silver Nanoparticles Biosynthesis by a Nanofactory *Streptomyces viridochromogenes*. *J Microbiol* **52,** 53–63 (2014).

151. Mott, D., Thuy, N. T. B., Aoki, Y. & Maenosono, S. Aqueous Synthesis and Characterization of Ag and Ag-Au Nanoparticles: Addressing Challenges in Size, Monodispersity and Structure. *Philosophical Transactions of the Royal Society A: Mathematical, Physical and Engineering Sciences* **368,** 4275–4292 (2010).

152. Wei, X., Luo, M., Li, W., Yang, L., Liang, X., Xu, L., Kong, P. & Liu, H. Synthesis of Silver Nanoparticles by Solar Irradiation of Cell-free *Bacillus amyloliquefaciens* Extracts and $AgNO_3$. *Bioresource technology* **103,** 273–278 (2012).

153. Durán, N., Nakazato, G. & Seabra, A. B. Antimicrobial Activity of Biogenic Silver Nanoparticles, and Silver Chloride Nanoparticles: An Overview and Comments. *Applied microbiology and biotechnology* **100,** 6555–6570 (2016).

154. Plaza, G. A., Chojniak, J., Mendrek, B., Trzebicka, B., Kvitek, L., Panacek, A., Prucek, R., Zboril, R., Paraszkiewicz, K. & Bernat, P. Synthesis of Silver Nanoparticles by *Bacillus subtilis* T-1 Growing on Agro-industrial Wastes and Producing Biosurfactant. *IET Nanobiotechnology* **10,** 62–68 (2016).

155. Safekordi, A., Attar, H & Ghorbani, H. *Optimization of Silver Nanoparticles Production by E. coli and the Study of Reaction Kinetics* in *International Conference on Chemical, Ecology and Environmental Sciences, Pattaya December* (2011).

156. Syed, B., Prasad, N., Dhananjaya, B., Yallappa, S, Satish, S, *et al.* Synthesis of Silver Nanoparticles by Endosymbiont *Pseudomonas fluorescens* CA 417 and Their Bactericidal Activity. *Enzyme and Microbial Technology* **95,** 128–136 (2016).

157. Ghorbani, H. R., Attar, H., Safekordi, A. A. & Sorkhabadi, S. M. Design of a Bioprocess to Produce Silver Nanoparticles. *IET Nanobiotechnol* **6,** 71–75 (2012).

158. Mäntele, W. & Deniz, E. UV-VIS Absorption Spectroscopy: Lambert-Beer reloaded (2017).

159. Moore, J. & Cerasoli, E. Particle Light Scattering Methods and Applications (2017).

160. Edwards, A. A. & Alexander, B. D. UV-Visible Absorption Spectroscopy, Organic Applications (2017).

161. Vaidyanathan, R., Gopalram, S., Kalishwaralal, K., Deepak, V., Pandian, S. R. K. & Gurunathan, S. Enhanced Silver Nanoparticle Synthesis by Optimization of Nitrate Reductase Activity. *Colloids and surfaces B: Biointerfaces* **75,** 335–341 (2010).

162. Lin, P.-C., Lin, S., Wang, P. C. & Sridhar, R. Techniques for Physicochemical Characterization of Nanomaterials. *Biotechnology advances* **32,** 711–726 (2014).

163. Bunaciu, A. A., UdriŞTioiu, E. G. & Aboul-Enein, H. Y. X-ray Diffraction: Instrumentation and Applications. *Critical Reviews in Analytical Chemistry* **45,** 289–299 (2015).

164. Paulkumar, K., Rajeshkumar, S., Gnanajobitha, G., Vanaja, M., Malarkodi, C. & Annadurai, G. Biosynthesis of silver chloride nanoparticles using Bacillus subtilis MTCC 3053 and assessment of its antifungal activity. *ISRN nanomaterials* **2013** (2013).

165. Durán, N., Nakazato, G. & Seabra, A. B. Antimicrobial Activity of Biogenic Silver Nanoparticles, and Silver Chloride Nanoparticles: An Overview and Comments. *Applied microbiology and biotechnology* **100,** 6555–6570 (2016).

166. Scimeca, M., Bischetti, S., Lamsira, H. K., Bonfiglio, R. & Bonanno, E. Energy Dispersive X-ray (EDX) Microanalysis: A Powerful Tool in Biomedical Research and Diagnosis. *European journal of histochemistry: EJH* **62** (2018).

167. Pennycook, S. J., Li, C., Li, M., Tang, C., Okunishi, E., Varela, M., Kim, Y.-M. & Jang, J. H. Material Structure, Properties, and Dynamics Through Scanning Transmission Electron Microscopy. *Journal of Analytical Science and Technology* **9,** 11 (2018).

168. Piro, M. H., Sunderland, D., Livingstone, S., Sercombe, J., Revie, W., Quastel, A., Terrani, K. & Judge, C. A review of pellet–clad interaction behavior in zirconium alloy fuel cladding (2017).

169. Worsfold, P., Poole, C., Townshend, A. & Miro, M. Microscopy - Semiconductors. *Encyclopedia of Analytical Science (Third Edition)* (2013).

170. Koh, A. L., Bao, K., Khan, I., Smith, W. E., Kothleitner, G., Nordlander, P., Maier, S. A. & McComb, D. W. Electron energy-loss spectroscopy (EELS) of surface plasmons in single silver nanoparticles and dimers: influence of beam damage and mapping of dark modes. *ACS nano* **3,** 3015–3022 (2009).

171. Engelhard, M. H., Droubay, T. C. & Du, Y. X-Ray photoelectron Spectroscopy Applications (2017).

172. Vasil'kov, A., Dovnar, R., Smotryn, S., Iaskevich, N. & Naumkin, A. Plasmon Resonance of Silver Nanoparticles as a Method of Increasing Their Antibacterial Action. *Antibiotics* **7,** 80 (2018).

173. Jiménez, J., Liu, H & Fachini, E. X-ray photoelectron spectroscopy of silver nanoparticles in phosphate glass. *Materials Letters* **64,** 2046–2048 (2010).

174. Radu, T, Benea, D, Ciceo-Lucacel, R, Barbu-Tudoran, L & Simon, S. X-ray photoelectron spectroscopic characterization of Ag nanoparticles embedded bioglasses. *The Journal of Physical Chemistry C* **116,** 17975–17979 (2012).

175. Jyoti, K., Baunthiyal, M. & Singh, A. Characterization of Silver Nanoparticles Synthesized Using Urtica Dioica Linn. Leaves and Their Synergistic Effects With Antibiotics. *Journal of Radiation Research and Applied Sciences* **9,** 217–227 (2016).

176. Saeb, A. T. M., Alshammari, A. S., Al-Brahim, H. & Al-Rubeaan, K. A. Production of Silver Nanoparticles With Strong and Stable Antimicrobial Activity Against Highly Pathogenic and Multidrug Resistant Bacteria. *The Scientific World Journal* **2014,** 9 (2014).

177. Bannock, J. H., Krishnadasan, S. H., Heeney, M. & de Mello, J. C. A Gentle Introduction to the Noble Art of Flow Chemistry. *Mater. Horiz.* **1,** 373–378 (4 2014).

178. Plutschack, M. B., Pieber, B., Gilmore, K. & Seeberger, P. H. The Hitchhiker's Guide to Flow Chemistry. *Chemical Reviews* **117,** 11796–11893 (2017).

179. Lee, C.-Y., Wang, W.-T., Liu, C.-C. & Fu, L.-M. Passive Mixers in Microfluidic Systems: A Review. *Chemical Engineering Journal* **288,** 146–160 (2016).

180. Calabrese, G. S. & Pissavini, S. From Batch to Continuous Flow Processing in Chemicals Manufacturing. *AIChE Journal* **57,** 828–834 (2011).

181. Carboni, M., Capretto, L., Carugo, D., Stulz, E. & Zhang, X. Microfluidics-based Continuous Flow Formation of Triangular Silver Nanoprisms With Tuneable Surface Plasmon Resonance. *Journal of Materials Chemistry C* **1,** 7540–7546 (2013).

182. Długosz, O. & Banach, M. Continuous Production of Silver Nanoparticles and Process Control. *Journal of Cluster Science* **30,** 541–552 (2019).

183. Baber, R., Mazzei, L., Thanh, N. T. K. & Gavriilidis, A. Synthesis of Silver Nanoparticles in a Microfluidic Coaxial Flow Reactor. *RSC Advances* **5,** 95585–95591 (2015).

184. Xu, L., Peng, J., Yan, M., Zhang, D. & Shen, A. Q. Droplet Synthesis of Silver Nanoparticles by a Microfluidic Device. *Chemical Engineering and Processing: Process Intensification* **102,** 186–193 (2016).

185. Yang, C.-H., Wang, L.-S., Chen, S.-Y., Huang, M.-C., Li, Y.-H., Lin, Y.-C., Chen, P.-F., Shaw, J.-F. & Huang, K.-S. Microfluidic Assisted Synthesis of Silver Nanoparticle–chitosan Composite Microparticles for Antibacterial Applications. *International Journal of Pharmaceutics* **510,** 493–500 (2016).

186. Liu, H., Huang, J., Sun, D., Lin, L., Lin, W., Li, J., Jiang, X., Wu, W. & Li, Q. Microfluidic Biosynthesis of Silver Nanoparticles: Effect of Process Parameters on Size Distribution. *Chemical Engineering Journal* **209,** 568–576 (2012).

187. Satapathy, S., Shukla, S. P., Sandeep, K. P., Singh, A. R. & Sharma, N. Evaluation of the Performance of an Algal Bioreactor for Silver Nanoparticle Production. *Journal of Applied Phycology* **27,** 285–291 (2015).

188. Robertson, J. D., Rizzello, L., Avila-Olias, M., Gaitzsch, J., Contini, C., Magoń, M. S., Renshaw, S. A. & Battaglia, G. Purification of Nanoparticles by Size and Shape. *Scientific reports* **6,** 27494 (2016).

189. Trefry, J. C., Monahan, J. L., Weaver, K. M., Meyerhoefer, A. J., Markopolous, M. M., Arnold, Z. S., Wooley, D. P. & Pavel, I. E. Size Selection and Concentration of Silver Nanoparticles by Tangential Flow Ultrafiltration for Sers-based Biosensors. *Journal of the American Chemical Society* **132,** 10970–10972 (2010).

190. Anders, C. B., Baker, J. D., Stahler, A. C., Williams, A. J., Sisco, J. N., Trefry, J. C., Wooley, D. P. & Sizemore, I. E. P. Tangential Flow Ultrafiltration: A “green” Method for the Size Selection and Concentration of Colloidal Silver Nanoparticles. *JoVE (Journal of Visualized Experiments),* e4167–e4167 (2012).

191. Sweeney, S. F., Woehrle, G. H. & Hutchison, J. E. Rapid Purification and Size Separation of Gold Nanoparticles via Diafiltration. *Journal of the American Chemical Society* **128,** 3190–3197 (2006).

192. Carboni, M., Carravetta, M., Zhang, X. L. & Stulz, E. Efficient Nir Light Blockage With Matrix Embedded Silver Nanoprism Thin Films for Energy Saving Window Coating. *Journal of Materials Chemistry C* **4,** 1584–1588 (2016).

193. Pelaz, B., del Pino, P., Maffre, P., Hartmann, R., Gallego, M., Rivera-Fernandez, S., de la Fuente, J. M., Nienhaus, G. U. & Parak, W. J. Surface Functionalization of Nanoparticles With Polyethylene Glycol: Effects on Protein Adsorption and Cellular Uptake. *ACS nano* **9,** 6996–7008 (2015).

194. Brandon, M. P., Ledwith, D. M. & Kelly, J. M. Preparation of Saline-stable, Silica-coated Triangular Silver Nanoplates of Use for Optical Sensing. *Journal of Colloid and Interface Science* **415,** 77–84 (2014).

195. Sooresh, A., Kwon, H., Taylor, R., Pietrantonio, P., Pine, M. & Sayes, C. M. Surface functionalization of silver nanoparticles: Novel applications for insect vector control. *ACS applied materials & interfaces* **3,** 3779–3787 (2011).

196. Liu, F., Rao, B. S. & Nunzi, J.-M. A Dye Functionalized Silver–Silica Core–Shell Nanoparticle Organic Light Emitting Diode. *Organic Electronics* **12,** 1279–1284 (2011).

197. Wang, Y., Ding, X., Chen, Y., Guo, M., Zhang, Y., Guo, X. & Gu, H. Antibiotic-Loaded, Silver Core-Embedded Mesoporous Silica Nanovehicles as a Synergistic Antibacterial Agent for the Treatment of Drug-Resistant Infections. *Biomaterials* **101,** 207–216 (2016).

198. Zhang, J., Sun, Y., Zhang, H., Xu, B., Zhang, H. & Song, D. Preparation and Application of Triangular Silver Nanoplates/chitosan Composite in Surface Plasmon Resonance Biosensing. *Analytica Chimica Acta* **769,** 114–120 (2013).

199. Kong, H. & Jang, J. One-Step Fabrication of Silver Nanoparticle Embedded Polymer Nanofibers by Radical-Mediated Dispersion Polymerization. *Chemical communications,* 3010–3012 (2006).

200. Dong, X.-Y., Gao, Z.-W., Yang, K.-F., Zhang, W.-Q. & Xu, L.-W. Nanosilver as a New Generation of Silver Catalysts in Organic Transformations for Efficient Synthesis of Fine Chemicals. *Catalysis Science and Technology* **5,** 2554–2574 (2015).

201. Tran, Q. H., Nguyen, V. Q. & Le, A. T. Silver Nanoparticles: Synthesis, Properties, Toxicology, Applications and Perspectives. *Advances in Natural Sciences-Nanoscience and Nanotechnology* **4,** 033001 (2013).

202. Wei, L., Lu, J., Xu, H., Patel, A., Chen, Z.-S. & Chen, G. Silver Nanoparticles: Synthesis, Properties, and Therapeutic Applications. *Drug discovery today* **20,** 595–601 (2015).

203. Alexander, J. W. History of the Medical Use of Silver. *Surgical infections* **10,** 289–292 (2009).

204. Klasen, H. Historical Review of the Use of Silver in the Treatment of Burns. I. Early Uses. *Burns* **2,** 117–130 (2000).

205. Sim, W., Barnard, R. T., Blaskovich, M. & Ziora, Z. M. Antimicrobial Silver in Medicinal and Consumer Applications: A Patent Review of the Past Decade (2007–2017). *Antibiotics* **7,** 93 (2018).

206. Meledandri, C. J., Schwass, D. R., Cotton, G. C. & Duncan, W. J. *Antimicrobial Gel Containing Silver Nanoparticles* US Patent App. 15/766,045. 2019.

207. Shastri, J. P., Rupani, M. G. & Jain, R. L. Antimicrobial Activity of Nanosilver-coated Socks Fabrics Against Foot Pathogens. *Journal of the textile institute* **103,** 1234–1243 (2012).

208. Lee, Y. S. *Clothes Washing Machine* US Patent 7,934,402. 2011.

209. Pradeep, T., Chaudhary, A., Sankar, M. U., Rajarajan, G., *et al. Sustained Silver Release Composition for Water Purification* US Patent App. 15/677,618. 2018.

210. Ruppert, K., Grundler, A. & Erdrich, A. *Antimicrobial Nano Silver Additive for Polymerizable Dental Materials* US Patent App. 10/583,441. 2007.

211. Durán, N., Durán, M., de Jesus, M. B., Seabra, A. B., Fávaro, W. J. & Nakazato, G. Silver Nanoparticles: A New View on Mechanistic Aspects on Antimicrobial Activity. *Nanomedicine: Nanotechnology, Biology and Medicine* **12,** 789–799 (2016).

212. Zille, A., Almeida, L., Amorim, T., Carneiro, N., Esteves, M. F., Silva, C. J. & Souto, A. P. Application of Nanotechnology in Antimicrobial Finishing of Biomedical Textiles. *Materials Research Express* **1,** 032003 (2014).

213. Maneerung, T., Tokura, S. & Rujiravanit, R. Impregnation of Silver Nanoparticles Into Bacterial Cellulose for Antimicrobial Wound Dressing. *Carbohydrate polymers* **72,** 43–51 (2008).

214. Yan, J., Abdelgawad, A. M., El-Naggar, M. E. & Rojas, O. J. Antibacterial Activity of Silver Nanoparticles Synthesized *in situ* by Solution Spraying Onto Cellulose. *Carbohydrate polymers* **147,** 500–508 (2016).

215. Lee, H., Yeo, S. Y. & Jeong, S. H. Antibacterial Effect of Nanosized Silver Colloidal Solution on Textile Fabrics. *Journal of Materials Science* **38,** 2199–2204 (2003).

216. El-Sheikh, M., El Gabry, L. & Ibrahim, H. Photosynthesis of Carboxymethyl Starch-stabilized Silver Nanoparticles and Utilization to Impart Antibacterial Finishing for Wool and Acrylic Fabrics. *Journal of Polymers* **2013** (2013).

217. Zhang, F., Wu, X., Chen, Y. & Lin, H. Application of Silver Nanoparticles to Cotton Fabric as an Antibacterial Textile Finish. *Fibers and Polymers* **10,** 496–501 (2009).

218. Zhang, G., Liu, Y., Gao, X. & Chen, Y. Synthesis of Silver Nanoparticles and Antibacterial Property of Silk Fabrics Treated by Silver Nanoparticles. *Nanoscale research letters* **9,** 216 (2014).

219. Li, H., Wang, L., Chai, Y., Cao, Y. & Lu, F. Synergistic Effect Between Silver Nanoparticles and Antifungal Agents on Candida Albicans Revealed by Dynamic Surface-enhanced Raman Spectroscopy. *Nanotoxicology* **12,** 1230–1240 (2018).

220. Fayaz, A. M., Balaji, K., Girilal, M., Yadav, R., Kalaichelvan, P. T. & Venketesan, R. Biogenic Synthesis of Silver Nanoparticles and Their Synergistic Effect With Antibiotics: A Study Against Gram-positive and Gram-negative Bacteria. *Nanomedicine: Nanotechnology, Biology and Medicine* **6,** 103–109 (2010).

221. Deng, H., McShan, D., Zhang, Y., Sinha, S. S., Arslan, Z., Ray, P. C. & Yu, H. Mechanistic Study of the Synergistic Antibacterial Activity of Combined Silver Nanoparticles and Common Antibiotics. *Environmental science & technology* **50,** 8840–8848 (2016).

222. Graves Jr, J. L., Tajkarimi, M., Cunningham, Q., Campbell, A., Nonga, H., Harrison, S. H. & Barrick, J. E. Rapid Evolution of Silver Nanoparticle Resistance in *Escherichia coli*. *Frontiers in genetics* **6,** 42 (2015).

223. Panáček, A., Kvítek, L., Smékalová, M., Večeřová, R., Kolář, M., Roderova, M., Dyčka, F., Šebela, M., Prucek, R., Tomanec, O., *et al.* Bacterial Resistance to Silver Nanoparticles and How to Overcome It. *Nature nanotechnology* **13,** 65 (2018).

224. Helmlinger, J, Sengstock, C, Groß-Heitfeld, C, Mayer, C, Schildhauer, T., Koller, M & Epple, M. Silver Nanoparticles With Different Size and Shape: Equal Cytotoxicity, but Different Antibacterial Effects. *Rsc Advances* **6,** 18490–18501 (2016).

225. Nam, S.-H. & An, Y.-J. Size-and Shape-dependent Toxicity of Silver Nanomaterials in Green Alga *Chlorococcum infusionum*. *Ecotoxicology and environmental safety* **168,** 388–393 (2019).

226. Graf, C., Nordmeyer, D., Sengstock, C., Ahlberg, S., Diendorf, J., Raabe, J., Epple, M., Koller, M., Lademann, J., Vogt, A., *et al.* Shape-dependent Dissolution and Cellular Uptake of Silver Nanoparticles. *Langmuir* **34,** 1506–1519 (2018).

227. Department of Energy and Climate Change. *United kingdom Housing Energy Fact File* https://www.gov.uk/government/uploads/system/uploads/attachment_data/file/345141/uk_housing_fact_file_2013.pdf. 2013.

228. Hee, W., Alghoul, M., Bakhtyar, B., Elayeb, O., Shameri, M., Alrubaih, M. & Sopian, K. The Role of Window Glazing on Daylighting and Energy Saving in Buildings. *Renewable and Sustainable Energy Reviews* **42,** 323–343 (2015).

229. Department of Energy and Climate Change. *Energy Consumption in the UK (2015) - Chapter 1: Overall Energy Consumption in the UK Since 1970* https://www.gov.uk/government/uploads/system/uploads/attachment_data/file/449102/ECUK_Chapter_1_-_Overall_factsheet.pdf. 2015.

230. Jelle, B. P., Hynd, A., Gustavsen, A., Arasteh, D., Goudey, H. & Hart, R. Fenestration of Today and Tomorrow: A State-of-the-art Review and Future Research Opportunities. *Solar Energy Materials and Solar Cells* **96,** 1–28 (2012).

231. Ando, E & Miyazaki, M. Moisture Resistance of the Low-emissivity Coatings With a Layer Structure of Al-doped ZnO/Ag/Al-doped ZnO. *Thin Solid Films* **392,** 289–293 (2001).

232. Chiba, K., Takahashi, T., Kageyama, T. & Oda, H. Low-emissivity Coating of Amorphous Diamond-like Carbon/Ag-alloy Multilayer on Glass. *Applied surface science* **246,** 48–51 (2005).

233. Ando, E, Suzuki, S, Aomine, N, Miyazaki, M & Tada, M. Sputtered Silver-based Low-emissivity Coatings With High Moisture Durability. *Vacuum* **59,** 792–799 (2000).

234. Gao, T., Jelle, B. P. & Gustavsen, A. Antireflection Properties of Monodisperse Hollow Silica Nanospheres. *Applied Physics A* **110,** 65–70 (2013).

235. Ministry of Defence. *Defence Imagery website* Accessed: 08/10/19. <http://www.defenceimagery.mod.uk/fotoweb/>.

236. Ramesh, G., Sudheendran, K, Raju, K., Sreedhar, B & Radhakrishnan, T. Microwave Absorber Based on Silver Nanoparticle-embedded Polymer Thin Film. *Journal of nanoscience and nanotechnology* **9,** 261–266 (2009).

237. Melvin, G. J. H., Ni, Q.-Q., Suzuki, Y. & Natsuki, T. Microwave-absorbing Properties of Silver Nanoparticle/carbon Nanotube Hybrid Nanocomposites. *Journal of Materials Science* **49,** 5199–5207 (2014).

238. Emborg, J. & Dalgaard, P. Growth, Inactivation and Histamine Formation of *Morganella psychrotolerans* and *Morganella morganii* - Development and Evaluation of Predictive Models. *Int J Food Microbiol* **128,** 234–243 (2008).

239. Pantidos, N., Edmundson, M. C. & Horsfall, L. Room Temperature Bioproduction, Isolation and Antimicrobial Properties of Stable Elemental Copper Nanoparticles. *New Biotechnology* **40,** 275–281 (2018).

240. Singh, M., Sinha, I. & Mandal, R. K. Role of pH in the Green Synthesis of Silver Nanoparticles. *Materials Letters* **63,** 425–427 (2009).

241. Alqadi, M. K., Abo Noqtah, O. A., Alzoubi, F. Y., Alzouby, J. & Aljarrah, K. pH Effect on the Aggregation of Silver Nanoparticles Synthesized by Chemical Reduction. *Materials Science-Poland* **32,** 107–111 (2014).

242. Zhang, L., Li, X., He, R., Wu, L., Zhang, L. & Zeng, J. Chloride-induced Shape Transformation of Silver Nanoparticles in a Water Environment. *Environmental Pollution* **204,** 145–151 (2015).

243. Carboni, M. *Silver nanoprisms embedded in a polymeric matrix for energy saving glazing* PhD thesis (University of Southampton, 2014).

244. Tang, B., Xu, S., An, J., Zhao, B., Xu, W. & Lombardi, J. R. Kinetic Effects of Halide Ions on the Morphological Evolution of Silver Nanoplates. *Physical Chemistry Chemical Physics* **11,** 10286–10292 (2009).

245. Emborg, J., Dalgaard, P. & Ahrens, P. *Morganella psychrotolerans* Sp. Nov., a Histamine-producing Bacterium Isolated From Various Seafoods. *International Journal of Systematic and Evolutionary Microbiology* **56,** 2473–2479 (2006).

246. Sun, Y. & Xia, Y. Triangular Nanoplates of Silver: Synthesis, Characterization, and Use as Sacrificial Templates for Generating Triangular Nanorings of Gold. *Advanced Materials* **15,** 695–699 (2003).

247. Metraux, G. S. & Mirkin, C. A. Rapid Thermal Synthesis of Silver Nanoprisms With Chemically Tailorable Thickness. *Advanced Materials* **17,** 412–415 (2005).

248. Ballottin, D., Fulaz, S., Souza, M. L., Corio, P., Rodrigues, A. G., Souza, A. O., Gaspari, P. M., Gomes, A. F., Gozzo, F., Tasic, L. & et al. Elucidating Protein Involvement in the Stabilization of the Biogenic Silver Nanoparticles. *Nanoscale Research Letters* **11** (2016).

249. Firdhouse, M. J. & Lalitha, P. Biosynthesis of Silver Nanoparticles and Its Applications. *Journal of Nanotechnology* **2015,** 18 (2015).

250. Maqdoom, F., Sabeen, H. & Zarina, S. Biosynthesis of Nanoparticles by Cell-free Extract of *Bacillus subtilis*. *Journal of Environmental Research and Development* **9,** 389–395 (2014).

251. Grzelczak, M. & Liz-Marzán, L. M. The Relevance of Light in the Formation of Colloidal Metal Nanoparticles. *Chemical Society Reviews* **43,** 2089–2097 (2014).

252. Jones, E., Oliphant, T., Peterson, P., *et al. scipy: Open Source Scientific Tools for python* 2001-.

253. Paramelle, D., Sadovoy, A., Gorelik, S., Free, P., Hobley, J. & Fernig, D. G. A Rapid Method to Estimate the Concentration of Citrate Capped Silver Nanoparticles From UV-visible Light Spectra. *Analyst* **139,** 4855–4861 (2014).

254. Kshirsagar, P., Sangaru, S. S., Malvindi, M. A., Martiradonna, L., Cingolani, R. & Pompa, P. P. Synthesis of Highly Stable Silver Nanoparticles by Photoreduction and Their Size Fractionation by Phase Transfer Method. *Colloids and Surfaces A: Physicochemical and Engineering Aspects* **392,** 264–270 (2011).

255. Rossi, L. M., Fiorio, J. L., Garcia, M. A. S. & Ferraz, C. P. The Role and Fate of Capping Ligands in Colloidally Prepared Metal Nanoparticle Catalysts. *Dalton Transactions* **47,** 5889–5915 (2018).

256. Maddinedi, S. B., Mandal, B. K. & Anna, K. K. Tyrosine Assisted Size Controlled Synthesis of Silver Nanoparticles and Their Catalytic, *in vitro* Cytotoxicity Evaluation. *Environmental Toxicology and Pharmacology* **51,** 23–29 (2017).

257. Shankar, S. & Rhim, J.-W. Amino Acid Mediated Synthesis of Silver Nanoparticles and Preparation of Antimicrobial Agar/silver Nanoparticles Composite Films. *Carbohydrate Polymers* **130,** 353–363 (2015).

258. Sato-Berr, R., Redón, R., Vázquez-Olmos, A. & Saniger, J. M. Silver Nanoparticles Synthesized by Direct Photoreduction of Metal Salts. Application in Surface-enhanced Raman Spectroscopy. *Journal of Raman Spectroscopy* **40,** 376–380 (2009).

259. Turkevich, J., Stevenson, P. C. & Hillier, J. A Study of the Nucleation and Growth Processes in the Synthesis of Colloidal Gold. *Discussions of the Faraday Society* **11,** 55–75 (1951).

260. Xuming, Z., Yu Lim, C., Ru-Shi, L. & Din Ping, T. Plasmonic Photocatalysis. *Reports on Progress in Physics* **76,** 046401 (2013).

261. Javaid, A., Oloketuyi, S. F., Khan, M. M. & Khan, F. Diversity of Bacterial Synthesis of Silver Nanoparticles. *BioNanoScience* **8,** 43–59 (2018).

262. Tilton, R. C. & Rosenberg, B. Reversal of the Silver Inhibition of Microorganisms by Agar. *Applied and environmental microbiology* **35,** 1116–1120 (1978).

263. Mafuné, F., Kohno, J.-y., Takeda, Y., Kondow, T. & Sawabe, H. Structure and Stability of Silver Nanoparticles in Aqueous Solution Produced by Laser Ablation. *The Journal of Physical Chemistry B* **104,** 8333–8337 (2000).

264. Jahn, A., Reiner, J. E., Vreeland, W. N., DeVoe, D. L., Locascio, L. E. & Gaitan, M. Preparation of Nanoparticles by Continuous-flow Microfluidics. *Journal of Nanoparticle Research* **10,** 925–934 (2008).

265. Ma, J., Lee, S. M.-Y., Yi, C. & Li, C.-W. Controllable Synthesis of Functional Nanoparticles by Microfluidic Platforms for Biomedical Applications – a Review. *Lab on a Chip* **17,** 209–226 (2017).

266. Zhao, C.-X. & Middelberg, A. P. J. Two-phase Microfluidic Flows. *Chemical Engineering Science* **66,** 1394–1411 (2011).

267. Liu, G., Ma, X., Sun, X., Jia, Y. & Wang, T. Controllable Synthesis of Silver Nanoparticles Using Three-phase Flow Pulsating Mixing Microfluidic Chip. *Advances in Materials Science and Engineering* **2018,** 14 (2018).

268. Lee, C.-Y., Chang, C.-L., Wang, Y.-N. & Fu, L.-M. Microfluidic Mixing: A Review. *International journal of molecular sciences* **12,** 3263–3287 (2011).

269. Wegner, J., Ceylan, S. & Kirschning, A. Ten Key Issues in Modern Flow Chemistry. *Chemical Communications* **47,** 4583–4592 (2011).

270. Newman, S. G. & Jensen, K. F. The Role of Flow in Green Chemistry and Engineering. *Green Chemistry* **15,** 1456–1472 (2013).

271. Wiles, C. & Watts, P. Continuous Flow Reactors: A Perspective. *Green Chemistry* **14,** 38–54 (2012).

272. Cristaldi, D. A., Yanar, F., Mosayyebi, A., García-Manrique, P., Stulz, E., Carugo, D. & Zhang, X. Easy-to-perform and Cost-effective Fabrication of Continuous-flow Reactors and Their Application for Nanomaterials Synthesis. *New Biotechnology* **47,** 1–7 (2018).

273. Huang, H., du Toit, H., Besenhard, M. O., Ben-Jaber, S., Dobson, P., Parkin, I. & Gavriilidis, A. Continuous Flow Synthesis of Ultrasmall Gold Nanoparticles in a Microreactor Using Trisodium Citrate and Their SERS Performance. *Chemical Engineering Science* **189,** 422–430 (2018).

274. Biedermann, G., Sillen, L. G., Lindberg, B. & Dodson, R. M. *Studies on the Hydrolysis of Metal Ions. Part 30. a Critical Survey of the Solubility Equilibria of Ag_2O.* in (1960).

275. Flom, D. G. & Porile, N. T. Friction of Teflon Sliding on Teflon. *Journal of Applied Physics* **26,** 1088–1092 (1955).

276. Zhang, J., Li, J. & Han, Y. Superhydrophobic PTFE Surfaces by Extension. *Macromolecular Rapid Communications* **25,** 1105–1108 (2004).

277. Huang, J., Lin, L., Li, Q., Sun, D., Wang, Y., Lu, Y., He, N., Yang, K., Yang, X., Wang, H., Wang, W. & Lin, W. Continuous-flow Biosynthesis of Silver Nanoparticles by Lixivium of Sundried *Cinnamomum camphora* Leaf in Tubular Microreactors. *Industrial and Engineering Chemistry Research* **47,** 6081–6090 (2008).

278. He, S. T., Liu, Y. L. & Maeda, H. Controlled Synthesis of Colloidal Silver Nanoparticles in Capillary Micro-flow Reactor. *Journal of Nanoparticle Research* **10,** 209–215 (2008).

279. Yan, W., Yang, L., Chen, J., Wu, Y., Wang, P. & Li, Z. *In situ* Two-step Photoreduced SERS Materials for On-chip Single-molecule Spectroscopy With High Reproducibility. *Advanced Materials* **29,** 1702893 (2017).

280. Zmijan, R., Carboni, M., Capretto, L., Stulz, E. & Zhang, X. *In situ* Microspectroscopic Monitoring Within a Microfluidic Reactor. *RSC Advances* **4,** 14569–14572 (2014).

281. Gunther, A. & Jensen, K. F. Multiphase Microfluidics: From Flow Characteristics to Chemical and Materials Synthesis. *Lab on a Chip* **6,** 1487–1503 (2006).

282. DeLaney, E. N., Lee, D. S., Elliott, L. D., Jin, J., Booker-Milburn, K. I., Poliakoff, M. & George, M. W. A Laboratory-scale Annular Continuous Flow Reactor for UV Photochemistry Using Excimer Lamps for Discrete Wavelength Excitation and Its Use in a Wavelength Study of a Photodecarboxlyative Cyclisation. *Green Chemistry* **19,** 1431–1438 (2017).

283. Pennathur, S. Flow Control in Microfluidics: Are the Workhorse Flows Adequate? *Lab on a Chip* **8,** 383–387 (2008).

284. Stone, H. A. & Kim, S. Microfluidics: Basic Issues, Applications, and Challenges. *AIChE Journal* **47,** 1250–1254 (2001).

285. Salafi, T., Zeming, K. K. & Zhang, Y. Advancements in Microfluidics for Nanoparticle Separation. *Lab on a Chip* **17,** 11–33 (2017).

286. Sajeesh, P. & Sen, A. K. Particle Separation and Sorting in Microfluidic Devices: A Review. *Microfluidics and Nanofluidics* **17,** 1–52 (2014).

287. Dalwadi, G., Benson, H. A. E. & Chen, Y. Comparison of Diafiltration and Tangential Flow Filtration for Purification of Nanoparticle Suspensions. *Pharmaceutical Research* **22,** 2152–2162 (2005).

288. Maurer, E. I., Sharma, M., Schlager, J. J. & Hussain, S. M. Systematic Analysis of Silver Nanoparticle Ionic Dissolution by Tangential Flow Filtration: Toxicological Implications. *Nanotoxicology* **8,** 718–727 (2014).

289. Dorney, K. M., Baker, J. D., Edwards, M. L., Kanel, S. R., O'Malley, M. & Pavel Sizemore, I. E. Tangential Flow Filtration of Colloidal Silver Nanoparticles: A "green" Laboratory Experiment for Chemistry and Engineering Students. *Journal of Chemical Education* **91,** 1044–1049 (2014).

290. Guo, W., Ngo, H.-H. & Li, J. A Mini-review on Membrane Fouling. *Bioresource Technology* **122,** 27–34 (2012).

291. Levard, C., Hotze, E. M., Lowry, G. V. & Brown, G. E. Environmental Transformations of Silver Nanoparticles: Impact on Stability and Toxicity. *Environmental Science & Technology* **46,** 6900–6914 (2012).

292. Chakraborty, I., Feliu, N., Roy, S., Dawson, K. & Parak, W. J. Protein-mediated Shape Control of Silver Nanoparticles. *Bioconjugate chemistry* **29,** 1261–1265 (2018).

293. Pu, F., Ran, X., Guan, M., Huang, Y., Ren, J. & Qu, X. Biomolecule-templated Photochemical Synthesis of Silver Nanoparticles: Multiple Readouts of Localized Surface Plasmon Resonance for Pattern Recognition. *Nano Research* **11,** 3213–3221 (2018).

294. Movasaghi, Z., Rehman, S. & Rehman, I. U. Raman Spectroscopy of Biological Tissues. *Applied Spectroscopy Reviews* **42,** 493–541 (2007).

295. Hervé, R, Collin, R, Pinchin, H., Secker, T. & Keevil, C. W. A Rapid Dual Staining Procedure for the Quantitative Discrimination of Prion Amyloid From Tissues Reveals How Interactions Between Amyloid and Lipids in Tissue Homogenates May Hinder the Detection of Prions. *Journal of microbiological methods* **77,** 90–97 (2009).

296. Consortium, T. U. uniprot: A Worldwide Hub of Protein Knowledge. *Nucleic Acids Research* **47,** D506–D515 (2018).

297. *Chapter 5 - the Value of UV, Fluorescence, and FTIR Spectroscopy in Biopharmaceutical Development* (eds Houde, D. J. & Berkowitz, S. A.) 87–107. ISBN: 978-0-444-59573-7 (Amsterdam, 2015).

298. Rivera, M. C., Maguire, B. & Lake, J. A. Isolation of Ribosomes and Polysomes. *Cold Spring Harbor Protocols* **2015** (2015).

299. Lodish, H., Berk, A., Zipursky, S. L., Matsudaira, P., Baltimore, D. & Darnell, J. Molecular Cell Biology 4th Edition. *National Center for Biotechnology Information, Bookshelf,* Section 3.5, Purifying, Detecting, and Characterizing Proteins. (2000).

300. Kapoor, S., Lawless, D., Kennepohl, P., Meisel, D. & Serpone, N. Reduction and Aggregation of Silver Ions in Aqueous Gelatin Solutions. *Langmuir* **10,** 3018–3022 (1994).

301. Israelsen, N. D., Hanson, C. & Vargis, E. Nanoparticle Properties and Synthesis Effects on Surface-enhanced Raman Scattering Enhancement Factor: an Introduction. *The Scientific World Journal* **2015** (2015).

302. Berthomieu, C. & Hienerwadel, R. Fourier Transform Infrared (FTIR) Spectroscopy. *Photosynthesis research* **101,** 157–170 (2009).

303. Liu, H., Zhu, J., Hu, Q. & Rao, X. *Morganella morganii*, a Non-negligent Opportunistic Pathogen. *International Journal of Infectious Diseases* **50,** 10–17 (2016).

304. Chen, Y.-T., Peng, H.-L., Shia, W.-C., Hsu, F.-R., Ken, C.-F., Tsao, Y.-M., Chen, C.-H., Liu, C.-E., Hsieh, M.-F., Chen, H.-C., *et al. Whole-genome Sequencing and Identification of Morganella morganii Kt Pathogenicity-related Genes* in *BMC genomics* **13** (2012), S4.

305. Pailin, T, Kang, D., Schmidt, K & Fung, D. Detection of Extracellular Bound Proteinase in Eps-producing Lactic Acid Bacteria Cultures on Skim Milk Agar. *Letters in applied microbiology* **33,** 45–49 (2001).

306. Invitrogen. *Simplyblue Safestainfast, Sensitive, and Safe Protein Staining* Accessed: 30/09/19. <\url{https://assets.thermofisher.com/TFS-Assets/LSG/manuals/simplyblue_man.pdf}>.

307. Invitrogen. *Sypro Ruby Protein Gel Stain* Accessed: 30/09/19. 2007. <\url{https://assets.thermofisher.com/TFS-Assets/LSG/manuals/mp12000.pdf}>.

308. Voeikova, T., Zhuravliova, O., Bulushova, N., Veiko, V., Ismagulova, T., Lupanova, T., Shaitan, K. & Debabov, V. The "protein Corona" of Silver-sulfide Nanoparticles Obtained Using Gram-negative And-positive Bacteria. *Molecular Genetics, Microbiology and Virology* **32,** 204–211 (2017).

309. Nakamura, S. & Minamino, T. Flagella-driven Motility of Bacteria. *Biomolecules* **9,** 279 (2019).

310. Chaban, B., Hughes, H. V. & Beeby, M. *The Flagellum in Bacterial Pathogens: For Motility and a Whole Lot More* in *Seminars in cell & developmental biology* **46** (2015), 91–103.

311. Saier Jr, M. H. Microcompartments and Protein Machines in Prokaryotes. *Journal of molecular microbiology and biotechnology* **23,** 243–269 (2013).

312. Aizawa, S.-I. & Kubori, T. Bacterial Flagellation and Cell Division. *Genes to cells* **3,** 625–634 (1998).

313. Schmidt, A., Kochanowski, K., Vedelaar, S., Ahrné, E., Volkmer, B., Callipo, L., Knoops, K., Bauer, M., Aebersold, R. & Heinemann, M. The Quantitative and Condition-dependent *Escherichia coli* Proteome. *Nature biotechnology* **34,** 104 (2016).

314. Weijland, A., Harmark, K., Cool, R. H., Anborgh, P. H. & Parmeggiani, A. Elongation Factor Tu: A Molecular Switch in Protein Biosynthesis. *Molecular microbiology* **6,** 683–688 (1992).

315. Ishihama, Y., Schmidt, T., Rappsilber, J., Mann, M., Hartl, F. U., Kerner, M. J. & Frishman, D. Protein Abundance Profiling of the *Escherichia coli* Cytosol. *BMC genomics* **9,** 102 (2008).

316. Kędziora, A., Speruda, M., Krzyżewska, E., Rybka, J., Łukowiak, A. & Bugla-Płoskońska, G. Similarities and Differences Between Silver Ions and Silver in Nanoforms as Antibacterial Agents. *International journal of molecular sciences* **19,** 444 (2018).

317. Juling, S., Niedzwiecka, A., Bohmert, L., Lichtenstein, D., Selve, S., Braeuning, A., Thunemann, A. F., Krause, E. & Lampen, A. Protein Corona Analysis of Silver Nanoparticles Links to Their Cellular Effects. *Journal of proteome research* **16,** 4020–4034 (2017).

318. Lee, Y. K., Choi, E.-J., Webster, T. J., Kim, S.-H. & Khang, D. Effect of the Protein Corona on Nanoparticles for Modulating Cytotoxicity and Immunotoxicity. *International journal of nanomedicine* **10,** 97 (2015).

319. Durán, N., Silveira, C. P., Durán, M. & Martinez, D. S. T. Silver Nanoparticle Protein Corona and Toxicity: A Mini-review. *Journal of nanobiotechnology* **13,** 55 (2015).

320. Sahneh, F. D., Scoglio, C. & Riviere, J. Dynamics of Nanoparticle-protein Corona Complex Formation: Analytical Results From Population Balance Equations. *PloS one* **8,** e64690 (2013).

321. Vilanova, O., Mittag, J. J., Kelly, P. M., Milani, S., Dawson, K. A., Radler, J. O. & Franzese, G. Understanding the Kinetics of Protein-Nanoparticle Corona Formation. *ACS nano* **10,** 10842–10850 (2016).

322. Dell'Orco, D., Lundqvist, M., Oslakovic, C., Cedervall, T. & Linse, S. Modeling the Time Evolution of the Nanoparticle-protein Corona in a Body Fluid. *PloS one* **5,** e10949 (2010).

323. Cedervall, T., Lynch, I., Lindman, S., Berggård, T., Thulin, E., Nilsson, H., Dawson, K. A. & Linse, S. Understanding the Nanoparticle-protein Corona Using Methods to Quantify Exchange Rates and Affinities of Proteins for Nanoparticles. *Proceedings of the National Academy of Sciences* **104,** 2050–2055 (2007).

324. Pugazhenthiran, N., Anandan, S., Kathiravan, G., Prakash, N. K. U., Crawford, S. & Ashokkumar, M. Microbial Synthesis of Silver Nanoparticles by *Bacillus* Sp. *Journal of Nanoparticle Research* **11,** 1811 (2009).

325. Sonkusre, P., Nanduri, R., Gupta, P. & Cameotra, S. S. Improved Extraction of Intracellular Biogenic Selenium Nanoparticles and Their Specificity for Cancer Chemoprevention. *Journal of Nanomedicine & Nanotechnology* **5,** 1 (2014).

326. Liu, S., Horak, J., Holdrich, M. & La.

327. Filbrun, S. L. & Driskell, J. D. A Fluorescence-based Method to Directly Quantify Antibodies Immobilized on Gold Nanoparticles. *Analyst* **141,** 3851–3857 (2016).

328. Yan, X., He, B., Liu, L., Qu, G., Shi, J., Hu, L. & Jiang, G. Antibacterial Mechanism of Silver Nanoparticles in *Pseudomonas aeruginosa*: Proteomics Approach. *Metallomics* **10,** 557–564 (2018).

329. Mirzajani, F., Askari, H., Hamzelou, S., Schober, Y., Rompp, A., Ghassempour, A. & Spengler, B. Proteomics Study of Silver Nanoparticles Toxicity on *Bacillus thuringiensis*. *Ecotoxicology and environmental safety* **100,** 122–130 (2014).

330. Cock, P. J., Antao, T., Chang, J. T., Chapman, B. A., Cox, C. J., Dalke, A., Friedberg, I., Hamelryck, T., Kauff, F., Wilczynski, B., *et al.* Biopython: Freely Available Python Tools for Computational Molecular Biology and Bioinformatics. *Bioinformatics* **25,** 1422–1423 (2009).

331. Kyte, J. & Doolittle, R. F. A Simple Method for Displaying the Hydropathic Character of a Protein. *Journal of molecular biology* **157,** 105–132 (1982).

332. Guruprasad, K., Reddy, B. B. & Pandit, M. W. Correlation Between Stability of a Protein and Its Dipeptide Composition: A Novel Approach for Predicting *in vivo* Stability of a Protein From Its Primary Sequence. *Protein Engineering, Design and Selection* **4,** 155–161 (1990).

333. Lobry, J. & Gautier, C. Hydrophobicity, Expressivity and Aromaticity Are the Major Trends of Amino-acid Usage in 999 *Escherichia coli* Chromosome-encoded Genes. *Nucleic Acids Research* **22,** 3174–3180 (1994).